

<sup>1</sup> Independent measurement of the T2K near detector constraint  
<sup>2</sup> using the off-axis pi-zero detector

<sup>3</sup> Hogan, Matthew<sup>1</sup>  
Toki, Walter<sup>2</sup>

<sup>4</sup> 21st October 2019

<sup>1</sup>[hoganman@rams.colostate.edu](mailto:hoganman@rams.colostate.edu)  
<sup>2</sup>[walter.toki@colostate.edu](mailto:walter.toki@colostate.edu)

## Abstract

The Tokai to Kamioka (T2K) experiment is a long-baseline neutrino oscillation experiment hosted in Japan searching for electron neutrino appearance in a high purity muon neutrino beam. In order to constrain the systematic uncertainties in the oscillation analysis, a dedicated near detector (ND) complex called ND280 is located 280 meters from the neutrino production source in line of the beam. To date, the Fine Grain Detector (FGD) in ND280 has provided the ND constraint using a binned maximum likelihood estimate fit. This thesis describes the effort to validate the ND constraint using the same framework, but with an independent data set from the ND280 pi-zero detector (PØD). Expanding on previously developed PØD selections, new selections have been developed to select neutrino and antineutrino events in one and multiple track topologies on water and carbon. These selections are shown to have similar sensitivity to the T2K flux and cross section systematic uncertainties. A comparison between the predicted neutrino energy spectrum at Super-Kamiokande is performed between the FGD-only and PØD-only fit results using the P-Theta framework.

# Contents

<sup>18</sup>	<b>Contents</b>	<b>1</b>
<sup>19</sup>	<b>List of Figures</b>	<b>3</b>
<sup>20</sup>	<b>List of Tables</b>	<b>7</b>
<sup>21</sup>	<b>1 Executive Summary</b>	<b>8</b>
<sup>22</sup>	<b>2 The BANFF Fit Likelihood</b>	<b>9</b>
<sup>23</sup>	2.1 Conditional Probability Density Functions . . . . .	10
<sup>24</sup>	2.2 The BANFF Fit Test Statistic . . . . .	11
<sup>25</sup>	2.3 Summary . . . . .	15
<sup>26</sup>	<b>3 The PØD Selections and Samples</b>	<b>16</b>
<sup>27</sup>	3.1 The ND280 Global Reconstruction . . . . .	17
<sup>28</sup>	3.2 Selection Cuts . . . . .	18
<sup>29</sup>	3.3 Selection Kinematics . . . . .	22
<sup>30</sup>	3.4 Summary . . . . .	43
<sup>31</sup>	<b>4 The BANFF Fit Parameters</b>	<b>45</b>
<sup>32</sup>	4.1 Fit Binning . . . . .	45
<sup>33</sup>	4.2 Systematic Uncertainties and Penalty Terms . . . . .	48
<sup>34</sup>	4.3 Summary . . . . .	76
<sup>35</sup>	<b>5 Validation of the BANFF Fit Procedure</b>	<b>79</b>
<sup>36</sup>	5.1 Asimov Data Fit . . . . .	79
<sup>37</sup>	5.2 Fake Data Fits . . . . .	83
<sup>38</sup>	5.3 Summary . . . . .	97

<sup>40</sup>	<b>6 Results of the BANFF Fit Using the PØD Samples</b>	<b>98</b>
<sup>41</sup>	6.1 Prefit Sample Distributions . . . . .	98
<sup>42</sup>	6.2 Postfit Results . . . . .	99
<sup>43</sup>	6.3 Summary . . . . .	127
<sup>44</sup>	<b>7 Discussion</b>	<b>136</b>
<sup>45</sup>	7.1 Prediction of the T2K Oscillation Analysis Samples . . . . .	137
<sup>46</sup>	7.2 Analysis Improvements . . . . .	139
<sup>47</sup>	7.3 Future Prospects: Joint PØD+FGD Fit . . . . .	145
<sup>48</sup>	<b>Bibliography</b>	<b>148</b>
<sup>49</sup>	<b>A Bin Normalizations</b>	<b>154</b>
<sup>50</sup>	<b>B Toy Experiment Variations</b>	<b>170</b>
<sup>51</sup>	<b>C Cross Section Variations</b>	<b>197</b>
<sup>52</sup>	<b>D Log-Likelihood Sample Scans</b>	<b>214</b>
<sup>53</sup>	<b>E Log-Likelihood Penalty Scans</b>	<b>227</b>
<sup>54</sup>	<b>F Computing Resources</b>	<b>239</b>
<sup>55</sup>	<b>G Postfit Parameters</b>	<b>241</b>
<sup>56</sup>	<b>H Postfit ROC Curves</b>	<b>262</b>
<sup>57</sup>	<b>I Cross-Validated Fit</b>	<b>273</b>

# 58 List of Figures

59	3.1 The PØD $\nu_\mu$ and $\bar{\nu}_\mu$ CC-0 $\pi$ Selection Kinematics . . . . .	17
60	3.2 Frequently Used Legends in the Analysis . . . . .	25
61	3.3 Reconstructed Kinematics of the $\nu_\mu$ in FHC Mode CC 1-Track Selection Categorized by CCQE 62 and Non-CCQE Interactions . . . . .	26
63	3.4 Reconstructed Kinematics of the $\nu_\mu$ in FHC Mode CC 1-Track Selection Categorized by the 64 True Particle Matched to the Main Track . . . . .	27
65	3.5 Reconstructed Vertex Z Position of the $\nu_\mu$ in FHC Mode CC 1-Track Selection . . . . .	28
66	3.6 Efficiency and Purity of the $\nu_\mu$ in FHC Mode CC 1-Track Selection . . . . .	29
67	3.7 True Kinematics of the $\nu_\mu$ in FHC Mode CC 1-Track Selection . . . . .	29
68	3.8 Reconstructed Kinematics of the $\nu_\mu$ in FHC Mode CC N-Tracks Selection Categorized by 69 CCQE and Non-CCQE Interactions . . . . .	30
70	3.9 Reconstructed Kinematics of the $\nu_\mu$ in FHC Mode CC N-Tracks Selection Categorized by the 71 True Particle Matched to the Main Track . . . . .	31
72	3.10 Reconstructed Vertex Z Position of the $\nu_\mu$ in FHC Mode CC N-Tracks Selection Categorized 73 by the True Target Nucleus . . . . .	31
74	3.11 Efficiency and Purity of the $\nu_\mu$ in FHC Mode CC N-Tracks Selection . . . . .	32
75	3.12 True Kinematics of the $\nu_\mu$ in FHC Mode CC N-Tracks Selection . . . . .	33
76	3.13 Reconstructed Kinematics of the $\bar{\nu}_\mu$ in RHC Mode CC 1-Track Selection Categorized by 77 CCQE and Non-CCQE Interactions . . . . .	34
78	3.14 Reconstructed Kinematics of the $\bar{\nu}_\mu$ in RHC Mode CC 1-Track Selection Categorized by the 79 True Particle Matched to the Main Track . . . . .	35
80	3.15 Efficiency and Purity of the $\bar{\nu}_\mu$ in RHC Mode CC 1-Track Selection . . . . .	35
81	3.16 True Kinematics of the $\bar{\nu}_\mu$ in RHC Mode CC 1-Track Selection . . . . .	36

82	3.17 Reconstructed Kinematics of the $\bar{\nu}_\mu$ in RHC Mode CC N-Tracks Selection Categorized by CCQE and Non-CCQE Interactions . . . . .	36
83		
84	3.18 Reconstructed Kinematics of the $\bar{\nu}_\mu$ in RHC Mode CC N-Tracks Selection Categorized by the True Particle Matched to the Main Track . . . . .	37
85		
86	3.19 Efficiency and Purity of the $\bar{\nu}_\mu$ in RHC Mode CC N-Tracks Selection . . . . .	38
87		
88	3.20 True Kinematics of the $\bar{\nu}_\mu$ in RHC Mode CC N-Tracks Selection . . . . .	39
89		
90	3.21 Reconstructed Kinematics of the $\nu_\mu$ Background in RHC Mode CC 1-Track Selection Cate- gorized by CCQE and Non-CCQE Interactions . . . . .	40
91		
92	3.22 Reconstructed Kinematics of the $\nu_\mu$ Background in RHC Mode CC 1-Track Selection Cate- gorized by the True Particle Matched to the Main Track . . . . .	40
93		
94	3.23 Efficiency and Purity of the $\nu_\mu$ Background in RHC Mode CC 1-Track Selection . . . . .	41
95		
96	3.24 True Kinematics of the $\nu_\mu$ Background in RHC Mode CC 1-Track Selection . . . . .	41
97		
98	3.25 Reconstructed Kinematics of the $\nu_\mu$ Background in RHC Mode CC N-Tracks Selection Cate- gorized by CCQE and Non-CCQE Interactions . . . . .	42
99		
100	3.26 Reconstructed Kinematics of the $\nu_\mu$ Background in RHC Mode CC N-Tracks Selection Cate- gorized by the True Particle Matched to the Main Track . . . . .	42
101		
102	3.27 Efficiency and Purity of the $\nu_\mu$ Background in RHC Mode CC N-Tracks Selection . . . . .	43
103		
104	3.28 True Kinematics of the $\nu_\mu$ Background in RHC Mode CC N-Tracks Selection . . . . .	44
105		
106	4.1 Main Track Momentum Resolution for the $\nu_\mu$ in FHC Mode CC 1-Track Sample . . . . .	46
107		
108	4.2 Main Track Angular Residuals for the $\nu_\mu$ in FHC Mode CC 1-Track Sample . . . . .	47
109		
110	4.3 The BANFF Prefit Flux Covariance Matrix . . . . .	50
111		
112	4.4 Neutrino Flux Prediction at SK and Flux Bin Edges . . . . .	50
113		
114	4.5 Vertex Distribution Showing Evidence of PØD Bulging . . . . .	59
115		
116	4.6 Bin Normalizations Edges for the $\nu_\mu$ in FHC Mode Samples . . . . .	63
117		
118	4.7 Bin Normalization Edges for the $\bar{\nu}_\mu$ in RHC Mode Samples . . . . .	64
119		
120	4.8 Bin Normalizations for the $\nu_\mu$ Background in RHC Mode Samples . . . . .	65
121		
122	4.9 Event Variations in Observable Normalization Bins . . . . .	66
123		
124	4.10 Detector Penalty Covariance Matrix . . . . .	69
125		
126	4.11 Principal Component for the Sample Variance . . . . .	70
127		
128	4.12 Cross Section Parameters Prefit Covariance and Correlation Matrices . . . . .	77
129		
130	5.1 Complete Prefit Correlation Matrix for the BANFF Fit. . . . .	80
131		
132	5.2 Test Statistic Scans for Variations of Fit Parameters in the Asimov Set . . . . .	84
133		

114	5.3 Asimov Fit Results for the Flux at ND280 . . . . .	85
115	5.4 Asimov Fit Results for the Flux at Super-K . . . . .	86
116	5.5 Asimov Fit Results for the Bin Normalization Parameters . . . . .	87
117	5.6 Asimov Fit Results for the Cross Section and FSI Parameters . . . . .	88
118	5.7 Complete Postfit Correlation Matrix for the Asimov Data Fit . . . . .	89
119	5.8 Flux and Cross Section Postfit Correlation Matrix for the Asimov Data Fit . . . . .	89
120	5.9 Neutrino Energy Distributions in the High Energy Neutrino Flux Variation Fake Data Set . . . . .	91
121	5.10 Neutrino Energy Distributions in the High Energy Neutrino Flux Variation Fake Data Set (Continued) . . . . .	92
122	5.11 Postfit Parameters for the High Energy Neutrino in FHC Flux Fake Data fit . . . . .	93
123	5.12 Lepton Candidate Momentum Distributions in the Single Pion Event Rate Variation Fake Data Set . . . . .	94
124	5.13 Lepton Candidate Momentum Distributions in the Single Pion Event Rate Variation Fake Data Set (Continued) . . . . .	95
125	5.14 Postfit Parameters for the $C_A^5$ Fake Data Fit . . . . .	96
126	6.1 Prefit for the Water-In $\nu_\mu$ in FHC Mode CC 1-Track Sample . . . . .	100
127	6.2 Prefit for the Water-In $\nu_\mu$ in FHC Mode CC N-Tracks Sample . . . . .	101
128	6.3 Prefit for the Water-In $\bar{\nu}_\mu$ in RHC Mode CC 1-Track Sample . . . . .	102
129	6.4 Prefit for the Water-In $\bar{\nu}_\mu$ in RHC Mode CC N-Tracks Sample . . . . .	103
130	6.5 Prefit for the Water-In $\nu_\mu$ in RHC Mode CC 1-Track Sample . . . . .	104
131	6.6 Prefit for the Water-In $\nu_\mu$ in RHC Mode CC N-Tracks Sample . . . . .	105
132	6.7 Prefit for the Water-Out $\nu_\mu$ in FHC Mode CC 1-Track Sample . . . . .	106
133	6.8 Prefit for the Water-Out $\nu_\mu$ in FHC Mode CC N-Tracks Sample . . . . .	107
134	6.9 Prefit for the Water-Out $\bar{\nu}_\mu$ in RHC Mode CC 1-Track Sample . . . . .	108
135	6.10 Prefit for the Water-Out $\bar{\nu}_\mu$ in RHC Mode CC N-Tracks Sample . . . . .	109
136	6.11 Prefit for the Water-Out $\nu_\mu$ in RHC Mode CC 1-Track Sample . . . . .	110
137	6.12 Prefit for the Water-Out $\nu_\mu$ in RHC Mode CC N-Tracks Sample . . . . .	111
138	6.13 Postfit for the Water-In $\nu_\mu$ in FHC Mode CC 1-Track Sample . . . . .	112
139	6.14 Postfit for the Water-In $\nu_\mu$ in FHC Mode CC N-Tracks Sample . . . . .	113
140	6.15 Postfit for the Water-In $\bar{\nu}_\mu$ in RHC Mode CC 1-Track Sample . . . . .	114
141	6.16 Postfit for the Water-In $\bar{\nu}_\mu$ in RHC Mode CC 1-Track Sample . . . . .	115
142	6.17 Postfit for the Water-In $\nu_\mu$ in RHC Mode CC 1-Track Sample . . . . .	116

146	6.18 Postfit for the Water-In $\nu_\mu$ in RHC Mode CC N-Tracks Sample . . . . .	117
147	6.19 Postfit for the Water-Out $\nu_\mu$ in FHC Mode CC 1-Track Sample . . . . .	118
148	6.20 Postfit for the Water-Out $\nu_\mu$ in FHC Mode CC N-Tracks Sample . . . . .	119
149	6.21 Postfit for the Water-Out $\bar{\nu}_\mu$ in RHC Mode CC 1-Track Sample . . . . .	120
150	6.22 Postfit for the Water-Out $\bar{\nu}_\mu$ in RHC Mode CC N-Tracks Sample . . . . .	121
151	6.23 Postfit for the Water-Out $\nu_\mu$ in RHC Mode CC 1-Track Sample . . . . .	122
152	6.24 Postfit for the Water-Out $\nu_\mu$ in RHC Mode CC N-Tracks Sample . . . . .	123
153	6.25 Postfit ND280 Flux Parameters for the PØD-only BANFF Fit . . . . .	128
154	6.26 Postfit SK Flux Parameters for the PØD-only BANFF Fit . . . . .	129
155	6.27 Postfit Cross Section Parameters for the PØD-only BANFF Fit . . . . .	130
156	6.28 Prefit and Postfit Bin Normalization Parameters . . . . .	131
157	6.29 The 2p2h Shape Mirrored Spline . . . . .	132
158	6.30 Postfit Correlation Matrix . . . . .	133
159	6.31 Prefit and Post Flux and Cross Section Parameter Correlations . . . . .	134
160	6.32 Prefit and Post Flux and Cross Section Parameter Correlations . . . . .	135
161	7.1 Reconstructed $\nu_\mu$ and $\bar{\nu}_\mu$ CCQE-enriched Energy Distributions at SK . . . . .	138
162	7.2 Reconstructed $\nu_e$ CCQE-enriched Energy Distribution at SK . . . . .	138
163	7.3 Reconstructed $\nu_e$ CCQE-Enriched Energy Distribution at SK . . . . .	139
164	7.4 Cross-Validation Curve for the BANFF Fit Regularization Strength. . . . .	141
165	7.5 The Lasso vs Elastic Net Constraint . . . . .	144
166	D.1 Corrected 2p2h Shape Location Scans . . . . .	226

# List of Tables

168	2.1 Parameters that Affect the Analysis Bins . . . . .	12
169	3.1 The PØD Water Target Fiducial Volume and Veto Corridor Definitions . . . . .	19
170	3.2 T2K Data-Taking Periods and Collected POT Used in the Analysis . . . . .	23
171	3.3 Enumeration of NEUT Interaction Modes . . . . .	24
172	4.1 Flux Binning and Uncertainties . . . . .	51
173	4.2 List of Detector Systematics in the Analysis . . . . .	57
174	4.3 Eigenvalues of the Sample Covariance . . . . .	70
175	4.4 Cross Section Model Fit Parameters in the BANFF Fit . . . . .	75
176	5.1 Event Rate Table for Asimov Set . . . . .	82
177	6.1 Neutrino-Nucleon Exposure on Target Elements . . . . .	125
178	7.1 Oscillation Parameters Used as Inputs for Studies of Simulated Data . . . . .	137
179	7.2 Number of Events Expected in the SK CCQE-enriched Samples . . . . .	139
180	7.3 Neutrino-Nucleon Exposure on Target Elements in a PØD+FGD Joint Fit . . . . .	147
181	A.1 Observable Normalization Fit Bins . . . . .	154
182	C.1 Event Rate Variations Per Cross Section Parameter Variation . . . . .	198
183	F.1 Computing Resources Used in this Thesis . . . . .	239
184	G.1 Prefit and Postfit Parameters with Errors . . . . .	242

<sub>185</sub> **Chapter 1**

<sub>186</sub> **Executive Summary**

<sub>187</sub> The Tokai to Kamioka (T2K) experiment is currently making critical measurements of  $\delta_{CP}$  and other prop-  
<sub>188</sub> erties that describe neutrino oscillations. Using a long-baseline of 295 km, a beam of muon-type neutrinos  
<sub>189</sub> (or antineutrinos) are detected to change flavor at the Super-Kamiokande (SK) detector. By counting the  
<sub>190</sub> number of oscillated neutrinos and antineutrinos, measurements on the oscillation parameters can be made.

<sub>191</sub> The largest sources of systematic uncertainty in the oscillation analysis are related to the flux of neutrinos  
<sub>192</sub> and the neutrino-nucleus cross section. Using data collected at the T2K near detector, ND280, stronger  
<sub>193</sub> constraints are placed on those systematic uncertainties in the analysis. The process for constraining these  
<sub>194</sub> uncertainties uses a binned maximum likelihood fit based on neutrino interaction topology. This technote  
<sub>195</sub> provides an independent measurement of the constraint using data collected using the T2K pi-zero detector  
<sub>196</sub> (PØD) in ND280.

<sub>197</sub> The technote is organized as follows. The binned likelihood procedure is described in Chapter 2 followed  
<sub>198</sub> by the data selections described in Chapter 3. The systematic uncertainties in the analysis and the fit  
<sub>199</sub> parameterization are described in Chapter 4. The validation of the fit procedure will be shown in Chapter  
<sub>200</sub> 5, which is followed by the results of the likelihood fit shown in Chapter 6. Finally, Chapter 7 provides some  
<sub>201</sub> concluding remarks and discussion on the results and possible analysis improvements.

202 **Chapter 2**

203 **The BANFF Fit Likelihood**

204 The T2K experiment has organized a task force dedicated to provide the near detector constraint for the  
205 oscillation analysis. This task force is called the “Beam And Near detector Flux task Force (BANFF)<sup>1</sup>. The  
206 BANFF group has implemented a binned likelihood maximization fit of the ND280 data for the oscillation  
207 analysis[1].

208 The BANFF near detector (ND) constraint fit is done separately from fitting the Super-Kamiokande  
209 (SK) data. In a joint fit, the measurements from both detectors are considered to estimate the oscillation  
210 parameters. This joint-fit approach is more computationally expensive since it must include all parameters  
211 that affect the both the ND and SK systematic uncertainties, also called nuisance parameters. Also the  
212 time to perform a fit increases non-linearly with increasing the number of fit parameters. Therefore the  
213 separate BANFF likelihood maximization, hitherto referred to as the “BANFF fit”, must include parameters  
214 that affect the measurement of the oscillation parameters. Then those fit parameters and their respective  
215 covariances are used as inputs in the oscillation analysis. This “divide-and-conquer” approach allows for  
216 more rapidly completed studies on the effects of model parameters and biases present. However, information  
217 encoded in the ND280 measurements for shared nuisances such as the neutrino flux is inevitably lost in the  
218 BANFF fit.

219 The modern BANFF fit is described in detail in the following reference [2]. To summarize the details,  
220 the BANFF fit uses a frequentist approach to find the best parameter set to maximize a binned likeli-  
221 hood. Subsequent updates to the BANFF fit have increased the sample sizes and systematic uncertainty  
222 parameterizations.

223 This chapter describes the BANFF fit and overview of the fitting procedure. First we introduce the  
224 concept of likelihood functions in Section 2.1. Then we explore the mechanics of the BANFF fit using

---

<sup>1</sup>Banff is a national park in Canada.

225 likelihood functions in Section 2.2. The final topic is a chapter summary in Section 2.3.

## 226 2.1 Conditional Probability Density Functions

227 Consider the problem of extracting physics parameters  $\vec{y}$  given some data vector  $\vec{N}$ . The conditional probability density function (PDF)  $\mathcal{P}$  to measure these parameters is given as

$$\mathcal{P}(\vec{y} \mid \vec{N}) = \frac{\mathcal{L}(\vec{N} \mid \vec{y}) \mathcal{P}(\vec{y})}{\int \mathcal{L}(\vec{N} \mid \vec{x}) \mathcal{P}(\vec{x}) d\vec{x}}, \quad (2.1)$$

229 where everything on the right of the vertical lines represents a condition on the probability.  $\mathcal{L}(\vec{N} \mid \vec{y})$  is the likelihood of the model with parameters  $\vec{y}$ ,  $\mathcal{P}(\vec{y})$  is the probability for the model, and the denominator is the normalization. A frequentist interpretation of the PDF is a proportion of outcomes of repeated trials or experiments. A likelihood function is an expression of the probability of observing data as a function of the model parameters in their appropriate ranges.

234 One arrives at Eqn. (2.1) by using the definition of compound probabilities

$$\mathcal{P}(A, B) = \mathcal{P}(B \mid A) \mathcal{P}(A), \quad (2.2)$$

235 to evaluate  $\mathcal{P}(\vec{y} \mid \vec{N})$  as

$$\mathcal{P}\left(\underbrace{\vec{y}}_B \mid \underbrace{\vec{N}}_A\right) = \frac{\mathcal{P}(\vec{N}, \vec{y})}{\mathcal{P}(\vec{N})}, \quad (2.3)$$

236 where the denominator is the normalization of the PDF. The compound PDF  $\mathcal{P}(\vec{N}, \vec{y})$  can be expanded 237 using Bayes' theorem which states

$$\mathcal{P}(A \mid B) \mathcal{P}(B) = \mathcal{P}(B \mid A) \mathcal{P}(A), \quad (2.4)$$

238 and combined with Eqn. (2.2) yields

$$\mathcal{P}\left(\underbrace{\vec{N}}_A, \underbrace{\vec{y}}_B\right) = \mathcal{P}(\vec{N} \mid \vec{y}) \times \mathcal{P}(\vec{y}), \quad (2.5)$$

239 where the PDFs to the left and right of the  $\times$  operator are the likelihoods and priors, respectively. Combining 240 resulting in Eqn. (2.3) and Eqn. (2.5) reproduces the original expression of Eqn. (2.1).

## 241 2.2 The BANFF Fit Test Statistic

242 Curve fitting is commonly used in particle physics in order to constrain unknown model parameters using  
243 histograms. This procedure seeks to find the “best” set of the model predictions,  $\theta$ , that match the data, as  
244 is the case for the BANFF fit. This analysis uses a chi-squared test to provide a goodness of fit metric, a  
245 parameter estimation (also referred to as “best fit parameters”), and a error estimation for the BANFF fit.

246 The BANFF fit is an attempt to maximize the agreement between the measured and predicted data  
247 curves at the ND280 detector. This is equivalent to maximizing a binned likelihood function  $\mathcal{L}$  of the ND280  
248 data given a set of parameters in the likelihood function that predict the measured rate. The use of likelihood  
249 functions in fits to histograms is explained further in reference [3] and the PDG review on statistics. By  
250 invoking Wilks’ theorem, also known as the likelihood ratio theorem, the likelihood maximization procedure  
251 is converted into a minimization problem involving a test statistic denoted as a chi-squared. Below is an  
252 explanation of the BANFF test statistic and the model terms.

### 253 2.2.1 Log-Likelihood Ratio

254 Consider many binned samples that select different charged current topologies. A convenient choice of  
255 observables for all the samples is the outgoing charged lepton  $l$  momentum  $P_l$  and angle  $\cos \theta_l$  as measured  
256 in the ND280 detector[4]. For each  $(P_l, \cos \theta_l)$  analysis bin  $i = 1, 2, \dots, M - 1, M$ , the likelihood is given by

$$\mathcal{L}(\vec{N}^d | \vec{N}^p) = \prod_{i=1}^M \frac{\left(\vec{N}_i^p\right)^{\vec{N}_i^d} \exp(-\vec{N}_i^p)}{\vec{N}_i^d!} \quad (2.6)$$

257 where  $\vec{N}_i^d$  is the number of observed data events in the  $i$ th bin and  $\vec{N}_i^p$  is the number of predicted events as  
258 a function of the fit parameters in the same bin. One recognizes the likelihood function in Eqn. (2.6) as a  
259 product of Poisson distributions, since this is counting data measured in  $M$  analysis bins. The parameters  
260 that affect the predicted event rate are:

- 261 • The cross section physics models, labeled as “xsec”,
- 262 • The neutrino flux, and
- 263 • The detector biases and inefficiencies.

Table 2.1: Parameters that affect the analysis bins. The top three parameters are fit while the others are constants set by the input data and bookkeeping.

Description	Symbol	Fit?
Fit bin normalizations	$\vec{d}$	Yes
Flux normalizations	$\vec{b}$	Yes
Cross section weights and norms.	$w(\vec{x})$	Yes
POT weight for the MC	$w^{\text{POT}}$	No
Flux bin selector	$\delta_{j,k}^{\text{Flux}}$	No
Number of flux parameters	$N^{\text{Flux}}$	No
Number of cross section parameters	$N^{\text{xsec}}$	No
Number of MC events	$N^{\text{MC}}$	No

264 We use these parameters to calculate the number of predicted charged current (CC) events  $N^{\nu_l}$  from any  
265 neutrino flavor  $\nu_l$  at ND280 as

$$N^{\nu_l} = \underbrace{\Phi_{\nu_l}}_{\text{Flux}} \times \left[ \sum_t \underbrace{(\sigma_{\nu_l}^t M^t)}_{\text{Effective area}} \right] \times \underbrace{\epsilon_{\nu_l}}_{\text{Efficiency}}, \quad (2.7)$$

266 where  $\Phi_{\nu_l}$  is the flux of  $l$  flavor neutrinos,  $\sigma_{\nu_l}^t$  is the cross section of the interaction for neutrino flavor  $l$  on  
267 target  $t$ ,  $M^t$  is the number of  $t$  targets, and  $\epsilon_{\nu_l}$  is the total efficiency to reconstruct and properly identify  
268 the event as  $\nu_l$ CC interactions. Since the cross section is a measure of interaction probability in units of  
269 area, multiplication of  $M_t$  represents the effective cross sectional area of material  $t$  in the detector. Each  
270 term in Eqn. (2.7) is modeled carefully using Monte Carlo (MC) simulations. For the efficiency term, control  
271 samples are used to constrain detector systematic uncertainties effects.

272 The number of events in a given analysis bin is varied in the BANFF fit using weight functions. The  
273 total number of predicted events in the  $i$ th analysis bin is given by

$$\vec{N}_i^p(\vec{b}, \vec{x}, \vec{d}) = \sum_{j=1}^{N_i^{\text{MC}}} \left\{ w_i^{\text{POT}} \sum_{k=1}^{N^{\text{Flux}}} (\delta_{j,k}^{\text{Flux}} \vec{b}_k) \times \left[ \prod_{l=1}^{N^{\text{xsec}}} w_{j,l}(\vec{x}_l) \right] \times \vec{d}_i \right\}, \quad (2.8)$$

274 where the parameters are described in Table 2.1 on page 12. While Eqn. (2.8) looks complicated as ex-  
275 pressed in the T2K model, it is functionally the same as Eqn. (2.7). Since the flux bins are categorized by  
276 neutrino energy, neutrino flavor, and horn current mode, the  $\delta_{j,k}^{\text{Flux}}$  term is needed to select the correct flux  
277 normalization bin for the  $j$ th MC event. Also the number of neutrino targets  $M$  in the detector is treated  
278 as a detector systematic uncertainty.

279 Using the likelihood ratio test theorem, a test statistic is defined as taking -2 times the natural logarithm

280 of the ratio of predicted to observed likelihoods from Eqn. (2.6). This test statistic is given as

$$\begin{aligned}\chi_{\text{LLR}}^2 &= -2 \log \frac{\mathcal{L}(\vec{N}^d | \vec{N}^p)}{\mathcal{L}(\vec{N}^d | \vec{N}^d)} \\ &= 2 \sum_{i=1}^M \left[ \vec{N}_i^p - \vec{N}_i^d + \vec{N}_i^d \log \left( \frac{\vec{N}_i^d}{\vec{N}_i^p} \right) \right],\end{aligned}\quad (2.9)$$

281 where this obeys a true chi-squared distribution for asymptotically large sample sizes. The denominator  
 282 in Eqn. (2.9) is the MC predicted probability, which assumes the best maximum likelihood estimate is the  
 283 number of observed events.

### 284 2.2.2 External Constraints on the Fit

285 Since the BANFF ND constraint is a predictive model fit to data, it is subject to the bias-variance problem.  
 286 This problem basically states that for a set of samples  $s \in \mathcal{S}$ , a predictive model  $f_1 \in \mathcal{F}$  would have larger  
 287 variance and smaller bias compared to a constrained or shrunken model  $f_2 \subseteq f_1$  of which has larger bias  
 288 but smaller variance. We wish to have a ND constraint measurement with as little variance as possible,  
 289 which is achieved by introducing one or more constraints, also called “penalty” terms, to the test statistic  
 290 Eqn. (2.9). These penalty terms will introduce the T2K experiment’s model on the flux, cross section, and  
 291 detector inefficiencies into the fit.

292 The new test statistic that includes the constraints,  $\chi_{\text{ND280}}^2$ , is given by

$$\begin{aligned}\chi_{\text{ND280}}^2 &= \chi_{\text{LLR}}^2 + \underbrace{\chi_{\text{xsec}}^2 + \chi_{\text{Flux}}^2 + \chi_{\text{Det}}^2}_{\text{Penalty terms}} \\ &= \chi_{\text{LLR}}^2 - 2 \left( \underbrace{\log \pi(\vec{x})}_{\text{xsec}} + \underbrace{\log \pi(\vec{b})}_{\text{Flux}} + \underbrace{\log \pi(\vec{d})}_{\text{Det}} \right),\end{aligned}\quad (2.10)$$

293 where each of the PDFs  $\pi(\vec{y} = \{\vec{x}, \vec{b}, \vec{d}\})$  is an assumed multivariate normal distribution

$$\pi(\vec{y}) = C_y \exp \left( -\frac{1}{2} (\vec{y} - \vec{y}_0)^T V_y^{-1} (\vec{y} - \vec{y}_0) \right), \quad (2.11)$$

294  $\vec{y}_0$  is a vector of the initial parameter values,  $T$  corresponds to the transpose operator,  $C_y$  is the normalization,  
 295 and  $V_y$  is the covariance matrix for vector  $\vec{y}$ . The full form of the test statistic  $\chi_{\text{ND280}}^2$  is given by

$$\chi_{\text{ND280}}^2 = 2 \sum_{i=1}^M \left[ \vec{N}_i^p - \vec{N}_i^d + \vec{N}_i^d \log \left( \frac{\vec{N}_i^d}{\vec{N}_i^p} \right) \right] + (\Delta \vec{y})^T (V_y^{-1}) (\Delta \vec{y}) \quad (2.12)$$

296 where  $\Delta\vec{y} = \vec{y} - \vec{y}_0$ . It must be stated that the test statistic Eqn. (2.12) purposefully excludes normalization  
 297 terms since they are constants that do not affect the minimization. Further details on the penalty terms and  
 298 covariance matrix in Eqn. (2.12) will be discussed in Chapter 4.

299 The best fit parameters,  $\hat{\vec{y}}$ , are those that minimizes the chi-squared statistic

$$\hat{\vec{y}} = \underset{\vec{y} \in \mathbb{R}^d}{\operatorname{argmin}} \left\{ \chi_{\text{LLR}}^2 \left( \vec{N}^d, \vec{N}^p(\vec{y}) \right) + \chi_{\text{Penalty}}^2(\vec{y}) \right\} \quad (2.13)$$

300 where

$$\chi_{\text{Penalty}}^2(\vec{y}) = (\Delta\vec{y})^T (V_y^{-1}) (\Delta\vec{y})$$

301 and we recall that  $\vec{N}^p$  is a function of  $\vec{y} = \{\vec{x}, \vec{b}, \vec{d}\}$  as well.

### 302 2.2.3 Postfit Covariance

303 Once the global minimum is found, the postfit covariance matrix needs to be calculated. Consider how the  
 304 chi-squared varies around the global minimum, or also called the maximum likelihood estimate,  $\hat{\vec{y}}$ . The test  
 305 statistic is given analytically by a Taylor series

$$\chi^2(\vec{y}) = \sum_{n=0}^{\infty} \frac{1}{n!} \left[ (\vec{y} - \hat{\vec{y}})^T \nabla_{\vec{y}} \chi^2 \Big|_{\vec{y}=\hat{\vec{y}}} \right]^n.$$

306 Since the gradient at  $\hat{\vec{y}}$  is zero, the first non-zero  $\vec{y}$ -dependent term is quadratic in  $\vec{y}$

$$\begin{aligned} \chi^2(\vec{y}) &\approx \chi^2(\hat{\vec{y}}) + \frac{1}{2} (\vec{y} - \hat{\vec{y}})^T \left( \nabla_{\vec{y}} \nabla_{\vec{y}}^T \chi^2(\vec{y}) \Big|_{\vec{y}=\hat{\vec{y}}} \right) (\vec{y} - \hat{\vec{y}}) \\ &\approx \chi^2(\hat{\vec{y}}) + \frac{1}{2} (\vec{y} - \hat{\vec{y}})^T \mathcal{H}(\vec{y} - \hat{\vec{y}}). \end{aligned}$$

307 where  $\mathcal{H}$  is a square matrix called the Hessian matrix

$$\mathcal{H}_{i,j} = \left. \frac{\partial^2 \chi^2}{\partial y_i \partial y_j} \right|_{\vec{y}=\hat{\vec{y}}}, \quad (2.14)$$

308 and  $y_i, y_j \in \vec{y}$ . Assuming that our test statistic is distributed according to a multivariate normal distribution  
 309 of the form Eqn. (2.11), we find that the inverse of the Hessian matrix is the covariance matrix.

## 310 2.3 Summary

311 This chapter describes the mathematical preliminaries of the BANFF fit analysis. We first saw the role of  
312 the likelihood function to express the plausibility of data samples given a set of model parameters. We then  
313 define a binned likelihood function to estimate model parameters in the oscillation analysis using the ND280  
314 data. Using Wilks' theorem, the likelihood maximization problem is converted to a chi-squared test statistic  
315 minimization that is iteratively maximized. Finally, penalty terms are included in the test statistic in order  
316 to assert parameter estimates that are consistent with prior systematic uncertainty measurements in T2K.

<sub>317</sub> **Chapter 3**

<sub>318</sub> **The PØD Selections and Samples**

<sub>319</sub> This chapter describes the development of PØD  $\nu_\mu$  and  $\bar{\nu}_\mu$  charged current (CC) inclusive<sup>1</sup> selections in both  
<sub>320</sub> FHC and RHC beam configurations for the BANFF fit. These selections are in continuation of previous  
<sub>321</sub> works that developed  $\nu_\mu$  CC-inclusive selections between the PØD and the TPC. The first such analysis was  
<sub>322</sub> the  $\nu_\mu$  CC-inclusive cross section using the previous ND280 simulation and reconstruction software release  
<sub>323</sub> called “Production 5”<sup>2</sup>[5]. That analysis relied on each subdetector’s reconstruction software and developed  
<sub>324</sub> a track matching algorithm since the ND280 “Global” reconstruction matching was not available in that  
<sub>325</sub> software production. Another cross section analysis measuring the cross section ratio of  $\bar{\nu}_\mu/\nu_\mu$  also used this  
<sub>326</sub> “pre-Global” technique with the modern ND280 “Production 6” software<sup>3</sup>[6]. As the inter-detector matching  
<sub>327</sub> reconstruction became available in Global, two cross section analyzes,  $\nu_\mu$  CC-0 $\pi$ [7] and  $\bar{\nu}_\mu$  CC-0 $\pi$ [8, 9], were  
<sub>328</sub> developed that also used the CC-inclusive selection as pre-selection cuts. A “cut” refers to one or more  
<sub>329</sub> criteria to select reconstructed events that have desired properties. The pre-selection cuts are designed in  
<sub>330</sub> particular to filter out poor data quality events. They are well validated with results using these cuts are  
<sub>331</sub> published as shown in Figure 3.1 on page 17. The selections described in this thesis also employ the same  
<sub>332</sub> pre-selection cuts with the latest stable Global reconstruction software, Production 6.

<sub>333</sub> This paragraph is a layout of the topics in the chapter. First discussed is the event reconstruction using  
<sub>334</sub> the “Global” reconstruction software in Section 3.1. The next discussion is on the sample selections in Section  
<sub>335</sub> 3.2. With the selections established, three CC-inclusive selection are described in the following order: the  
<sub>336</sub>  $\nu_\mu$  in foreword horn current (FHC) mode selection, the  $\bar{\nu}_\mu$  in reverse horn current (RHC) mode selection,

---

<sup>1</sup>A CC-inclusive selection is a set of criteria that select all CC neutrino interaction events as opposed to an CC-exclusive selection like CC-0 $\pi$ .

<sup>2</sup>The ND280 detector reconstruction and Monte Carlo official software updates are given a “Production” designation. The Production 5 software was actively used between 2012 and early 2014 until it was replaced by Production 6. However, physics analyzers are not as rapid to adopt the software updates.

<sup>3</sup>The ND280 “Production 6” software was released in 2014 and is still in active use.

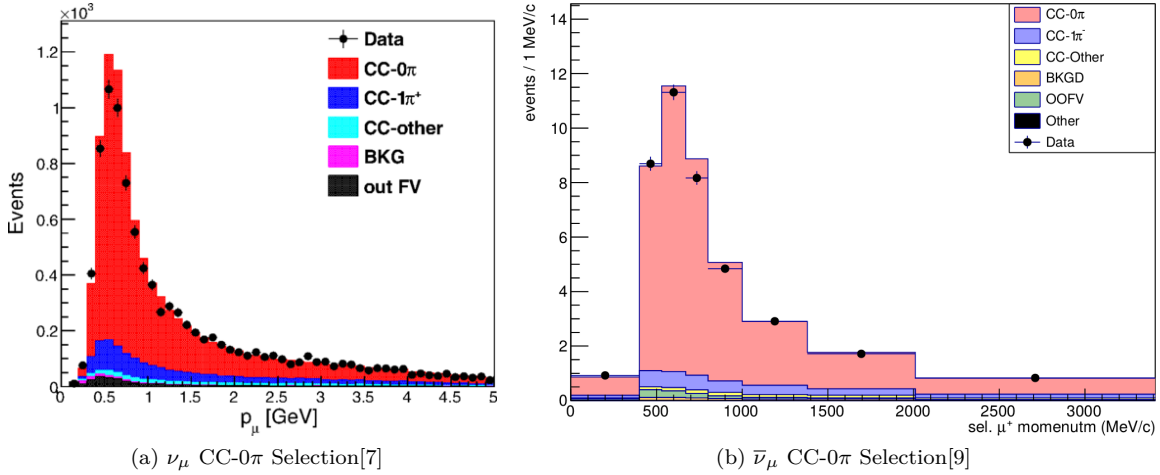


Figure 3.1: The PØD  $\nu_\mu$  and  $\bar{\nu}_\mu$  CC-0 $\pi$  selection kinematics. They importantly share the same pre-selection cuts as this analysis. The error bars are statistical only with the prediction sorted into various truth topologies.

and the  $\nu_\mu$  background in RHC mode selection. The penultimate topic is an examination of the collected samples and their kinematic properties in Section 3.3. Finally, the chapter summary is provided in Section 3.4.

### 3.1 The ND280 Global Reconstruction

The task of the Global reconstruction is to combine all of the ND280 information into a combined reconstructed object. It was originally designed to identify CC-0 $\pi$  events in the Tracker, FGD+TPC, region and has been extended to operate with all of ND280.

The Global reconstruction is a software package that attempts to recognize patterns of deposited energy in ND280 and categorize it accordingly. Particles that deposit energy in long, linear segments are categorized as tracks. If multiple tracks originate from a common origin (vertex), it is likely that a true neutrino interaction event occurred near the reconstructed vertex. Particle cascade or shower reconstruction in Global will not be discussed since they are not selected in this thesis.

Each subdetector reconstruction algorithm is run separately as the seed to Global’s track matching algorithms. This includes the PØD’s track-finding algorithm, which defines a PØD track as a linear sequence of “nodes” with one node at each bar layer. Each node represents the approximate position where the particle intersected the bar layer. To facilitate inter-detector matching, Global attempts to “re-fit” the PØD track using a Kalman filter[10]. The re-fit procedure also corrects for particle energy loss as a function of length and multiple scattering processes. A PØD vertex, which is the assumed location of the neutrino interaction,

355 is then associated with the re-fit track using another Kalman filter algorithm. Matching tracks between the  
356 PØD and the TPC is done automatically in the ND280 Global fit.

## 357 3.2 The PØD Selection Cuts

358 The selection of CC-inclusive events uses a series of cuts to select the muon track. Prior to any cuts and  
359 after the reconstruction, corrections are applied first to both data and MC events to correct for well known  
360 residual differences between them. This includes correcting the MC flux prediction using the secondary  
361 beamline data and reconstruction efficiency corrections. A complete list of the corrections applied are given  
362 in the following reference[1]. The pre-selection cuts (“precuts”) are then applied to extract events that start  
363 in the PØD water target (WT) fiducial volume (FV).

364 The following sections will describe the precuts common to all CC-inclusive selections. The next section  
365 describes the specific selections and their cuts to select the main track associated as the lepton candidate.  
366 Finally the lepton candidate and event kinematics for all the samples are described.

### 367 3.2.1 Precuts

368 The precuts were initially developed to select  $\nu_\mu$  CC-inclusive events using the PØD and TPC subdetector  
369 reconstruction algorithms separately[6, 5]. They were then used with the Global reconstruction software for  
370 the  $\nu_\mu$  CC- $0\pi$  selection in the FHC beam configuration[7]. All cuts were implemented in psyche[11] which is  
371 the software interface that BANFF uses to select events.

372 Prior to the precuts, neutrino interaction data event must be collected and reconstructed for each T2K  
373 beam spill. Each T2K beam spill has eight bunches that are 58 ns long and temporally separated by 581 ns.  
374 When the beam spill occurs, the PØD’s Trip-T electronics are triggered to collect data in preset integration  
375 cycles aligned with the bunches. Each integration cycle is 480 ns long and is followed by a 100 ns dead-time  
376 to prepare for the next cycle[5]. The data collected in each cycle is used to reconstruct neutrino interaction  
377 events using the ND280 subdetector and Global software packages.

378 Each reconstructed event must pass the following cuts before being assigned to a selection:

379 1. The event has a “good” data quality flag.

380 • An event is rejected if any electronics element or subdetector in ND280 is reported as “bad” during  
381 the corresponding bunch.

382 2. There is at least one (1) track reconstructed in the TPC.

- 383     • There are no restrictions on the number of tracks fully contained in the PØD or exiting into other  
 384       subdetectors.

385     3. The track in the TPC must have more than 18 nodes.

- 386       • The TPC reconstruction gathers the vertical and horizontal micromegas that registered collected  
 387       charge into clusters of “hits”. Each cluster’s charge distribution is used to get a vertical (horizontal)  
 388       position that is more accurate than the individual readout micromegas. A node is constructed  
 389       out of each cluster with associated track state information. The set of nodes are used to fit a helix  
 390       shaped track.

391     4. The reconstructed vertex is within the PØD WT FV.

- 392       • The PØD FV is defined to include as much of the WT regions as possible. Its X and Y borders are  
 393       25 cm away from the PØDule edges while the Z borders intersect the last and first half downstream  
 394       PØDule in the upstream ECal and central ECal, respectively. The FV edges are listed in Table  
 395       3.1 on page 19. This volume, while used for track-based analyzes in the past, was optimized for  
 396        $\pi^0$  and  $\nu_e$  analyses.

397     5. All tracks that enter the TPC pass the veto cut

- 398       • An event is rejected if any PØD track enters the TPC from outside the “corridor” volume. This cut  
 399       was designed to eliminate broken tracks when the pre-Global separate subdetector reconstruction  
 400       was used [12]. In practice, this cut ensures that Global tracks entering the TPC are away from  
 401       its X and Y edges. The corridor definition is the same as defined in the  $\bar{\nu}_\mu/\nu_\mu$  cross section ratio  
 402       analysis technical note[13] and shown in Table 3.1 on page 19.

Table 3.1: The PØD WT FV (left) and veto corridor volume (right) in the ND280 coordinate system. The corridor spans from the 5th (8th) to 40th (80th) PØDule (scintillator layer). All the units are given in millimeters.

PØD WT FV	Corridor Volume
$-836 < X < 764$	$-988 < X < 910$
$-871 < Y < 869$	$-1020 < Y < 1010$
$-2969 < Z < -1264$	$-3139 < Z < -900$

403     After passing of all the precuts, a single, global track, which is observed in the TPC, is assigned as the  
 404       lepton candidate or “main track” of a selected event. While the main track is different for each selected event,  
 405       the momentum reconstruction is the same. The momentum of the main track,  $P$ , is sum of its measured

406 momentum in the TPC,  $P_{\text{TPC}}$ , with the estimate momentum lost in the PØD,  $\Delta P_{\text{PØD}}$

$$P = P_{\text{TPC}} + \Delta P_{\text{PØD}}. \quad (3.1)$$

407 The momentum lost in the PØD is estimated by summing the total momentum loss along the track path  $\mathcal{C}$

$$\Delta P = \int_{\mathcal{C}} \left( \frac{dP}{dx} \right) dx, \quad (3.2)$$

408 where  $dP/dx$  is the momentum loss function. The momentum loss function is related to the energy loss  
409 function,  $dE/dx$  via the chain rule

$$\begin{aligned} \frac{dE}{dx} &= \left( \frac{dE}{dP} \right) \left( \frac{dP}{dx} \right) \\ &= \frac{d}{dP} \left( \sqrt{P^2 c^2 + m^2 c^4} \right) \left( \frac{dP}{dx} \right) \\ &= \left( \frac{P c^2}{E} \right) \left( \frac{dP}{dx} \right) \\ &= \beta c \left( \frac{dP}{dx} \right), \end{aligned} \quad (3.3)$$

410 where  $\beta$  is the particle velocity as a ratio of the speed of light  $c$ . Since the reconstructed track's path  $\mathcal{C}$  is  
411 not infinitesimally precise due to inherent detector resolution, we must replace the integral with a sum and  
412 differential  $dx \rightarrow \Delta x$ . We then arrive at the expression of the momentum loss estimate in the PØD as

$$\Delta P_{\text{PØD}} = \frac{1}{c} \sum_t \left[ \left( \frac{dE}{dx} \right) \left( \frac{\Delta x}{\beta} \right) \right]_t, \quad (3.4)$$

413 where  $t$  is a discrete step in  $x$  connecting the track nodes. For most tracks entering the TPC, they will be  
414 highly relativistic in the PØD ( $\beta \approx 1$ ), and Eqn. (3.4) simplifies to

$$\Delta P_{\text{PØD}} = \frac{1}{c} \sum_t \left[ \left( \frac{dE}{dx} \right) \Delta x \right]_t. \quad (3.5)$$

415 The next sections describe the selection cuts, first in FHC mode and then RHC mode.

### 416 3.2.2 The $\nu_{\mu}$ in FHC Mode CC-Inclusive Selection

417 As discussed in Section 3.2.1, this selection is the basis for the PØD  $\nu_{\mu}$  CC-0 $\pi$  analysis[7]. In FHC mode,  
418 the vast majority of neutrino interactions are  $\nu_{\mu}$  CC events that produce an outgoing, negatively charged  
419 muon. If there is no negatively charged track in the TPC, the event is likely not a  $\nu_{\mu}$ -induced interaction.

420 Therefore, the  $\nu_\mu$  in FHC mode CC-inclusive selection in FHC mode has one final cut after the precuts:

421 1. At least one negatively charged track is reconstructed in the TPC.

422 • An event is rejected if none of the TPC tracks have a reported negative curvature.

423 If the event passes this cut, the highest momentum negative (curvature) track, or HMNT, is selected as the  
424 lepton candidate. This selection and all subsequent selections are branched into two categories based on the  
425 number of tracks counted in the PØD. If there is only one PØD track, and hence only one track in the TPC  
426 as required by the precuts, the event is categorized as a “ $\nu_\mu$  in FHC Mode CC 1-Track” event. Otherwise,  
427 the event is categorized as a “ $\nu_\mu$  in FHC Mode CC N-Tracks” event.

428 **3.2.3 The  $\bar{\nu}_\mu$  in RHC Mode CC-Inclusive Selection**

429 In RHC mode, the majority of the beam neutrinos are  $\bar{\nu}_\mu$  since the horn focuses negatively charged pions  
430 and deflects positively charged pions. However, the  $\nu_\mu$  background interaction rate in RHC mode is larger  
431 than the  $\bar{\nu}_\mu$  background in FHC mode. The reason for this is two fold. Firstly, the antineutrino-nuclear  
432 scattering cross section is suppressed by  $\sim 1/3$  compared to the neutrino-nuclear scattering cross section as  
433 explained in Section ???. Secondly, the  $\nu_\mu$  flux in RHC is relatively large due to the excess of positively  
434 charged pions generated at the target. Therefore there is a non-negligible “wrong-sign” background in RHC  
435 mode that we need to reject.

436 Prior to this analysis, a  $\bar{\nu}_\mu$  CC-0 $\pi$  selection was developed for the PØD[9]. The  $\bar{\nu}_\mu$  CC-0 $\pi$  selection is  
437 quite similar to the  $\nu_\mu$  CC-inclusive selection in FHC mode, but relied on the PØD local reconstruction for  
438 a particle identification cut. The PØD local reconstruction is, however, unavailable in the event selection  
439 software used in the BANFF fit called psyche. So a new selection was developed specifically for this analysis  
440 to select  $\bar{\nu}_\mu$  interactions in RHC mode.

441 The  $\bar{\nu}_\mu$  in RHC mode CC-inclusive selection uses the precuts described in Section 3.2.1 and the has two  
442 cuts:

443 1. At least one positively charged track is reconstructed in the TPC.

444 • An event is rejected if none of the TPC tracks have a reported positive curvature.

445 2. The highest momentum positive (curvature) track, or HMPT, must be the highest momentum track.

446 • If the highest momentum track has negative curvature, then the event is rejected.

447 If the event passes these two cuts, the HMPT is the lepton candidate. If there is only one PØD track, the  
448 event is categorized as a “ $\bar{\nu}_\mu$  in RHC Mode CC 1-Track” event. Otherwise, the event is categorized as a “ $\bar{\nu}_\mu$   
449 in RHC Mode CC N-Tracks” event.

450 **3.2.4 The  $\nu_\mu$  in RHC Mode CC-Inclusive Selection**

451 As explained in the previous subsection, the  $\nu_\mu$  background interaction rate in RHC mode is relatively large  
452 compared to the  $\bar{\nu}_\mu$  interaction rate. Having a measurement of this background is critical for the oscillation  
453 analysis due to the small number of expected  $\bar{\nu}_\mu \rightarrow \bar{\nu}_e$  counts. To date, there is no PØD measurement of  
454  $\nu_\mu$  background in RHC mode, nor any PØD selection to do so. So like the  $\bar{\nu}_\mu$  CC-inclusive selection, a new  
455 PØD selection was developed exclusively for this analysis to select  $\nu_\mu$  background events in RHC mode.

456 The  $\nu_\mu$  background in RHC mode CC-inclusive selection uses the precuts described in Subsection 3.2.1  
457 and has two cuts:

458 1. At least one negatively charged track is reconstructed in the TPC.

459 • An event is rejected if none of the TPC tracks have a reported negative curvature.

460 2. The HMNT must be the highest momentum track.

461 • If the highest momentum track has positive curvature, then the event is rejected.

462 If the event passes these two cuts, the HMNT is the lepton candidate. If there is only one PØD track,  
463 the event is categorized as a “ $\nu_\mu$  Background in RHC Mode CC 1-Track” event. Otherwise, the event is  
464 categorized as a “ $\nu_\mu$  Background in RHC Mode CC N-Tracks” event.

465 **3.3 Selection Kinematics**

466 This section examines the kinematics for each of selections and their respective branches while differentiating  
467 between water-in and water-out mode. The data sets used in this analysis are runs 2-8 in both PØD water-  
468 in and water-out (air) modes as shown in Table 3.2 on page 23. There will be no data events shown to  
469 prevent any potential analysis biases. Simulated events will be arranged into various true categories to study  
470 selection kinematics, efficiencies, and purities.

471 True interactions for these selections are generally divided into four classes:

472 • A neutrino-induced CCQE interaction ( $\nu$  CCQE):

473 – Only NEUT generated neutrino-induced CCQE event at the interaction vertex.

Table 3.2: T2K data-taking periods and collected POT used in the analysis. The bottom four rows are the aggregated periods grouped by horn current and PØD status, which is how the data analysis is performed. Note that the horns were run briefly at +205 kA for Run 3b when operations resumed after 2011 Tohoku earthquake.

Run period	Horn current [kA]	PØD status	Data POT ( $\times 10^{20}$ )	MC POT ( $\times 10^{20}$ )
2	+250	Water	0.433934	12.0341
		Air	0.359149	9.23937
3b	+205		0.217273	4.47864
3c	+250		1.36447	26.3227
4			1.78271	34.996
		Water	1.64277	34.9712
5c	-250		0.43468	22.7766
6b		Air	1.28838	14.174
6c			0.505895	5.27562
6d			0.775302	6.884
6e			0.847902	8.59439
7b		Water	2.43682	33.7046
8	+250		1.58053	26.4664
		Air	4.14897	36.0694
Sand	+250		-	11.1988
Sand	-250		-	12.9201
2, 3b, 3c, 4, 8		FHC	Air	7.872757
2, 4, 8			Water	3.656589
6b, 6c, 6d, 6e		RHC	Air	3.382490
5c, 7b			Water	2.852340
				54.53

Table 3.3: Enumeration of the NEUT interaction modes which are also used in Figure 3.2 on page 25. An arrow indicates a sequence of integer steps from left to right of the arrow.

Interaction mode	$\nu$ ( $\bar{\nu}$ ) NEUT enumeration
CCQE	1 (-1)
2p2h	2 (-2)
CC-1 $\pi$	11 → 16 ( $-11 \rightarrow -16$ )
non-CCQE	CC-N $\pi$ 21 (-21) CC-DIS      26 (-26) CC-Other      17, 22, 23 ( $-17, -22, -23$ ) NC      31 → 100 ( $-31 \rightarrow -100$ )

- A neutrino-induced non-CCQE interaction ( $\nu$  non-CCQE):
    - Any NEUT generated neutrino-induced CC and NC event *except* neutrino-induced CCQE at the interaction vertex.
  - An antineutrino-induced CCQE interaction ( $\bar{\nu}$  CCQE):
    - Only NEUT generated antineutrino-induced CCQE event at the interaction vertex.
  - An antineutrino-induced non-CCQE interaction ( $\bar{\nu}$  non-CCQE):
    - Any NEUT generated antineutrino-induced CC and NC event *except* antineutrino-induced CCQE at the interaction vertex.
- These signal classes must occur in the PØD WT FV in order to be selected. The non-CCQE category can be further divided among the dominant T2K CC and all NC interactions modes as enumerated in Table 3.3 on page 24. An out of FV (OOFV) event is any true event that occurs in ND280, but is falsely reconstructed in the PØD FV. Another important ND280 background are true neutrino and antineutrino CC interactions occurring in the sand surrounding the ND280 pit with the muon track falsely reconstructed in the FV. These events are referred to as “sand muon” events and are accounted for accordingly. Since these categories are used frequently in this chapter, the legends used in the histograms are enlarged for the reader’s convenience in Figure 3.2 on page 25.
- The ND280 MC uses the GEANT4 software toolkit [14] to simulate the passage of particles through matter. A GEANT4 particle is assigned to a reconstructed track if it contributed the most to the track’s reconstructed hits. The most likely truth matched particles include protons ( $p$ ), both negatively and positively charged muons ( $\mu^\pm$ ), pions ( $\pi^\pm$ ), and electrons/positrons ( $e^\pm$ ). In addition, any electron and positron

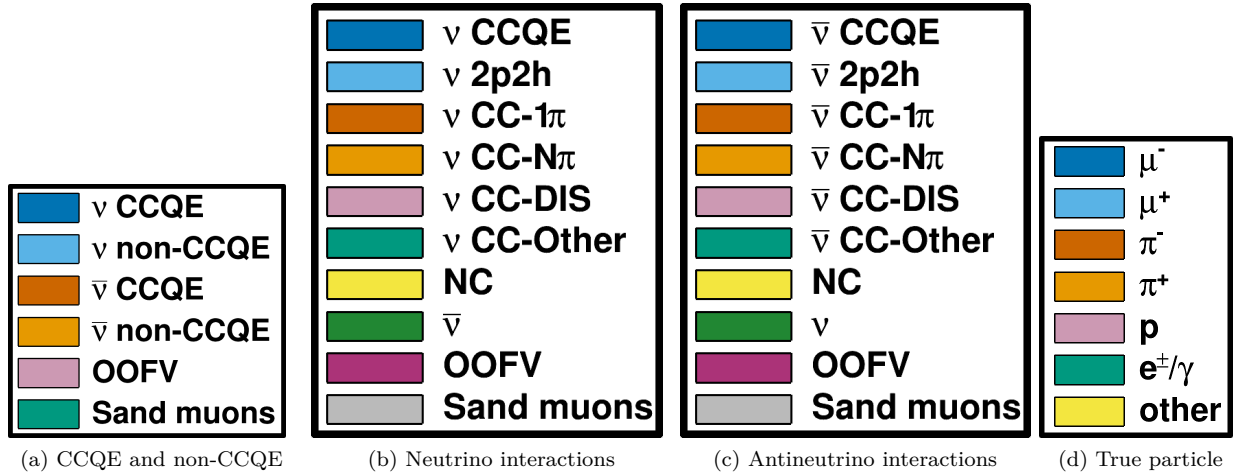


Figure 3.2: Frequently used legends that are enlarged for the reader’s convenience.

generated from pair production are grouped together as “ $e^\pm/\gamma$ ”. Particles that do not match any of these categories is labeled as “other”.

### 3.3.1 The $\nu_\mu$ in FHC Mode CC 1-Track Sample

This selection provides the CCQE-like samples in FHC mode. Figure 3.3 on page 26 and Figure 3.4 on page 27 displays the momentum and angular distributions that are inputs to BANFF. Comparing between water-in and water-out modes, we see that the reconstructed kinematics are nearly identical. In the majority of cases, the lepton candidate is the true muon, making this a very pure  $\nu_\mu$  sample. We also see that there are non-CCQE events, which without a particle identification cut, are a irreducible background. Following this paragraph and the following sections, only the PØD water-in mode kinematics will be shown.

The target nuclei between water-in and water-out modes is shown in Figure 3.5 on page 28. Scattering on the carbon nucleus is the dominant interaction in both modes since the scintillating bars are constructed of polyethylene  $[(\text{CH}_2\text{CH}_2)_n]$  plastic. In water-in mode, the oxygen nucleus is a significant target with hydrogen having a small contribution as well. The brass layers between the PØDules and the water bags introduce copper and zinc nuclei scattering events too. The events on lead nuclei are true OOFV and primarily occur in the last PØDule.

We can examine the efficiencies and purities differentially for true  $\nu_\mu$  CCQE interactions in Figure 3.6 on page 29. The efficiency,  $\epsilon$ , and purity,  $\rho$ , are defined as

$$\epsilon = \frac{N_{\text{Selected}}^{\text{True}}}{N^{\text{True}}} \quad \rho = \frac{N_{\text{Selected}}^{\text{True}}}{N_{\text{Selected}}}, \quad (3.6)$$

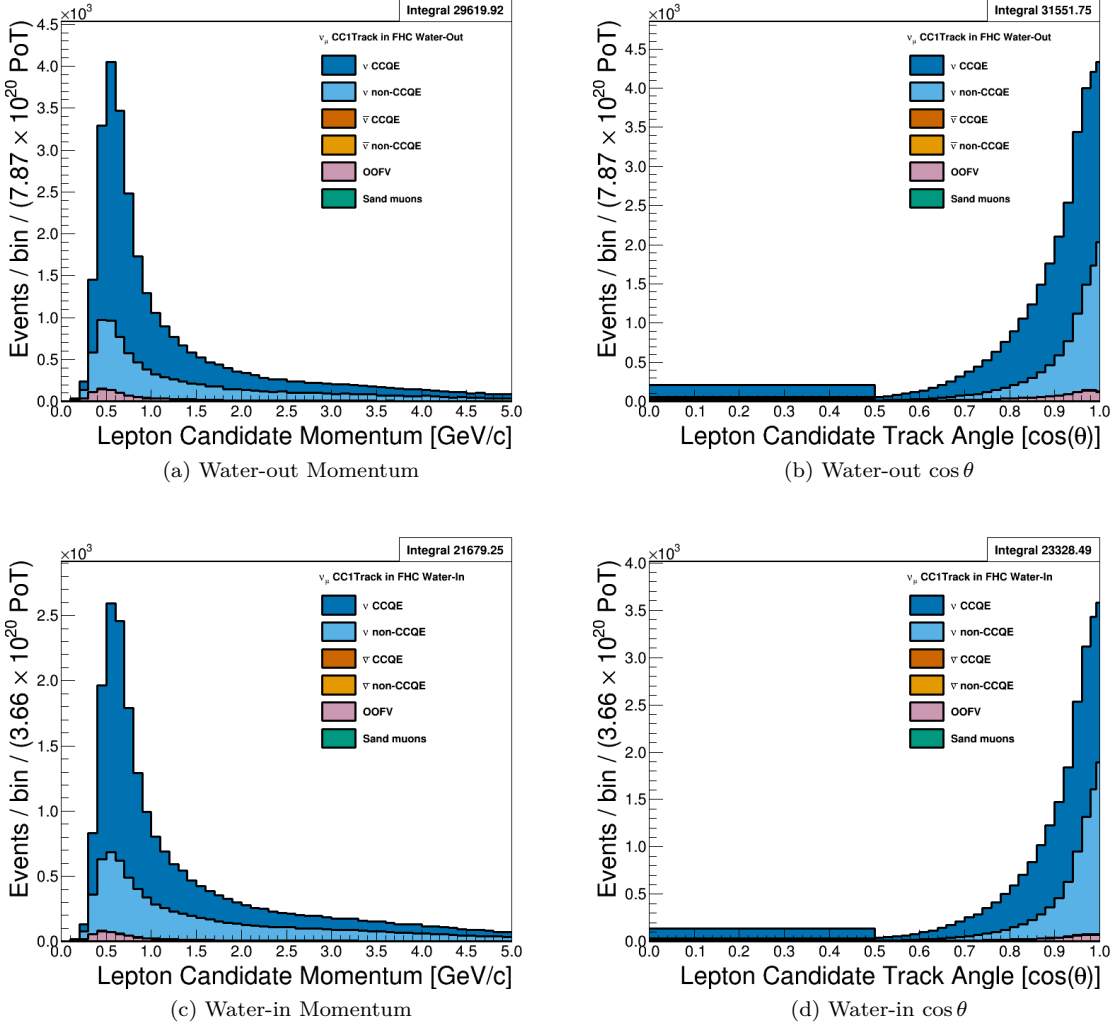


Figure 3.3: Reconstructed kinematics of the  $\nu_\mu$  in FHC Mode CC 1-Track selection categorized by CCQE and non-CCQE interactions. The top figures, (a) and (b), use the PØD water-out MC and are normalized to the FHC water-out mode POT. The bottom figures, (c) and (d), use the PØD water-in MC and are normalized to the FHC water-in mode POT. Also a single bin is used in the range of  $0 \leq \cos\theta < 0.5$  in figures (b) and (d).

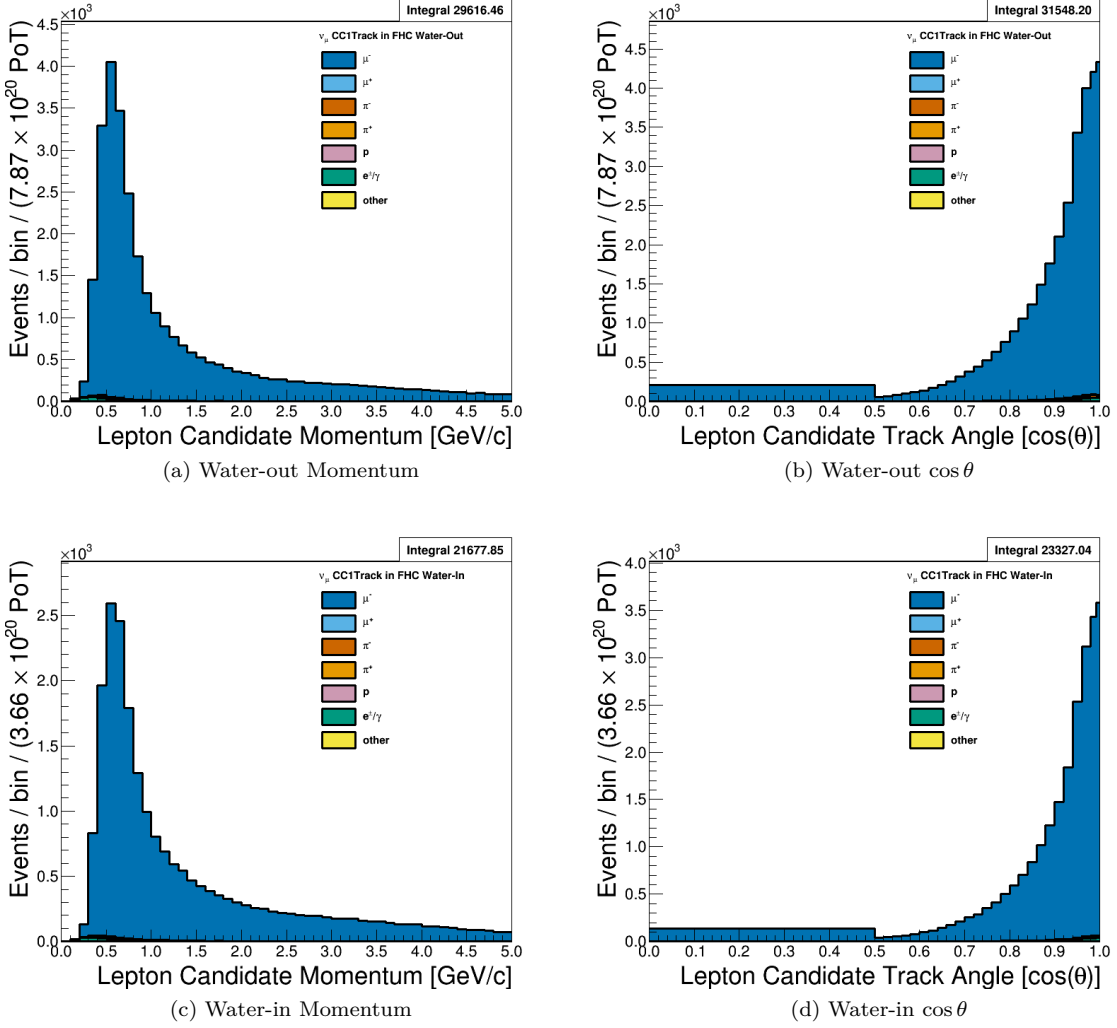


Figure 3.4: Reconstructed kinematics of the  $\nu_\mu$  in FHC Mode CC 1-Track selection categorized by the true particle matched to the main track. The top figures, (a) and (b), use the PØD water-out MC and are normalized to the FHC water-out mode POT. The bottom figures, (c) and (d), use the PØD water-in MC and are normalized to the FHC water-in mode POT. Also a single bin is used in the range of  $0 \leq \cos \theta < 0.5$  in figures (b) and (d).

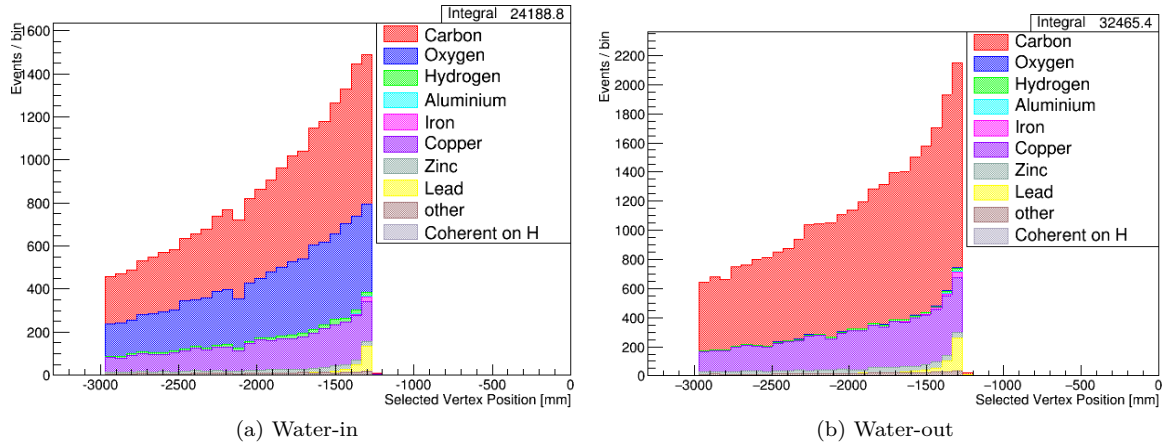


Figure 3.5: Reconstructed vertex Z position of the  $\nu_\mu$  in FHC Mode CC 1-Track selection. The events are categorized by the true target nucleus. The number of selected events increases with increasing Z since the probability of an interaction increases as the neutrino crosses more media in the PØD. Due to a software bug in the MC, coherent events on hydrogen (Coherent on H) are a unique category.

511 where  $N_{\text{Selected}}^{\text{True}}$  is the number of true, selected events,  $N^{\text{True}}$  is the number of true events, and  $N_{\text{Selected}}$  is the  
 512 number of selected events. They demonstrate that the purity is highest near 0.5 GeV/c with the efficiency  
 513 highly dependent on the track angle.

514 The underlying true kinematics of the interactions are shown in Figure 3.7 on page 29. Using Figure ?? on  
 515 page ?? as reference, the kinematics shown are the true neutrino energy  $E_\nu = k_0$  and 4-momentum transfer  
 516  $Q^2 = -q^2$ . These two variables are of theoretical importance since they are used to generate events using  
 517 NEUT and are used in the BANFF fit. An interesting CCQE-like final state in this selection are correlated  
 518 nucleon pair scattering called “2 particle, 2 hole” (2p2h)<sup>4</sup> events[15]. Interaction model parameters for 2p2h  
 519 have large systematic uncertainties in T2K and are included the BANFF fit. Therefore these events could  
 520 help reduce the 2p2h model uncertainties.

521 This selection contains a modest fraction of non-CCQE interactions. The largest contamination is  $1\pi$   
 522 interactions, which can happen primarily for a couple of reasons. Firstly, when the final state pion is  
 523 produced, it is subject to final state interactions (FSI) where a pion can be absorbed or scattered in the  
 524 nucleus. Secondly, and more importantly, a pion might not be reconstructed as a track in the PØD if its  
 525 energy is below reconstruction threshold. Together, the large  $1\pi$  background affects the sensitivity to CC- $0\pi$   
 526 and CC- $1\pi$  model parameters in the BANFF fit.

---

<sup>4</sup>The name 2p2h originates from Condensed Matter Physics which motivated the model. In solid state matter, a “hole” refers to the absence of an electron in a valence band. In the High Energy Physics context, 2p2h considers neighboring and interacting nucleon pairs (2p) scattering from an incoming neutrino. The imparted energy on the pair excites them to higher energy states leaving two “hole” states (2h) behind.

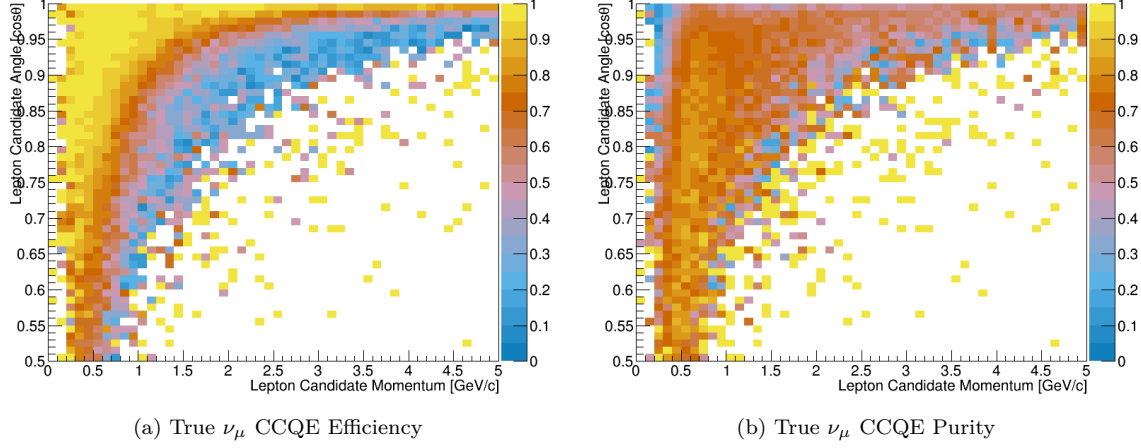


Figure 3.6: Efficiency and purity of the  $\nu_\mu$  in FHC Mode CC 1-Track selection. True events are defined as correctly matched  $\mu^-$  tracks from  $\nu_\mu$ -induced CCQE interactions at the vertex.

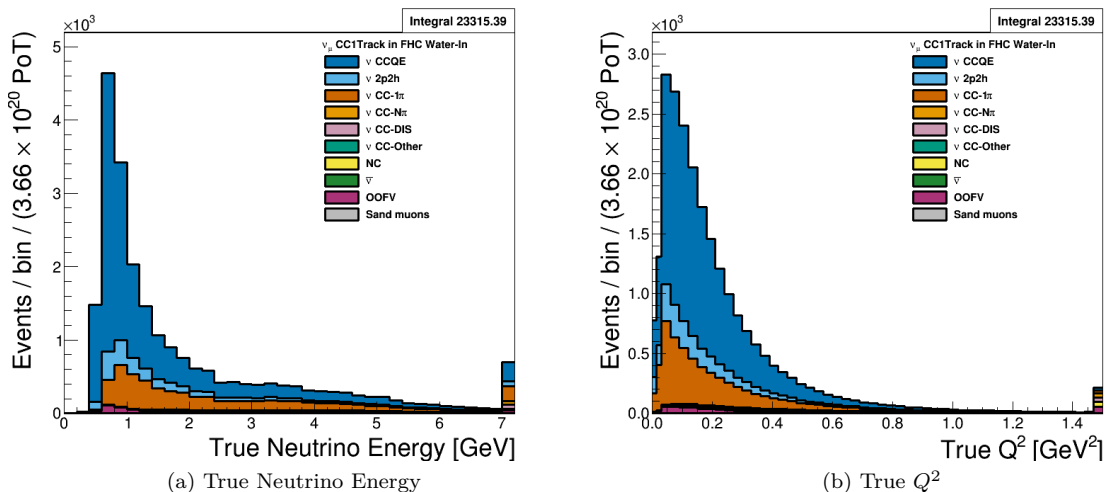


Figure 3.7: True kinematics of the  $\nu_\mu$  in FHC Mode CC 1-Track selection. Water-in mode is displayed here only with the last bin shown as overflow. The figures use the PØD water-in MC and are normalized to the FHC water-in mode POT.

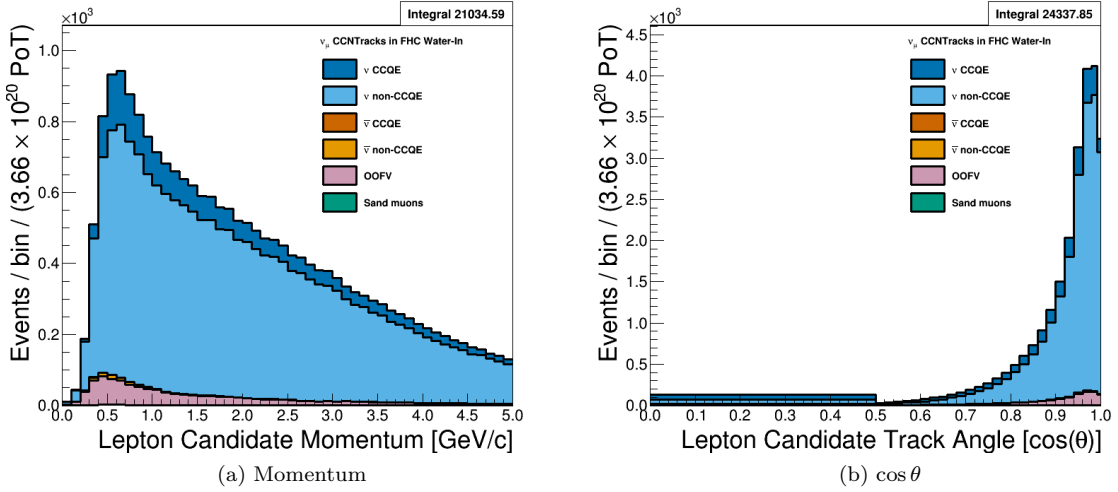


Figure 3.8: Reconstructed kinematics of the  $\nu_\mu$  in FHC Mode CC N-Tracks selection categorized by CCQE and non-CCQE interactions. The figures use the PØD water-in MC and are normalized to the FHC water-in mode POT. Also a single bin is used in the range of  $0 \leq \cos \theta < 0.5$  in figure (b).

### 527 3.3.2 The $\nu_\mu$ in FHC Mode CC N-Tracks Sample

528 This selection provides non-CCQE-like samples in FHC mode inputs to the BANFF fit. The reconstructed  
 529 momentum and angular distributions are shown in Figure 3.8 on page 30 and Figure 3.9 on page 31. Since  
 530 this selection is not optimized for any particular CC topology, there are a variety of interaction modes present  
 531 including  $1\pi$ , multiple pion ( $N\pi$ ) and deep inelastic scattering (DIS). There are a number of events with a  
 532 mis-identified main track that are matched to electrons and pions. There is also a relatively larger OOFV  
 533 contamination compared with the 1-Track selection with some events originating in the upstream ECal as  
 534 seen in Figure 3.10 on page 31. The vertex position and target materials are quite similar between the  
 535 1-Track and N-Tracks selections.

536 We can examine the efficiencies and purities differentially for the selection in Figure 3.11 on page 32.  
 537 For the efficiency and purity only, the true signal is any  $\nu_\mu$  CC interaction except  $\nu_\mu$  CCQE (CC non-QE),  
 538 which the CC 1-Track topology selection is designed to select. The efficiency is high for the higher momenta  
 539 and higher angle tracks suggesting this is a high  $Q^2$  selection. In addition, the purity is around ~70% in this  
 540 region.

541 The fundamental kinematics of the selection are shown in Figure 3.12 on page 33. The selection is  
 542 relatively  $\nu_\mu$ -pure and captures the high energy tail of the neutrino flux. True kinematics that describe the  
 543  $1\pi$ ,  $N\pi$ , and DIS models are parameterized in  $Q^2$  and the hadronic system mass  $W$ . Using Figure ?? on

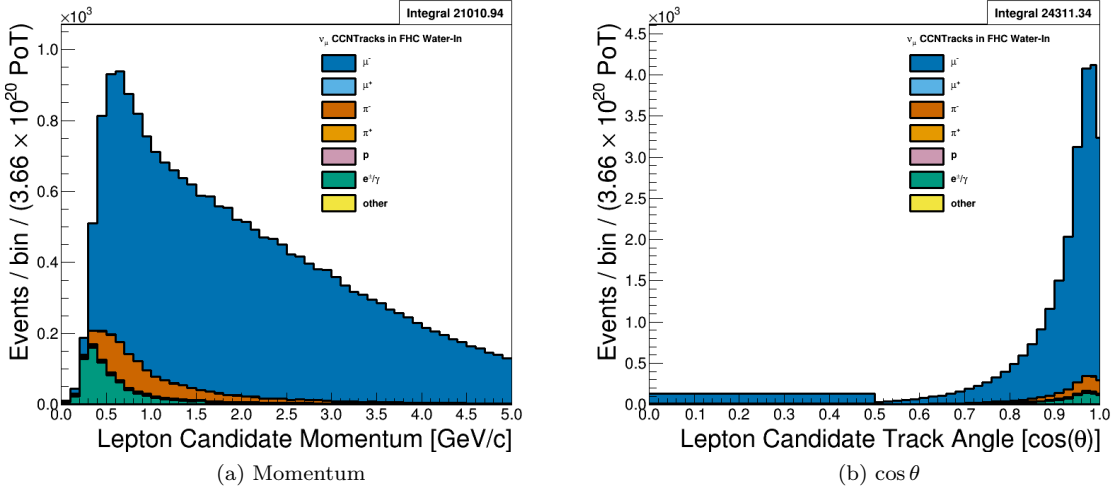


Figure 3.9: Reconstructed kinematics of the  $\nu_\mu$  in FHC Mode CC N-Tracks selection categorized by the true particle matched to the main track. The figures use the PØD water-in MC and are normalized to the FHC water-in mode POT. Also a single bin is used in the range of  $0 \leq \cos \theta < 0.5$  in figures (b) and (d).

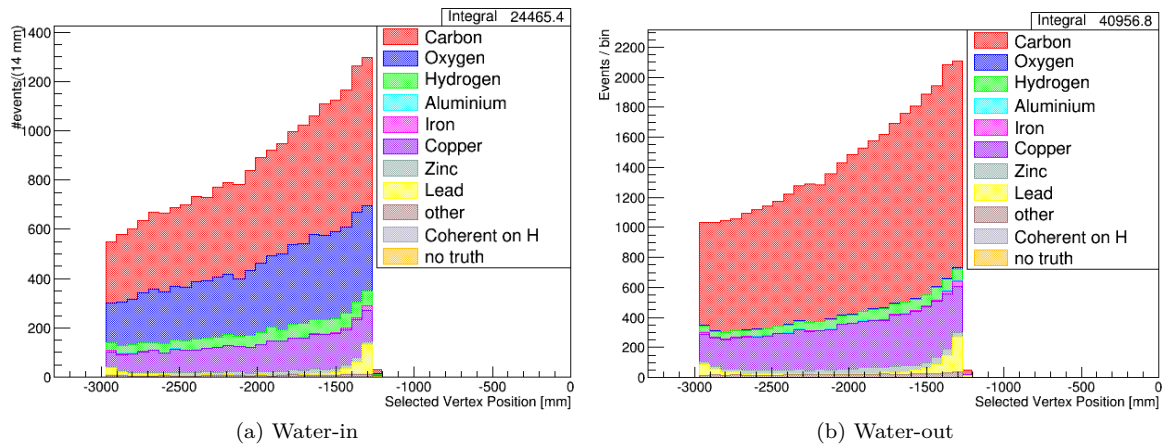


Figure 3.10: Reconstructed vertex Z position of the  $\nu_\mu$  in FHC Mode CC N-Tracks selection categorized by the true target nucleus. The number of events increases with increasing Z since the probability of an interaction increases as the neutrino crosses more media in the PØD. Due to a software bug in the MC, coherent events on hydrogen (Coherent on H) are a unique category.

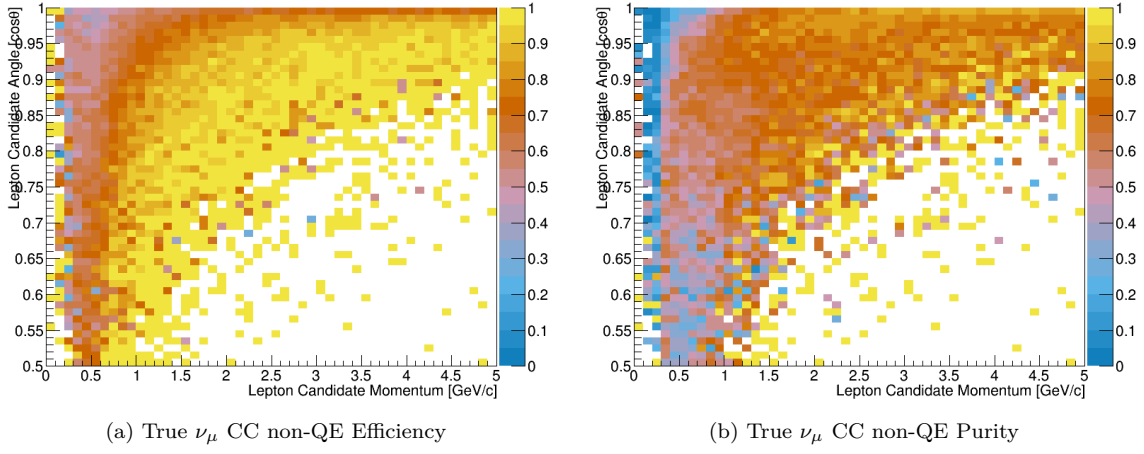


Figure 3.11: Efficiency and purity of the  $\nu_\mu$  in FHC Mode CC N-Tracks selection. True events are defined as correctly matched  $\mu^-$  tracks from  $\nu_\mu$ -induced CC non-QE interactions at the vertex.

page ??, we can define the invariant mass of hadronic system as

$$\begin{aligned}
 W^2 c^4 &= (p + q)^2 = p^2 + 2p \cdot q + q^2 \\
 &= M_N^2 c^4 + 2M_N c^2 (k_0 - k'_0) - Q^2,
 \end{aligned} \tag{3.7}$$

where  $M_N$  is the mass of the struck nucleon and  $k_0/k'_0$  is the energy of the neutrino/outgoing lepton. A dominant mode in the selection is from the  $1\pi$  interaction from a  $\Delta$  resonance. A resonance is clearly seen in the  $W$  distribution in Figure 3.12 on page 33, which comes from the  $\Delta$  baryon which has a rest mass of 1.232 GeV/c<sup>2</sup>.

The origin of the mis-identified tracks, in particular the pion matched tracks, becomes more clear since this is a high  $Q^2$  selection. The  $N\pi$  and DIS events, which are high  $Q^2$  events, can yield a post-FSI charged pion track. These pions could have more energy than the outgoing muon or could be the only particle observed in the TPC.

### 3.3.3 The $\bar{\nu}_\mu$ in RHC Mode CC 1-Track Sample

This selection provides the  $\bar{\nu}_\mu$  CCQE-like samples in RHC mode that are inputs to the BANFF fit. In Figure 3.13 on page 34 and Figure 3.14 on page 35 display the momentum and angular distributions for this selection. The selection is highly  $\bar{\nu}_\mu$ -pure with the selected lepton candidate being positively charged muons. There is a large OOFV background from proton tracks. They are high momentum ( $> 1$  GeV/c) tracks which, at these energies, are minimum ionizing and can reach into the TPC.

We can examine the efficiencies and purities differentially for the selection in Figure 3.15 on page 35. For

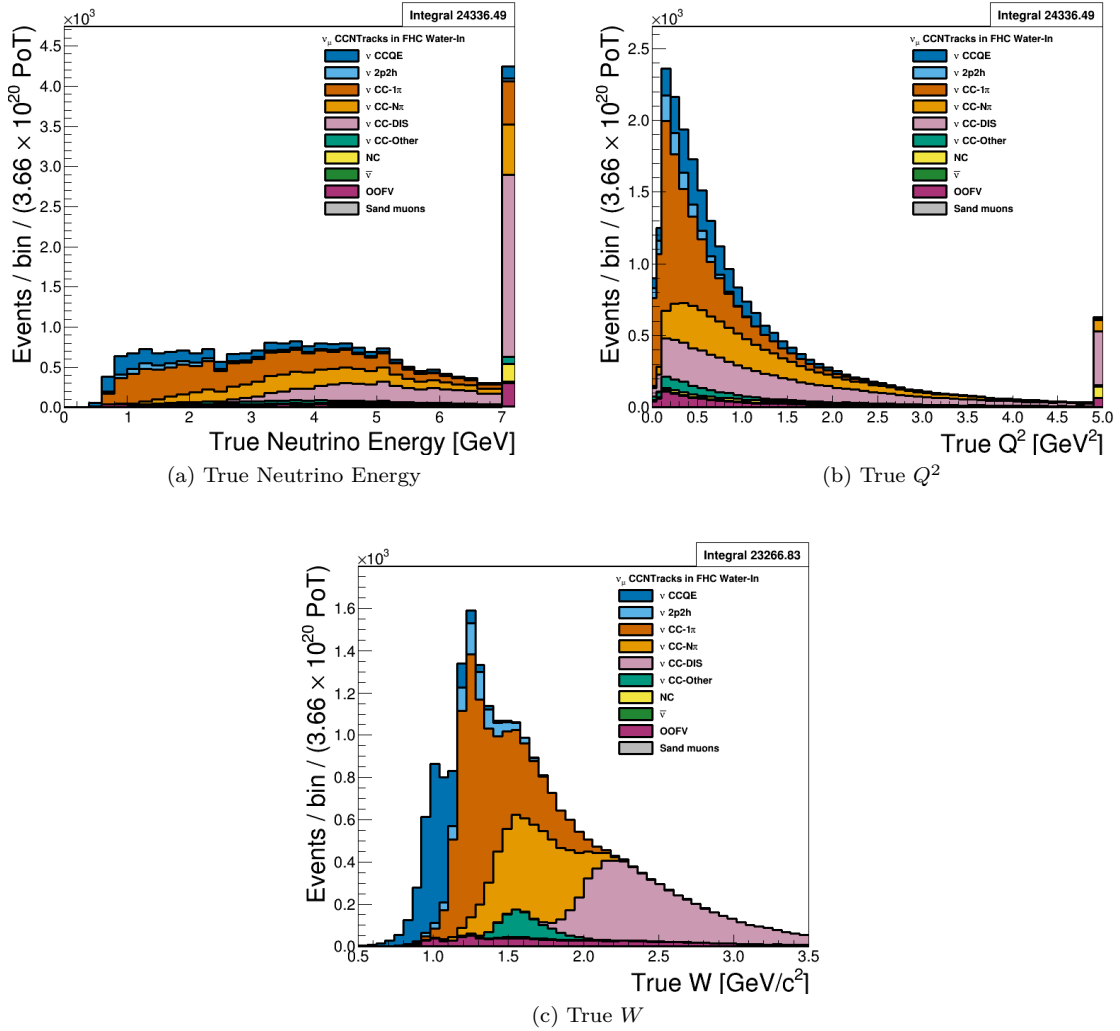


Figure 3.12: True kinematics of the  $\nu_\mu$  in FHC Mode CC N-Tracks selection. The last bin shown in (a) and (b) is used as overflow. The figures use the PØD water-in MC and are normalized to the FHC water-in mode POT. In figure (c), the largest resonance comes from the  $\Delta$  baryon. There are higher order resonances in (c) as well.

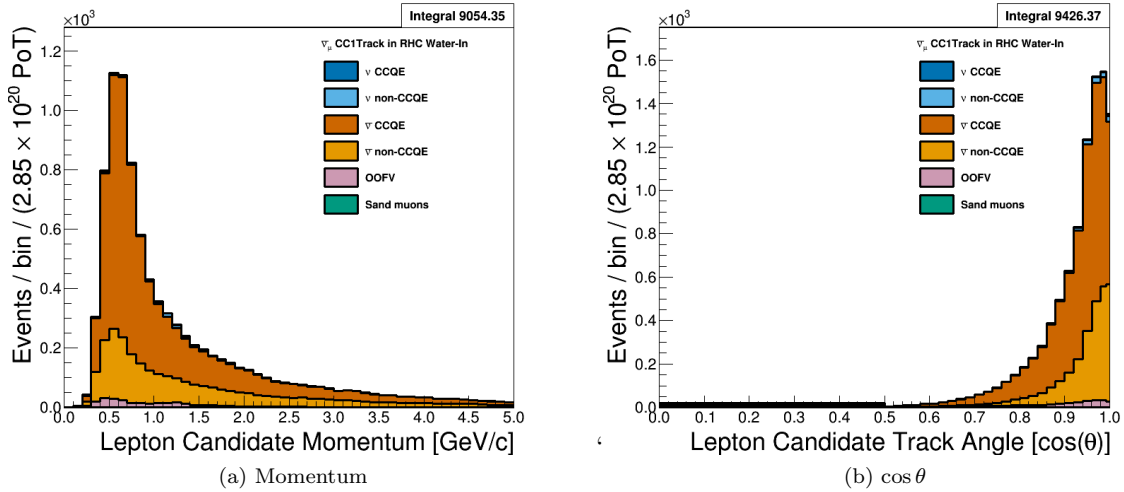


Figure 3.13: Reconstructed kinematics of the  $\bar{\nu}_\mu$  in RHC Mode CC 1-Track selection categorized by CCQE and non-CCQE interactions. The figures use the PØD water-in MC and are normalized to the RHC water-in mode POT. Also a single bin is used in the range of  $0 \leq \cos \theta < 0.5$  in figure (b).

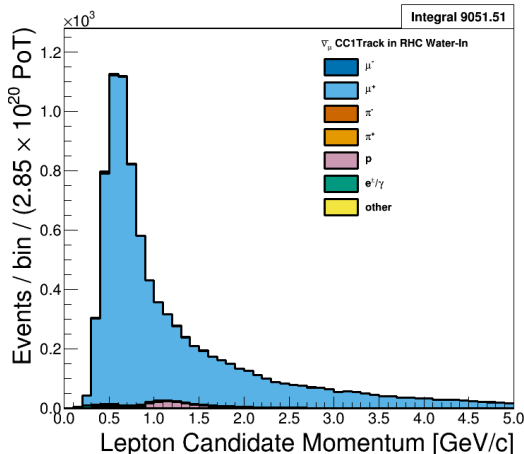
the efficiency and purity only, the true signal is a true  $\bar{\nu}_\mu$  CCQE interaction. The two distributions are very similar to the efficiency and purity observed in the  $\nu_\mu$  in FHC Mode CC 1-Track sample, with the efficiency being relatively high (90%) for high statistics regions.

The underlying true kinematics,  $E_\nu$  and  $Q^2$ , of the interactions are shown in Figure 3.16 on page 36. We see a similar true reaction composition with that of the  $\nu_\mu$  in FHC Mode sample in Section 3.3.1. Most reactions are true CCQE with a mixture of 2p2h and 1 $\pi$  events. As previously seen in Section 3.3.1, the significant 1 $\pi$  contamination may reduce the sensitivity to both CC-0 $\pi$  and CC-1 $\pi$  model parameters in the BANFF fit.

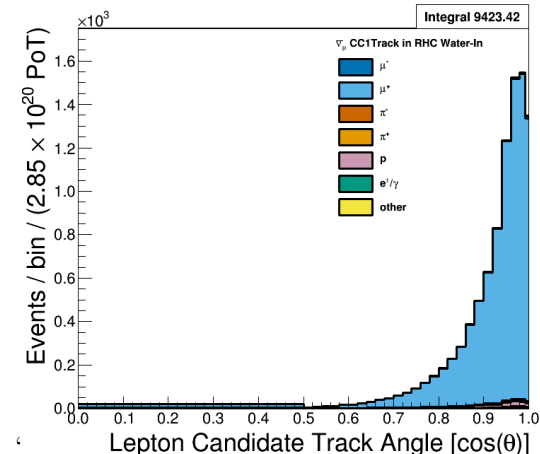
### 3.3.4 The $\bar{\nu}_\mu$ in RHC Mode CC N-Tracks Sample

This selection provides the  $\bar{\nu}_\mu$  non-CCQE-like samples in RHC mode. Figure 3.17 on page 36 and Figure 3.18 on page 37 display the momentum and angular distributions that are inputs to BANFF. The most striking feature of this selection is the number of mis-identified events. In particular tracks matched to protons are selected as the HMPT when the protons are minimum ionizing particles themselves, which is about 1.3 GeV/c. In addition, the intrinsic  $\nu_\mu$  background contribution is comparable to the desired  $\bar{\nu}_\mu$  flavor. These two features should be addressed to increase the utility of the selection for the next iteration of the analysis.

We can examine the efficiencies and purities differentially for the selection in Figure 3.11 on page 32. For the efficiency and purity only, the true signal is any  $\bar{\nu}_\mu$  CC interaction except  $\bar{\nu}_\mu$  CCQE which the CC 1-Track selection is designed to select. Both the efficiency and purity are low where statistics are high due

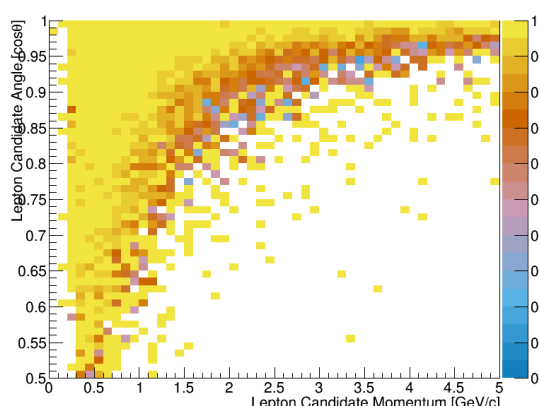


(a) Water-in

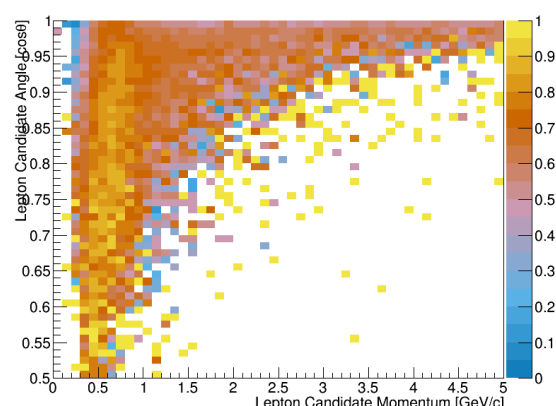


(b) Water-in

Figure 3.14: Reconstructed kinematics of the  $\bar{\nu}_\mu$  in RHC Mode CC 1-Track selection categorized by the true particle matched to the main track. The figures use the PØD water-in MC and are normalized to the RHC water-in mode POT. Also a single bin is used in the range of  $0 \leq \cos \theta < 0.5$  in figure (b).



(a) True  $\bar{\nu}_\mu$  CCQE Efficiency



(b) True  $\bar{\nu}_\mu$  CCQE Purity

Figure 3.15: Efficiency and purity of the  $\bar{\nu}_\mu$  in RHC Mode CC 1-Track selection. The true events are  $\bar{\nu}_\mu$  CCQE at the vertex and the selected lepton candidate is the true  $\mu^+$ .

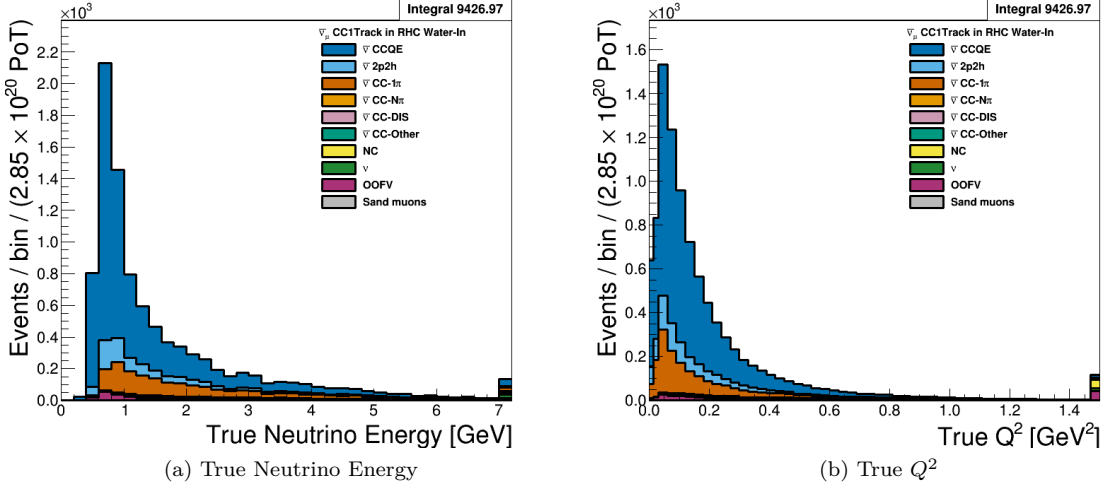


Figure 3.16: True kinematics of the  $\bar{\nu}_\mu$  in RHC Mode CC 1-Track selection. Water-in mode is displayed here only with the last bin shown is used as overflow. The figures use the PØD water-in MC and are normalized to the RHC water-in mode POT.

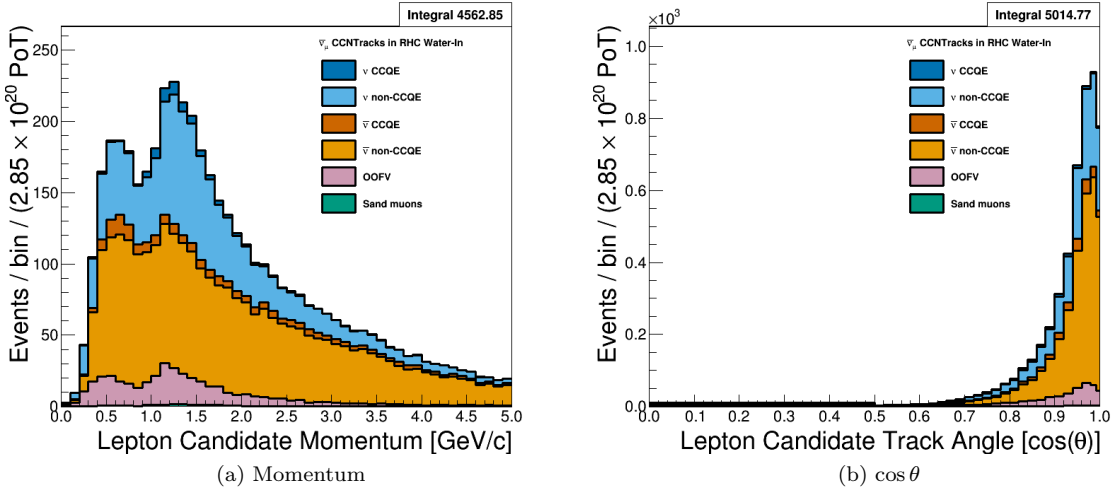


Figure 3.17: Reconstructed kinematics of the  $\bar{\nu}_\mu$  in RHC Mode CC N-Tracks selection categorized by CCQE and non-CCQE interactions. The figures use the PØD water-in MC and are normalized to the RHC water-in mode POT. Also a single bin is used in the range of  $0 \leq \cos \theta < 0.5$  in figure (b).

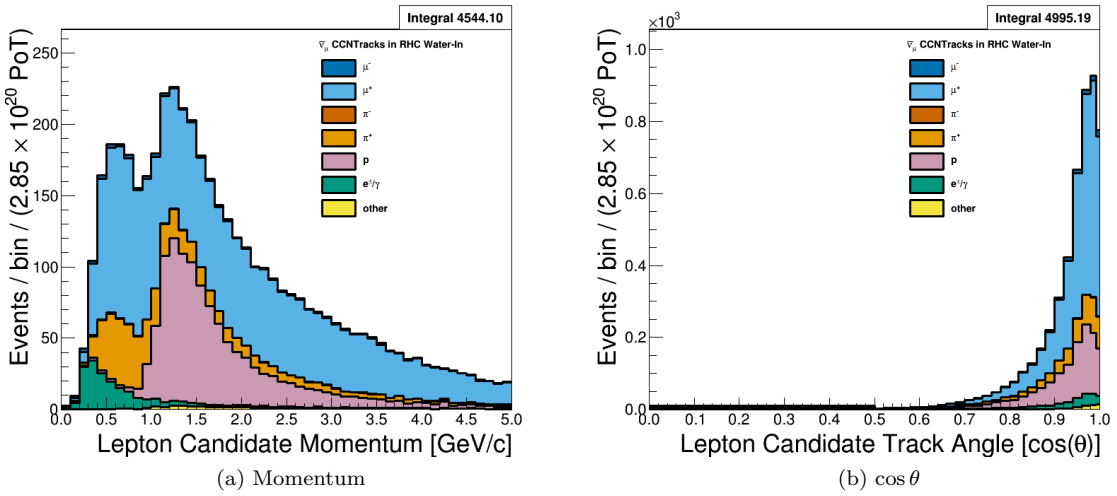


Figure 3.18: Reconstructed kinematics of the  $\bar{\nu}_\mu$  in RHC Mode CC N-Tracks selection categorized by the true particle matched to the main track. The figures use the PØD water-in MC and are normalized to the RHC water-in mode POT. Also a single bin is used in the range of  $0 \leq \cos \theta < 0.5$  in figure (b).

578 to the wrong sign background.

579 The underlying true kinematics,  $E_\nu$ ,  $Q^2$ , and  $W$ , of the interactions are shown in Figure 3.20 on page 39.

580 Here we see in better detail the origin of the  $\nu_\mu$  contamination. As a function of increasing energy, the  $\bar{\nu}_\mu$   
 581 content is decreasing while the relative  $\nu_\mu$  contribution is increasing. The  $\nu_\mu$  events also have high  $Q^2$  which  
 582 explains the significant number of misidentified proton main track events. For the hadronic final states, the  
 583 shape of the  $\bar{\nu}_\mu$ -induced resonances is similar to what we saw in Figure 3.12 on page 33. Interestingly, the  
 584  $\nu_\mu$  background hadronic mass distribution does not peak in any one region.

### 585 3.3.5 The $\nu_\mu$ Background in RHC Mode CC 1-Track Sample

586 This selection provides the  $\nu_\mu$  in RHC, also called wrong-sign background, CCQE-like samples . Figure  
 587 3.21 on page 40 and Figure 3.22 on page 40 display the momentum and angular distributions inputs to the  
 588 BANFF fit. We can see this is a relatively low-angle selection compared to previous selections. Importantly  
 589 the selection is relatively  $\nu_\mu$ -pure which should help constrain the wrong-sign background in the fit. However,  
 590 the CCQE purity is modest given number of correctly identified lepton candidates. This feature needs to be  
 591 addressed in the next iteration of the analysis.

592 We can examine the efficiencies and purities differentially for the selection in Figure 3.23 on page 41. For  
 593 the efficiency and purity only, the true signal is a true  $\nu_\mu$  CCQE interaction. The efficiency is similar to the  
 594  $\nu_\mu$  in FHC Mode CC 1-Track topology efficiency with banded  $p - \theta$  regions. As for the purity, it is roughly  
 595 70% in a banded region between low momenta, low angle and high momenta, high angle tracks.

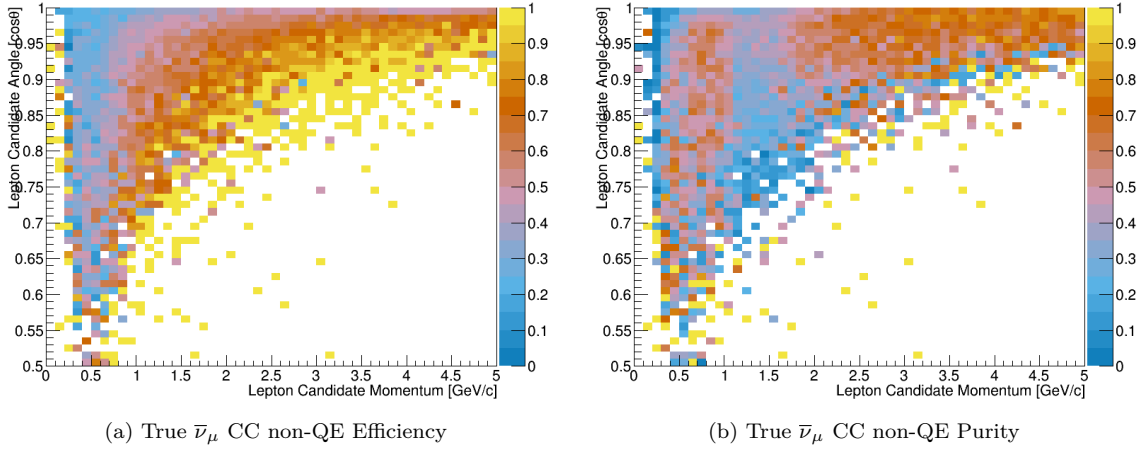


Figure 3.19: Efficiency and purity of the  $\bar{\nu}_\mu$  in RHC Mode CC N-Tracks selection. True events are defined as correctly matched  $\mu^+$  tracks from  $\bar{\nu}_\mu$ -induced CC non-QE interactions at the vertex.

The underlying true kinematics,  $E_\nu$  and  $Q^2$ , of the selection are shown in Figure 3.24 on page 41. The number of the wrong-sign background events peaks at 1 GeV and is a broad peak compared to the designed sharp  $\bar{\nu}_\mu$  peak at 0.6 GeV as shown in Figure 3.16 on page 36. Since these are higher energy events, there is more available energy to produce resonance states that produce  $1\pi$  topologies. This explains the significant non-CCQE event contamination.

### 3.3.6 The $\nu_\mu$ Background in RHC Mode CC N-Tracks Sample

This selection provides the non-CCQE-like samples for the  $\nu_\mu$  background in RHC mode. Figure 3.25 on page 42 and Figure 3.26 on page 42 show the momentum and angular distributions that are inputs to the BANFF fit. We can see the selection is relatively  $\nu_\mu$ -pure with a significant mis-identified track rate. Interestingly, the misidentified pion main tracks have a high momentum tail.

We can examine the  $\nu_\mu$  CC non-QE efficiency and purity of the selection in Figure 3.27 on page 43. There is a reduction in the purity below 1.5 GeV/c due to the the  $\bar{\nu}_\mu$  selections occupying the same phase space. Fortunately, the efficiency and purity are relatively high above 1.5 GeV/c.

The underlying true kinematics,  $E_\nu$ ,  $Q^2$ , and  $W$ , of the interactions are shown in Figure 3.28 on page 44. As we have seen before with the CC N-Tracks samples, these are high  $E_\nu$  events with large  $Q^2$  exchanges. The invariant hadronic system displays the previously seen resonances, with the largest still being from the  $\Delta$  baryon.

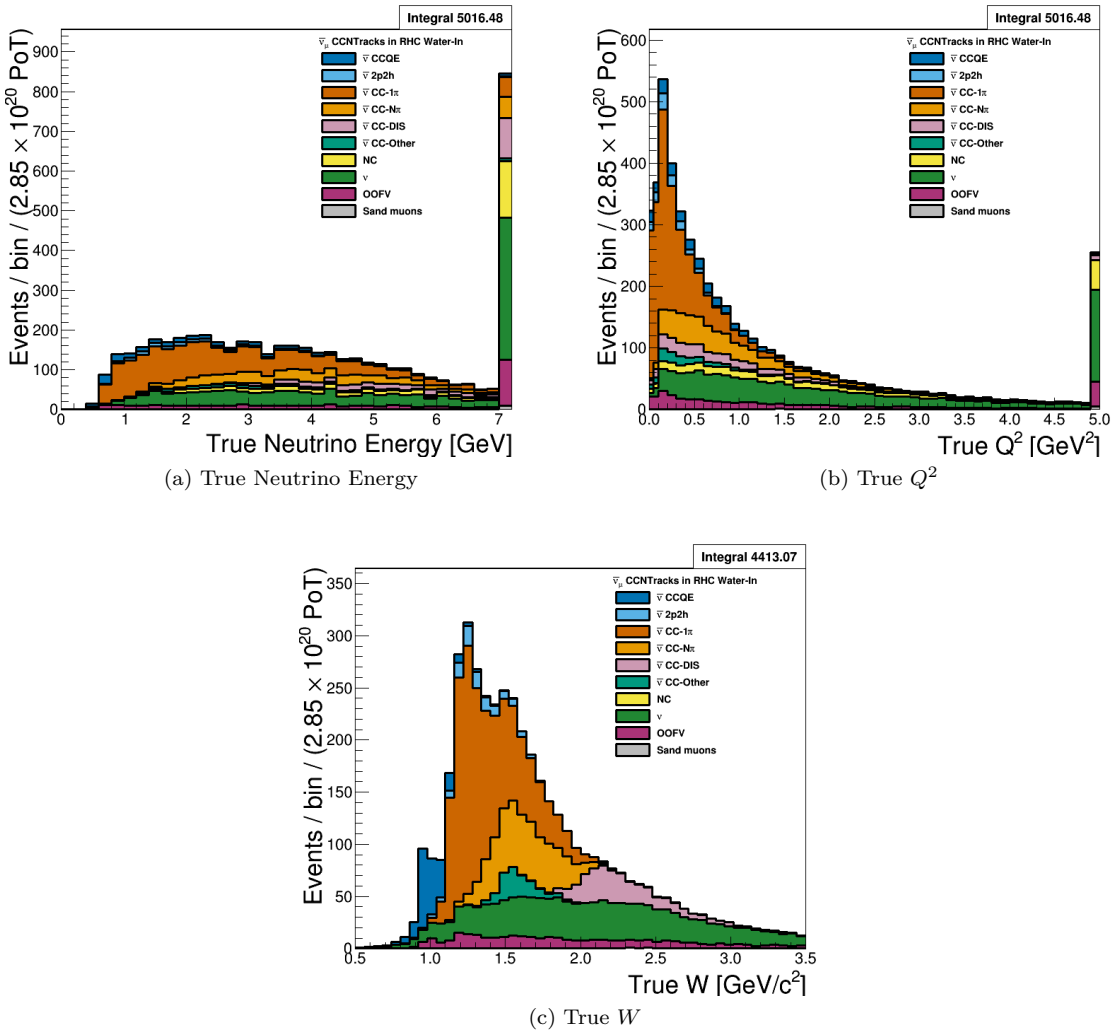


Figure 3.20: True kinematics of the  $\bar{\nu}_\mu$  in RHC Mode CC N-Tracks selection. The last bin shown in (a) and (b) is used as overflow. The figures use the PØD water-in MC and are normalized to the RHC water-in mode POT.

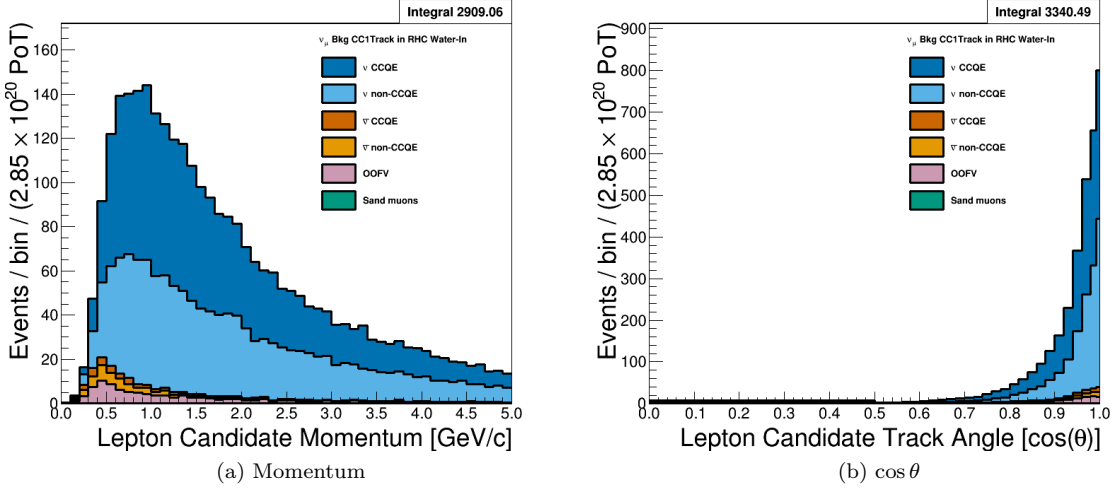


Figure 3.21: Reconstructed kinematics of the  $\nu_\mu$  Background in RHC Mode CC 1-Track selection categorized by CCQE and non-CCQE interactions. The figures use the PØD water-in MC and are normalized to the RHC water-in mode POT. Also a single bin is used in the range of  $0 \leq \cos \theta < 0.5$  in figure (b).

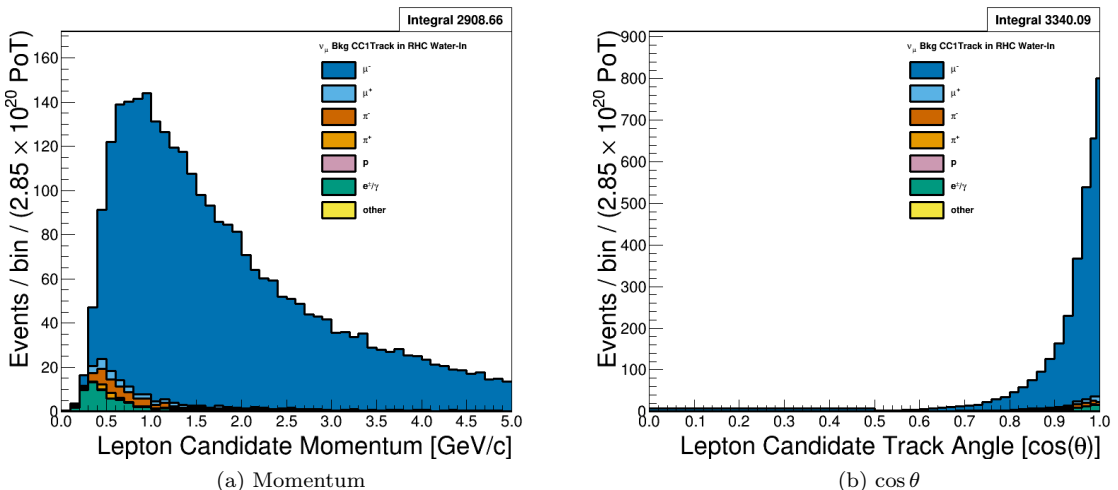


Figure 3.22: Reconstructed kinematics of the  $\nu_\mu$  Background in RHC Mode CC 1-Track selection categorized by the true particle matched to the main track. The figures use the PØD water-in MC and are normalized to the RHC water-in mode POT. Also a single bin is used in the range of  $0 \leq \cos \theta < 0.5$  in figure (b).

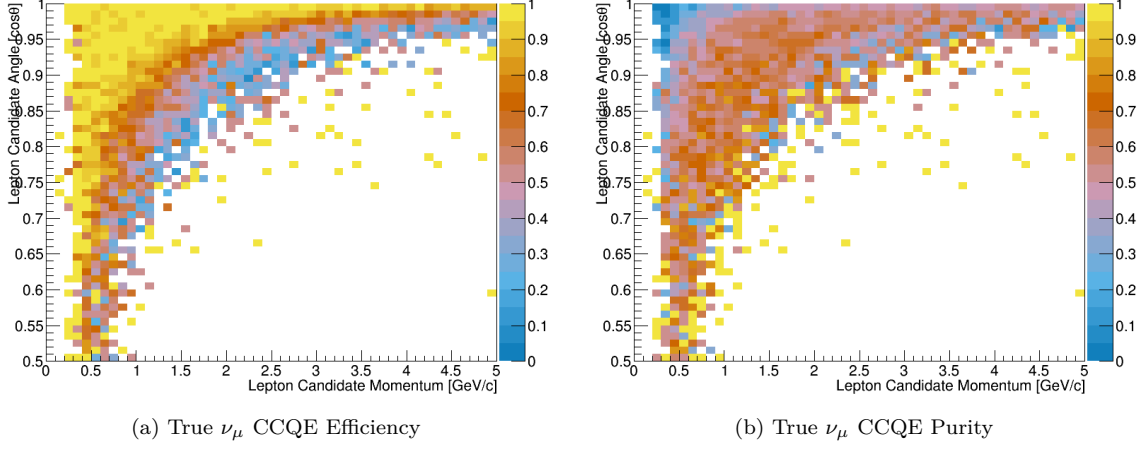


Figure 3.23: Efficiency and purity of the  $\nu_\mu$  Background in RHC Mode CC 1-Track selection. The true events are  $\nu_\mu$  CCQE at the vertex and the selected lepton candidate is the true  $\mu^-$ .

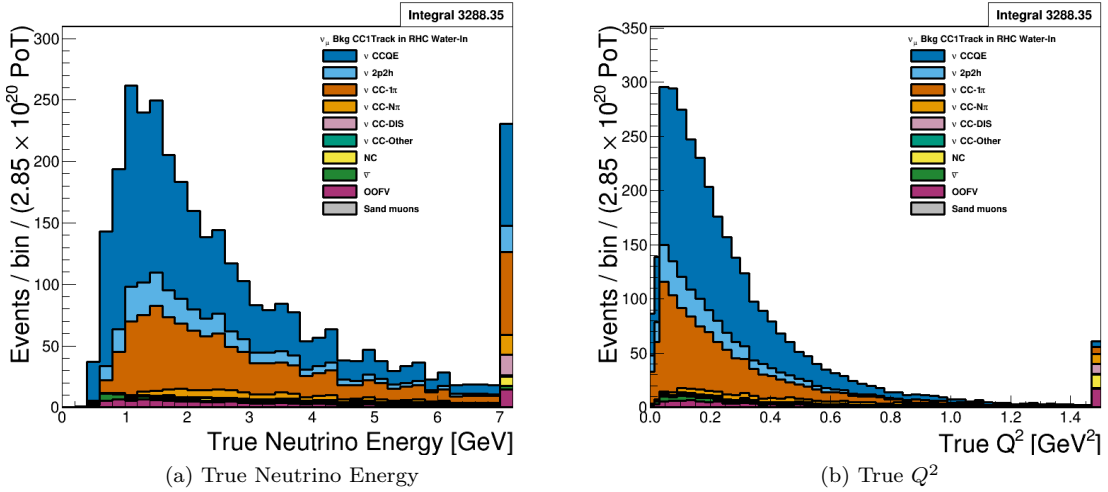


Figure 3.24: True kinematics of the  $\nu_\mu$  Background in RHC Mode CC 1-Track selection. Water-in mode is displayed here only with the last bin shown as overflow. The figures use the PØD water-in MC and are normalized to the RHC water-in mode POT.

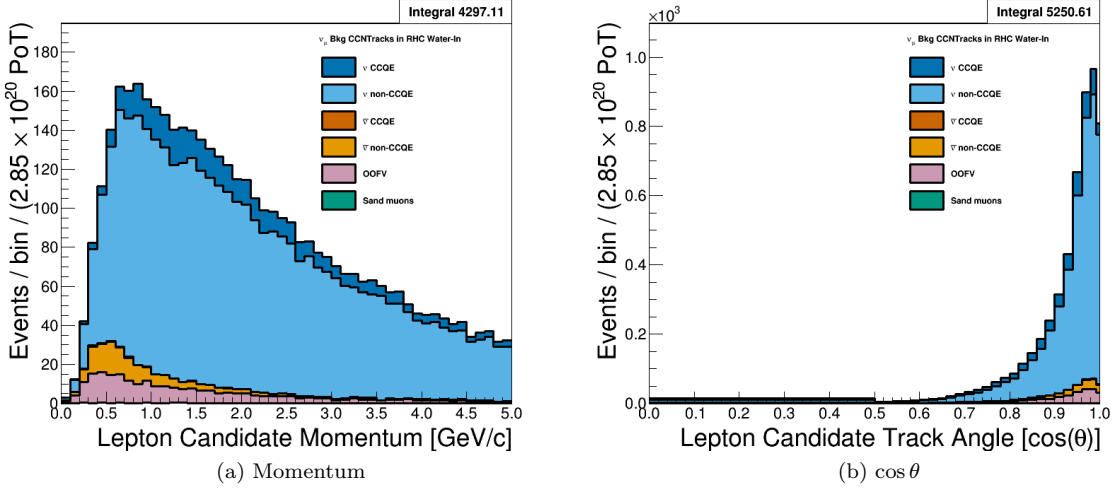


Figure 3.25: Reconstructed kinematics of the  $\nu_\mu$  Background in RHC Mode CC 1-Track selection categorized by CCQE and non-CCQE interactions. The figures use the PØD water-in MC and are normalized to the RHC water-in mode POT. Also a single bin is used in the range of  $0 \leq \cos \theta < 0.5$  in figure (b).

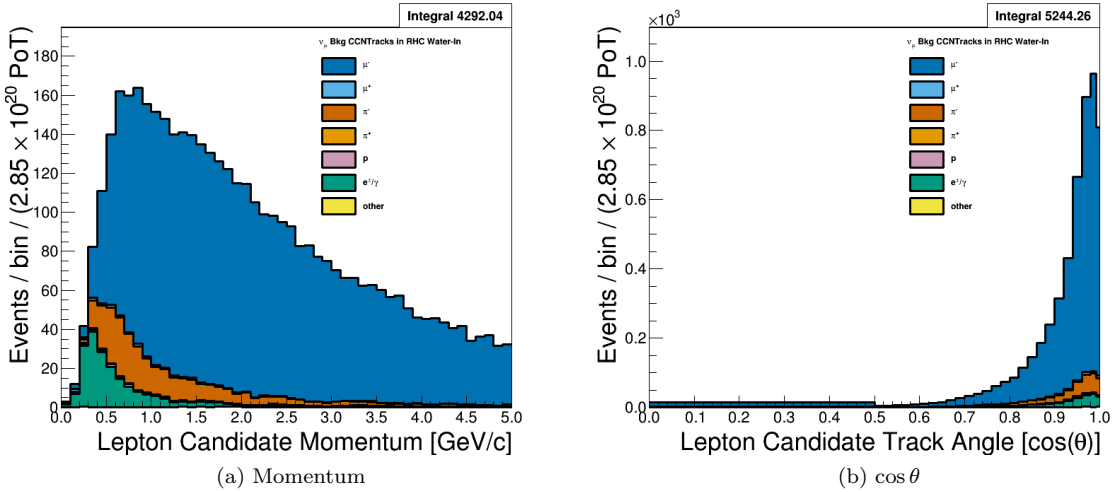


Figure 3.26: Reconstructed kinematics of the  $\nu_\mu$  Background in RHC Mode CC 1-Track selection categorized by the true particle matched to the main track. The figures use the PØD water-in MC and are normalized to the RHC water-in mode POT. Also a single bin is used in the range of  $0 \leq \cos \theta < 0.5$  in figure (b).

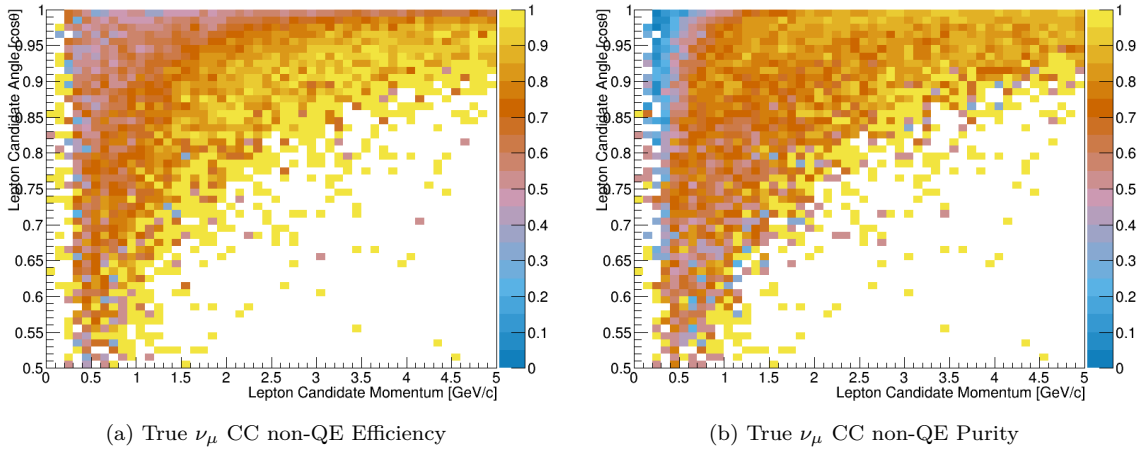


Figure 3.27: Efficiency and purity of the  $\nu_\mu$  Background in RHC Mode CC N-Tracks selection. True events are defined as correctly matched  $\mu^-$  tracks from  $\nu_\mu$ -induced CC non-QE interactions at the vertex.

## 613 3.4 Summary

614 In this chapter we have examined the selection true and reconstruction kinematics that will be used in the  
 615 BANFF fit. We see the 1-Track selections yield some reasonably pure CCQE samples. By inverting that  
 616 cut, we obtain some information on the rate of other topologies like CC- $1\pi$  and high  $Q^2$  CCDIS events.  
 617 Importantly is the ability of these samples to constrain the correct sign ( $\bar{\nu}_\mu$ ) and wrong sign ( $\nu_\mu$ ) backgrounds  
 618 in RHC mode, which are very important in the oscillation analysis. We can now move forward to the next  
 619 chapter to describe the fit parameters and the systematic uncertainties present in the analysis.

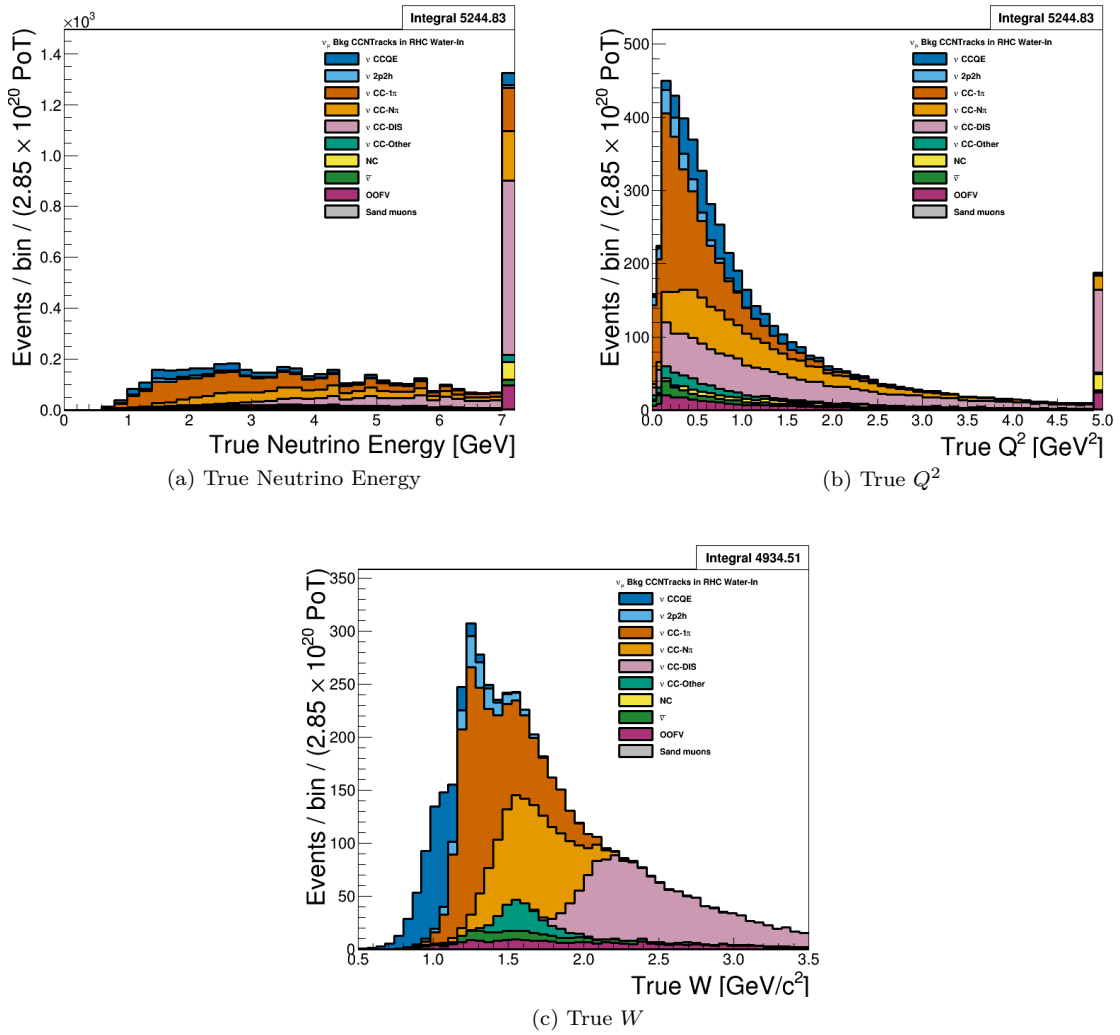


Figure 3.28: True kinematics of the  $\nu_\mu$  Background in RHC Mode CC N-Tracks selection. The last bin shown in (a) and (b) is used as overflow. The figures use the PØD water-in MC and are normalized to the RHC water-in mode POT.

620    **Chapter 4**

621    **The BANFF Fit Parameters**

622    This chapter explores the fit binning and penalty terms in the test statistic used for this analysis. The  
623    BANFF fit includes three sources of systematic uncertainties: neutrino flux, cross section model, and detector  
624    inefficiencies. The sources of systematic uncertainty, also referred to just as systematics, will be defined and  
625    their effects on the analysis will be examined. These three terms directly affect the flux of neutrinos, efficiency  
626    of reconstruction, and the cross section for  $\nu_\alpha$  terms, respectively, in the predicted rate equation given in  
627    Eqn. (??).

628    This chapter is presented in the following order. The method to define histogram fit bins in the likelihood  
629    ratio is discussed in Section 4.1. The parameterization of each penalty term in the test statistic is described  
630    in Section 4.2 in the following order: the neutrino flux model, the detector inefficiencies, and the cross section  
631    model. The chapter summary is provided in Section 4.3.

632    **4.1 Fit Binning**

633    The PØD-only BANFF fit uses the samples described in Chapter 3 to evaluate the log-likelihood ratio term,  
634     $\chi^2_{\text{LLR}}$ . Since this is a binned likelihood in  $(p, \cos \theta)$ , the bin edges need to be defined first.

635    The BANFF fit binning is optimized to ensure at least 1 predicted Monte Carlo (MC) event in each bin  
636    for every PØD sample when scaled to the collected data POT. The fit bins must also account for detector  
637    smearing effects. In order to mitigate smearing and event migration, the reconstructed muon track kinematics  
638    were examined against correctly identified tracks in one-dimensional kinematic slices. The kinematics are  
639    scanned across their full phase spaces in order to understand the required width for a fit bin. The first fit  
640    bin is always defined starting from the kinematic maximum.

641    To determine the optimal momentum fit bins, the momentum resolution with the MC truth matched

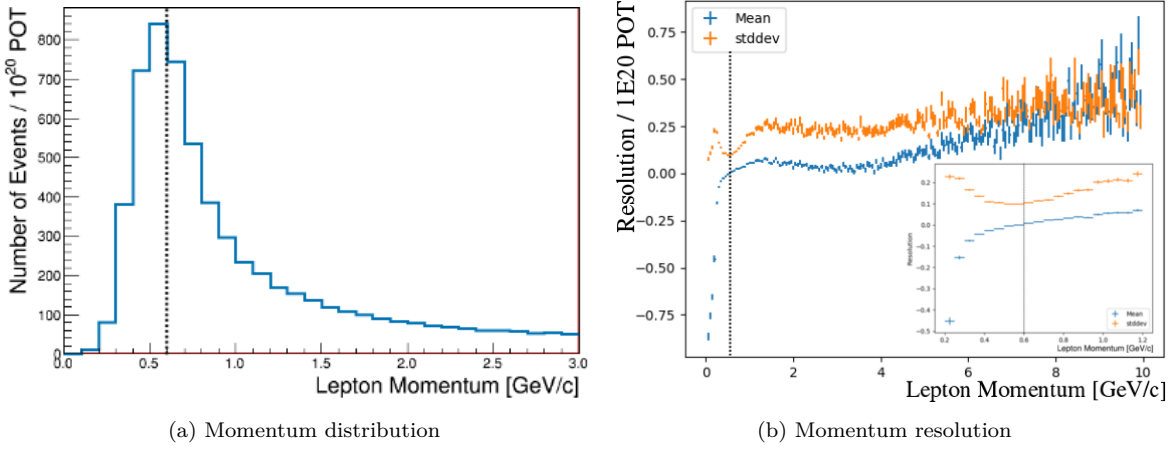


Figure 4.1: Main track momentum resolution for the  $\nu_\mu$  in FHC Mode CC 1-Track sample. Only correctly identified muons are used. The number of events is scaled to  $10^{20}$  POT, which is the approximate scale for all the samples in this analysis. A dashed line indicates the maximum of the distribution peak from figure (a). The resolution of the momentum measurement is shown in figure (b) whose error bars are estimated using bootstrapping. In the inset is the momentum resolution zoomed near the momentum distribution maximum.

642 muon is analyzed. The momentum resolution is defined as

$$R(r, t) = \frac{r - t}{t},$$

643 where  $r$  is the reconstructed momentum and  $t$  is the true muon momentum. The mean (bias) and standard  
 644 deviation (stddev) of  $R$  are used as proxies for the true bias and resolution for the prediction. Both quantities  
 645 and prediction errors were extracted using a bootstrapping algorithm[16] in very fine bins of reconstructed  
 646 momentum. The bootstrapping algorithm works by random sampling with replacement of the true muon  
 647 momentum. For each bias and stddev prediction, at least 1000 bootstrapping samples were generated.  
 648 Each bootstrap bias and stddev value were saved to calculate a prediction mean and error. In the case of  
 649 relatively “large” prediction errors, additional 10000 bootstrapping samples were generated. The main track  
 650 momentum resolution for the  $\nu_\mu$  in FHC Mode CC 1-Track sample is shown in Figure 4.1 on page 46 to  
 651 illustrate the results.

652 The optimal  $\cos\theta$  fit bins were determined in a very similar manner with the momentum fit bins. While  
 653 the fit bins and physics are dictated in  $\cos\theta$  space, the detector smearing is a function  $\theta$ . In addition, since  
 654 the angle can be nearly zero for the most forward-going tracks, the resolution was not used to characterize  
 655 the angular uncertainties. Instead, the difference (“residual”) between the true and reconstructed angle  $\theta$   
 656 with respect to (wrt) the ND280 Z-axis was analyzed. The same bootstrapping algorithm described above  
 657 was used to determine the mean and stddev of the  $\theta$  residuals. The main track angular residuals for the  $\nu_\mu$

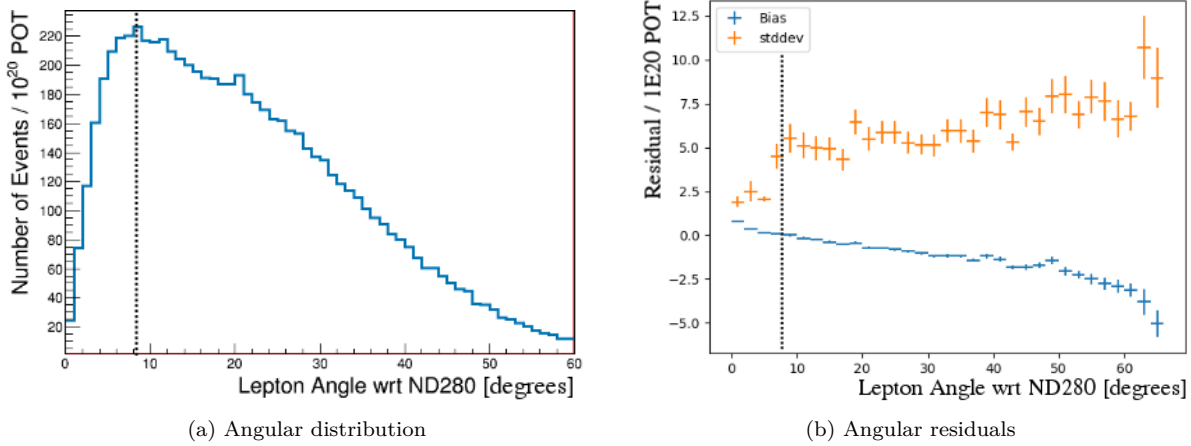


Figure 4.2: Main track angular residuals for the  $\nu_\mu$  in FHC Mode CC 1-Track sample. Only correctly identified muons are used. The number of events is scaled to  $10^{20}$  POT, which is the approximate scale for all the samples in this analysis. A dashed line indicates the maximum of the distribution peak from figure (a). The residual of the angular measurement is shown in figure (b) whose error bars are estimated using bootstrapping.

in FHC Mode CC 1-Track sample are shown in Figure 4.2 on page 47 to illustrate the results.

This procedure to define fit bin edges emphasizes regions of high statistics and mitigates regions with low statistics. Since the MC provides about  $10\times$  the data statistics, the statistical uncertainty for each bin should be negligible in high statistics regions. However, this does not account for the low statistics regions predicted by the nominal MC. We tackle this problem and other systematic uncertainties for the fit bins using bin normalizations as explained in Chapter 2.

### 664 4.1.1 Fit Bin Edges

665 There are a total 988 fit bins with water-in and water-out modes sharing the same bin edges. The finalized  
666 fit bins are tabulated below.

- The  $\nu_\mu$  in FHC Mode CC 1-Track water-in and water-out samples:
    - $p$  [GeV/c]: 0, 0.3, 0.4, 0.5, 0.6, 0.7, 0.8, 1, 1.25, 1.5, 2, 3, 4, 5.5, 30
    - $\cos \theta$ : -1, 0.7, 0.8, 0.88, 0.94, 0.96, 0.975, 0.99, 1
  - The  $\nu_\mu$  in FHC Mode CC N-Tracks water-in and water-out samples:
    - $p$  [GeV/c]: 0, 0.4, 0.5, 0.6, 0.7, 0.8, 1, 1.2, 1.5, 1.8, 2.2, 2.7, 3.5, 5, 10, 30
    - $\cos \theta$ : -1, 0.65, 0.77, 0.85, 0.9, 0.94, 0.97, 0.99, 1
  - The  $\bar{\nu}_\mu$  in RHC Mode CC 1-Track water-in and water-out samples:

- 674           –  $p$  [GeV/c]: 0, 0.4, 0.5, 0.6, 0.7, 0.8, 1, 1.25, 1.5, 2, 3, 30
- 675           –  $\cos \theta$  : -1, 0.82, 0.87, 0.9, 0.93, 0.95, 0.97, 0.99, 1
- 676       • The  $\bar{\nu}_\mu$  in RHC Mode CC N-Tracks water-in and water-out samples:
- 677           –  $p$  [GeV/c]: 0, 0.5, 0.9, 1.25, 1.6, 2, 3, 8, 30
- 678           –  $\cos \theta$  : -1, 0.8, 0.89, 0.95, 0.97, 0.99, 1
- 679       • The  $\nu_\mu$  in RHC CC 1-Track water-in and water-out samples:
- 680           –  $p$  [GeV/c]: 0, 0.4, 0.6, 0.8, 1.1, 2, 10
- 681           –  $\cos \theta$  : -1, 0.78, 0.84, 0.89, 0.92, 0.95, 0.97, 0.98, 0.99, 1
- 682       • The  $\nu_\mu$  in RHC CC N-Tracks water-in and water-out samples:
- 683           –  $p$  [GeV/c]: 0, 0.4, 0.6, 0.8, 1, 1.5, 2, 3, 10
- 684           –  $\cos \theta$  : -1, 0.7, 0.8, 0.85, 0.9, 0.94, 0.965, 0.98, 0.99, 1

## 685   **4.2 Systematic Uncertainties and Penalty Terms**

686   This section provides details on the penalty terms, and hence fit parameters, in the BANFF fit. The  
 687   cross section and flux penalty terms in this analysis are identical to the previous near detector constraint  
 688   studies[17, 18]. This provides a one-to-one comparison between the PØD-only and FGD-only flux and cross  
 689   section predictions. However, due to the different detector technologies between the PØD and FGD, different  
 690   bin normalization parameters are necessary.

691   The fit parameters are described in the following order. The first set of parameters are the flux terms.  
 692   This is followed by a description of the fit bin normalization parameters. The final topic is a description of  
 693   the cross section parameters.

### 694   **4.2.1 Flux Model Parameters**

695   The T2K neutrino flux model is a description of the neutrino beam energy spectrum for each run period and  
 696   flavor. This model includes simulations of the proton beam interactions and subsequent hadron production at  
 697   the target. The predicted hadron production rate, including inside and outside the graphite target, is tuned to  
 698   the results from the replica target<sup>1</sup> experiment NA61/SHINE[19] and other hadron production experiments.

---

<sup>1</sup>The NA61/SHINE experiment has two graphite targets. A thin 2 cm target and a thick 90 cm target. The thick target is a replica of the T2K graphite target.

699 The uncertainties in the unoscillated flux tuning are dominated by hadron production. Smaller effects on  
 700 the unoscillated flux uncertainty include the proton beam profile, off-axis angle, horn current, and horn  
 701 alignment. Further details about the flux model and uncertainties can be found in the following reference[2].  
 702 The flux parameters are especially important since they are used as inputs to the oscillation analysis.  
 703

The flux penalty term in the BANFF fit is defined as

$$\chi_{\text{Flux}}^2 = \left( \vec{b} - \vec{b}_0 \right)^T \left( V^{\text{Flux}} \right)^{-1} \left( \vec{b} - \vec{b}_0 \right), \quad (4.1)$$

704 where  $\vec{b}$  is the vector of flux parameter values,  $\vec{b}_0$  is the vector of the initial parameter values, and  $V^{\text{Flux}}$  is the  
 705 flux covariance matrix. As a remainder, all penalty terms in this analysis have the form of Eqn. (4.1). Each  
 706 flux parameter is a neutrino energy bin normalization starting at one (1). Formally, a flux bin is defined as

$$b_i = \frac{N'_{\nu_\alpha, i}}{N_{\nu_\alpha, i}}, \quad (4.2)$$

707 where  $N_{\nu_\alpha, i}$  and  $N'_{\nu_\alpha, i}$  are the predicted and ND constrained  $\nu_\alpha$  event rates, respectively, in the  $i$ th energy  
 708 bin. In other words, *each flux term is a ratio of rates. Further, all penalty terms and covariance terms are*  
 709 *dimensionless.* A postfit value of 1.1 indicates that all events in that energy bin have an additional weight of  
 710 1.1, signaling that the postfit prefers to increase that neutrino flux by 10%. Equivalently, this means  $N'_{\nu_\alpha, i}$   
 711 is 10% greater than  $N_{\nu_\alpha, i}$ .

712 In the BANFF fit, both ND280 and SK flux parameters are estimated simultaneously. This is achieved  
 713 using correlations between ND280 and SK flux parameters in the covariance matrix. The covariance matrix  
 714 is provided by the T2K flux group and is shown in Figure 4.3 on page 50. Also shown in Figure 4.3 on page  
 715 50 is the Pearson linear correlation coefficient matrix which is defined as

$$\rho_{i,j} = \frac{V_{i,j}}{\sqrt{V_{i,i}V_{j,j}}}, \quad (4.3)$$

716 where  $i$  and  $j$  are bins in  $V$ .

717 The tabulated flux parameters/bins and uncertainties in this analysis are given in Table 4.1 on page 51.  
 718 These are the first set of parameters in the fit. The flux parameters are differentiated by neutrino energy,  
 719 horn current/polarity (FHC mode and RHC mode), neutrino flavor ( $\nu_\mu$ ,  $\bar{\nu}_\mu$ ,  $\nu_e$ , and  $\bar{\nu}_e$ ), and detector (ND280  
 720 and SK). There are 50 ND280 and 50 SK flux parameters to yield a total of 100 flux normalizations. In  
 721 addition, the bin edges are shared between the ND280 and SK. The SK neutrino flux and the flux bin edges  
 722 are shown in Figure 4.4 on page 50.

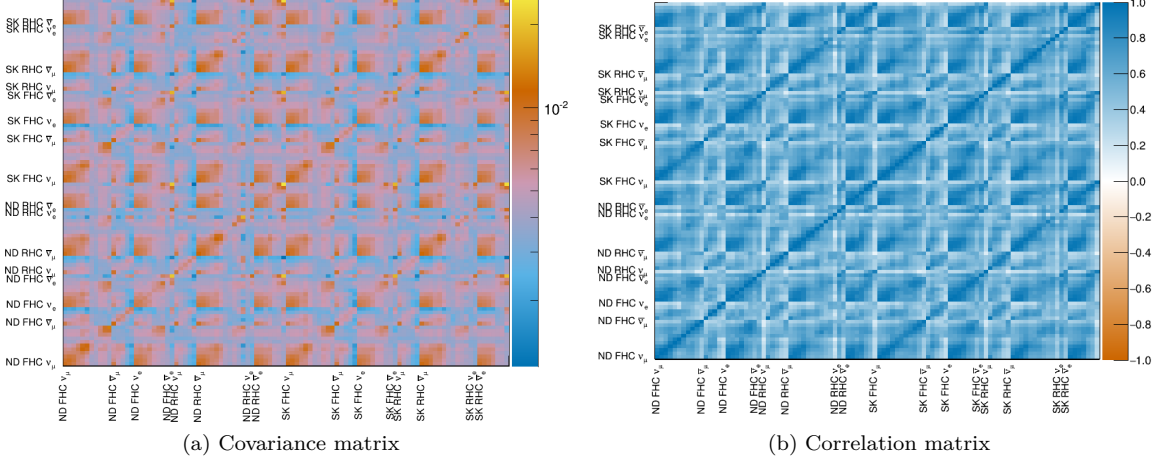


Figure 4.3: The BANFF prefit flux covariance matrix. Figure (a) shows the covariance matrix which is the uncertainty of the normalization for the neutrino flux at both ND280 and SK. The covariance matrix is divided into submatrices in groups by detector, beam mode, and neutrino flavor. Figure (b) is the linear correlation coefficient for each covariance term.

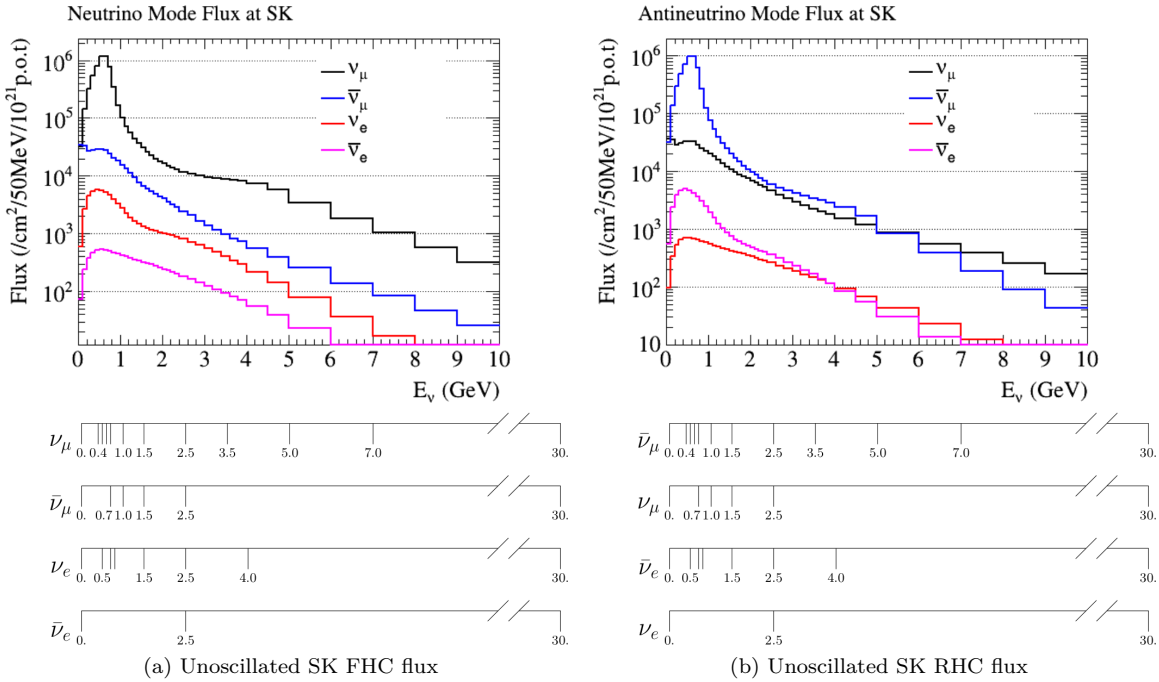


Figure 4.4: Neutrino flux prediction at SK and flux bin edges. The flux prediction for FHC (RHC) mode is shown in figure on the left (right). The flux normalization parameters have an assigned energy range and are the same for both the SK and ND280 detectors. The energy binning used is shown below the plots.

---

 Table 4.1: Flux binning and uncertainties used in the BANFF fit.

<b>Fit index</b>	<b>Beam mode</b>	<b>Bin edges [GeV]</b>	<b>Prefit</b>
0	ND280 $\nu_\mu$ FHC	0.0 - 0.4	$1 \pm 0.100909$
1		0.4 - 0.5	$1 \pm 0.099431$
2		0.5 - 0.6	$1 \pm 0.092025$
3		0.6 - 0.7	$1 \pm 0.085239$
4		0.7 - 1.0	$1 \pm 0.105356$
5		1.0 - 1.5	$1 \pm 0.104375$
6		1.5 - 2.5	$1 \pm 0.073612$
7		2.5 - 3.5	$1 \pm 0.068993$
8		3.5 - 5.0	$1 \pm 0.082334$
9		5.0 - 7.0	$1 \pm 0.097308$
10		7.0 - 30	$1 \pm 0.114706$
11	ND280 $\bar{\nu}_\mu$ FHC	0.0 - 0.7	$1 \pm 0.103804$
12		0.7 - 1.0	$1 \pm 0.084158$
13		1.0 - 1.5	$1 \pm 0.081349$
14		1.5 - 2.5	$1 \pm 0.085208$
15		2.5 - 30	$1 \pm 0.087735$
16	ND280 $\nu_e$ FHC	0.0 - 0.5	$1 \pm 0.091336$
17		0.5 - 0.7	$1 \pm 0.089699$
18		0.7 - 0.8	$1 \pm 0.084648$
19		0.8 - 1.5	$1 \pm 0.079722$
20		1.5 - 2.5	$1 \pm 0.079766$
21		2.5 - 4.0	$1 \pm 0.081399$
22		4.0 - 30	$1 \pm 0.095795$
23	ND280 $\bar{\nu}_e$ FHC	0.0 - 2.5	$1 \pm 0.072069$
24		2.5 - 30	$1 \pm 0.142921$
25	ND280 $\nu_\mu$ RHC	0.0 - 0.7	$1 \pm 0.094066$
26		0.7 - 1.0	$1 \pm 0.079866$
27		1.0 - 1.5	$1 \pm 0.080948$
28		1.5 - 2.5	$1 \pm 0.083251$

<b>Fit index</b>	<b>Beam mode</b>	<b>Bin edges [GeV]</b>	<b>Prefit</b>
29		2.5 - 30	$1 \pm 0.082653$
30	ND280 $\bar{\nu}_\mu$ RHC	0.0 - 0.4	$1 \pm 0.107277$
31		0.4 - 0.5	$1 \pm 0.098851$
32		0.5 - 0.6	$1 \pm 0.089710$
33		0.6 - 0.7	$1 \pm 0.084692$
34		0.7 - 1.0	$1 \pm 0.106871$
35		1.0 - 1.5	$1 \pm 0.098711$
36		1.5 - 2.5	$1 \pm 0.073350$
37		2.5 - 3.5	$1 \pm 0.070520$
38		3.5 - 5.0	$1 \pm 0.092905$
39		5.0 - 7.0	$1 \pm 0.089083$
40		7.0 - 30	$1 \pm 0.134911$
41	ND280 $\nu_e$ RHC	0.0 - 2.5	$1 \pm 0.066214$
42		2.5 - 30	$1 \pm 0.086977$
43	ND280 $\bar{\nu}_e$ RHC	0.0 - 0.5	$1 \pm 0.095575$
44		0.5 - 0.7	$1 \pm 0.089033$
45		0.7 - 0.8	$1 \pm 0.088406$
46		0.8 - 1.5	$1 \pm 0.081472$
47		1.5 - 2.5	$1 \pm 0.078353$
48		2.5 - 4.0	$1 \pm 0.089427$
49		4.0 - 30	$1 \pm 0.156972$
50	SK $\nu_\mu$ FHC	0.0 - 0.4	$1 \pm 0.102555$
51		0.4 - 0.5	$1 \pm 0.101771$
52		0.5 - 0.6	$1 \pm 0.092573$
53		0.6 - 0.7	$1 \pm 0.084265$
54		0.7 - 1.0	$1 \pm 0.102271$
55		1.0 - 1.5	$1 \pm 0.084528$
56		1.5 - 2.5	$1 \pm 0.066909$
57		2.5 - 3.5	$1 \pm 0.072355$
58		3.5 - 5.0	$1 \pm 0.085299$

<b>Fit index</b>	<b>Beam mode</b>	<b>Bin edges [GeV]</b>	<b>Prefit</b>
59		5.0 - 7.0	$1 \pm 0.096725$
60		7.0 - 30	$1 \pm 0.114112$
61	SK $\bar{\nu}_\mu$ FHC	0.0 - 0.7	$1 \pm 0.103129$
62		0.7 - 1.0	$1 \pm 0.078327$
63		1.0 - 1.5	$1 \pm 0.082367$
64		1.5 - 2.5	$1 \pm 0.082121$
65		2.5 - 30	$1 \pm 0.085123$
66	SK $\nu_e$ FHC	0.0 - 0.5	$1 \pm 0.090918$
67		0.5 - 0.7	$1 \pm 0.087065$
68		0.7 - 0.8	$1 \pm 0.082527$
69		0.8 - 1.5	$1 \pm 0.076514$
70		1.5 - 2.5	$1 \pm 0.075773$
71		2.5 - 4.0	$1 \pm 0.082078$
72		4.0 - 30	$1 \pm 0.092882$
73	SK $\bar{\nu}_e$ FHC	0.0 - 2.5	$1 \pm 0.071921$
74		2.5 - 30	$1 \pm 0.128982$
75	SK $\nu_\mu$ RHC	0.0 - 0.7	$1 \pm 0.093954$
76		0.7 - 1.0	$1 \pm 0.076369$
77		1.0 - 1.5	$1 \pm 0.074900$
78		1.5 - 2.5	$1 \pm 0.078108$
79		2.5 - 30	$1 \pm 0.077505$
80	SK $\bar{\nu}_\mu$ RHC	0.0 - 0.4	$1 \pm 0.108593$
81		0.4 - 0.5	$1 \pm 0.101912$
82		0.5 - 0.6	$1 \pm 0.092787$
83		0.6 - 0.7	$1 \pm 0.082669$
84		0.7 - 1.0	$1 \pm 0.102090$
85		1.0 - 1.5	$1 \pm 0.087732$
86		1.5 - 2.5	$1 \pm 0.068117$
87		2.5 - 3.5	$1 \pm 0.069902$
88		3.5 - 5.0	$1 \pm 0.091711$

---

<b>Fit index</b>	<b>Beam mode</b>	<b>Bin edges [GeV]</b>	<b>Prefit</b>
89		5.0 - 7.0	$1 \pm 0.084736$
90		7.0 - 30	$1 \pm 0.115488$
91	SK $\nu_e$ RHC	0.0 - 2.5	$1 \pm 0.066204$
92		2.5 - 30	$1 \pm 0.082645$
93	SK $\bar{\nu}_e$ RHC	0.0 - 0.5	$1 \pm 0.095453$
94		0.5 - 0.7	$1 \pm 0.088889$
95		0.7 - 0.8	$1 \pm 0.085644$
96		0.8 - 1.5	$1 \pm 0.078536$
97		1.5 - 2.5	$1 \pm 0.075246$
98		2.5 - 4.0	$1 \pm 0.086384$
99		4.0 - 30	$1 \pm 0.152507$

---

723

### 724 4.2.2 Detector Inefficiencies And Bins Normalization Parameters

725 In the BANFF fit, fit bin normalization parameters are used to penalize variations in the fit bins. Varying fit  
 726 bins without constraint is nonphysical due to known detector inefficiencies and their systematic uncertainties.  
 727 This information is incorporated into the penalty term,  $\chi^2_{\text{Det}}$ . Since improperly modeled inefficiencies can  
 728 cause events to migrate from bin-to-bin, numerous fake “toy experiments” are performed to evaluate the  
 729 systematic uncertainties in detector inefficiencies. When all toy experiments are analyzed together, correlated  
 730 variations among fit bins become apparent. These correlations provide the constraints on freely changing  
 731 bin normalizations. We will see the result of running such toy experiment variations in the coming pages.  
 732 Hitherto in this thesis, detector inefficiency uncertainties will be referred to as detector systematics.

733 All the detector systematics are evaluated either as observable variations or weights. An observable  
 734 variation affects the physical observables of selected events like the calculated energy loss of a track in the  
 735 PØD. A weight is a multiplicative factor that alters the normalization of a single event in a bin. There are  
 736 detector systematics that affect the PØD-only, TPC-only, or both.

737 This section is organized as follows. The systematics treatment model for the detector systematics  
 738 developed to evaluate their effects on the analysis is described in Section 4.2.2.1. The specific systematic  
 739 uncertainties relevant to this analysis are described in Section 4.2.2.2. The detector systematics penalty

740 term used in the BANFF fit is described in Section 4.2.2.3. Finally, the procedure to determine the initial  
 741 bin normalization is presented in Section 4.2.2.4.

#### 742 4.2.2.1 Systematic Treatment Models

743 The BANFF fit analysis uses toy experiment variations to evaluate the effect of detector systematics on the  
 744 analysis samples. Each toy experiment loops over all the predicted events and varies the known detector  
 745 systematic effects. Each systematic effect either varies the event’s efficiency weight or event observables.  
 746 Both the observable variation and efficiency-like weight treatments rely on data-driven studies by comparing  
 747 data and MC predictions in a control sample<sup>2</sup> (CS). By using a large ensemble of toy experiments, the effect  
 748 of the detector systematics on the samples is evaluated.

749 Efficiency-like corrections alter the number of predicted events in a fit bin. The model used to evaluate  
 750 efficiency-like systematics is given by

$$\epsilon_{\text{Data}}(o) = \left( \frac{\epsilon_{\text{Data}}(o)}{\epsilon_{\text{MC}}(o)} \right)_{\text{CS}} \epsilon_{\text{MC}}(o), \quad (4.4)$$

751 where  $\epsilon_{\text{MC}}/\epsilon_{\text{Data}}$  denotes the mean selection efficiency of the MC/data as a function of some observable  
 752 kinematic  $o$ , and  $( )_{\text{CS}}$  refers to the selection efficiency measured in a CS. We need to update this model to  
 753 account for statistical uncertainties in the CS. The updated model, with  $o$  dependence assumed, is now

$$\epsilon'_{\text{Data}} = \left( \frac{\epsilon_{\text{Data}} + x_{\text{Data}} \cdot \sigma_{\epsilon_{\text{Data}}}}{\epsilon_{\text{MC}} + x_{\text{MC}} \cdot \sigma_{\epsilon_{\text{MC}}}} \right)_{\text{CS}} \epsilon_{\text{MC}} \quad (4.5)$$

754 where  $\sigma_{\epsilon_{\text{MC}}}/\sigma_{\epsilon_{\text{Data}}}$  is the standard deviation of the efficiency of the MC/Data and  $x_{\text{Data}}$  and  $x_{\text{MC}}$  are  
 755 uncorrelated, random normally distributed numbers from  $\mathcal{N}(\mu = 0, \sigma^2 = 1)$ . All the variations are applied  
 756 to the event, simultaneously affecting all observables, and the event selection is rerun. A weight is derived  
 757 depending if the event is selected,  $w_{\text{eff}}$ , or not selected,  $w_{\text{ineff}}$ . These weights are given below

$$w_{\text{eff}} = \frac{\epsilon'_{\text{Data}}}{\epsilon_{\text{MC}}} \quad (4.6)$$

$$w_{\text{ineff}} = \frac{1 - \epsilon'_{\text{Data}}}{1 - \epsilon_{\text{MC}}}.$$

758 Observable variation systematics are evaluated as shifts to physically measured quantities like particle  
 759 track momentum and track length. The systematic can be evaluated in two different ways:

- 760 1. If the reconstructed observable,  $o_{\text{reco}}$ , has a known true value,  $o_{\text{true}}$ , then the difference between those

---

<sup>2</sup>Each control sample is validated in T2K prior to introduction to the BANFF analysis.

761 two is used as scaling. The varied observable is given by

$$o' = o_{\text{true}} + (o_{\text{reco}} - o_{\text{true}}) (s + x\sigma_s), \quad (4.7)$$

762 where  $s$  is the mean scaling parameter used to match the true value,  $\sigma_s$  is the uncertainty on  $s$ , and  
763  $x$  is a random number from  $\mathcal{N}(\mu = 0, \sigma^2 = 1)$ . The mean scaling parameter and its uncertainty are  
764 determined from the standard deviations observed in the data and MC by

$$s = \frac{\delta^{\text{data}}}{\delta^{\text{MC}}} \quad \sigma_s = s \left| \frac{\sigma_{\delta^{\text{data}}}}{\delta^{\text{data}}} - \frac{\sigma_{\delta^{\text{MC}}}}{\delta^{\text{MC}}} \right|. \quad (4.8)$$

765 2. If the MC reconstructed observable is corrected to match the mean from some CS reconstructed  
766 observable. The varied observable in this case is given by

$$o' = o_{\text{Nom}} + \Delta o + x\sigma_{\Delta o}, \quad (4.9)$$

767 where  $o'$  is the varied observable value,  $o_{\text{Nom}}$  is the nominal MC value,  $\Delta o$  is the average correction  
768 to the observable,  $\sigma_{\Delta o}$  is the uncertainty on the correction, and  $x$  is a random, normal number from  
769  $\mathcal{N}(\mu = 0, \sigma^2 = 1)$ .

770 Additional uncertainties from the magnetic field are also special cases of the 2nd observable variation method  
771 specifically for the TPC momentum[17]. They are:

- 772 • The TPC laser calibration corrections are applied after the magnetic field (B-field) mapping corrections.  
773 The B-field corrections are applied at event reconstruction while the calibration corrections are treated  
774 as a systematic uncertainty. The varied momentum is given by

$$p' = p_{\text{Nom}} + x(p_{\text{Map}} - p_{\text{Nom}}), \quad (4.10)$$

775 where  $p_{\text{Nom}}$  is the nominal MC prediction using the B-field corrections and  $p_{\text{Map}}$  is the updated  
776 momentum using the additional laser calibration mapping.

- 777 • The momentum depends on some scale parameter  $s$ . The varied momentum due to the scale uncertainty  
778 is given by

$$p' = p_{\text{Nom}} (1 + x\sigma_s), \quad (4.11)$$

779 where  $\sigma_s$  is the uncertainty on the scale. In this parameterization,  $s$  is the scale of the ND280 solenoid

Table 4.2: List of detector systematics in the analysis. The TPC-only systematics are discussed in the following reference[2]. The PØD mass and track matching systematics were not available in the BANFF framework and treated as uncorrelated additions to the covariance matrix.

Systematic effect	Affected detectors	Treatment
PØD energy loss scale	PØD	observable variation
PØD energy loss resolution	PØD	observable variation
PØD mass	PØD	(see text)
PØD-TPC matching eff.	PØD, TPC	(see text)
Pion secondary interactions	PØD, TPC	efficiency
Proton secondary interactions	PØD, TPC	efficiency
Magnetic field distortion	TPC	observable variation
TPC charge misassignment	TPC	efficiency
TPC cluster efficiency	TPC	efficiency
TPC momentum resolution	TPC	observable variation
TPC momentum scale	TPC	observable variation
TPC particle identification	TPC	observable variation
TPC track quality efficiency	TPC	efficiency
TPC tracking efficiency	TPC	efficiency

780 current.

781 After all observables are varied and applied to the event, the event selection cuts are applied again. By doing  
 782 so after all variations are applied, the full impact of the systematic on the sample and analysis bins can be  
 783 evaluated.

784 **4.2.2.2 Detector Systematics**

785 Since this analysis uses the PØD and TPC detectors, systematics that affect both must be included in the  
 786 toy experiments. The complete set of detector systematics and their treatment in the analysis are listed in  
 787 Table 4.2 on page 57. The TPC-only systematics that have been used in previous BANFF fit analysis are  
 788 included in this analysis. Details on the TPC-only systematics are discussed in the following references[2, 17].  
 789 There are four PØD-only detector systematics that are considered for this BANFF fit analysis:

- 790 • The PØD detector energy loss scale,  
 791 • The PØD detector energy loss resolution,  
 792 • The PØD-TPC inter-detector matching efficiency, and  
 793 • The PØD detector fiducial mass.

794 The PØD energy loss scale and resolution affect the measured momentum in the PØD and are very  
 795 significant sources of uncertainty. In the  $\nu_\mu$  CC-0 $\pi$  cross section analysis[7], the same selection as the  $\nu_\mu$   
 796 in FHC Mode CC 1-Track selection, the scale and resolution contributed 1.3% and 6.7%, respectively, to

797 the cross section uncertainty. Those large uncertainties can be attributed to the design of the PØD. It is  
798 optimized for  $\pi^0$  detection as opposed to a dedicated tracking detector like the FGD. Slight variations in the  
799 track reconstruction can significantly alter the energy loss as measured in Eqn. (3.4).

800 The remaining systematics, the PØD mass and the PØD-TPC matching efficiency, were not available to  
801 analyze in toy experiments variations. They were not implemented in the BANFF framework and unavailable  
802 to implement due to time constraints on this author. Instead, they were treated as additional uncorrelated  
803 systematics on each bin normalization uncertainty with the normalization value remaining fixed.

804 The PØD mass uncertainty is a normalization systematic which affects the event rate. This is a chal-  
805 lenging systematic for analyses of recent T2K data due to increasingly faulty sensors to measure the water  
806 content. The procedure to fill the water bags required filling them in unison to prevent uneven bulging.  
807 However, faulty sensors would provide poor quality data, hence bags were under and overfilled. This effect  
808 alters the expected event rate as a function of position.

809 Another problem with the mass uncertainty is due to structure deformations in the PØD. To understand  
810 how the PØD has deformed, it is important to understand how the PØD is mounted in the ND280 detector.  
811 Each corner of the PØD is mounted to the ND280 basket leaving those corners spatially fixed. When the  
812 water bags are filled, the WT volume expands or “bulges” from the middle. The upstream end of the PØD,  
813 the Upstream ECal, resists deformations since it is physically against the ND280 support structure and  
814 magnet yoke. The downstream end of the PØD, or the Central ECal (CECal), is free to deform, however,  
815 since there is a few centimeters air gap between it and the TPC. The CECal, which has a design thickness  
816 of 304 mm[20], was observed to bulge about 7-8 mm from its center due to WT bulging as well[21].

817 This left more water volume, and importantly more mass, in the most downstream water bags compared  
818 to the upstream bags. This additional mass or bulging effect is evident in the vertex distribution as a function  
819 of the Z-position as shown in Figure 4.5 on page 59.

820 Prior PØD analyses have estimated the mass uncertainty using similar toy experiment techniques, but  
821 did not integrate them into the BANFF framework. In particular in the  $\nu_\mu$  in CC-0 $\pi$  analysis[7], the PØD  
822 mass had an 1.5% systematic effect on the cross section. Since the PØD mass uncertainty estimate was  
823 determined using the same toy experiment variation method, a conservative estimate of 2% on the mass  
824 uncertainty is included in this analysis.

825 The PØD and TPC (PØD-TPC) inter-detector track matching efficiency is estimated to have a small  
826 systematic effect on the analysis. It was analyzed to have over a 99.8% data and MC efficiency in the single  
827 track  $\nu_\mu$  CC-0 $\pi$  analysis and thus was neglected. However, since this analysis includes > 1 track samples,  
828 the matching efficiency for non-single track samples is unknown. The best constraint on multiple track  
829 inter-detector matching is from the private T2K technical note on the single bin  $\bar{\nu}_\mu/\nu_\mu$  cross section analysis

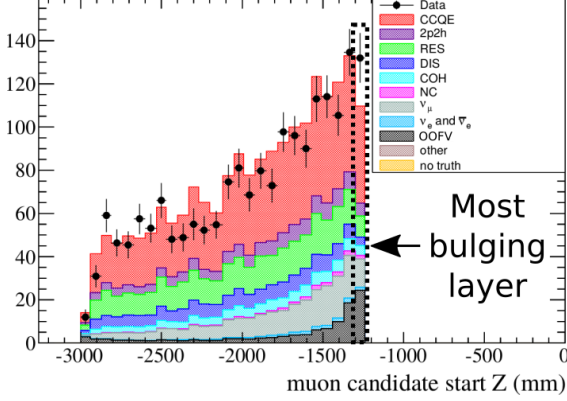


Figure 4.5: Vertex distribution showing evidence of bulging. In the  $\bar{\nu}_\mu/\nu_\mu$  cross section ratio analysis, a significant excess of events in the most downstream layer of the PØD (black, dashed line box) was observed. Initially thought to be OOFV events, the analyzers removed the most downstream and upstream layers in their analysis. This distribution was produced using the run 5, RHC period using selection precuts 1 through 4 and a having a positive track in the TPC. Each event is categorized by true interaction mode according to NEUT. This figure was altered for clarity from the following reference [13].

[13]. The analysis estimated the uncertainty at less than 0.14%, albeit using the “pre-Global” technique mentioned in Chapter 3. Because their track matching algorithm is different than Global’s algorithm, the uncertainty is not guaranteed to remain constant across the fit bins. A conservative estimate of 1% for the PØD-TPC matching efficiency was chosen in order to account for the inherent uncertainty in this systematic.

Now that we know the systematics that affect the analysis, we can now begin to understand how the detector systematic penalty term  $\chi^2_{\text{Det}}$  is modeled in the BANFF fit.

#### 4.2.2.3 Toy Experiments and the Detector Systematics Penalty

The bin normalization penalty parameters are restrictions on freely varying fit bins. To determine the correlations between bins, a large ensemble of toy experiments is generated. As described in Section 4.2.2.1, each toy experiment varies event observables, the momentum and angle of the main track, and number of events in a fit bin. The bin normalization parameter for the  $i$ th bin, or  $d_i$ , is defined as

$$d_i = \frac{\langle N_i \rangle_{\text{toys}}}{N_i}, \quad (4.12)$$

where  $N_i$  predicted number of events in fit bin  $i$  and  $\langle N_i \rangle_{\text{toys}}$  is the average number of events in fit bin  $i$  evaluated over all toy experiments (toys). The predicted event rate for bin  $i$  is given by

$$N_i = \sum_k^{N_{\text{MC}}} \delta_{i,k}^{\text{bin}} w_k, \quad (4.13)$$

843 where  $N_{\text{MC}}$  being the number of unweighted MC events,  $\delta_{i,k}^{\text{bin}}$  determines if the  $k$ th event goes into analysis  
 844 bin  $i$  as a function of  $(p, \cos \theta)$ , and  $w_k$  is the product of all of the weights applied to the  $k$ th event. The  
 845 weights used in Eqn. (4.13) are

$$w_k = w_k^{\text{POT}} \times w_k^{\text{Flux}} \times w_k^{\text{xsec}} \times w_k^{\text{Det}}, \quad (4.14)$$

846 (see Eqn. (2.8) for all possible weights). The number of events in fit bin  $i$ , averaged over all toy experiments  
 847 (toys), is given by

$$\begin{aligned} \langle N_i \rangle_{\text{toys}} &= \frac{1}{N_{\text{toys}}} \sum_{t=1}^{N_{\text{toys}}} (N_i)_t \\ &= \frac{1}{N_{\text{toys}}} \sum_{t=1}^{N_{\text{toys}}} \left( \sum_k^{N_{\text{MC}}} [\delta_{i,k}^{\text{bin}} w_k] \right)_t, \end{aligned} \quad (4.15)$$

848 where now each MC event has a toy variation out of  $N_{\text{toys}}$  total toys. We average the results of the toys to  
 849 smooth out variations among all toy experiments. In this analysis, and in previous BANFF analyses as well,  
 850  $N_{\text{toys}} = 2000$  toys were generated as to have a small sample size uncertainty.

851 As stated before, all the penalty parameters are dimensionless and the detector systematics covariance  
 852 matrix must be constructed carefully. The bin-to-bin event rate covariance,  $V_{i,j}^{\text{Cov}}$ , between bins  $i$  and  $j$  is

$$V_{i,j}^{\text{Cov}} = \frac{1}{N_{\text{toys}}} \sum_{t=1}^{N_{\text{toys}}} ((N_i)_t - \langle N_i \rangle_{\text{toys}}) ((N_j)_t - \langle N_j \rangle_{\text{toys}}), \quad (4.16)$$

853 where  $(N_i)_t$  is defined in Eqn. (4.15). We also need to account for statistical uncertainties in the fit bins,  
 854 and so let us define  $V_{i,j}^{\text{Stat}}$  as

$$V_{i,j}^{\text{Stat}} = \delta_{i,j} \sum_k^{N_{\text{MC}}} \delta_{i,k}^{\text{bin}} w_k^2, \quad (4.17)$$

855 where  $\delta_{i,j}$  is the Kronecker delta function. In order to incorporate  $V_{i,j}^{\text{Cov}}$  and  $V_{i,j}^{\text{Stat}}$  uncertainties, the total  
 856 detector covariance matrix,  $V_{i,j}^{\text{Det}}$ , in the BANFF fit is defined as

$$V_{i,j}^{\text{Det}} = \frac{V_{i,j}^{\text{Cov}} + V_{i,j}^{\text{Stat}}}{N_i N_j}, \quad (4.18)$$

857 which is indeed dimensionless as required by Eqn. (4.12) since we divided out the predicted event rate in  
 858 bins  $i$  and  $j$ .

859 As stated before, the PØD mass and track matching efficiency systematics are treated as uncorrelated  
 860 systematics. In order to propagate their systematic uncertainties into the analysis, the detector covariance

861 matrix given in Eqn. (4.18) needs to be updated. The updated covariance matrix is given by

$$V_{i,j}^{\text{Det}} \leftarrow \left( \tilde{V}_{i,j}^{\text{Det}} + \tilde{\sigma}_{\text{Mass}}^2 + \tilde{\sigma}_{\text{Match}}^2 \right) d_i d_j, \quad (4.19)$$

862 where  $\tilde{V}_{i,j}^{\text{Det}}$  is the fractional covariance

$$\tilde{V}_{i,j}^{\text{Det}} = \frac{V_{i,j}^{\text{Det}}}{d_i d_j}, \quad (4.20)$$

863  $d_i/d_j$  are the bin normalization parameters, and  $\tilde{\sigma}_{\text{Mass}}^2 = 2\%$  and  $\tilde{\sigma}_{\text{Match}}^2 = 1\%$  are the PØD mass and PØD-  
864 TPC matching efficiency systematic uncertainties, respectively, estimated in Section 4.2.2.2. Together, the  
865 two additional sources of uncertainty increase each term in the covariance matrix by  $0.0005 d_i d_j$ . Specifically,  
866 the uncertainty in all the bin normalization parameters (square-root of the diagonal terms in the covariance  
867 matrix) increases by about 2.23%. The updated detector covariance matrix now accounts for the PØD mass  
868 and TPC matching inefficiency systematics.

869 The penalty term,  $\chi_{\text{Det}}^2$ , in the fit is given by

$$\chi_{\text{Det}}^2 = \left( \vec{d} - \vec{d}_0 \right)^T \left( V^{\text{Det}} \right)^{-1} \left( \vec{d} - \vec{d}_0 \right)^T, \quad (4.21)$$

870 where  $\vec{d}_0$  is the initial values of the parameters, and  $V^{\text{Det}}$  is given by Eqn. (4.19).

#### 871 4.2.2.4 Bin Normalization Parameters

872 While there could be one observable normalization for each analysis bin, a single normalization can be  
873 assigned to multiple analysis bins. The purpose is to reduce the number of fit parameters since the time to fit  
874 increases non-linearly with the number of fit parameters and events. Previously, the observable normalization  
875 edges were determined by combining fit bins with “similar” covariance. This method proved problematic since  
876 the fit bins with relatively higher statistics were shared with the same observable normalization parameter.  
877 This left the remaining low statistics regions of  $(p, \cos \theta)$  phase space more susceptible to systematic variations  
878 in the toy experiments.

879 A new procedure was developed to improve the shortcomings of old procedure which required careful  
880 consideration of the statistical uncertainties and variations between observable normalization prefit values.  
881 This procedure can be imagined as reducing the number of contours in a topographic map while considering  
882 external constraints from other sensing data. The first step in the procedure is to initialize all of the  
883 observable normalization bin edges to be the same as the fit bin edges. All steps after this are performed  
884 iteratively.

885 Starting with observable normalization bin with the highest statistics, a decision is made to merge it

886 with all immediate adjacent bins. If the individual fractional errors differ significantly before the merge,  
 887 do not merge them. In this analysis, a factor of 10 in fractional uncertainty was determined to sufficiently  
 888 describe bin similarity by using values larger and smaller than 10 and observing no significant differences in  
 889 the end result. Additionally if the two unmerged bin normalizations differ by more than 10%, perform the  
 890 bin merging. This step serves to smooth out the observable normalization prefit space. The procedure is  
 891 also written in pseudocode in Algorithm 1.

```

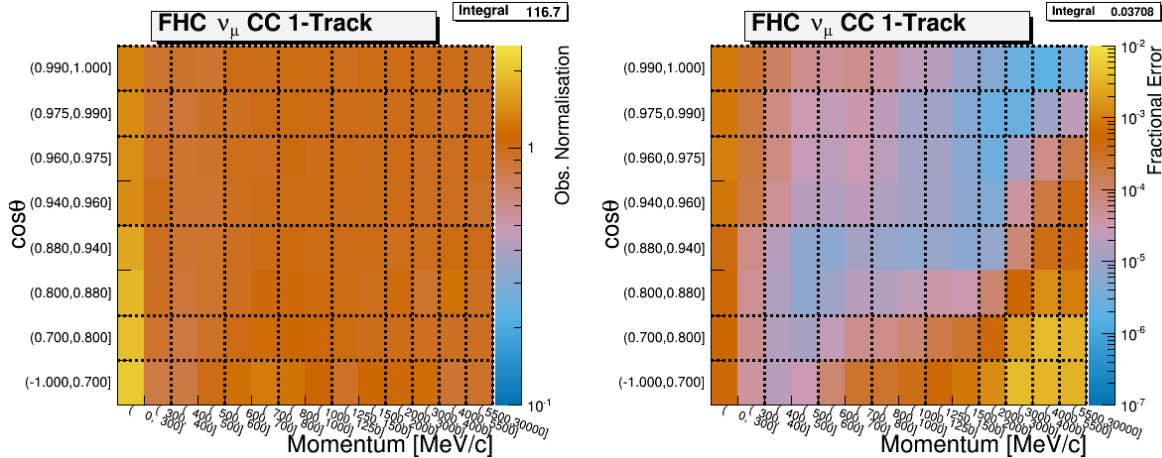
repeat
  redo  $\leftarrow$  False;
  for each normalization bin d do //sorted from min to max  $\delta\%$ 
    for each neighboring analysis bin f do
      d'  $\leftarrow$  normalization bin assigned to f;
      if d' is same as d then
        | Continue to next analysis bin;
      end
      if  $\delta\%(d) \geq 10 \times \delta\%(d')$  then
        | d is assigned as normalization bin for f;
        redo  $\leftarrow$  True;
        | Continue to next analysis bin;
      end
      max_norm  $\leftarrow$  max(norm(d), norm(d'));
      min_norm  $\leftarrow$  min(norm(d), norm(d'));
      if max_norm  $\geq 1.1 \times$  min_norm then
        | d is assigned as normalization bin for f;
        redo  $\leftarrow$  True;
      end
    end
  end
  Recalculate bin normalizations;
  until redo is False;

```

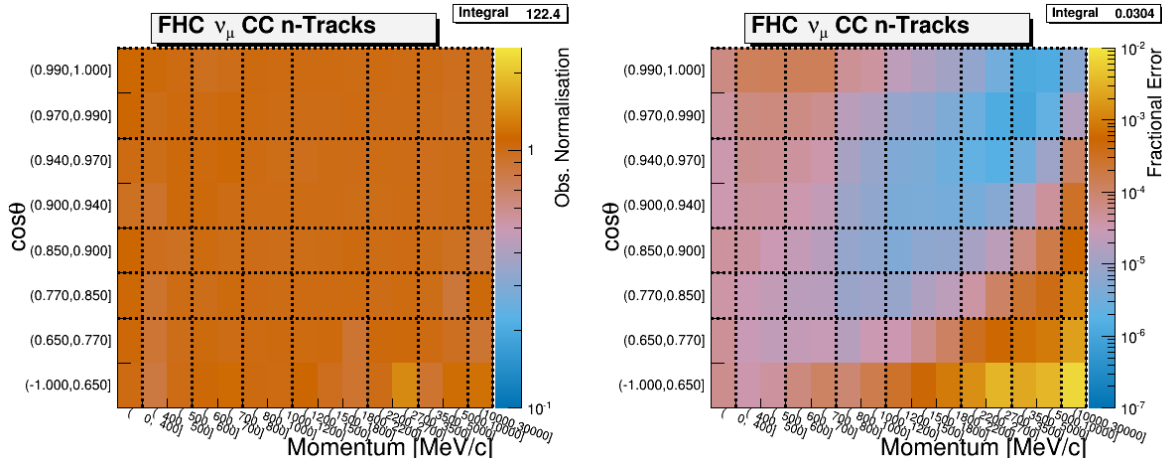
**Algorithm 1:** Algorithm to merge normalization bins. The “ $\delta\%$ ” operator returns the fractional statistical uncertainty for the bin. Since multiple fit bins can be assigned to a single normalization bin, the statistics of all fits bins are included. The “norm” operator returns the normalization value for a normalization bin determined by Eqn. (4.13). Finally, the min/max functions return the minimum/maximum element in a tuple, respectively.

892 The results of the procedure are shown visually in Figure 4.6 on page 63, Figure 4.7 on page 64, and  
 893 Figure 4.8 on page 65. While the problem of the highest statistics bins being assigned to a single observable  
 894 normalization parameter is still present, fluctuations between adjacent observable normalization parameters  
 895 is iteratively minimized.

896 A considerable drawback to using toy experiments to estimate the bin normalization values and covariance  
 897 matrix is that not all detector systematics affect the fit observables ( $p, \cos \theta$ ) in the same way. There are  
 898 non-symmetric systematics and they are especially non-Gaussian in their effects. Therefore, the covariance  
 899 matrix from Eqn. (4.18) is not an exact representation of the detector systematics. To demonstrate this,



(a) The  $\nu_\mu$  in FHC Mode CC 1-Track sample

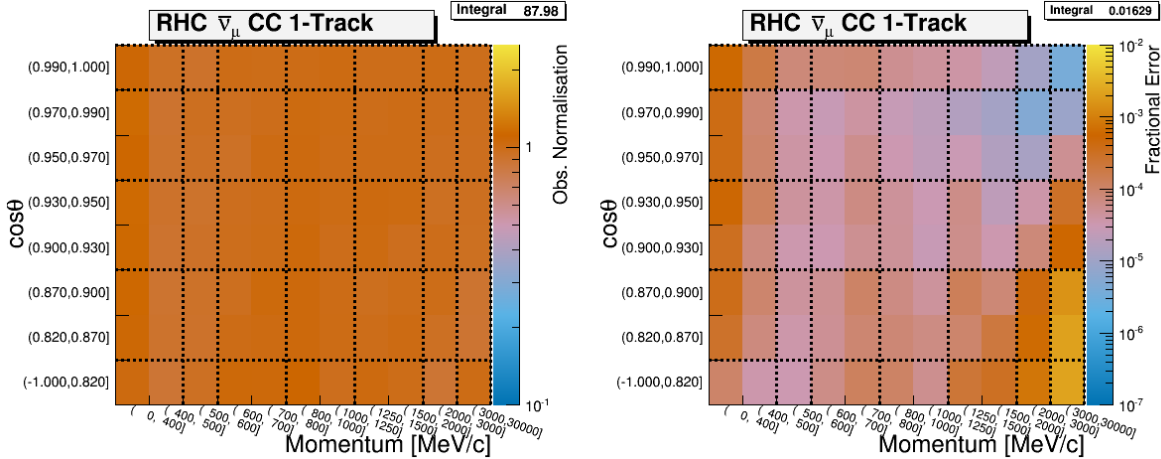


(b) The  $\nu_\mu$  in FHC Mode CC N-Tracks sample

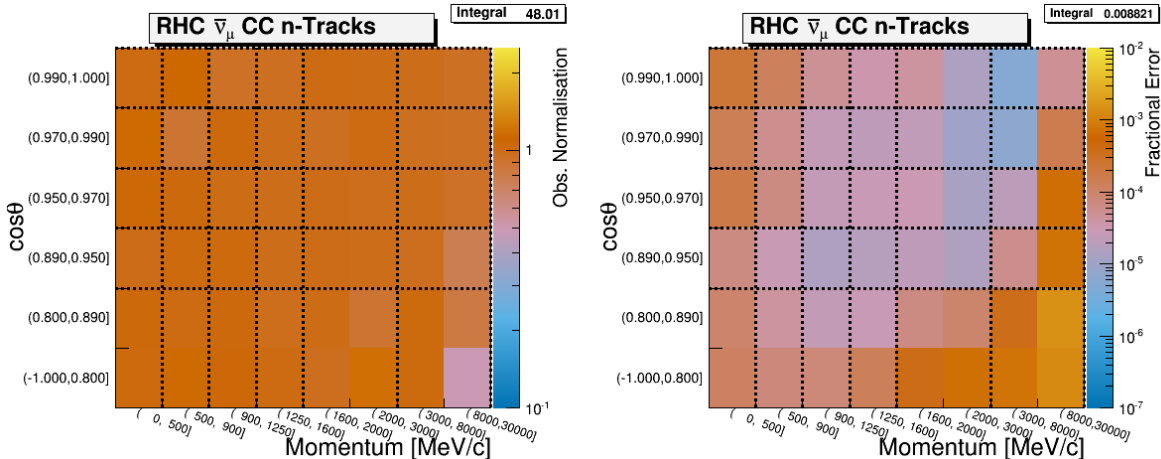
Figure 4.6: Bin normalization edges for the  $\nu_\mu$  in FHC Mode samples. The left and right plots show the bin normalization and the bin statistical fractional error, respectively, if each fit bin had a single bin normalization. The dashed lines indicate the edges of the bin normalization parameters finalized for this analysis. Water-in and water-out modes are qualitatively the same.

900 results of varied number of events are shown in Figure 4.9 on page 66. However, the bin normalization  
 901 standard deviations are very wide and able to effectively cover the range of possible bin normalizations,  
 902 which minimizes the non-Gaussian effects of the systematic. All the varied toy experiment results are  
 903 provided in Appendix C.

904 The detector systematic that had the largest effect on the observable normalization prediction was the  
 905 PØD energy loss resolution (ELossRes) which alters the amount of particle energy deposited in the PØD.  
 906 This systematic was developed for the  $\nu_\mu$  CC- $0\pi$  cross section analysis, it was identified as the largest  
 907 detector systematic uncertainty in the cross section measurement[22]. When the deposited energy in the  
 908 PØD is varied, it also changes the distance the truth matched particle travels in the PØD. Hence, this

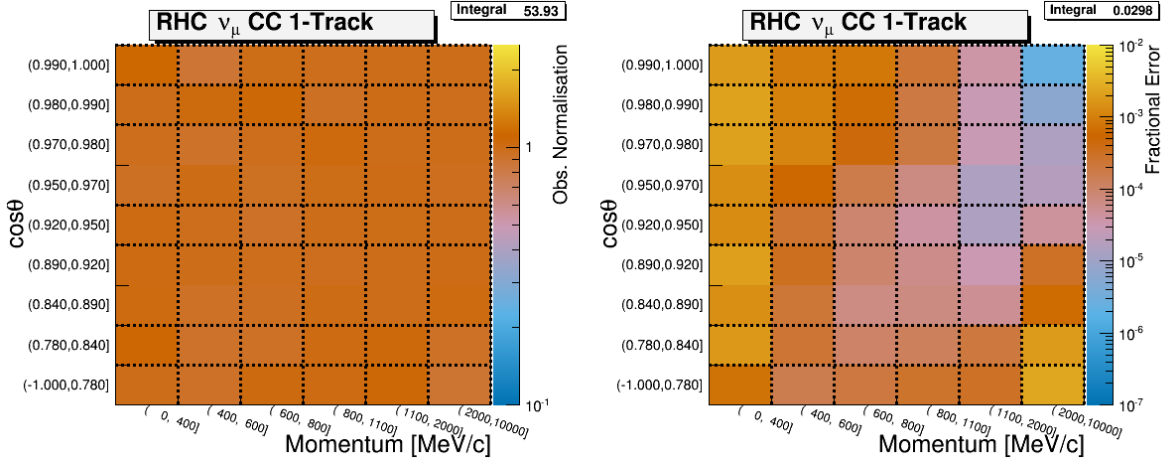


(a) The  $\bar{\nu}_\mu$  in RHC Mode CC 1-Track sample

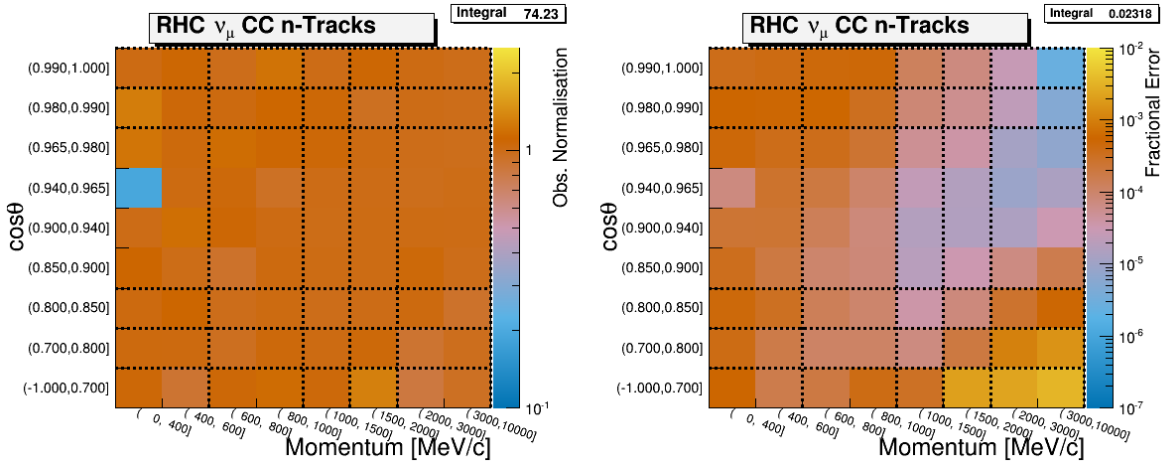


(b) The  $\bar{\nu}_\mu$  in RHC Mode CC N-Tracks sample

Figure 4.7: Bin normalization edges for the  $\bar{\nu}_\mu$  in RHC Mode samples. The left and right plots show the bin normalization and the bin statistical fractional error, respectively, if each fit bin had a single bin normalization. The dashed lines indicate the edges of the bin normalization parameters finalized for this analysis. Water-in and water-out modes are qualitatively the same.



(a) The  $\nu_\mu$  in RHC CC 1-Track sample



(b) The  $\nu_\mu$  in RHC CC N-Tracks sample

Figure 4.8: Bin normalization edges for the  $\nu_\mu$  Background in RHC Mode samples. The left and right plots show the bin normalization and the bin statistical fractional error, respectively, if each fit bin had a single bin normalization. The dashed lines indicate the edges of the bin normalization parameters finalized for this analysis. Water-in and water-out modes are qualitatively the same.

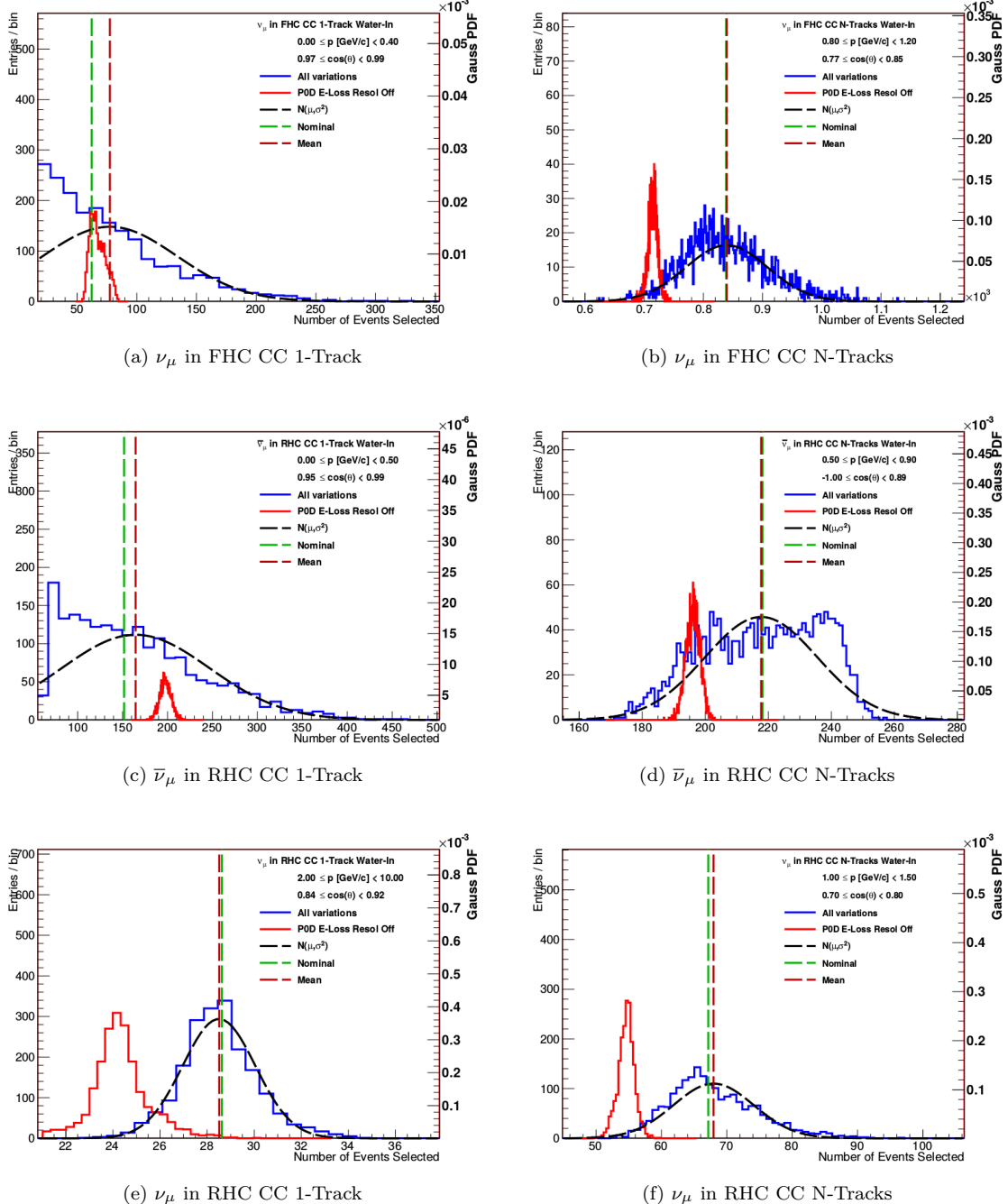


Figure 4.9: Event variations in representative observable normalization bins. Shown in each sub-figure the varied event rate from all toy experiments in a particular observable normalization bin. The blue curve has all the systematics enabled while the red curve has the ELossRes systematic disabled. Vertical dashed lines show the unvaried, weighted MC prediction and varied mean of all toy experiments. The ratio of the horizontal positions of each vertical line is the prefit normalization value for that bin. A Gaussian with variance extracted from the covariance matrix is shown to illustrate the bin's estimate on the normalization uncertainty.

909 systematic changes the likelihood of a particle being reconstructed as a track. The observed effect is that  
910 for bins with relatively low muon momentum, the number of predicted events can vary in a non-Gaussian  
911 manner as shown in Figure 4.9 on page 66.

912 An unexpected phenomenon was observed when comparing the toy experiments with and without the  
913 ELossRes variation applied. With the ELossRes variation disabled in the toy experiments, a relatively large  
914 shift in the bin prediction was observed compared to the nominal prediction. This shift was expected, but  
915 what was not expected was the direction of the shift as shown in Figure 4.9 on page 66. In most cases, the  
916 shift is below the nominal MC value. However, in many of the bins, that the shape location of the prediction  
917 is above the expectation. This behavior was unexpected prior to running the toy experiment variations.

918 A relationship between the prediction shape location and selection purity as a function of  $(p, \cos \theta)$  was  
919 discovered. In high purity  $(p, \cos \theta)$ -regions of the 1-Track samples, the shape location of the prediction in  
920 the disabled ELossRes toy experiments was below the nominal MC prediction. When the 1-Track sample  
921 purity was lower, however, the shape location was above it. This effect is likely due to events migrating from  
922 the 1-Track samples into the N-Tracks samples due to multiple particles in the event.

923 The finalized observable normalization bins are listed below. There are in total  $N_d = 461$  bin normaliza-  
924 tion parameters. The covariance matrix used in the BANFF fit is shown in Figure 4.10 on page 69. Their  
925 respective fit indices, prefit values, and prefit standard deviations are tabulated in Appendix A.

926 • The  $\nu_\mu$  in FHC Mode CC 1-Track samples bin normalization edges:

927 –  $p$  [GeV/c]: 0, 0.4, 0.6, 0.8, 1.25, 2, 3, 4, 5.5, 30

928 –  $\cos \theta$ : -1, 0.7, 0.8, 0.94, 0.975, 0.99, 1

929 • The  $\nu_\mu$  in FHC Mode CC N-Tracks samples bin normalization edges:

930 –  $p$  [GeV/c]: 0, 0.4, 0.6, 0.8, 1.2, 2.2, 3.5, 10, 30

931 –  $\cos \theta$  : -1, 0.77, 0.85, 0.9, 0.97, 1

932 • The  $\bar{\nu}_\mu$  in RHC Mode CC 1-Track samples bin normalization edges:

933 –  $p$  [GeV/c]: 0, 0.5, 0.6, 0.8, 1.25, 2, 3, 30

934 –  $\cos \theta$  : -1, 0.82, 0.9, 0.95, 0.99, 1

935 • The  $\bar{\nu}_\mu$  in RHC Mode CC N-Tracks samples bin normalization edges:

936 –  $p$  [GeV/c]: 0, 0.5, 0.9, 1.25, 1.6, 3, 30

937 –  $\cos \theta$  : -1, 0.89, 0.95, 0.97, 0.99, 1

- 938     • The  $\nu_\mu$  in RHC Mode CC 1-Track samples bin normalization edges:

939       –  $p$  [GeV/c]: 0, 0.4, 0.6, 0.8, 1.1, 2, 10

940       –  $\cos \theta$  : -1, 0.78, 0.84, 0.92, 0.95, 0.98, 0.99, 1

- 941     • The  $\nu_\mu$  in RHC Mode CC N-Tracks samples bin normalization edges:

942       –  $p$  [GeV/c]: 0, 0.6, 1, 1.5, 2, 10

943       –  $\cos \theta$  : -1, 0.7, 0.8, 0.85, 0.98, 0.99, 1

944     To better understand how effective the choice of bin normalizations parameters are at characterizing  
 945     the data variance, principal component analysis was performed using all the available toy experiments.  
 946     Principal component analysis is the process of a eigenvalue decomposition of a square matrix,  $M$ . The  
 947     principal components of  $M$ , which describe the data variance, are the eigenvectors. The relative importance  
 948     of each eigenvector is set by the magnitude of the associated eigenvalue.

949     Using this prescription, we define the sample variance,  $S$ , as

$$S = \frac{1}{N_{\text{toys}}} X^T X,$$

950     where  $X$  is a  $N_{\text{toys}} \times N_d$  matrix of the predicted number of events (not the normalization!) in each normal-  
 951     ization bin. The eigenvalue decomposition of  $S$  is given by

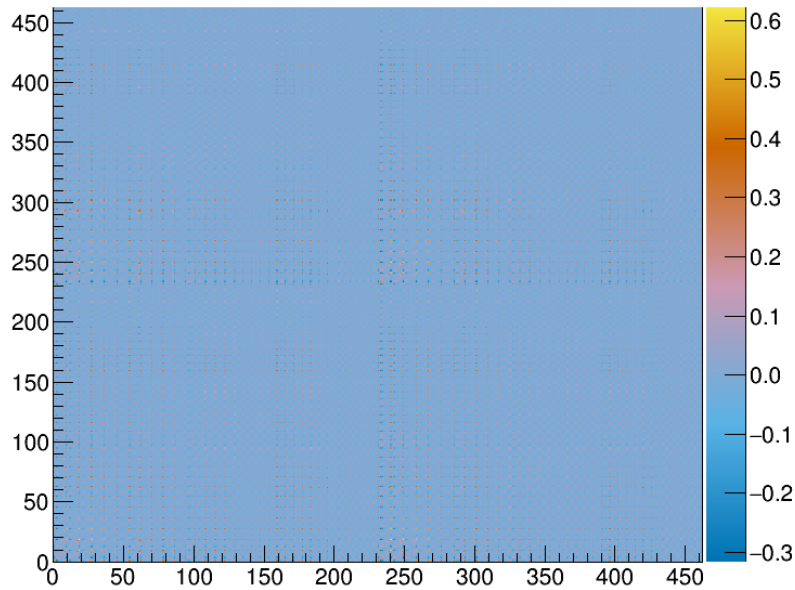
$$S = U^T \Lambda U,$$

952     where  $U$  is the eigenvector matrix of  $S$  and  $\Lambda$  is a diagonal matrix of the  $S$  matrix eigenvalues. What is  
 953     useful using principal component analysis is that the eigenvalues and eigenvectors are sorted from largest  
 954     to smallest magnitude. The sample variance eigenvalues are shown in Table 4.3 on page 70. The first, and  
 955     hence largest, eigenvalue is two orders of magnitude larger than the next largest eigenvalue, which means  
 956     that the majority of the bin-to-bin variance can be explained by the first eigenvector. The first eigenvector's  
 957     coefficients are shown in Figure 4.11 on page 70. We see that all the components are negative and clustered.  
 958     This result is interpreted to mean we can expect the bins normalizations postfit values to shift all together  
 959     uniformly.

960     Additionally, we can estimate the effective degrees of freedom for the bin normalization parameters. The  
 961     effective degrees of freedom is given by

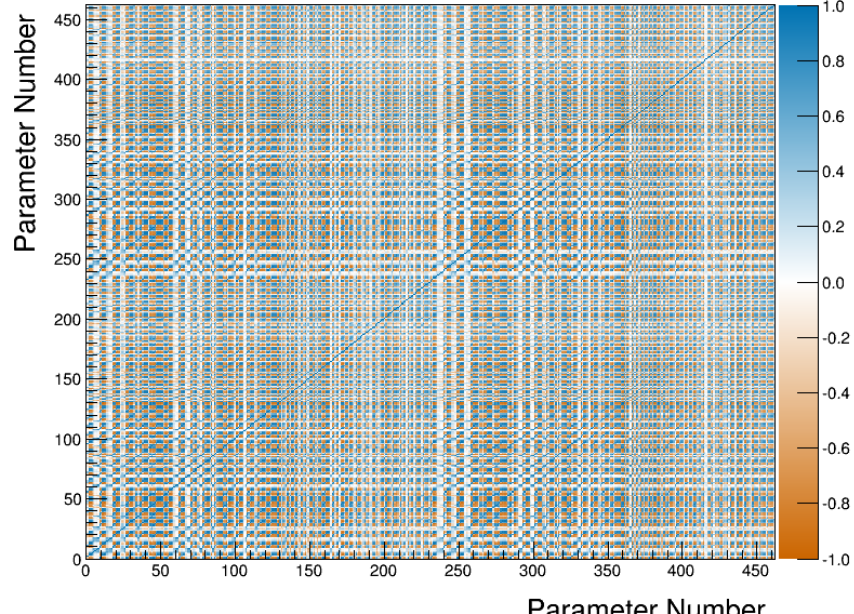
$$\text{df}(r) = \sum_{i=0}^{N_d} \frac{\lambda_i}{\lambda_i + r}, \quad (4.22)$$

**Updated Covariance**



(a) Covariance matrix

**Prefit Detector Correlation Matrix**



(b) Correlation matrix

Figure 4.10: Detector penalty covariance matrix. Shown in figure (a) is covariance matrix and (b) is the correlation matrix. Note that the parameter indices, which represent the bin normalization indices, are offset from their fit indices value by 99.

Table 4.3: Eigenvalues of the sample covariance. The values are sorted from largest to smallest in magnitude. Note that the parameter indices, which represent the bin normalization indices, are offset from their fit indices value by 99.

Index	0	1	2	3	...	458	459	460	461
Eigenvalue	2029	16.45	12.87	11.10	...	0.05325	0.05129	0.04955	0.03992

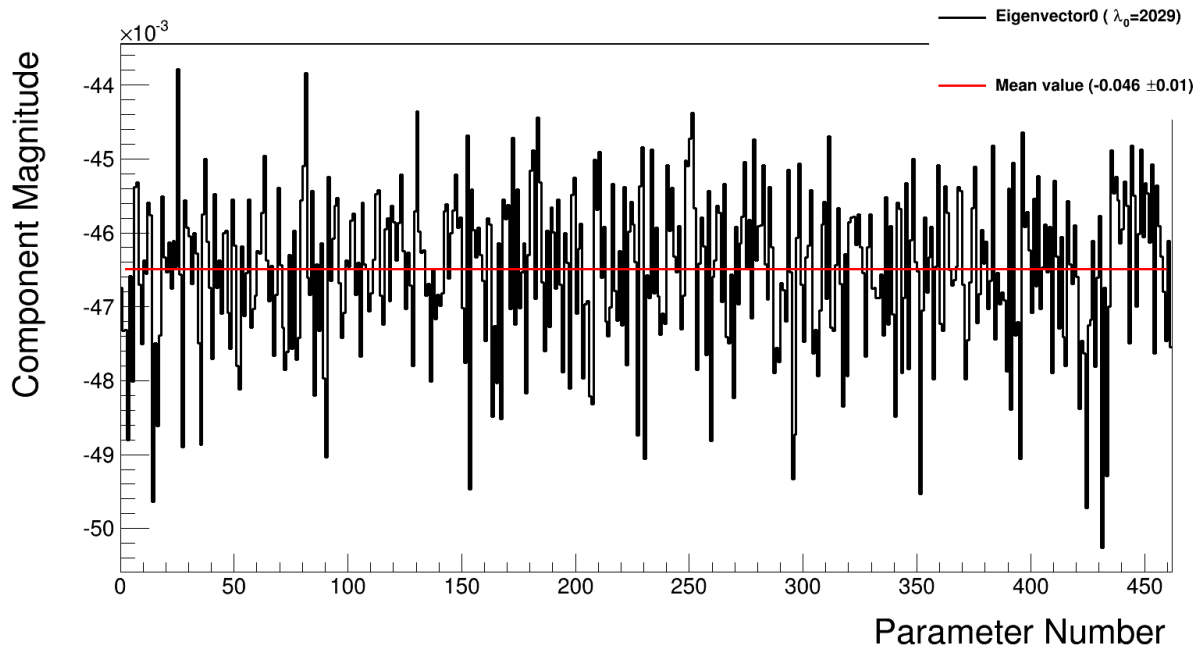


Figure 4.11: Principal component for the sample variance. This is the eigenvector associated with the largest eigenvalue of magnitude. Each parameter coefficient refers to the slope of the axis that describes most of the variance in the sample. The coefficients are all negative and are of similar magnitude. Together, they suggest all the normalization parameters respond linearly and uniformly. Note that the parameter indices, which represent the bin normalization indices, are offset from their fit indices value by 99.

where  $\lambda_i$  are the eigenvalues of  $\Lambda$  and  $r$  is a tunable parameter[16]. The idea behind Eqn. (4.22) is that although all  $N_d$  coefficients will be non-zero, they are restricted to vary by the magnitude of  $r$ . In particular,  $r$  represents the regularization strength for the detector systematics penalty, which is set to one ( $r = 1$ ) in the BANFF fit. If there was no (regularization) penalty, or  $r = 0$ , then the number of degrees of freedom is  $df(0)=N_d$ . It is found that there are about 137 effective degrees of freedom for the bin normalization parameters, or 29% of  $N_d$ . This suggests that a much smaller number bin normalization parameters can effectively describe the sample variance. This is particularly important to consider for a future BANFF fit analysis since this can provide a computational performance while maintaining predictability power in the ND constraint measurement. No further reduction in the number of bin normalization parameters were pursued due to time constraints.

### 4.2.3 Cross Section Model

There are a number of neutrino-nucleus interaction model parameters implemented in the BANFF fit to account for the uncertainties in cross section measurements. They are frequently updated to account for new models and constraints from external data. The cross section models used in this analysis use the T2K 2017 parameterization, which is a canonical set of parameters shared among all analyses in T2K. A gross description of the cross section model is provided here with a full description in the following reference[?].

There are three types of cross section parameters: shape, normalization, and functional. A cross section shape parameter,  $x^{\text{Shape}}$ , is defined as a shift in the location of a certain feature in the cross section. The shape parameters are stored in one dimensional splines

$$w(x^{\text{Shape}}) = \frac{d^n\sigma(x^{\text{Shape}})}{dz^n} / \frac{d^n\sigma(x_0^{\text{Shape}})}{dz^n},$$

where  $d^n\sigma/dz^n$  is a  $n$  dimensional cross section of  $z$  dependent parameters, and  $x_0^{\text{Shape}}$  is the nominal value of the shape parameter. As a design choice, the shape location parameters all start with a prefit value of zero (0). A cross section normalization parameter,  $x_i^{\text{Norm}}$ , is defined as

$$x^{\text{Norm}} = \frac{p'}{p}, \quad (4.23)$$

where  $p$  and  $p'$  are NEUT nominal and ND constrained parameters, respectively. And finally functional parameters are scalars to model a cross section function of a true kinematic. For example, if a cross section is given by  $\sigma(x) = mx + b$ ,  $m$  and  $b$  are the functional parameters in the model. Combining these parameters

987 into a single vector  $\vec{x}$ , the cross section penalty term,  $\chi_{\text{Det}}^2$ , is given by

$$\chi_{\text{Det}}^2 = (\vec{x} - \vec{x}_0)^T (V^{\text{xsec}})^{-1} (\vec{x} - \vec{x}_0),$$

988 where  $\vec{x}_0$  is the initial values of the cross section parameters, and  $V^{\text{xsec}}$  is the cross section model covariance  
989 matrix.

990 The next sections deal with the model parameterizations and systematic uncertainties in the NEUT  
991 version 5.3.3[17] interaction library which is used in T2K MC and oscillation analysis.

#### 992 4.2.3.1 The CC-0 $\pi$ Model

993 The cross section models with the largest impact on T2K’s oscillation sensitivity are CCQE and CCQE-like  
994 interactions, collectively called CC-0 $\pi$ . At energies near the  $\nu_e$  appearance maximum,  $E_\nu = 0.6$  GeV, the  
995 CCQE interaction is the largest contributor to the neutrino cross section as shown in Figure ?? on page  
996 ???. The nominal CCQE model in NEUT is a Spectral Function (SF) from Benhar *et al*[23]. An alternative  
997 CCQE model incorporates the Llewellyn-Smith dipole axial form factor<sup>3</sup>[24, 25] and BBBA05 vector form  
998 factors coupled to a Smith-Moniz Relativistic Fermi Gas[26, 27, 28] (RFG). A CCQE-like excitation mode  
999 involves correlated nucleon pair scattering called “2 particle, 2 hole”[15] (2p2h). An additional nuclear model  
1000 called the “Random Phase Approximation” (RPA)[29, 30] is used to modify single nucleon scattering  
1001 by accounting for nucleon correlations inside the nucleus. The default CC-0 $\pi$  model for T2K analyses  
1002 is the combination of the Llewellyn-Smith+RFG model, 2p2h excitation, and RPA nuclear model. This  
1003 combination was selected due to poor data matching with the SF model[17].

1004 The CC-0 $\pi$  model has three CCQE parameters: the dipole axial form factor mass  $M_A^{\text{QE}}$  from the  
1005 Llewellyn-Smith model, and two Fermi momentum parameters  $p_F$ , one for  $^{12}\text{C}$  and one for  $^{16}\text{O}$  that de-  
1006 scribe the momentum of nucleons on the surface of a RFG. In the past, using these parameters has been  
1007 shown to work as effective parameters in T2K when unconstrained. In this analysis, these three parameter  
1008 are unconstrained. In other words, a flat prior is used for  $M_A^{\text{QE}}$ ,  $p_F^C$ , and  $p_F^O$ .

1009 For the 2p2h excitation, there are a total of five parameters to describe the model. Three are normalization  
1010 terms: the  $\nu$  interaction on  $^{12}\text{C}$ , the  $\bar{\nu}$  interaction on  $^{12}\text{C}$ , and the scaling for  $^{12}\text{C} \rightarrow ^{16}\text{O}$ . The remaining  
1011 two systematic parameters in the 2p2h excitation are shape parameters, one for  $^{12}\text{C}$  and one for  $^{16}\text{O}$ . They  
1012 are used constrain the interplay of the contributing modes in 2p2h. One contributing mode is the Meson  
1013 Exchange Current (MEC) which involves a virtual meson exchange between the nucleons. The other mode is  
1014 nucleon-nucleon (NN) correlations which involves virtual particle exchange. A shape value of -1 determines

---

<sup>3</sup>A form factor is a measure of scattering amplitude in the form of the Fourier transform of some charge distribution.

1015 2p2h is completely due to MEC, 0 is the nominal MC 2p2h model, and +1 determines 2p2h is completely due  
1016 to NN. Any differences in the event rate in the region between  $\pm 1$  is absorbed by a interference term. However,  
1017 since no existing T2K nor external neutrino data can constrain the neutrino-induced 2p2h interaction, a flat  
1018 prior is set for all 2p2h parameters.

1019 The other nuclear interaction in the CC-0 $\pi$  model uses the Nieves RPA model[30] to describe nucleon  
1020 correlations. The RPA model primarily alters the single nucleon cross section and has dependence on both  
1021  $E_\nu$  and  $Q^2$ . A functional weighting scheme called “BeRPA” having only  $Q^2$  dependence was found to work  
1022 well to mimic the inherent uncertainties in the Nieves RPA model. The BeRPA functional is given by

$$w(Q^2) = \begin{cases} A\beta_0^3(x) + B\beta_1^3(x) + p_1\beta_2^3(x) + D\beta_3^3(x) & Q^2 \leq U \\ 1 + p_2 \exp(-E [Q^2 - U]), & Q^2 > U \end{cases} \quad (4.24)$$

1023 where  $x = Q^2/U$ ,  $\beta_i^n(x)$  are the Bernstein polynomials[31]

$$\beta_i^n(x) = \binom{n}{i} x^i (1-x)^{n-i} \quad x \in [0, 1], \quad (4.25)$$

1024  $p_1$  and  $p_2$  absorb the continuity conditions,

$$p_1 = D + \frac{UE(D-1)}{3}, \quad p_2 = D-1, \quad (4.26)$$

1025 and  $A$ ,  $B$ ,  $D$ ,  $E$ , and  $U$  are the functional parameters. The parameter  $U$  is fixed to prevent unwieldy  
1026 correlations from appearing.

#### 1027 4.2.3.2 The CC-1 $\pi$ Model

1028 Another important exclusive channel in NEUT is resonance states that produce a single pion or CC-1 $\pi$ . The  
1029 CC-1 $\pi$  model incorporates the Rein-Seghal model of neutrino-induced  $\Delta$  resonance decay[32, 33, 34, 35] with  
1030 lepton mass corrections[36, 37]. There are just three tunable parameters in the model. They are resonant  
1031 axial mass  $M_A^{\text{Res}}$ , the axial form factor normalization  $C_A^5$ , and the isospin=1/2 ( $I_{1/2}$ ) background normaliza-  
1032 tion. These three parameters are known to effectively describe neutrino-induced single pion production data  
1033 from Brookhaven National Laboratory[38] and Argonne National Laboratory[39]. It is important to know  
1034 that  $M_A^{\text{Res}}$  and  $C_A^5$  are strongly anticorrelated due to the parameterization of the form factor

$$f(Q^2) = C_A^5 \left( 1 + \frac{Q^2}{(M_A^{\text{Res}} c^2)^2} \right)^{-2}. \quad (4.27)$$

1035 **4.2.3.3 Coherent Pion Production**

1036 Coherent scattering refers to scattering where the wavelength of the incoming particle is larger than the  
1037 target. In the case of coherent neutrino-nucleus scattering, the neutrino's de Broglie wavelength is larger than  
1038 the size of the nucleus. In the scattering, no quantum numbers are exchanged, but the nucleus experiences a  
1039 momentum boost. In coherent pion production, the in-flight virtual boson is converted into a pion with that  
1040 pion exchanging a Pomeron[40] with the nucleus. The coherent scattering model is described by Rein-Sehgal  
1041 [41]. Lookup tables are used to scale the cross section to external data[17] and the Berger-Sehgal model  
1042 [37]. Three tunable normalization parameters are used describe the coherent production model: CC on  $^{12}\text{C}$ ,  
1043 CC on  $^{16}\text{O}$ , and NC on all nuclei. As a design choice, both CC parameters are 100% correlated with one  
1044 another, meaning that any change in one parameter changes the other identically.

1045 **4.2.3.4 High Energy Scattering Model**

1046 There are two parameters that describe high energy neutrino scattering. One is a CC deep inelastic scattering  
1047 (DIS) interaction shape parameter called "CC DIS". The other is a normalization for NC interactions called  
1048 "NC Other". The CC DIS parameter, which also includes multiple pion production, is modeled as a function  
1049 of  $E_\nu$  with a simple uncertainty relation of

$$\frac{0.4}{E_\nu \text{ [GeV]}} (\%),$$

1050 where the uncertainty at 4.0 GeV is 10%. The NC Other parameter is a normalization on NC DIS, single kaon  
1051 production, single  $\eta$ -meson production, and NC elastic processes with a flat 30% fractional uncertainty[17].

1052 **4.2.3.5 Final State Interactions**

1053 Final state interactions[42] (FSI) are effects that alter final state pions from neutrino-nucleus events before  
1054 the pion exits the nucleus. The microscopic model in NEUT is a cascade implementation of the Salcedo-Oset  
1055 model[43] which describes interactions in the nucleus as probabilities of position and momentum tuned to  
1056 the world data[44]. These processes are divided into six classes with one parameter for each. These classes  
1057 are the low energy inelastic scattering (INEL), high energy INEL, pion absorption (ABS), pion production  
1058 (PROD), low energy charge exchange (CEX), and high energy CEX. The low and high energy transition for  
1059 both the inelastic scattering and charge exchange processes occurs at  $p_\pi = 500$  MeV/c.

1060 **4.2.3.6 Fixed Parameters**

1061 As mentioned in the CC-0 $\pi$  model, the BeRPA  $U$  parameter is fixed to minimize correlations with the other  
 1062 BeRPA scale parameters. However, there are four other fixed normalization parameters in the BANFF fit  
 1063 since they correspond to SK only parameters. They are included in the fit in order to maintain consistency  
 1064 between the ND280 constraint and oscillation analysis parameterizations. In other words, they are spectators  
 1065 in the BANFF fit. These parameters are the CC  $\nu_e/\nu_\mu$  event rate ratio, CC  $\bar{\nu}_e/\bar{\nu}_\mu$  event rate ratio, NC-1 $\gamma$   
 1066 event rate, and NC other far detector event rate.

1067 **4.2.3.7 Prefit Values and Covariance Matrix**

1068 There are a total of 31 cross section parameters in the BANFF fit, five of which are fixed. The fit parameters  
 1069 are listed in Table 4.4 on page 75 with the associated covariance matrix shown in Figure 4.12 on page 77.  
 1070 Following the definition of the flux and bin normalization parameters, cross section parameters are defined  
 1071 as fractional differences either in shape, scale, or normalization. If no prefit uncertainty is shown in Table  
 1072 4.4 on page 75, and emphasized using red font, then the parameter had a flat prior assigned. A model  
 1073 parameter with an asterisk (\*) next to it is fixed in the fit. Abbreviations used in this table are “dim.-less”  
 1074 for dimensionless, “norm.” for normalization, “Near” for ND280, “Far” for Super-Kamiokande, and “bkg”  
 1075 for background. Parameters with physical units are shown in both dimensionless and dimensional values for  
 1076 comparison. Prefit values are relative to the NEUT nominal value.

---

Table 4.4: Cross section model parameters in the fit. See the text  
 for a full description.

Fit index	Topology	Model	Parameter	Prefit
562	All	FSI	Low energy INEL	$0 \pm 0.41$
563			High energy INEL	$0 \pm 0.34$
564			PROD	$0 \pm 0.41$
565			ABS	$0 \pm 0.5$
566			Low energy CEX	$0 \pm 0.57$
567			High energy CEX	$0 \pm 0.28$
568	CC-0 $\pi$	Llewellyn-Smith	$M_A^{QE}$ (dim.-less)	1
			$M_A^{QE}$ (GeV/c <sup>2</sup> )	1.20
569		RFG	$p_F^C$ (dim.-less)	1
			$p_F^C$ (MeV/c)	217

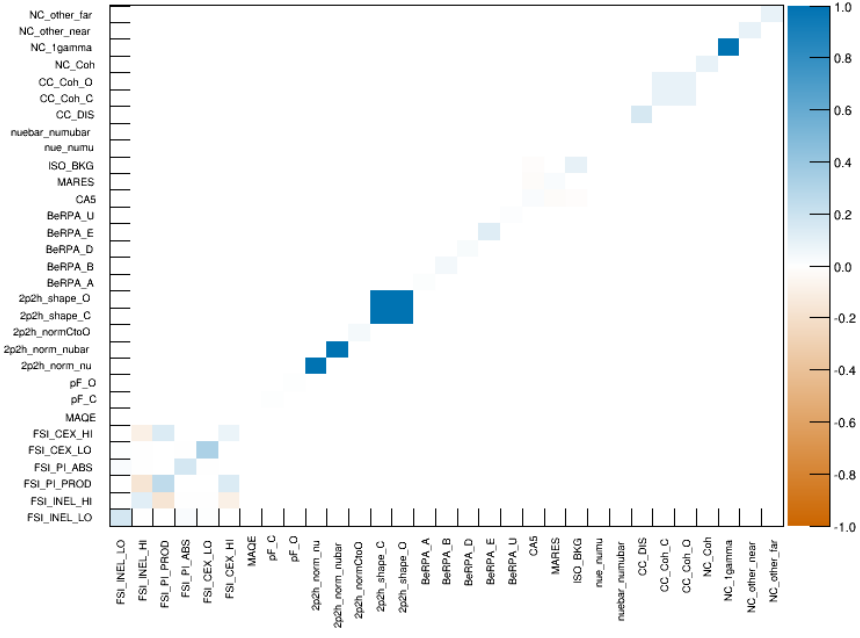
Fit index	Topology	Model	Parameter	Prefit
570	Nieves 2p2h		$p_F^O$ (dim.-less)	1
			$p_F^O$ (MeV/c)	225
571		$\nu$ norm. on $^{12}\text{C}$	$\nu$ norm. on $^{12}\text{C}$	1
572			$\bar{\nu}$ norm. on $^{12}\text{C}$	1
573			$^{12}\text{C} \rightarrow ^{16}\text{O}$ norm.	1
574			$^{16}\text{C}$ shape location	0
575			$^{12}\text{O}$ shape location	0
576		BeRPA	$A$	$0.59 \pm 0.118$
577			$B$	$1.05 \pm 0.21$
578			$D$	$1.13 \pm 0.1695$
579			$E$	$0.88 \pm 0.352$
580			$U^*$	$1.2 \pm 0.1$
581	CC-1 $\pi$	Rein-Seghal resonant 1 $\pi$ prodction	$C_A^5$	$0.96 \pm 0.148$
582			$M_A^{\text{Res}}$ (dim.-less)	$1.1263 \pm 0.157$
			$M_A^{\text{Res}}$ (GeV/c $^2$ )	$1.07 \pm 0.15$
583			$I_{1/2}$ bkg. norm.	$0.74 \pm 0.307$
584	Other	Event rate at SK	CC- $\nu_e/\nu_\mu^*$	$1 \pm 0.0282$
585			CC- $\bar{\nu}_e/\bar{\nu}_\mu^*$	$1 \pm 0.0282$
586		Coherent pion production	CC DIS shape location	$0 \pm 0.4$
587			CC norm. on $^{12}\text{C}$	$1 \pm 0.3$
588			CC norm. on $^{16}\text{O}$	$1 \pm 0.3$
589			NC norm.	$1 \pm 0.3$
590		Event rate	NC-1 $\gamma^*$	$1 \pm 1$
591			NC Other Near	$1 \pm 0.3$
592			NC Other Far*	$1 \pm 0.3$

1077

## 1078 4.3 Summary

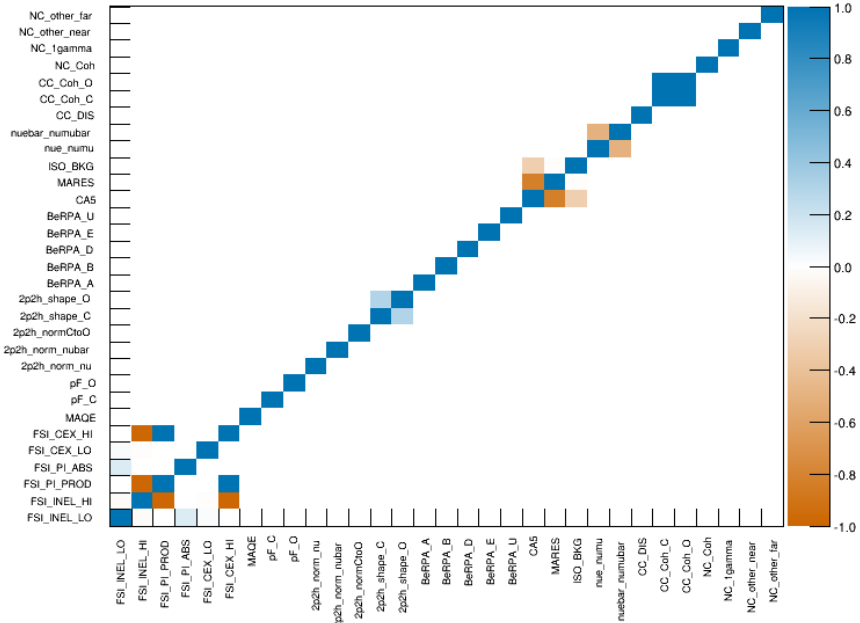
1079 This chapter has described all the fit bins and parameters that go into the BANFF fit. For the fit bins,  
 1080 they are used in the LLR term to model the best possible fit between data and MC without any constraints.

**Prefit XSec Covariance Matrix**



(a) Covariance matrix

**Prefit XSec Correlation Matrix**



(b) Correlation correlation

Figure 4.12: Cross section parameters prefit covariance and correlation matrices.

1081 However, since there are known systematic uncertainties in the flux, detector inefficiencies, and cross sections,  
1082 we have described their parameterizations to force the fit work within those constraints. The flux model  
1083 is constrained by T2K primary and secondary beamline data while the cross sections are constrained by  
1084 external data. Finally, the detector systematics are determined via an ensemble of toy experiments based  
1085 on well established control samples in the ND280 detector.

1086 The next chapter describe the set of validation studies used to examine how the BANFF fit performs.

1087 **Chapter 5**

1088 **Validation of the BANFF Fit**

1089 **Procedure**

1090 This chapter will present the checks, tests and validations of the BANFF fit using the MC simulation as  
1091 input. The test using the weighted MC as the data is referred as an Asimov<sup>1</sup> data fit[45]. There next are two  
1092 other validation tests that use two different data sets that have altered events weights (reweighted) compared  
1093 to the MC. These are referred to as fake data sets.

1094 The chapter is presented in the following order. The first topic is the Asimov data fit discussed in Section  
1095 5.1. The following section explores the results of the two fake data fits in Section 5.2. A chapter summary  
1096 is provided in Section 5.3.

1097 **5.1 Asimov Data Fit**

1098 Asimov data refers to replacing the ensemble of simulated data sets by a single representative one[45]. In  
1099 this analysis, this involves fitting the MC data set to itself for the primary purpose of checking the closure of  
1100 the fitting framework. The Asimov set is produced with the same models as is implemented in the fitter and  
1101 has all parameters set to their prior central values as defined in Chapter 4. Instead of statistically sampling  
1102 from the MC, which can insert statistical variations into the fit, the Asimov data set is created by scaling  
1103 the set down to the full T2K POT with additional finer corrections like flux and cross section weights. The  
1104 prefit correlation matrix is shown in Figure 5.1 on page 80.

1105 In addition to running an Asimov fit, other metrics were examined in the Asimov set. Shown first is a

---

1An Asimov data refers replacing the ensemble of simulated data sets by a single representative one.

### Prefit Correlation Matrix

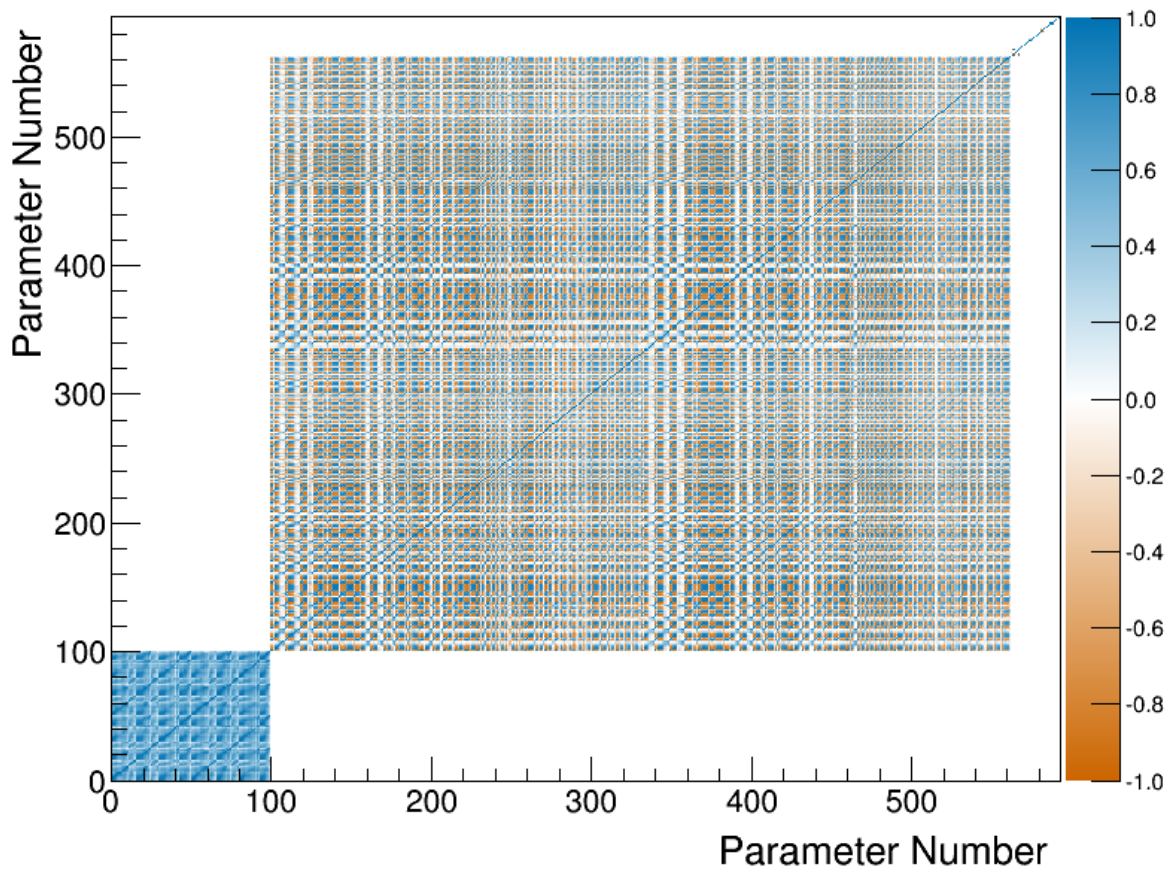


Figure 5.1: Complete prefit correlation matrix for the BANFF fit. The first 100 parameters are the flux bins. Between 100 and 561 are the bin normalization parameters. Finally 562 through 592 are the cross section parameters.

1106 comparison of the event rates before and after applying weights to the MC. Next is an examination of the  
1107 cross section weight functions. Finally is a set of scans of the test statistic space to check that the sample  
1108 and penalty terms are behaving as expected. Then the Asimov data set fit is examined.

1109 **5.1.1 Event Rate**

1110 Shown in Table 5.1 on page 82 are the event rates for the various samples for the Asimov fit. The data events  
1111 column refers to real T2K data collected in ND280. The proceeding columns refer to MC events only after  
1112 applying different weights. The POT weight is a gross normalization that scales the MC event rate to the  
1113 data rate. The other weights, which were discussed in Chapter 2, are the flux, cross section, and detector  
1114 corrections. As expected, we see that applying the POT weight scales the MC event rate close to that of the  
1115 data. The other weights are fine tuning corrections to the rate from known systematics like flux and cross  
1116 sections. The set of samples after applying all the weights is referred to as Asimov data set.

Table 5.1: Event rate table for Asimov set. The “Raw MC” column refers the number of events in the sample from the nominal MC prediction without any weights applied. From left to right, applications of weights are applied to understand their affect on the samples. The “POT only” column refers to applying the POT weight to all events. Columns with “POT+Flux”, “POT+xsec”, and “POT+Det” refer to applying the POT weight together with the flux, cross section, and detector weights, respectively. The “Prefit” column has the POT, flux, cross section, and detector (POT+Flux+xsec+Det) weights all multiplied together.

Sample name	Data events	Raw MC events	Application of weights				Prefit
			POT only	POT+Flux	POT+xsec	POT+Det	POT+flux+xsec+Det
$\nu_\mu$ 1-Trk Wtr	27151.00	526226.00	26270.98	28766.86	24222.45	26286.14	27327.94
$\nu_\mu$ N-Trks	31013.00	529538.00	26708.61	31464.27	26267.19	26708.74	31098.20
$\bar{\nu}_\mu$ RHC 1-Trk	8779.00	176007.00	9152.04	9365.78	8321.76	9161.91	8461.37
$\bar{\nu}_\mu$ RHC N-Trks	4613.00	93132.00	4876.93	5014.74	4652.01	4876.81	4802.12
$\nu_\mu$ RHC 1-Trk	3502.00	56861.00	2933.20	3182.20	2747.29	2938.29	3025.76
$\nu_\mu$ RHC N-Trks	5424.00	85599.00	4460.10	4988.89	4413.01	4464.45	4956.19
$\nu_\mu$ 1-Trk Air	23504.00	309373.00	23383.39	25319.17	21594.49	23402.63	23603.03
$\nu_\mu$ N-Trks	32736.00	371986.00	28495.10	33255.58	27822.42	28505.66	32302.08
$\bar{\nu}_\mu$ RHC 1-Trk	6681.00	75374.00	7374.13	7512.47	6732.25	7381.37	6767.79
$\bar{\nu}_\mu$ RHC N-Trks	4437.00	47951.00	4689.16	4820.43	4446.52	4690.57	4544.72
$\nu_\mu$ RHC 1-Trk	2324.00	20943.00	2049.01	2198.46	1916.33	2052.56	2067.12
$\nu_\mu$ RHC N-Trks	4801.00	42098.00	4119.63	4586.22	4050.71	4122.39	4567.72
Total	154965.00	2335088.00	144512.28	160475.06	137186.41	144591.53	153524.03

### **5.1.2 One Sigma Variation of Cross Section Parameters**

It is difficult to predict the impact of cross section parameters variations in the BANFF fit since the fit samples contain many interaction modes themselves. In particular, a single parameter variation can also be explained by many parameters individually varied. To understand the effect of the cross section parameter variations on the fit samples, each cross section parameter was varied by  $\pm 1$  standard deviation. This also ensures the spline weight functions, which are generated for each event prior to the BANFF fit, are functioning properly. The results of the variations are shown in Appendix C.

### **5.1.3 Log-Likelihood Scans**

Log-likelihood scans of the sample and penalty terms were examined in the Asimov data set. The results of the scans are shown in Figure 5.2 on page 84 with comparisons between the PØD-only samples and FGD-only samples shown. It can be seen that the PØD-only data has similar sensitivity and shape dependence on the flux parameters to that of the FGD-only data. Also observed is that the penalties are the identical for both PØD- and FGD-only sets and parabolic in shape as expected since the penalties are modeled using a Gaussian. The complete set of scans is contained in Appendix D and Appendix E.

### **5.1.4 Fit Results**

The postfit results of the Asimov data fit are shown from Figure 5.3 on page 85 to Figure 5.6 on page 88. In order to provide a unified graphical representation for all the parameters, the prefit and postfit cross section shape parameters are adjusted to be relative to one (1).

We see that the postfit parameters have uncertainties that are different compared to their prefit values. This is expected since correlations between the sub-matrices in the covariance matrix, which were assumed uncorrelated to start, have been calculated. The complete postfit correlation matrix is shown in Figure 5.7 on page 89 and the flux and cross section only correlation matrix is shown in Figure 5.8 on page 89. We observe significant anti-correlations between each of the sub-matrices, which is predicted from Eqn. (2.7) since any increase in one parameter weight forces a decrease in the others.

## **5.2 Fake Data Fits**

In this section, we examine the results of BANFF fits when given data sets with nonphysical alterations. As stated earlier, these are called fake data sets since we are treating these as data in the fit. The fake data sets initially start as the Asimov data set and have variations applied to them. Here we are only interested

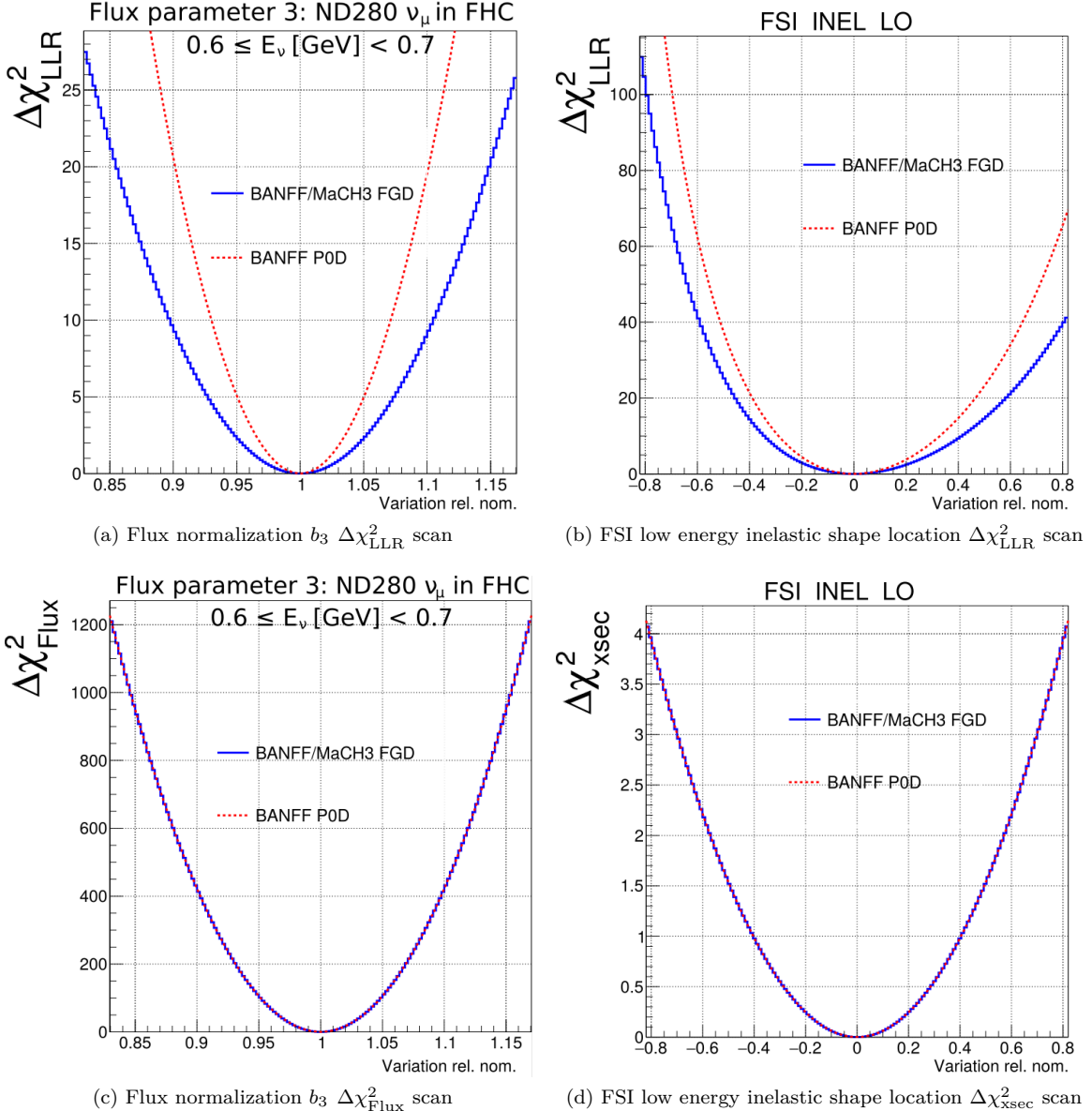


Figure 5.2: Comparison of  $\Delta\chi^2$  scans for variations in fit parameters in the Asimov set. Two parameters are varied: parameter 3 (left) corresponding to a flux bin normalization and 562 (right) corresponding to a FSI shape location parameter. The top panel shows the change in the LLR test statistic  $\Delta\chi^2_{\text{LLR}}$  while the bottom panel shows the penalty terms. In all sub-figures are comparisons between the BANFF/MaCH3 FGD 2017 results[2] against the BANFF PØD-only results. Special thanks goes to Clarence Wret (c.wret@rochester.edu) of the University of Rochester for generating the plots.

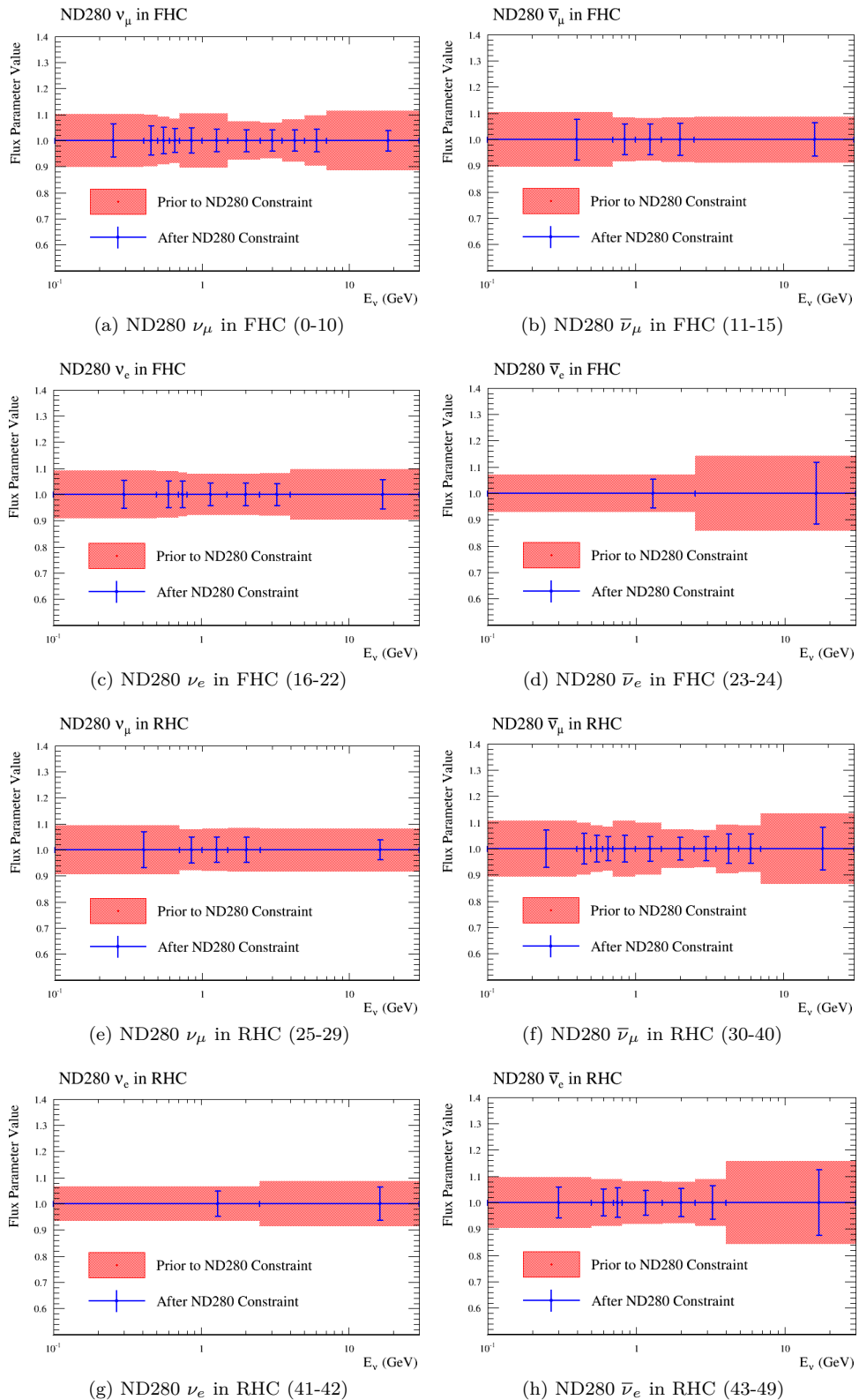


Figure 5.3: Asimov fit results for the Flux at ND280. The numbers in parentheses indicate the fit indices.

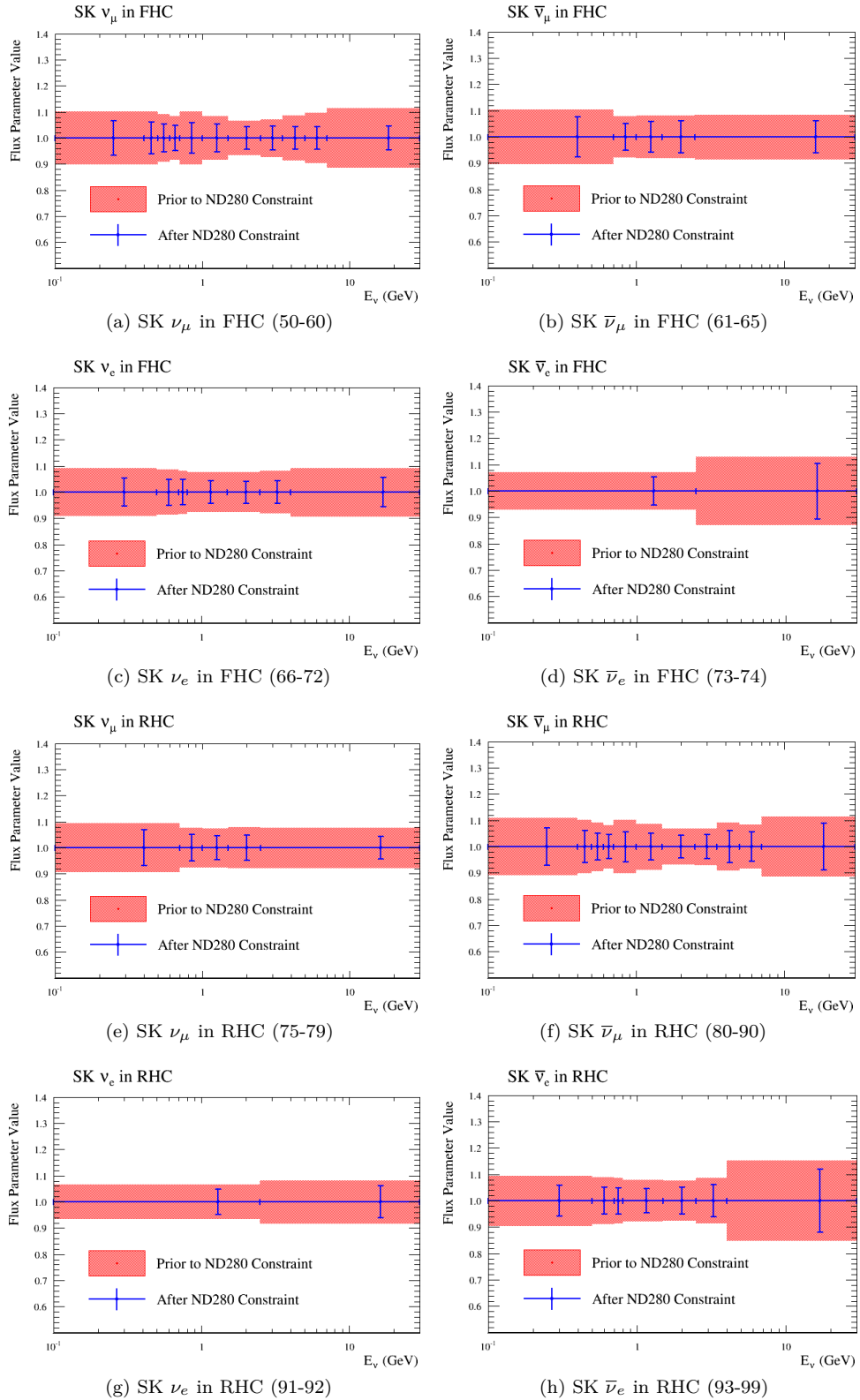


Figure 5.4: Asimov fit results for the Flux at Super-K. The numbers in parentheses indicate the fit indices .

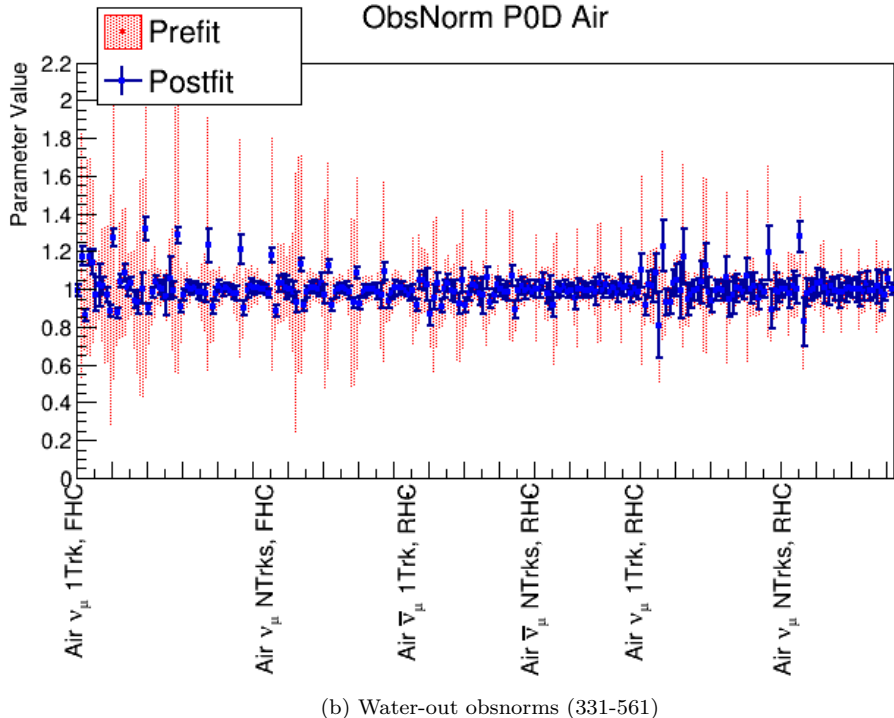
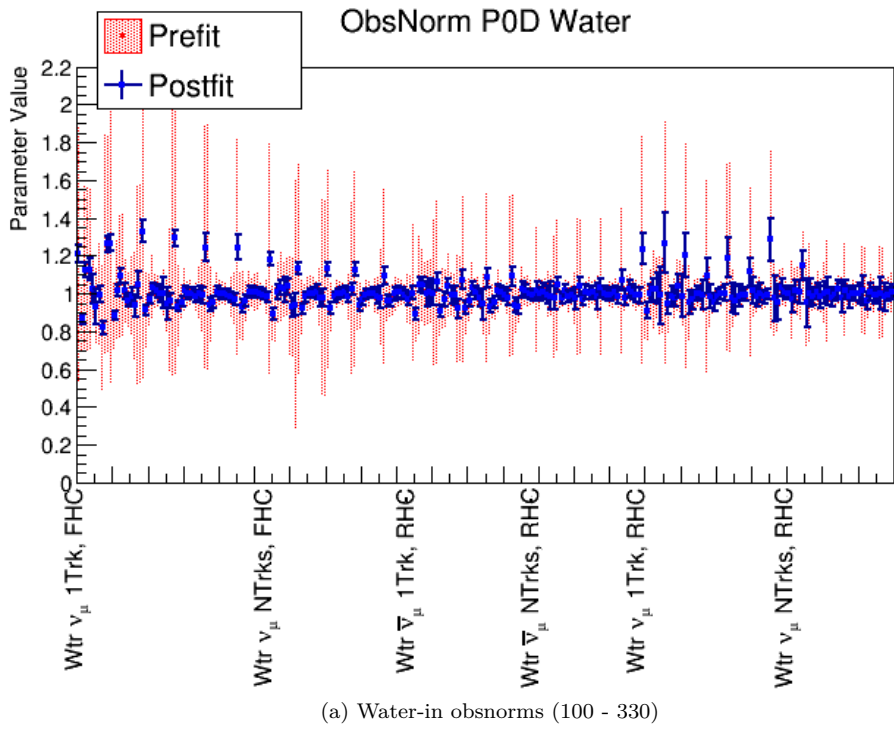
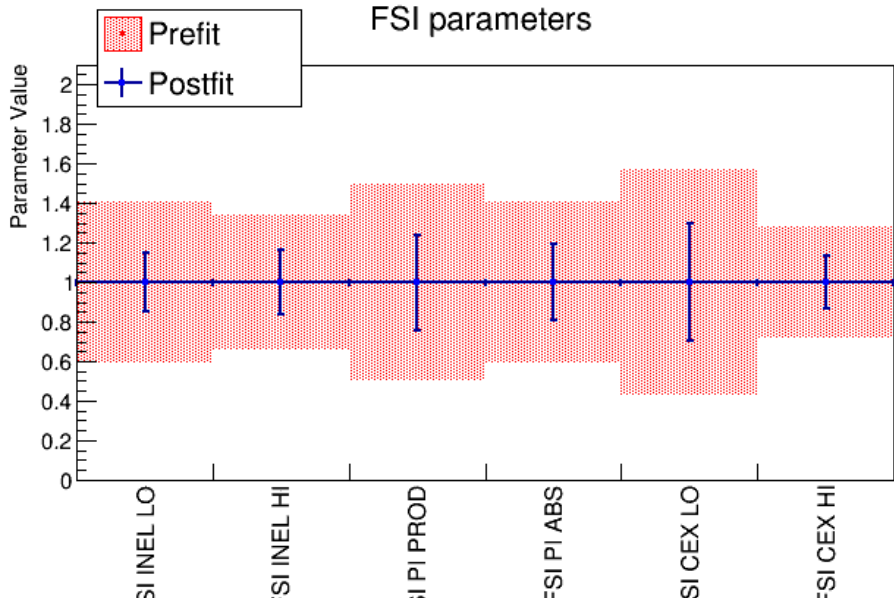
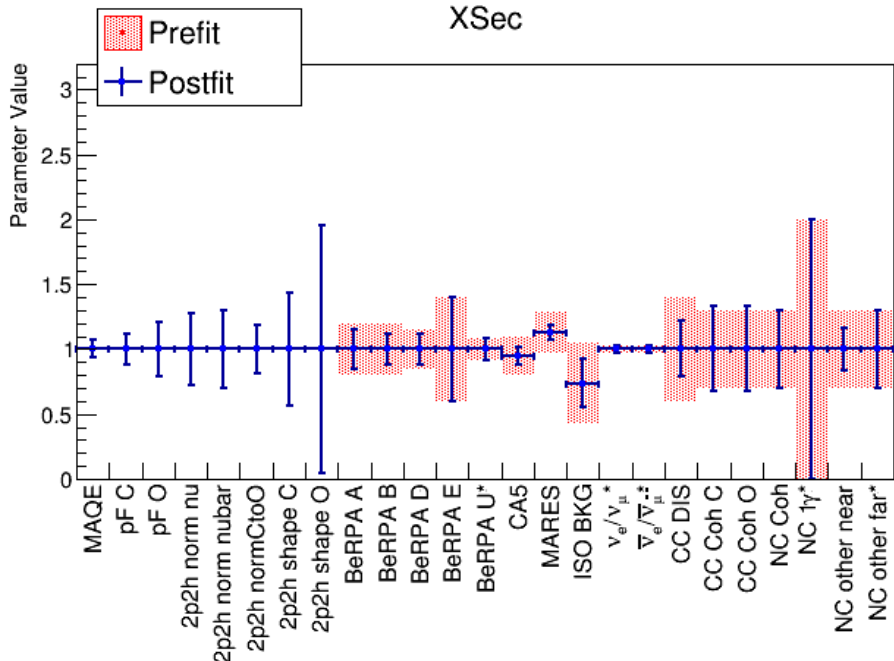


Figure 5.5: Asimov fit results for the obsnorm parameters. The numbers in parentheses indicate the fit indices. The large jumps in the bin normalization parameters is an artifact of the indexing choice with the indices increasing in increasing momentum in constant angular slices. Compare the changes in the bin normalizations in the  $\nu_\mu$  in FHC Mode CC 1-Track in Figure 4.6 on page 63.



(a) FSI (562-567)



(b) Cross Section (568-592)

Figure 5.6: Asimov fit results for the FSI and cross section parameters. The numbers in parentheses indicate the fit indices. In order to provide a consistent presentation of parameter changes between prefit and postfit among all parameters, shape location and scale parameters are adjusted to prefits of one (1). In effect, the value and uncertainties for all parameters are fractional changes.

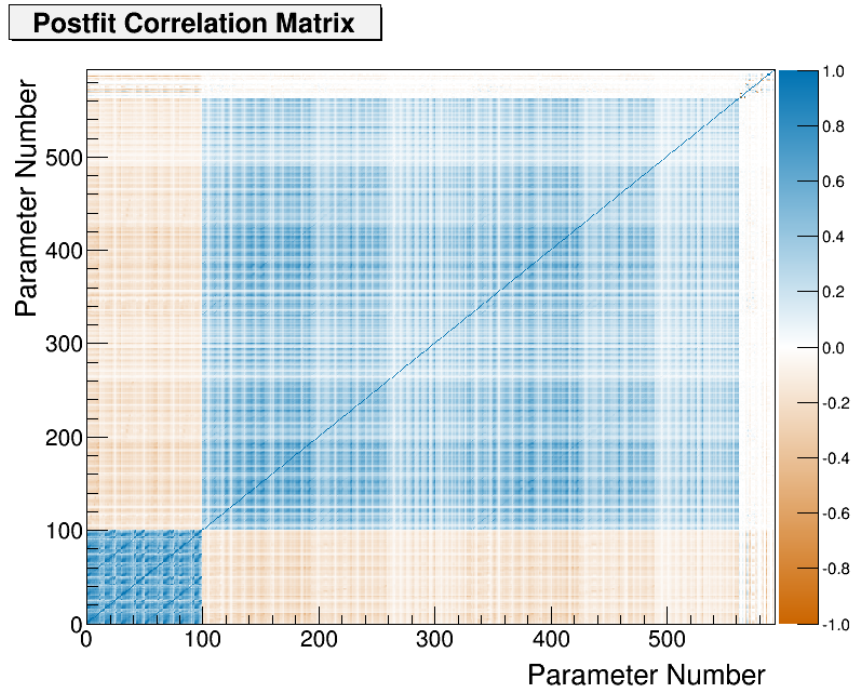


Figure 5.7: Complete postfit correlation matrix for the Asimov data fit.

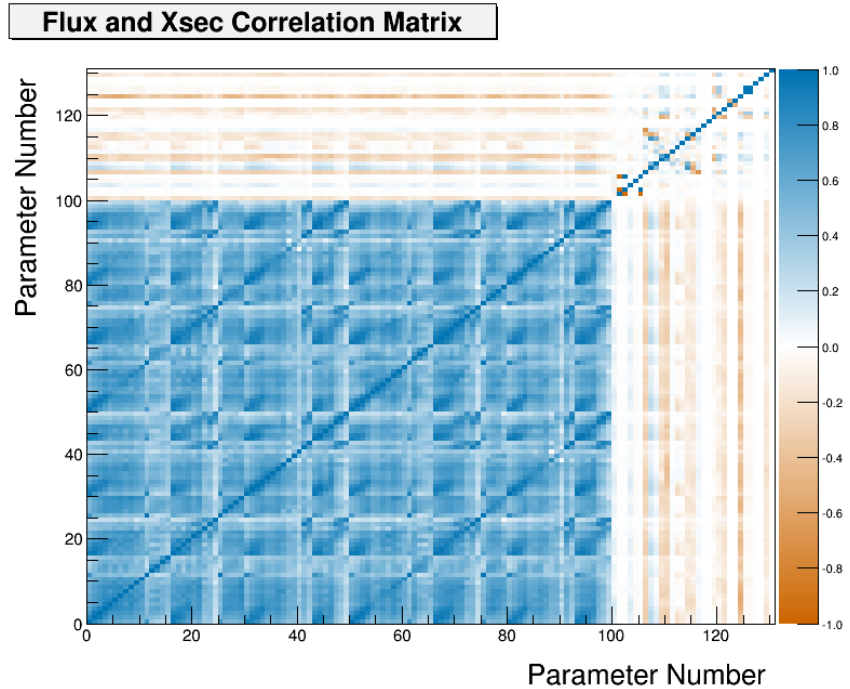


Figure 5.8: Flux and cross section postfit correlation matrix for the Asimov data fit. The parameters from 1-100 are the flux parameters and all parameters after are the cross section.

1145 in varying the flux and cross section parameters since they are the parameters that are propagated to the  
1146 oscillation analysis. There were two fake data sets generated for the tests. One data set varies the neutrino  
1147 flux in a single flux bin and the other varies the single pion production rate.

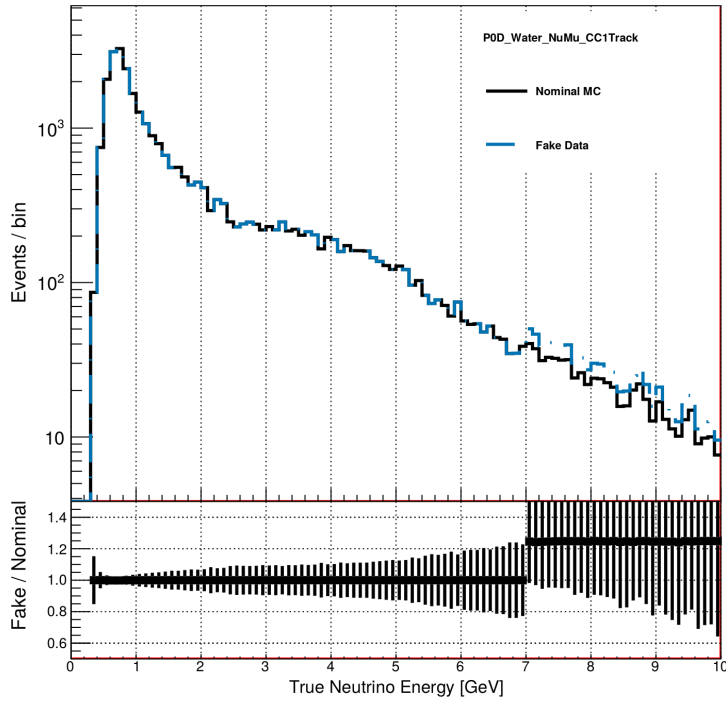
1148 While other fake data sets could be generated that are more or less similar to the Asimov data set, that  
1149 is not the purpose of fitting to fake data sets. *The purpose of these tests is to show the fit can converge when*  
1150 *provided with non-Asimov data sets and we can understand the results.* It is known in the BANFF group  
1151 that the BANFF fitting software is not guaranteed to converge on a global minimum when using altered  
1152 Asimov data. In particular, fitting FGD-only data generated from random and uncorrelated variations of all  
1153 fit flux, cross section, and bin normalization parameters, 127 out of 500 fits ( $\sim 25\%$ ) reported fit convergence  
1154 problems. So convergence is not assured in all situations, but is possible. We can establish that a credible  
1155 PØD-only real data fit result is possible by demonstrating 1) the BANFF fit converges with PØD-only fake  
1156 data and 2) that we can sensibly understand those fit results.

1157 The information provided from fake data tests is also useful to understand possible biases in the fit  
1158 results. For instance, since the PØD samples have a relatively low sensitivity to CC- $1\pi$  interactions, real  
1159 differences between data and MC could be explained by variations in non CC- $1\pi$  model parameters. We will  
1160 get a sense of the biases in the following two fake data tests. The first fake data test analyzed is referred  
1161 to as the “High Energy Neutrino Flux Variation” which varies the high energy  $\nu_\mu$  flux in FHC mode. The  
1162 following fake data test is referred to as the “Single Pion Event Rate Variation” which alters the single pion  
1163 production event rate uniformly.

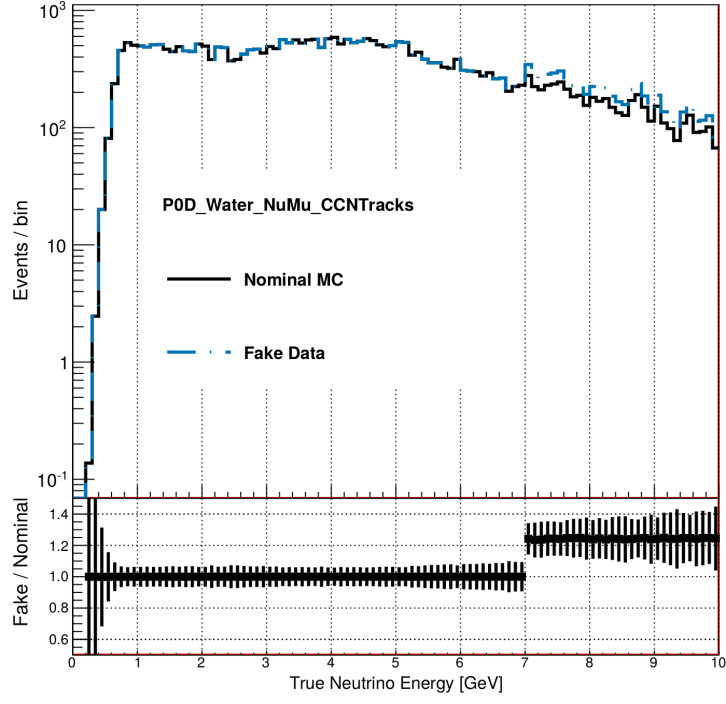
### 1164 5.2.1 High Energy Neutrino Flux Variation

1165 This fake data set is almost identical to the Asimov data set expect an arbitrarily large increase in the  $\nu_\mu$   
1166 flux between 7 and 30 GeV by +25% in FHC mode only. This variation was chosen since this energy range  
1167 corresponds precisely to flux parameter  $b_{10}$  and it could affect all analysis bins. The true neutrino energy  
1168 distribution of the fake data used in this study is shown in Figure 5.9 on page 91 and Figure 5.10 on page  
1169 92.

1170 The postfit parameter plots are shown in Figure 5.11 on page 93. We see that the target flux parameter  
1171  $b_{10}$  has significantly increased from its prefit value by almost +20%. However, due to correlations in the flux  
1172 covariance matrix, other flux parameters have also changed. The BANFF fit prefers to increase the previous  
1173 energy flux parameter and the high energy  $\nu_e$  flux parameters as well. While we saw that the flux and  
1174 hence event rate was not changed in the RHC samples, the RHC flux parameters are also slightly affected.  
1175 However, the RHC flux parameters are still well within prefit uncertainties. The statement is true for the



(a) The  $\nu_\mu$  in FHC Mode CC 1-Track sample



(b) The  $\nu_\mu$  in FHC Mode CC N-Tracks sample

Figure 5.9: Neutrino energy distributions in the High Energy Neutrino Flux variation fake data set. The fake data (dashed-blue) is nearly identical to the Asimov set (black) except the +25% increase in the  $\nu_\mu$  in FHC mode rate at energies greater than 7 GeV. In the figures, “Nominal MC” refers to the Asimov prediction and “Fake Data” is the altered data set. The ratio of the fake data to the nominal MC is shown below each histogram with the errors being statistical only.

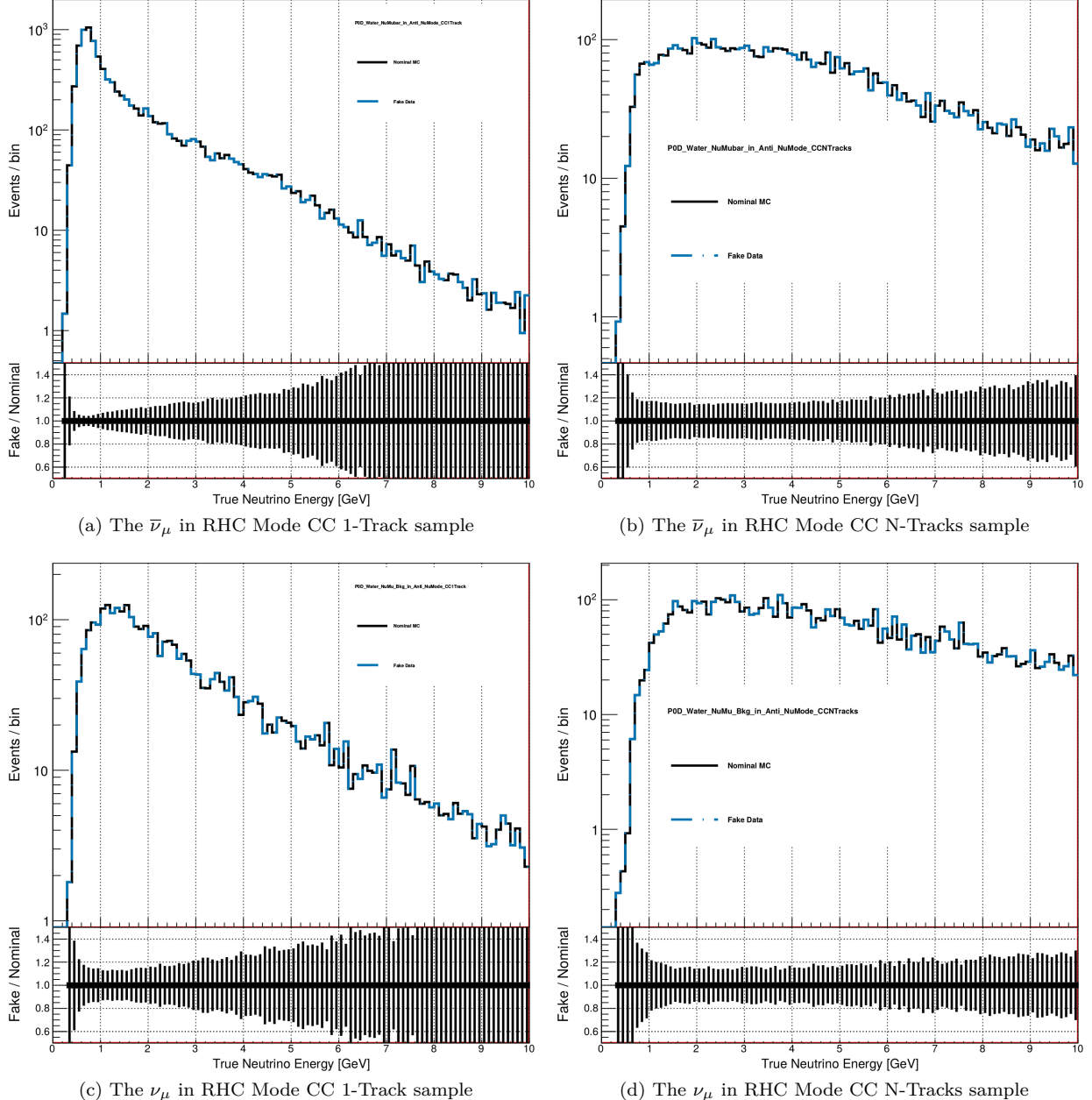
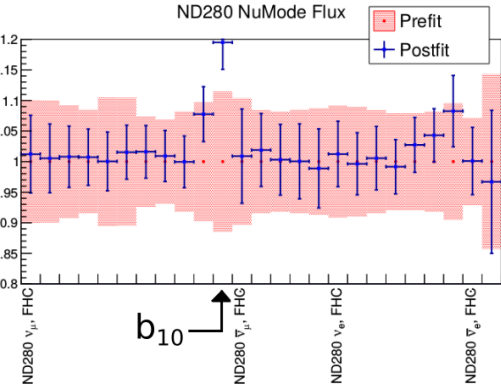
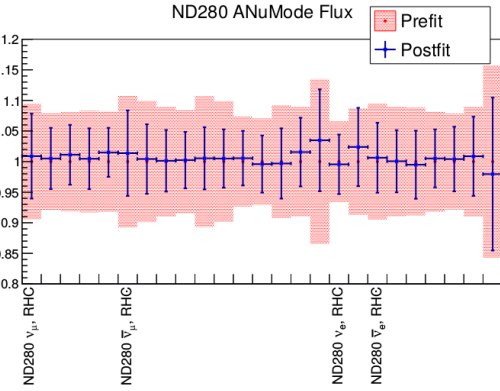


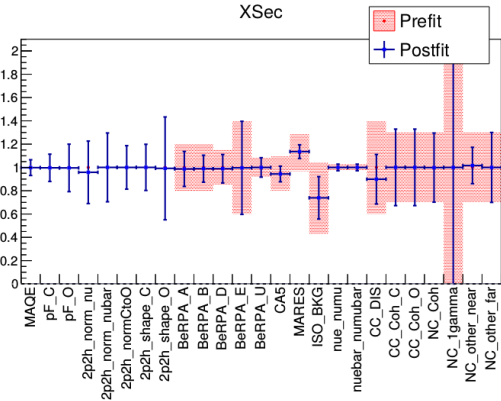
Figure 5.10: Neutrino energy distributions in the High Energy Neutrino Flux variation fake data set (continued). The fake data (dashed-blue) is nearly identical to the Asimov set (black) except the +25% increase in the  $\nu_\mu$  in FHC mode rate at energies greater than 7 GeV. In the figures, “Nominal MC” refers to the Asimov prediction and “Fake Data” is the altered data set. The ratio of the fake data to the nominal MC is shown below each histogram with the errors being statistical only.



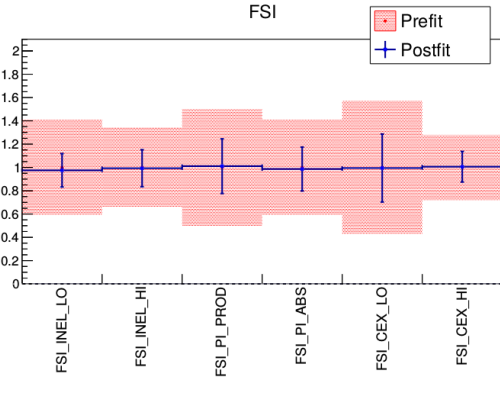
(a) The ND280 FHC mode flux parameters



(b) The ND280 RHC mode flux parameters



(c) Cross section parameters



(d) The FSI parameters

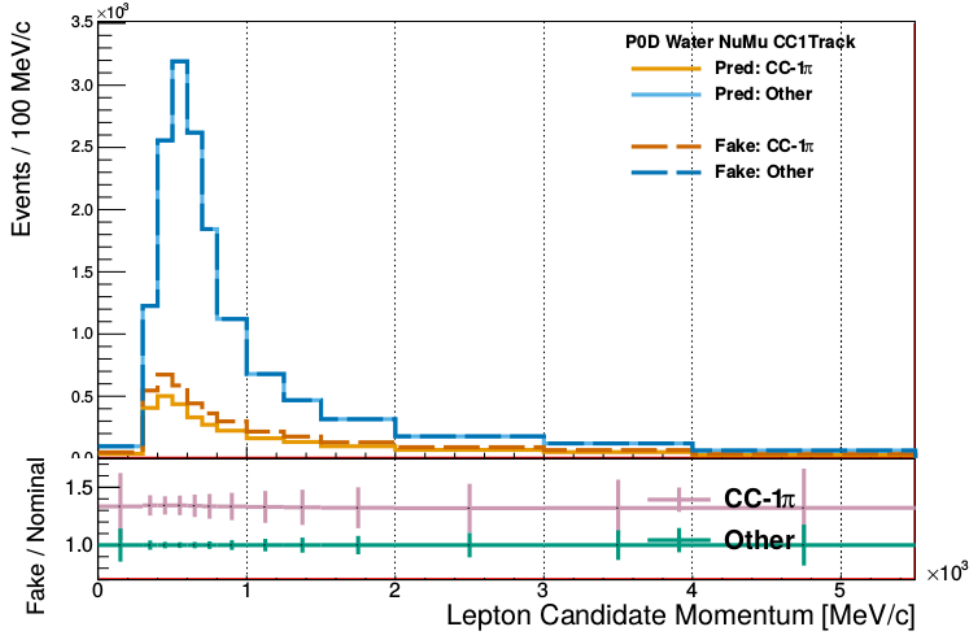
Figure 5.11: Postfit parameters for the high energy  $\nu_\mu$  in FHC flux variation fake data fit. All the flux parameters in FHC are shown together and ordered sequentially from left to right. The same is true the RHC flux.

1176 cross section and FSI parameters. We can conclude from this study that the fit will resolve large, nonphysical  
 1177 differences between the Asimov prediction and the data with many correlated parameter variations.

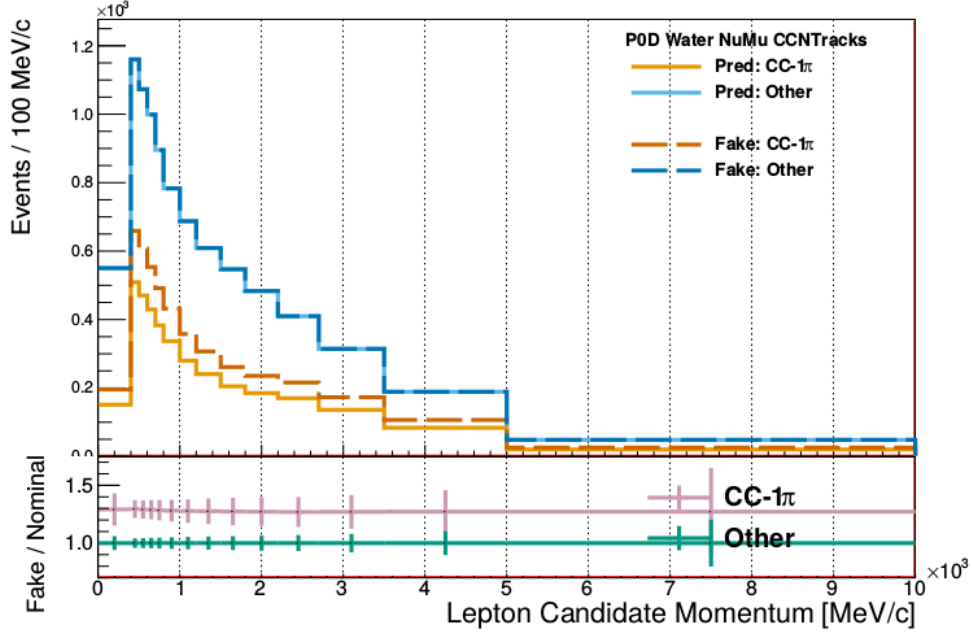
### 1178 5.2.2 Single Pion Event Rate Variation

1179 This fake data set is very similar to the Asimov set except for a +25% increase in the number of resonant  
 1180 single pion events in all analysis samples. This was implemented by taking all true NEUT CC-1 $\pi$  events,  
 1181 extracting the event weight, and increasing it by +25%. This is what is observed in the lepton candidate  
 1182 momentum distributions as shown in Figure 5.12 on page 94 and Figure 5.13 on page 95.

1183 This fake data test will help us understand the BANFF fit response due to poor data matching with  
 1184 a cross section model. The ideal result of this test is that the postfit value of  $C_A^5$  is increased by +25%  
 1185 and all other parameters are unchanged like the results seen in Appendix C. However, this is not a realistic  
 1186 expectation given that there are no dedicated CC-1 $\pi$  samples, thus the sensitivity to CC-1 $\pi$  parameters



(a) The  $\nu_\mu$  in FHC Mode CC 1-Track sample



(b)  $\nu_\mu$  in FHC Mode CC N-Tracks

Figure 5.12: Lepton candidate momentum distributions in the Single Pion Event Rate Variation fake data set. The nominal MC and fake data predictions are shown as solid and dashed lines, respectively. True CC-1 $\pi$  events are differentiated from all other interactions to illustrate the event scaling applied. A ratio plot of CC-1 $\pi$  events to all other interaction events shown beneath each main histogram.

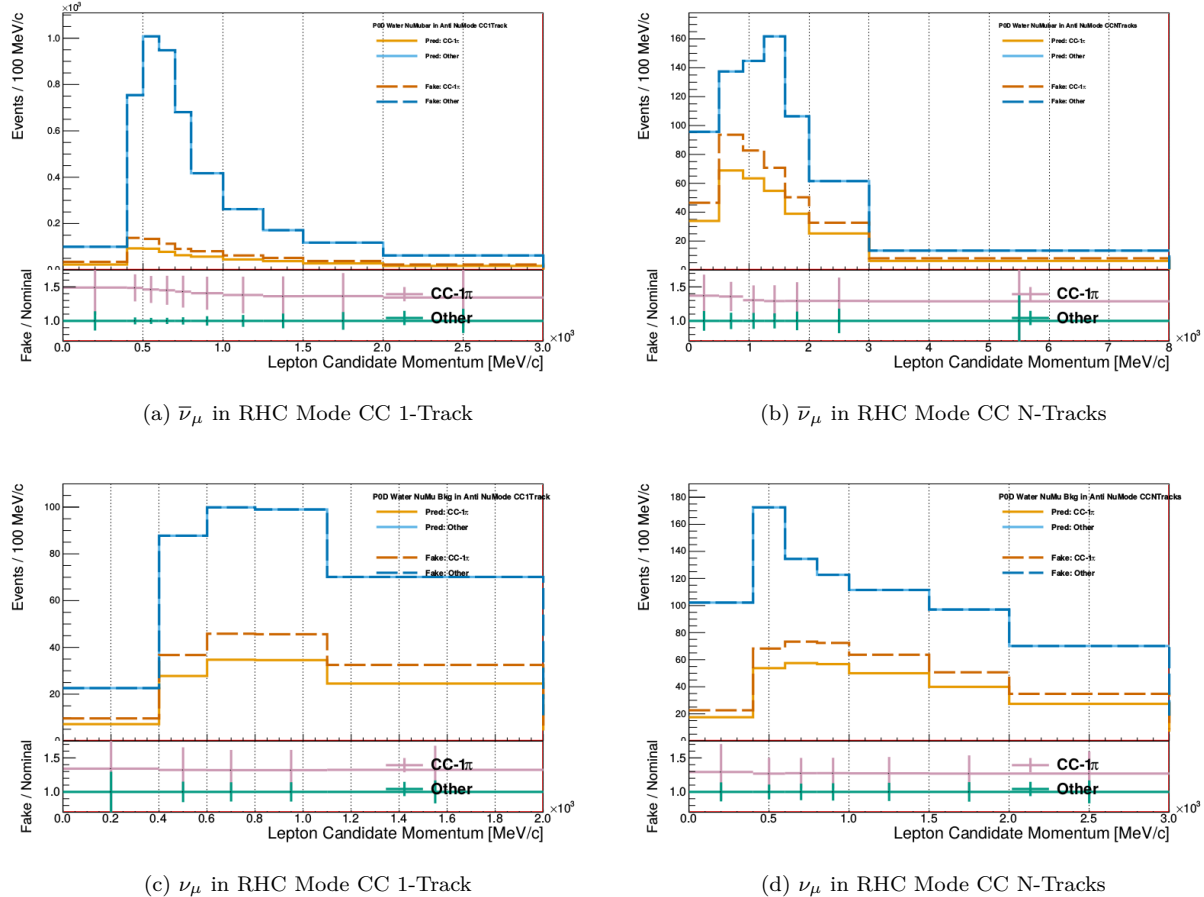


Figure 5.13: Lepton candidate momentum distributions in the Single Pion Event Rate Variation fake data set (continued). The nominal MC and fake data predictions are shown as solid and dashed lines, respectively. True CC-1 $\pi$  events are differentiated from all other interactions to illustrate the event scaling applied. A ratio plot of CC-1 $\pi$  events to all other interaction events shown beneath each main histogram.

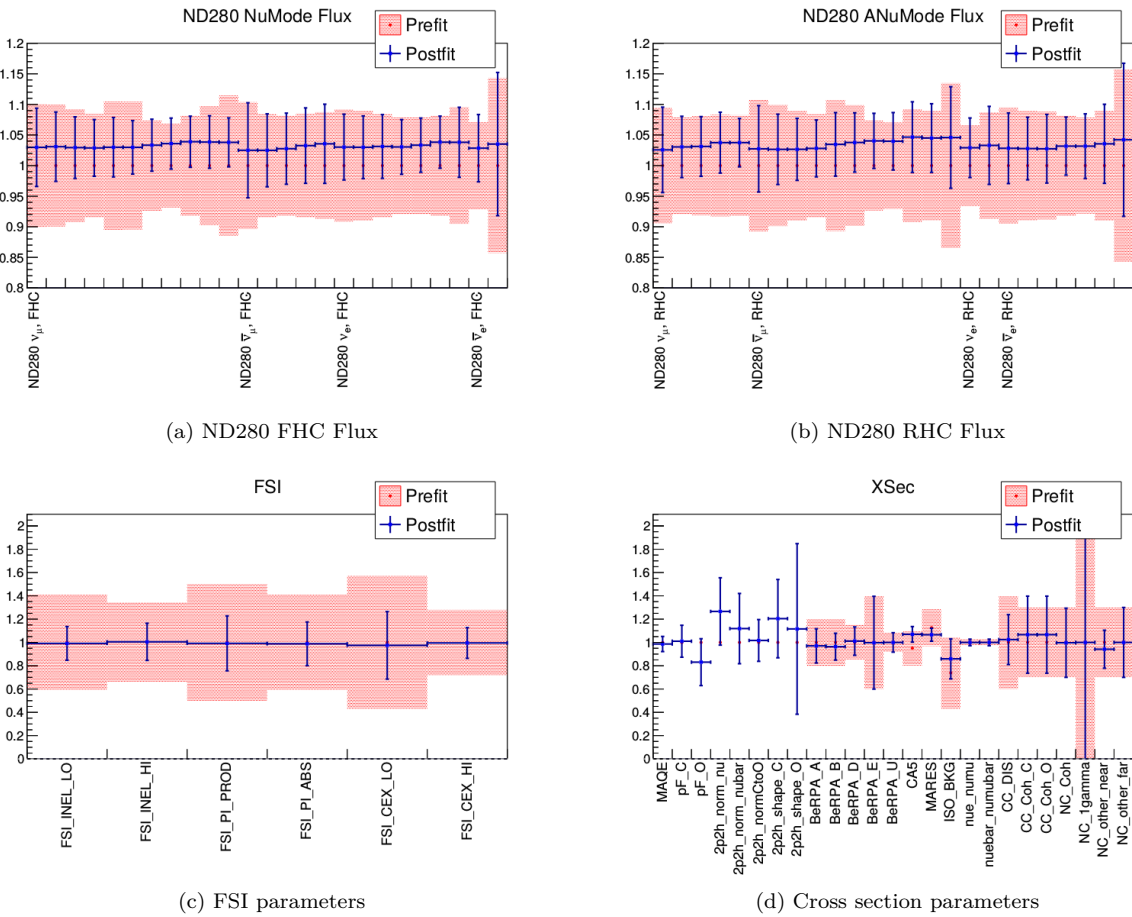


Figure 5.14: Postfit parameters for the Single Pion Event Rate Variation fake data fit. All the flux parameters in FHC are shown together and ordered sequentially from left to right. The same is true the RHC flux.

is expected to be small. In particular, the  $C_A^5$  and  $M_A^{\text{Res}}$  parameters are strongly anticorrelated with one another, meaning that these parameters will be forced to shift in opposite directions. From our intuition gained in the first fake data fit, we can expect non-CC- $1\pi$  parameters to vary especially groups of flux parameters together.

The postfit results for this fake data set are shown in Figure 5.14 on page 96. We observe that the CC- $1\pi$  parameter  $C_A^5$  increased by  $\sim 10\%$ , but this is not enough to account for the input fake data shift. We also notice that due to anticorrelations,  $M_A^{\text{Res}}$  was decreased by several percent. What the fit prefers is to increase the isospin= $1/2$  background, 2p2h normalization, and all the flux parameters. As seen in the first fake data set, we see that in the presence of nonphysical variations to the physics, the fit prefers to spread out variations among the other parameters. However, this time the variations are shared among both the flux and cross section parameters.

<sub>1198</sub> **5.3 Summary**

<sub>1199</sub> We have validated that the BANFF fit works and tested its robustness in a variety of scenarios. We learned  
<sub>1200</sub> from the Asimov data set, which is the T2K nominal MC corrected to data POT with fine tuning corrections,  
<sub>1201</sub> in particular how the flux and cross section parameters affect the samples. In the fake data sets, we saw  
<sub>1202</sub> the effect of the penalty terms and how their correlations influence the fit. While more rigorous tests could  
<sub>1203</sub> establish where biases exist, these limitations are beyond the scope of this thesis. What has been established  
<sub>1204</sub> is that sensible fit results using the PØD selections are possible. We will now use the real PØD data in the  
<sub>1205</sub> BANFF fit.

1206 **Chapter 6**

1207 **Results of the BANFF Fit Using the**  
1208 **PØD Samples**

1209 This chapter explores the results of performing the BANFF fit using the PØD-only samples. We have  
1210 confirmed that the fit machinery is working and that the samples demonstrate sensitivity to flux and cross  
1211 section parameters. The focus in this chapter is to examine the results of the PØD-only data fit and compare  
1212 it against the FGD-only result.

1213 The chapter will proceed in the following order. First, since we have remained purposefully blind up to  
1214 this state in the analysis, the data will be examined in Section 6.1. Next the postfit results will be carefully  
1215 examined and compared with that of the FGD-only fit in Section 6.2. Finally, a chapter summary is provided  
1216 in Section 6.3.

1217 **6.1 Prefit Sample Distributions**

1218 This section presents the first look at the data for the 12 samples according to the fit bins set in Chapter 4.  
1219 The samples are categorized into four true interaction modes as described earlier:  $\nu$  CCQE,  $\nu$  non-CCQE,  $\bar{\nu}$   
1220 CCQE, and  $\bar{\nu}$  non-CCQE. However, true fiducial volume (FV) and out of FV events are not differentiated in  
1221 this case. The prefit samples with the data shown are presented between Figure 6.1 on page 100 and Figure  
1222 6.12 on page 111. First the water-in samples are displayed, and then the water-out samples are shown. As  
1223 we saw before, the water-in and water-out samples are qualitatively the same.

1224 In general, we notice good agreement between the data and prefit distributions. Their agreement is  
1225 represented in one-dimensional profiles with the data to prefit ratio shown below the histograms. Evidence

1226 of the PØD bulging effect in the most downstream layers can be seen in all water-in samples. In particular,  
1227 since there is more true mass in the most downstream layers, particles with lower momenta are more likely  
1228 to enter the TPC than predicted by the MC using the as-built mass. Better agreement is observed in the  
1229 water-out periods, but there is some data tension.

## 1230 6.2 Postfit Results

1231 The results of the PØD-only BANFF fit are presented here. Starting with an initial test statistic of  $\chi^2_{\text{ND}280} =$   
1232 3022.2, the MINUIT optimization routine required 149661 iterations to find the global minimum at  $\hat{\chi}^2_{\text{ND}280} =$   
1233 1412.28. An additional 176000 iterations were required to calculate the Hessian matrix. The computing  
1234 resources used for the fit are presented in Appendix Chapter F.

1235 Specific topics on the postfit results are presented in the following order. First is an examination of  
1236 the postfit samples in one-dimensional profiles and two-dimensional spaces. Next is a comparison of the  
1237 parameter values among the prefit, PØD-only, and FGD-only results. And the final topic is a hypothesis  
1238 test on the level of agreement between the PØD-only and FGD-only BANFF fit results.

### 1239 6.2.1 Postfit Sample Distributions

1240 Presented below are the 12 samples again, but with the parameters extracted from the fit applied to the fit  
1241 bins. This ensures that we have a) not altered the data, and b) that the fitted parameters (postfit) have  
1242 improved the data matching as a result. The samples are shown in Figure 6.13 on page 112 to Figure 6.24  
1243 on page 123 in the same order as presented in the previous section.

1244 We see an improved agreement between the postfit prediction and the data. Still, there is some poor  
1245 data matching, in particular, in the lowest momentum bins. This seems to be balanced between the water-in  
1246 and water-out modes since the flux parameters affect the samples the same way. Given there still is tension  
1247 in those lowest momentum bins, perhaps the water mass systematic uncertainty was under estimated in this  
1248 analysis.

1249 It is hypothesized that if the mass systematic was indeed underestimated, the data to postfit ratio would  
1250 converge towards 1 with decreasing  $\cos \theta$  in the water-in sample's lowest momentum bins. If better agreement  
1251 is observed in those higher angle bins compared to the lower angle bins, this would support the idea that the  
1252 mass systematic uncertainty is underestimated. However, there was a weak trend observed in the water-in  
1253 samples, and such a weak one could be coincidental given the number of bins. Therefore, it is difficult  
1254 to draw any conclusions if the mass systematic uncertainty was underestimated until other constraints are  
1255 provided.

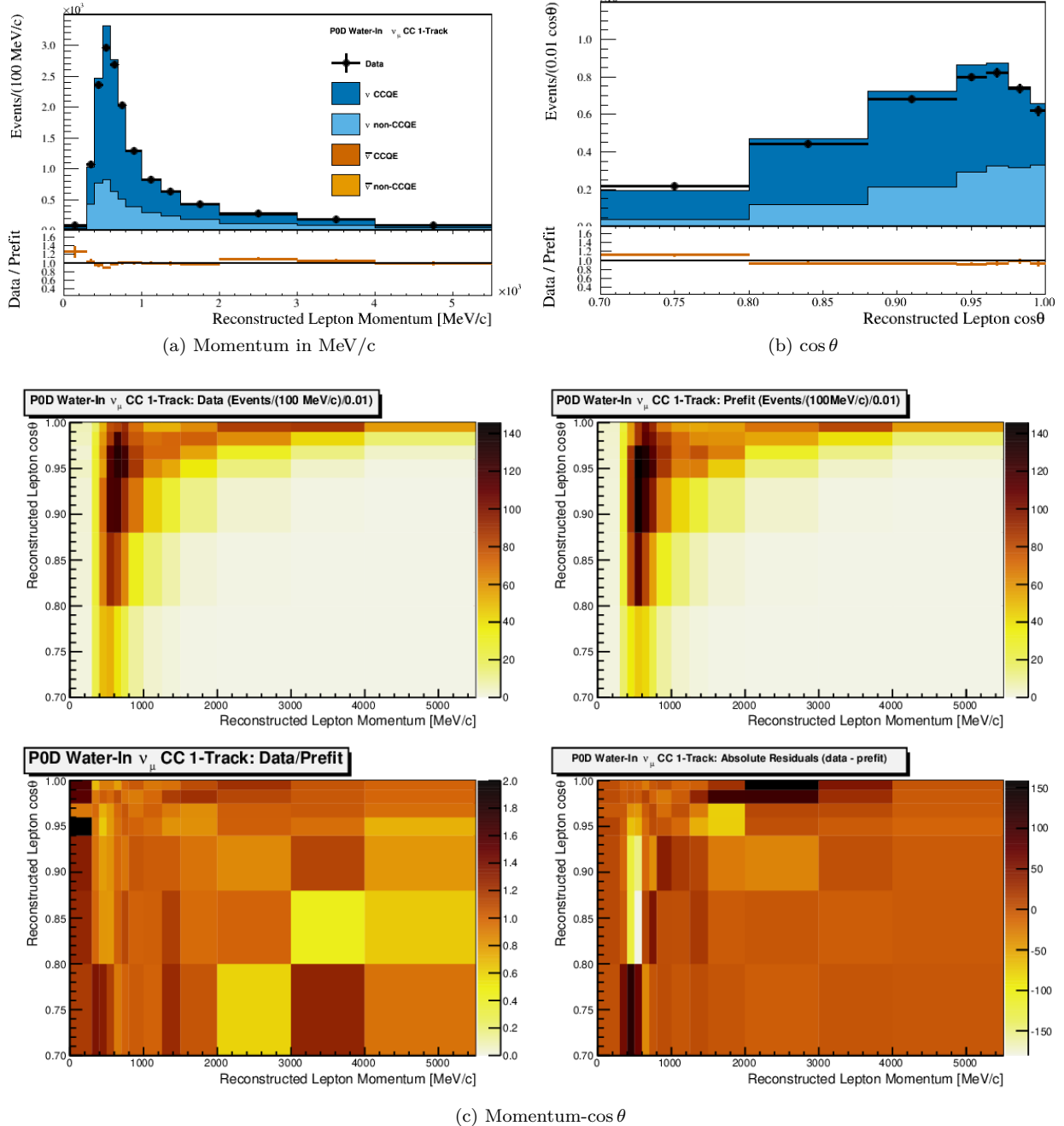


Figure 6.1: Data and prefit expectation for the PØD Water-In  $\nu_\mu$  in FHC Mode CC 1-Track sample. Sub-figure (a) shows the momentum one-dimensional profile in all but the highest momentum fit bin. Sub-figure (b) shows the  $\cos\theta$  one-dimensional profile in all but the highest angle fit bin. Shown in both (a) and (b) is the ratio between data and the prefit value. Sub-figure (c) shows a grid of two-dimensional data and prefit distributions in the same phase space as (a) and (b). Moving from top-left to bottom-right in (c) is the data, prefit, data to prefit ratio, and data to prefit difference.

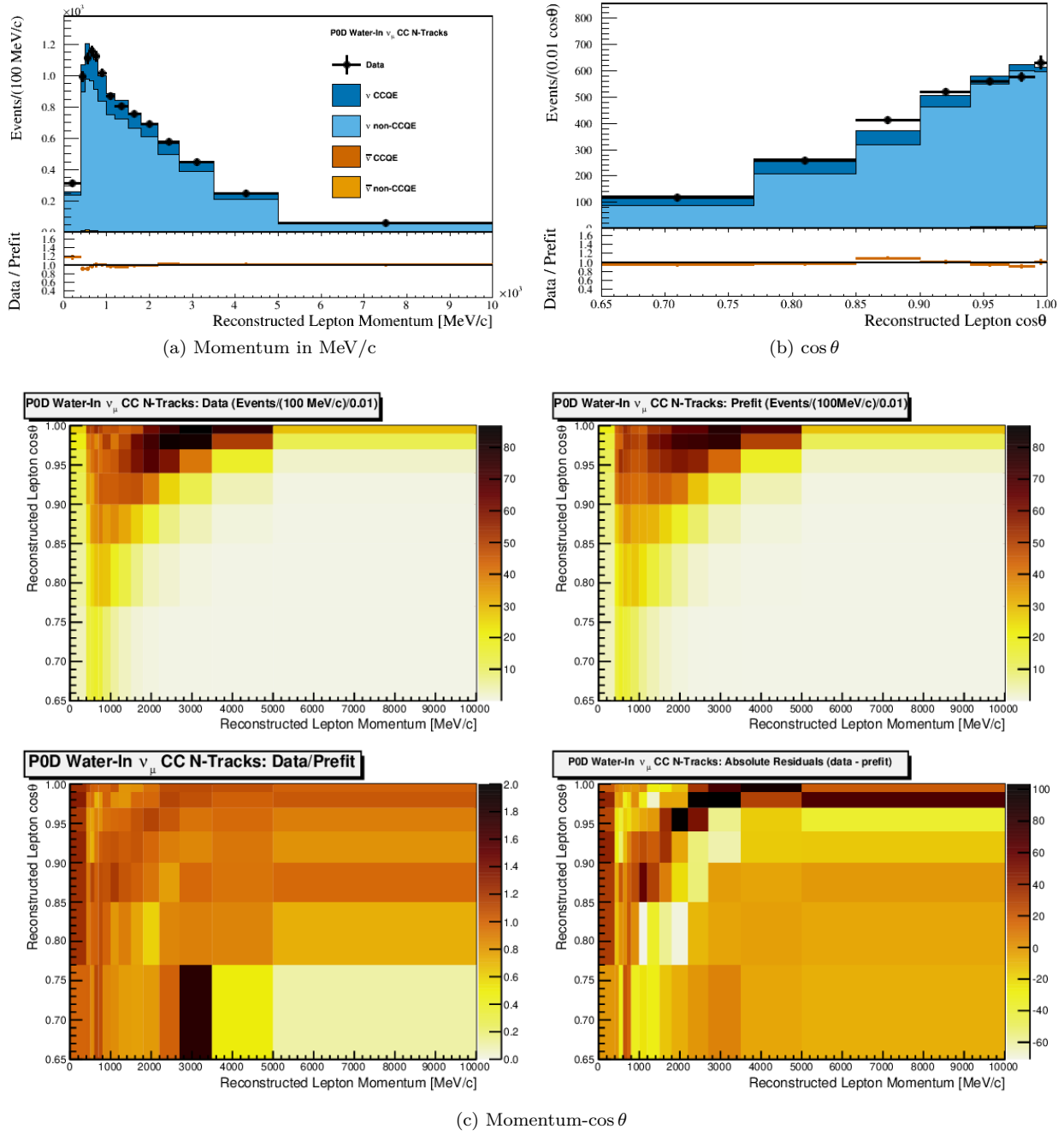


Figure 6.2: Data and prefit expectation for the PØD Water-In  $\nu_\mu$  in FHC Mode CC N-Tracks sample. Sub-figure (a) shows the momentum one-dimensional profile in all but the highest momentum fit bin. Sub-figure (b) shows the  $\cos\theta$  one-dimensional profile in all but the highest angle fit bin. Shown in both (a) and (b) is the ratio between data and the prefit value. Sub-figure (c) shows a grid of two-dimensional data and prefit distributions in the same phase space as (a) and (b). Moving from top-left to bottom-right in (c) is the data, prefit, data to prefit ratio, and data to prefit difference.

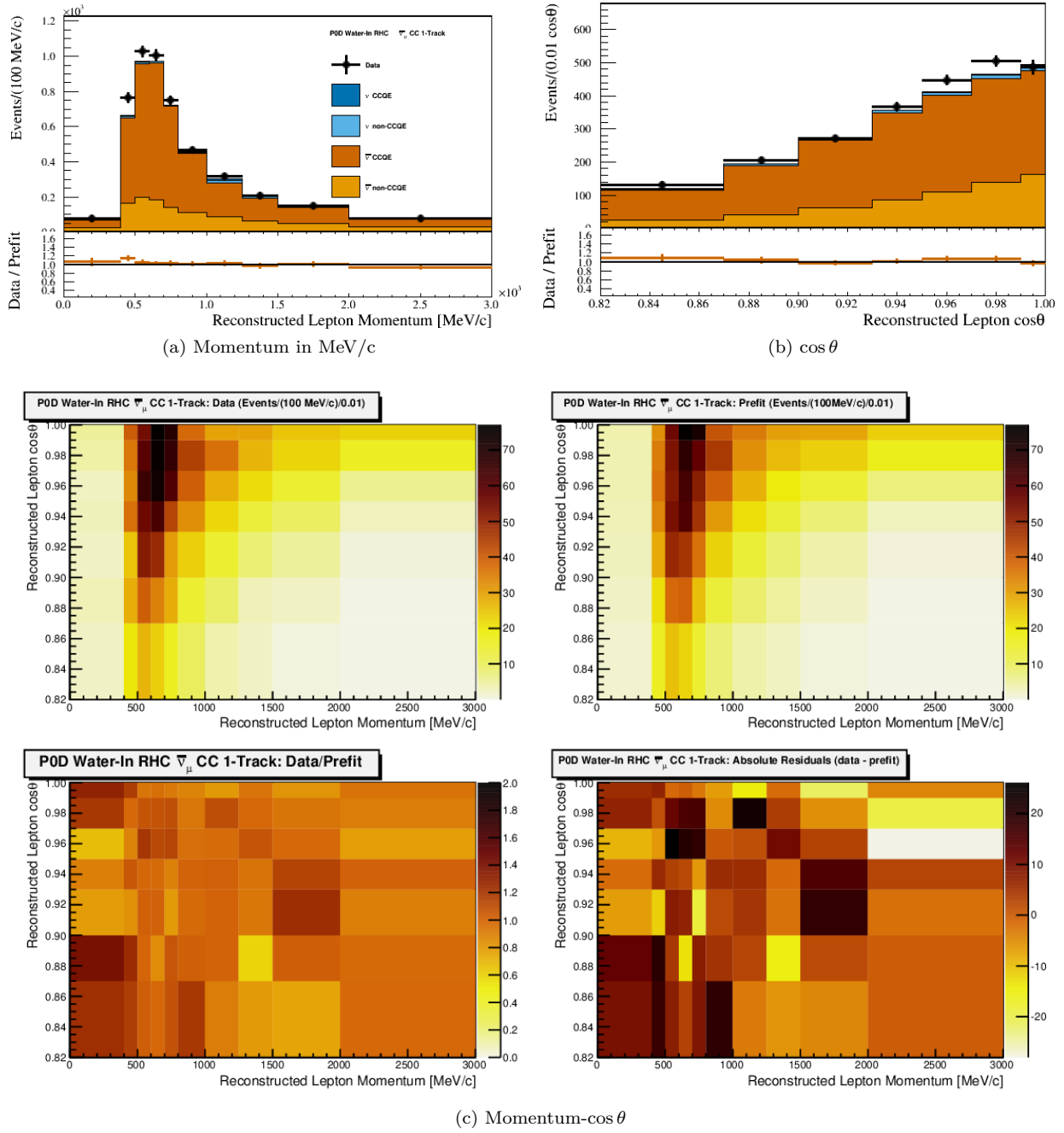


Figure 6.3: Data and prefit expectation for the PØD Water-In  $\bar{\nu}_\mu$  in RHC Mode CC 1-Track sample. Sub-figure (a) shows the momentum one-dimensional profile in all but the highest momentum fit bin. Sub-figure (b) shows the  $\cos\theta$  one-dimensional profile in all but the highest angle fit bin. Shown in both (a) and (b) is the ratio between data and the prefit value. Sub-figure (c) shows a grid of two-dimensional data and prefit distributions in the same phase space as (a) and (b). Moving from top-left to bottom-right in (c) is the data, prefit, data to prefit ratio, and data to prefit difference.

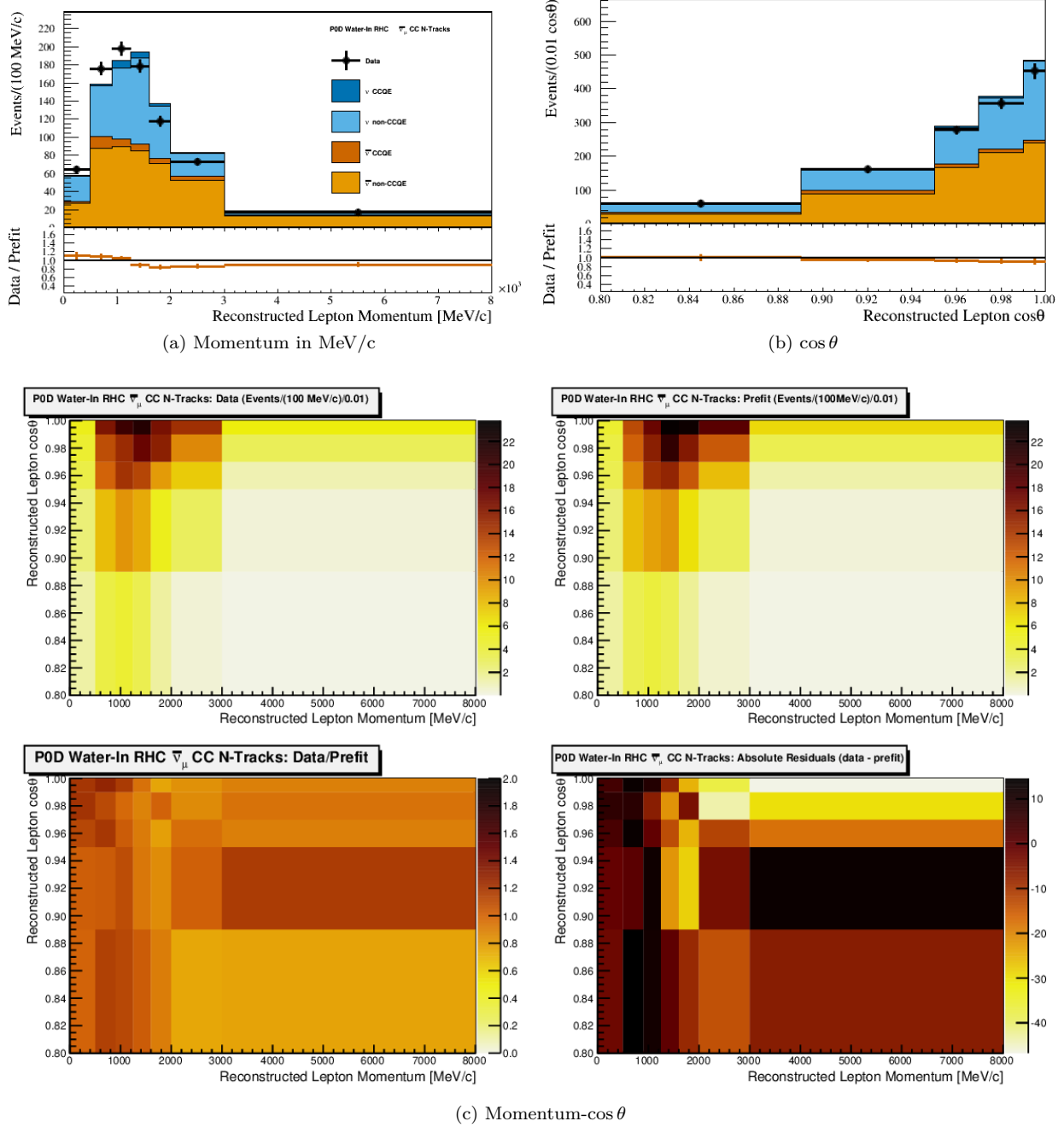


Figure 6.4: Data and prefit expectation for the PØD Water-In  $\bar{\nu}_\mu$  in RHC Mode CC N-Tracks sample. Sub-figure (a) shows the momentum one-dimensional profile in all but the highest momentum fit bin. Sub-figure (b) shows the  $\cos \theta$  one-dimensional profile in all but the highest angle fit bin. Shown in both (a) and (b) is the ratio between data and the prefit value. Sub-figure (c) shows a grid of two-dimensional data and prefit distributions in the same phase space as (a) and (b). Moving from top-left to bottom-right in (c) is the data, prefit, data to prefit ratio, and data to prefit difference.

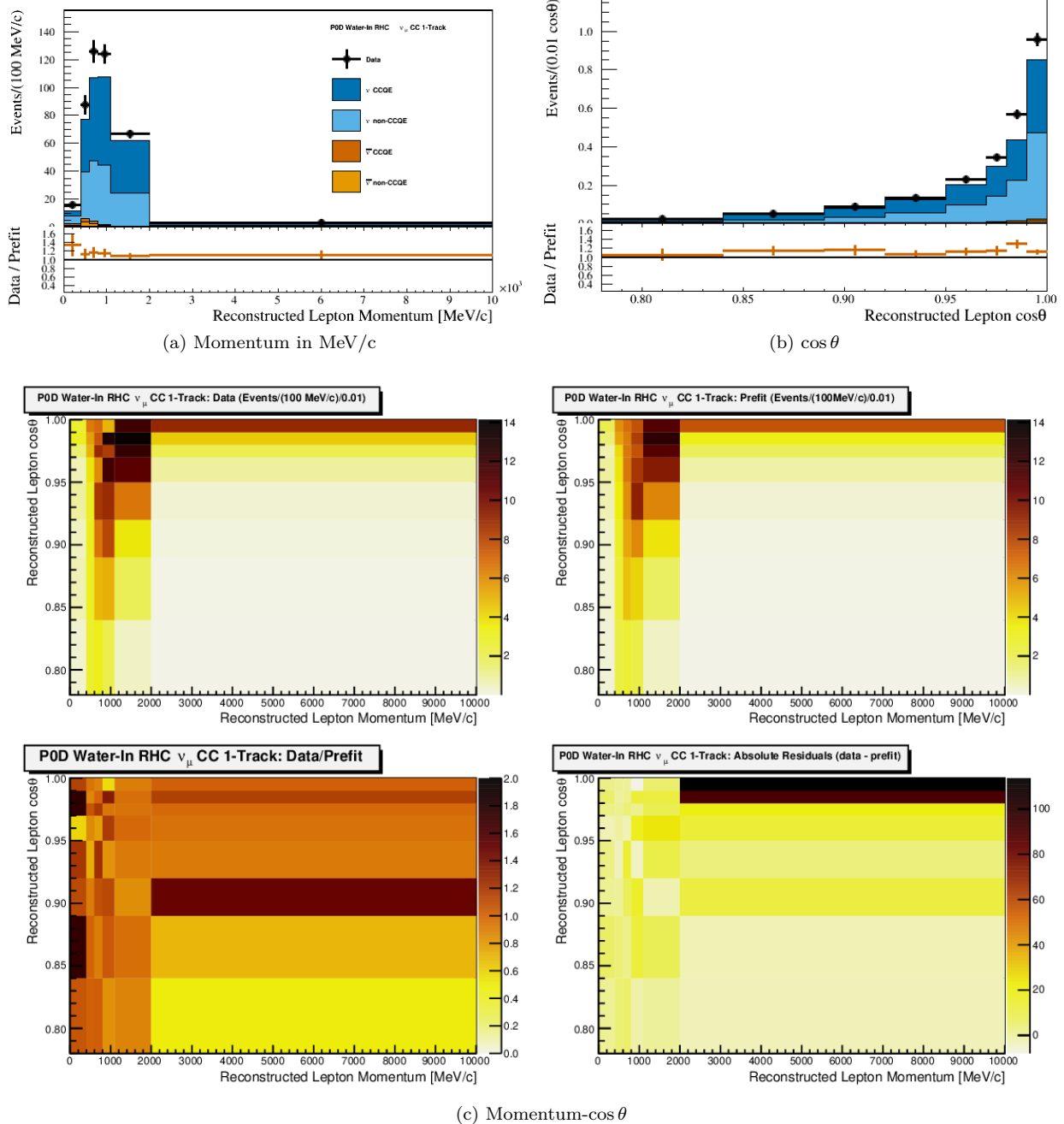


Figure 6.5: Data and prefit expectation for the PØD Water-In  $\nu_\mu$  in RHC Mode CC 1-Track sample. Sub-figure (a) shows the momentum one-dimensional profile in all but the highest momentum fit bin. Sub-figure (b) shows the  $\cos\theta$  one-dimensional profile in all but the highest angle fit bin. Shown in both (a) and (b) is the ratio between data and the prefit value. Sub-figure (c) shows a grid of two-dimensional data and prefit distributions in the same phase space as (a) and (b). Moving from top-left to bottom-right in (c) is the data, prefit, data to prefit ratio, and data to prefit difference.

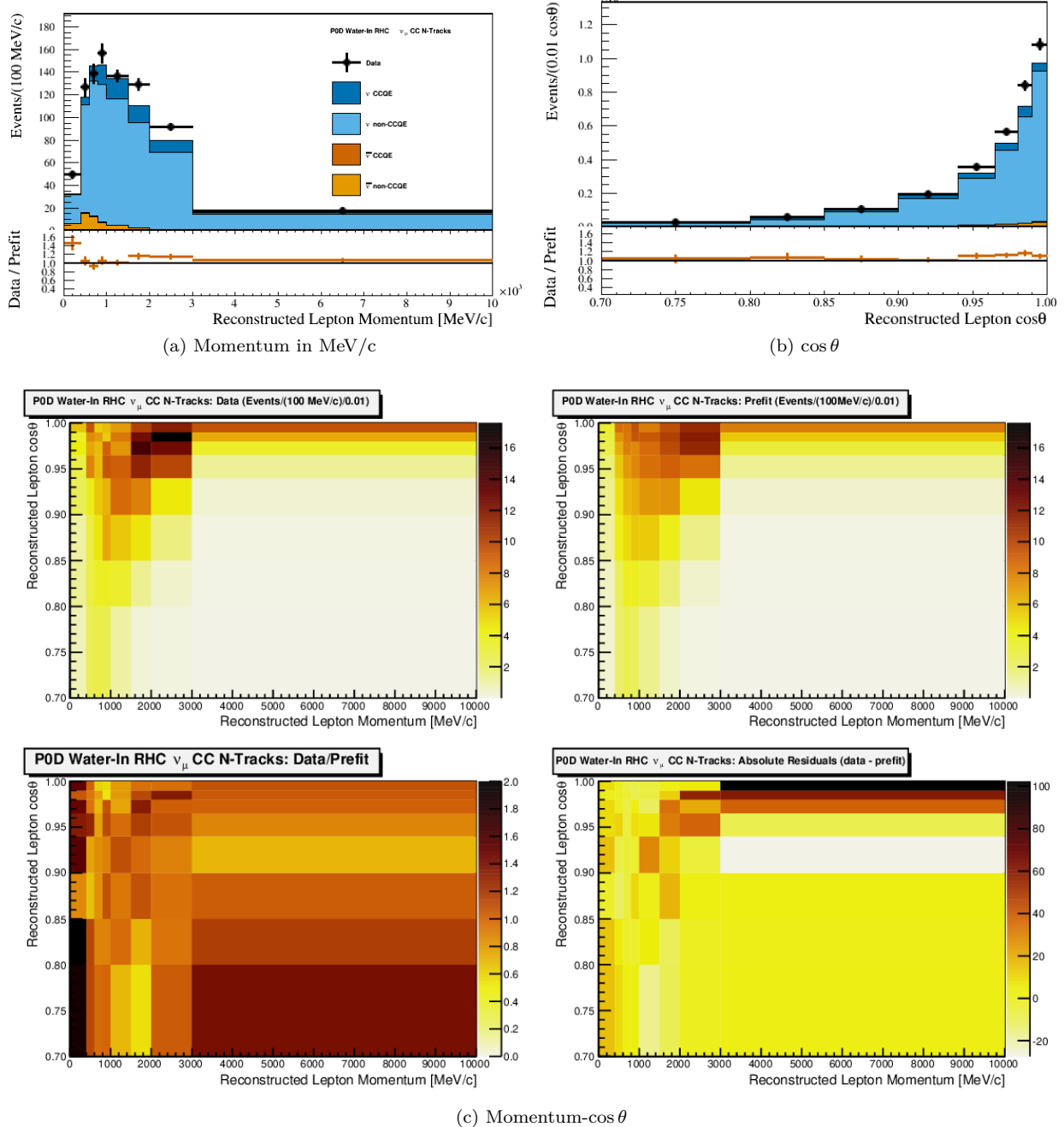


Figure 6.6: Data and prefit expectation for the PØD Water-In  $\nu_\mu$  in RHC Mode CC N-Tracks sample. Sub-figure (a) shows the momentum one-dimensional profile in all but the highest momentum fit bin. Sub-figure (b) shows the  $\cos\theta$  one-dimensional profile in all but the highest angle fit bin. Shown in both (a) and (b) is the ratio between data and the prefit value. Sub-figure (c) shows a grid of two-dimensional data and prefit distributions in the same phase space as (a) and (b). Moving from top-left to bottom-right in (c) is the data, prefit, data to prefit ratio, and data to prefit difference.

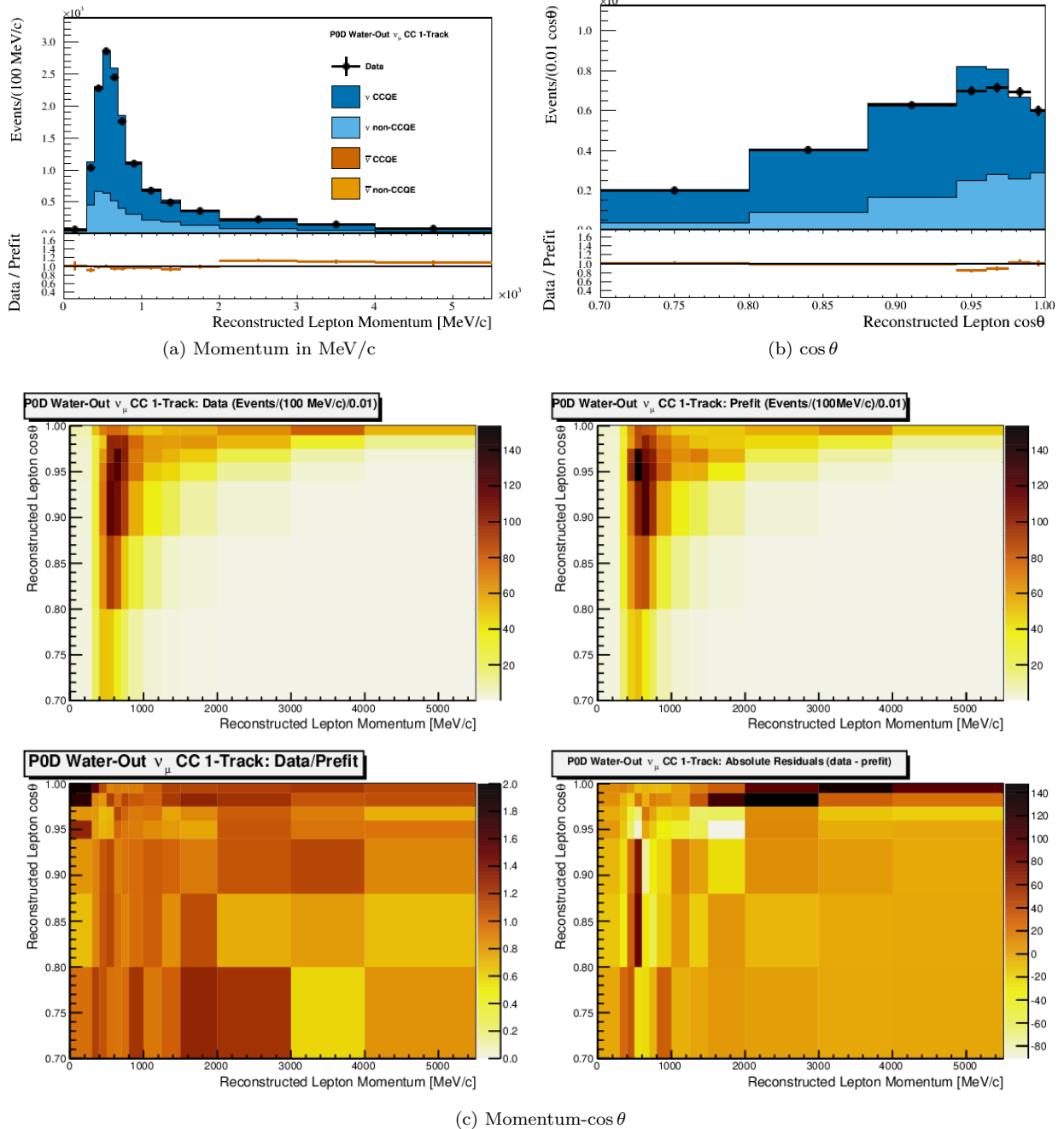


Figure 6.7: Data and prefit expectation for the PØD Water-Out  $\nu_\mu$  in FHC Mode CC 1-Track sample. Sub-figure (a) shows the momentum one-dimensional profile in all but the highest momentum fit bin. Sub-figure (b) shows the  $\cos\theta$  one-dimensional profile in all but the highest angle fit bin. Shown in both (a) and (b) is the ratio between data and the prefit value. Sub-figure (c) shows a grid of two-dimensional data and prefit distributions in the same phase space as (a) and (b). Moving from top-left to bottom-right in (c) is the data, prefit, data to prefit ratio, and data to prefit difference.

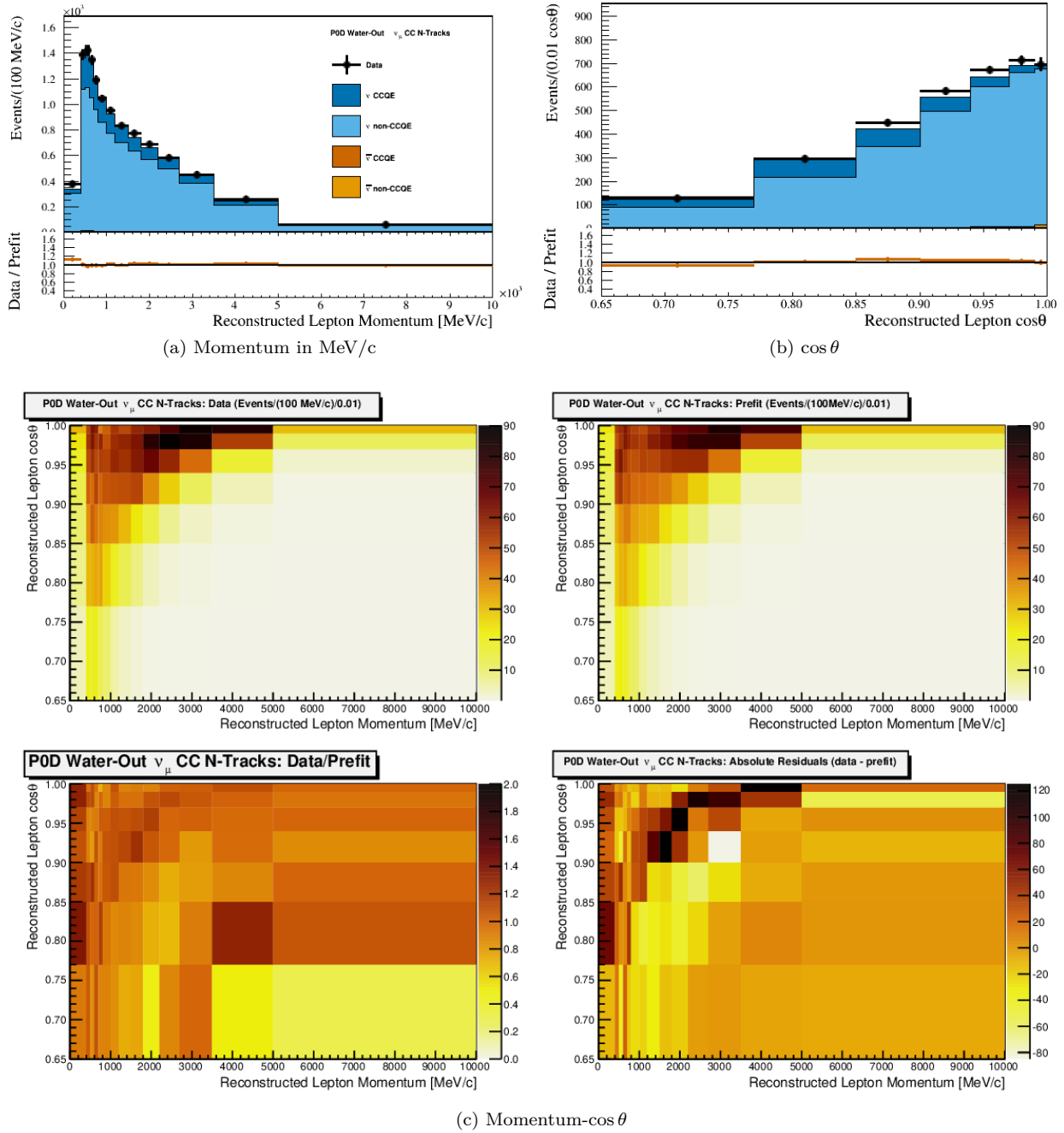


Figure 6.8: Data and prefit expectation for the PØD Water-Out  $\nu_\mu$  in FHC Mode CC N-Tracks sample. Sub-figure (a) shows the momentum one-dimensional profile in all but the highest momentum fit bin. Sub-figure (b) shows the  $\cos \theta$  one-dimensional profile in all but the highest angle fit bin. Shown in both (a) and (b) is the ratio between data and the prefit value. Sub-figure (c) shows a grid of two-dimensional data and prefit distributions in the same phase space as (a) and (b). Moving from top-left to bottom-right in (c) is the data, prefit, data to prefit ratio, and data to prefit difference.

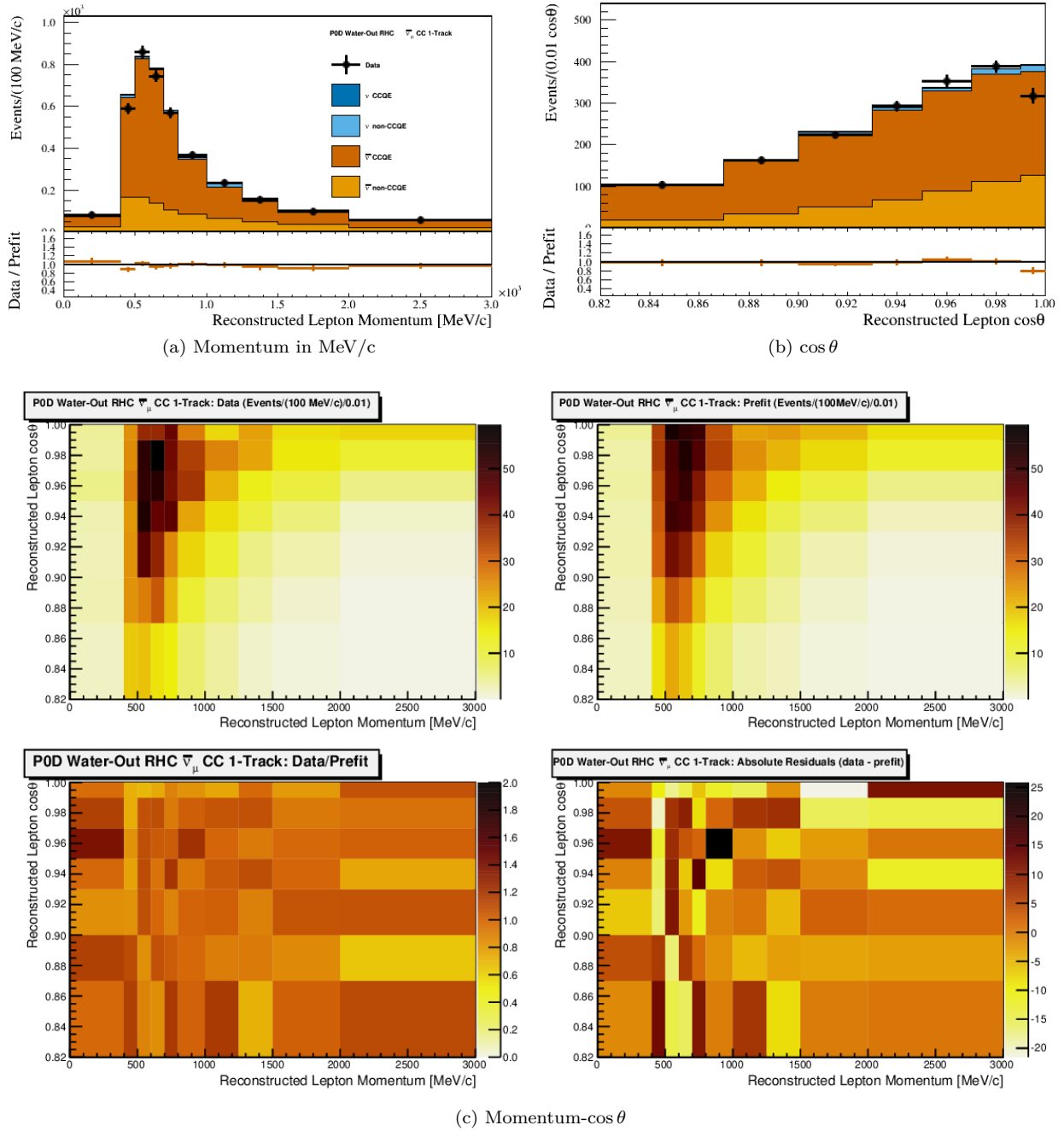


Figure 6.9: Data and prefit expectation for the PØD Water-Out  $\bar{\nu}_\mu$  in RHC Mode CC 1-Track sample. Sub-figure (a) shows the momentum one-dimensional profile in all but the highest momentum fit bin. Sub-figure (b) shows the  $\cos \theta$  one-dimensional profile in all but the highest angle fit bin. Shown in both (a) and (b) is the ratio between data and the prefit value. Sub-figure (c) shows a grid of two-dimensional data and prefit distributions in the same phase space as (a) and (b). Moving from top-left to bottom-right in (c) is the data, prefit, data to prefit ratio, and data to prefit difference.

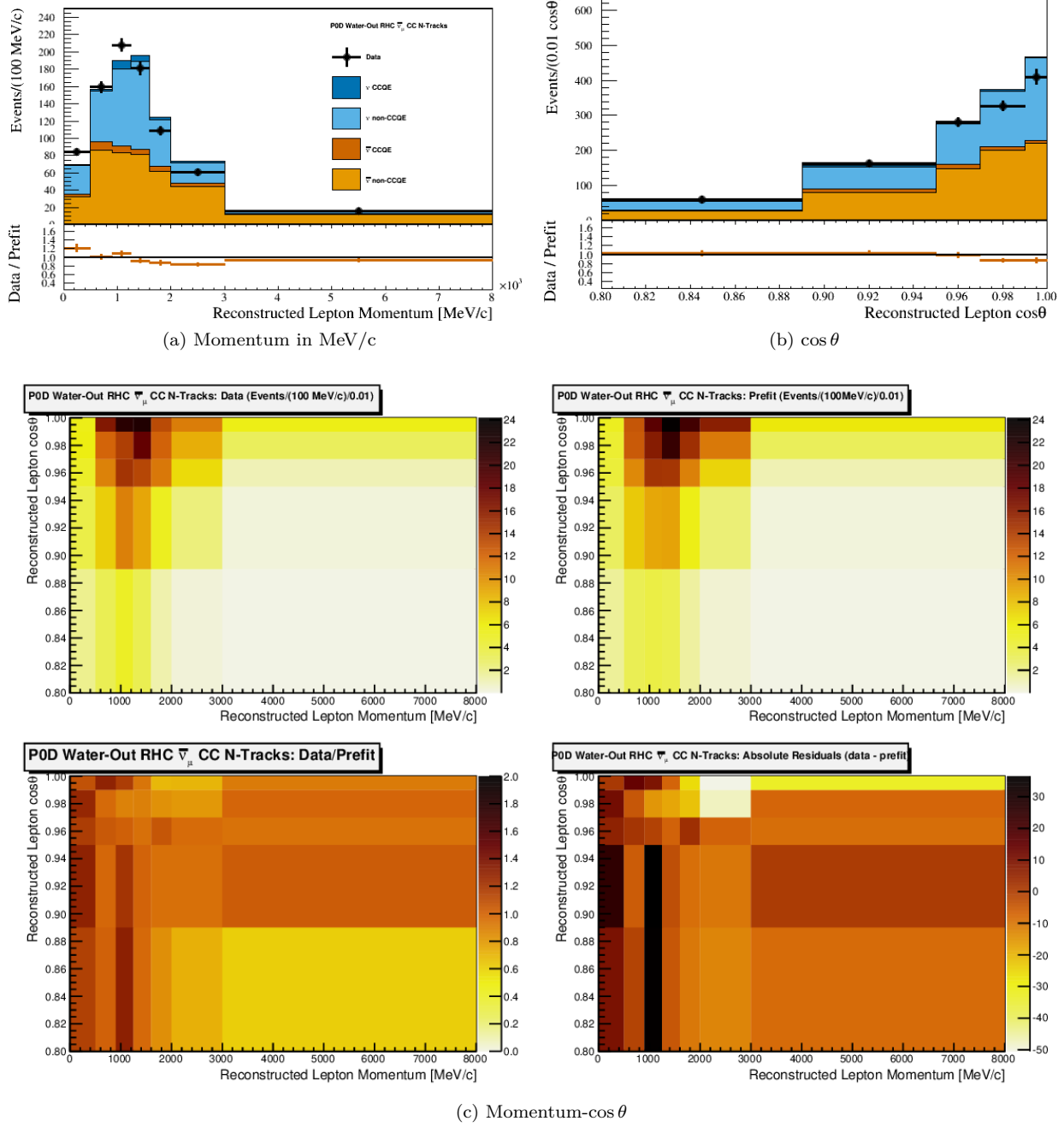


Figure 6.10: Data and prefit expectation for the PØD Water-Out  $\bar{\nu}_\mu$  in RHC Mode CC N-Tracks sample. Sub-figure (a) shows the momentum one-dimensional profile in all but the highest momentum fit bin. Sub-figure (b) shows the  $\cos \theta$  one-dimensional profile in all but the highest angle fit bin. Shown in both (a) and (b) is the ratio between data and the prefit value. Sub-figure (c) shows a grid of two-dimensional data and prefit distributions in the same phase space as (a) and (b). Moving from top-left to bottom-right in (c) is the data, prefit, data to prefit ratio, and data to prefit difference.

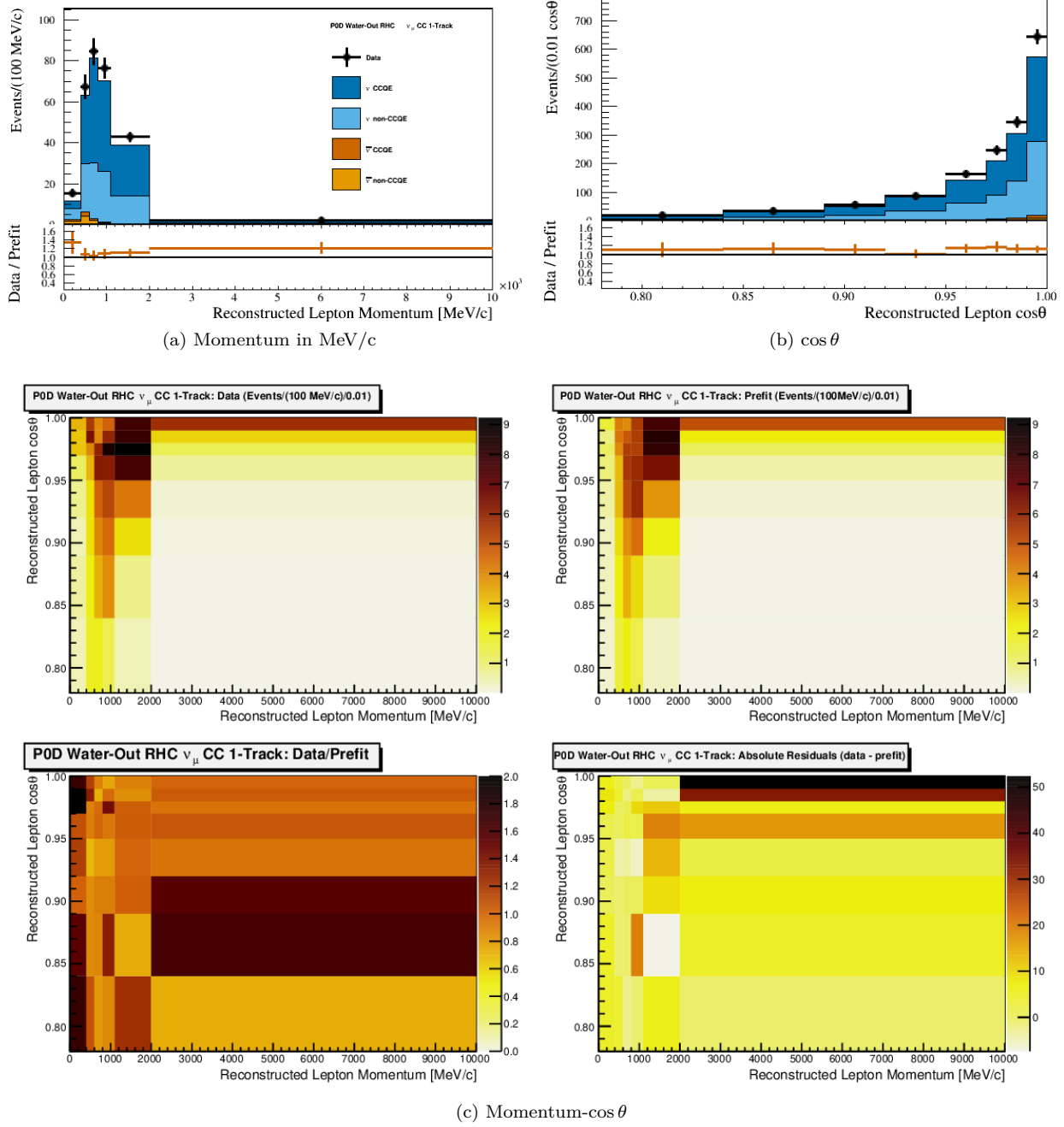


Figure 6.11: Data and prefit expectation for the PØD Water-Out  $\nu_\mu$  in RHC Mode CC 1-Track sample. Sub-figure (a) shows the momentum one-dimensional profile in all but the highest momentum fit bin. Sub-figure (b) shows the  $\cos \theta$  one-dimensional profile in all but the highest angle fit bin. Shown in both (a) and (b) is the ratio between data and the prefit value. Sub-figure (c) shows a grid of two-dimensional data and prefit distributions in the same phase space as (a) and (b). Moving from top-left to bottom-right in (c) is the data, prefit, data to prefit ratio, and data to prefit difference.

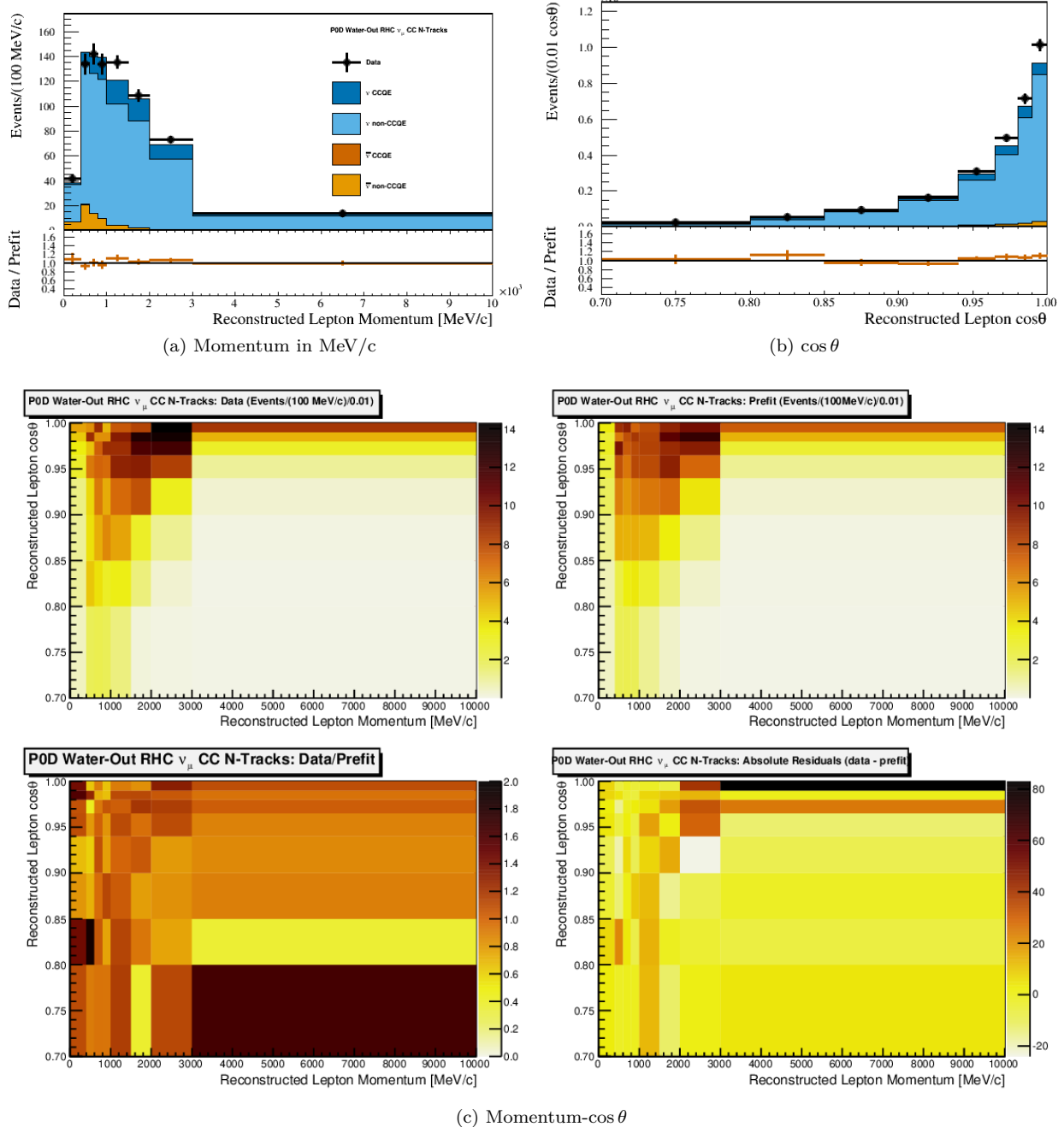


Figure 6.12: Data and prefit expectation for the PØD Water-Out  $\nu_\mu$  in RHC Mode CC N-Tracks sample. Sub-figure (a) shows the momentum one-dimensional profile in all but the highest momentum fit bin. Sub-figure (b) shows the  $\cos\theta$  one-dimensional profile in all but the highest angle fit bin. Shown in both (a) and (b) is the ratio between data and the prefit value. Sub-figure (c) shows a grid of two-dimensional data and prefit distributions in the same phase space as (a) and (b). Moving from top-left to bottom-right in (c) is the data, prefit, data to prefit ratio, and data to prefit difference.

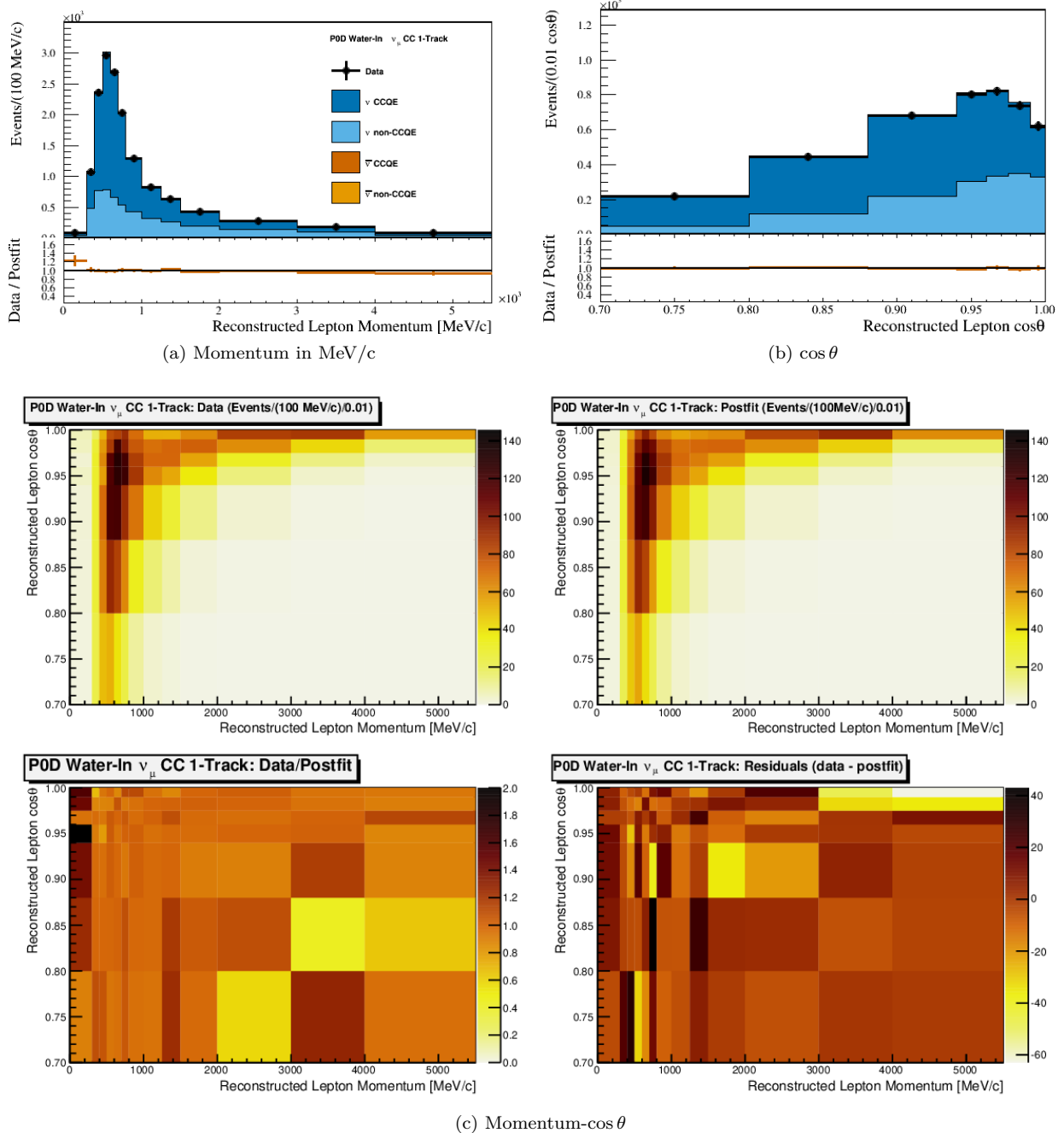


Figure 6.13: Data and postfit for the PØD Water-In  $\nu_\mu$  in FHC Mode CC 1-Track sample. Sub-figure (a) shows the momentum one-dimensional profile in all but the highest momentum fit bin. Sub-figure (b) shows the  $\cos \theta$  one-dimensional profile in all but the highest angle fit bin. Shown in both (a) and (b) is the ratio between data and the postfit value. Sub-figure (c) shows a grid of two-dimensional data and postfit distributions in the same phase space as (a) and (b). Moving from top-left to bottom-right in (c) is the data, postfit, data to postfit ratio, and data to postfit difference.

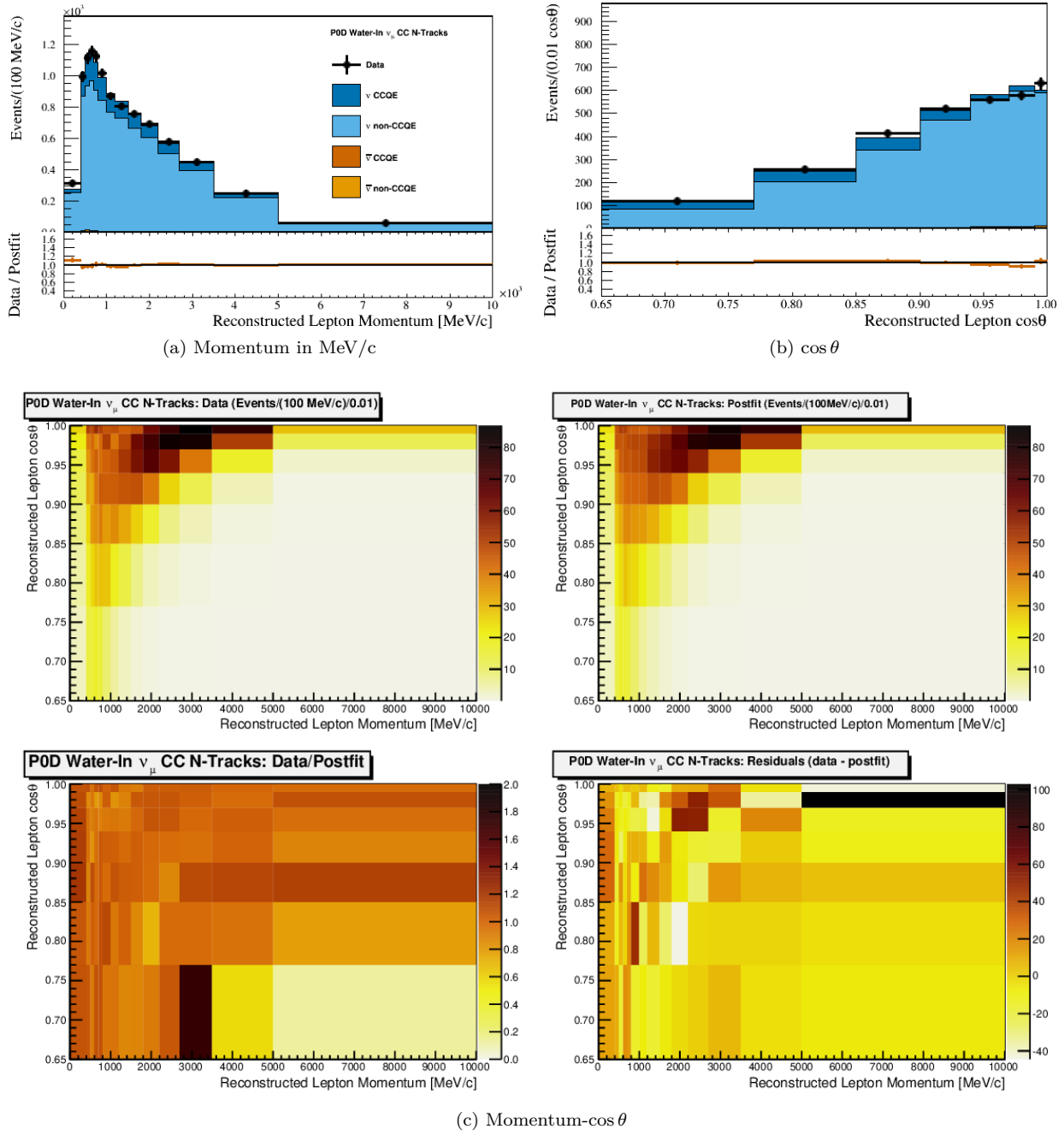


Figure 6.14: Data and postfit for the PØD Water-In  $\nu_\mu$  in FHC Mode CC 1-Track sample. Sub-figure (a) shows the momentum one-dimensional profile in all but the highest momentum fit bin. Sub-figure (b) shows the  $\cos \theta$  one-dimensional profile in all but the highest angle fit bin. Shown in both (a) and (b) is the ratio between data and the postfit value. Sub-figure (c) shows a grid of two-dimensional data and postfit distributions in the same phase space as (a) and (b). Moving from top-left to bottom-right in (c) is the data, postfit, data to postfit ratio, and data to postfit difference.

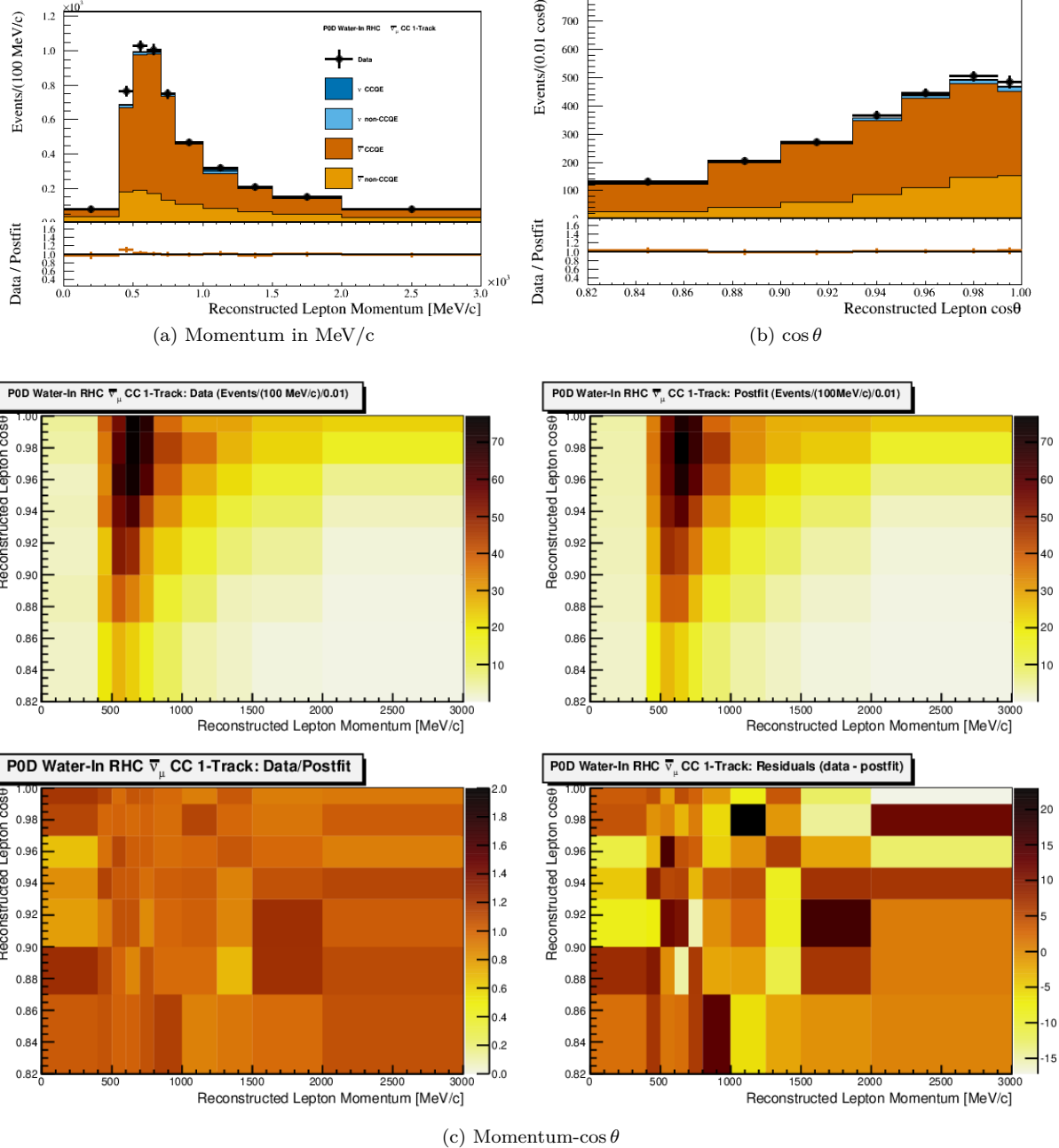


Figure 6.15: Data and postfit for the PØD Water-In  $\bar{\nu}_{\mu}$  in RHC Mode CC 1-Track sample. Sub-figure (a) shows the momentum one-dimensional profile in all but the highest momentum fit bin. Sub-figure (b) shows the  $\cos\theta$  one-dimensional profile in all but the highest angle fit bin. Shown in both (a) and (b) is the ratio between data and the postfit value. Sub-figure (c) shows a grid of two-dimensional data and postfit distributions in the same phase space as (a) and (b). Moving from top-left to bottom-right in (c) is the data, postfit, data to postfit ratio, and data to postfit difference.

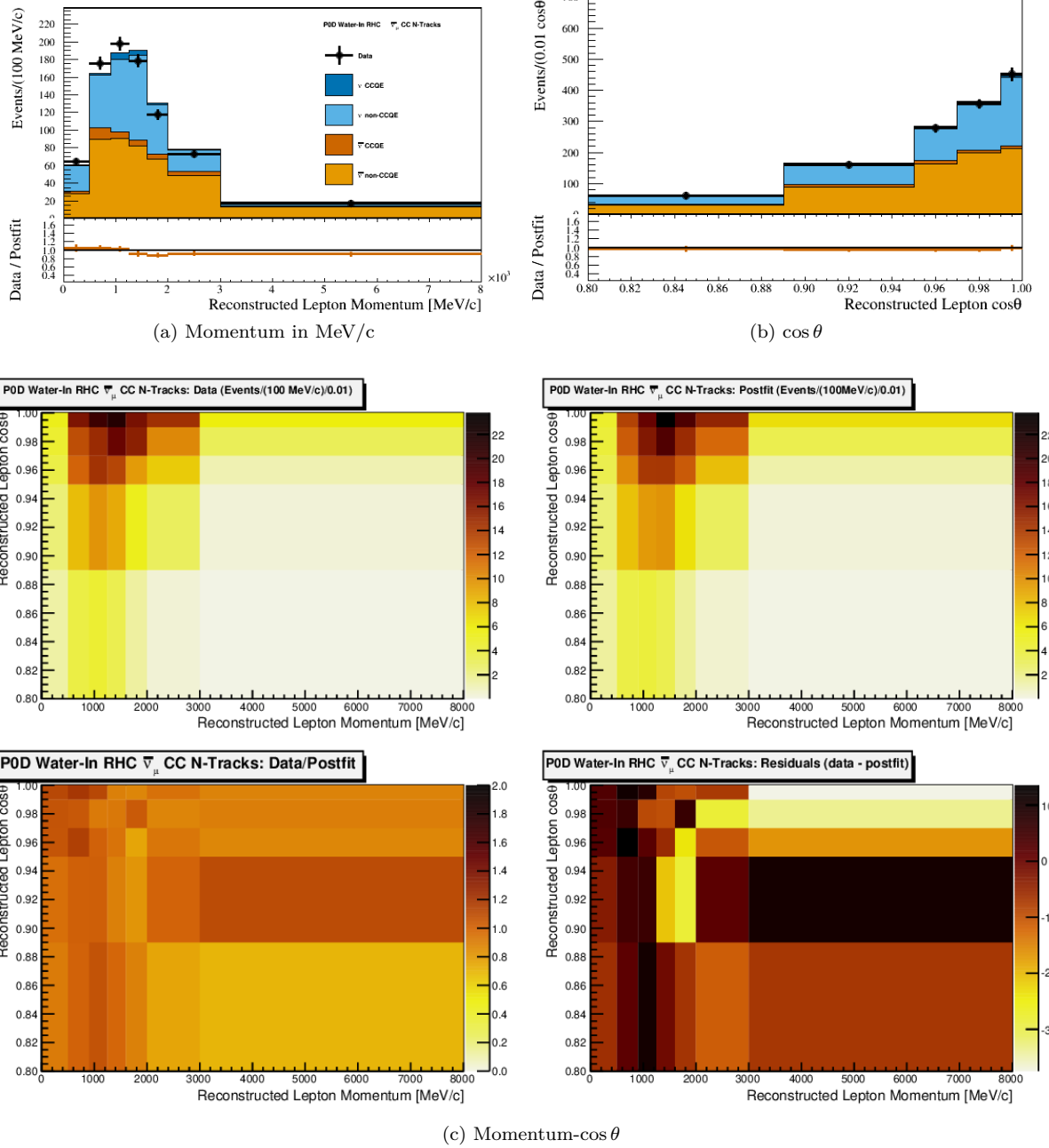


Figure 6.16: Data and postfit for the PØD Water-In  $\bar{\nu}_\mu$  in RHC Mode CC N-Tracks sample. Sub-figure (a) shows the momentum one-dimensional profile in all but the highest momentum fit bin. Sub-figure (b) shows the  $\cos \theta$  one-dimensional profile in all but the highest angle fit bin. Shown in both (a) and (b) is the ratio between data and the postfit value. Sub-figure (c) shows a grid of two-dimensional data and postfit distributions in the same phase space as (a) and (b). Moving from top-left to bottom-right in (c) is the data, postfit, data to postfit ratio, and data to postfit difference.

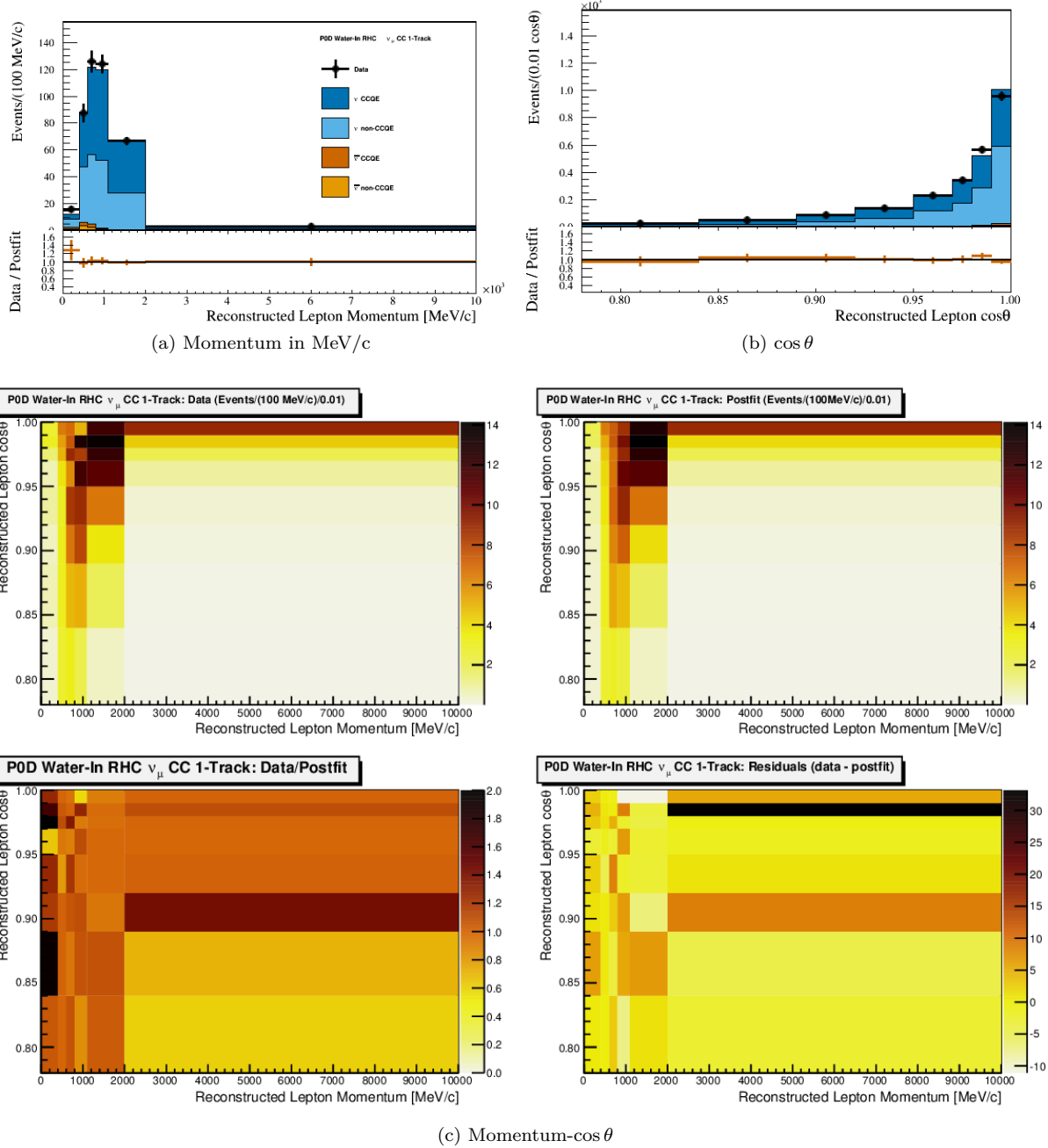


Figure 6.17: Data and postfit for the PØD Water-In  $\nu_\mu$  in RHC Mode CC 1-Track sample. Sub-figure (a) shows the momentum one-dimensional profile in all but the highest momentum fit bin. Sub-figure (b) shows the  $\cos \theta$  one-dimensional profile in all but the highest angle fit bin. Shown in both (a) and (b) is the ratio between data and the postfit value. Sub-figure (c) shows a grid of two-dimensional data and postfit distributions in the same phase space as (a) and (b). Moving from top-left to bottom-right in (c) is the data, postfit, data to postfit ratio, and data to postfit difference.

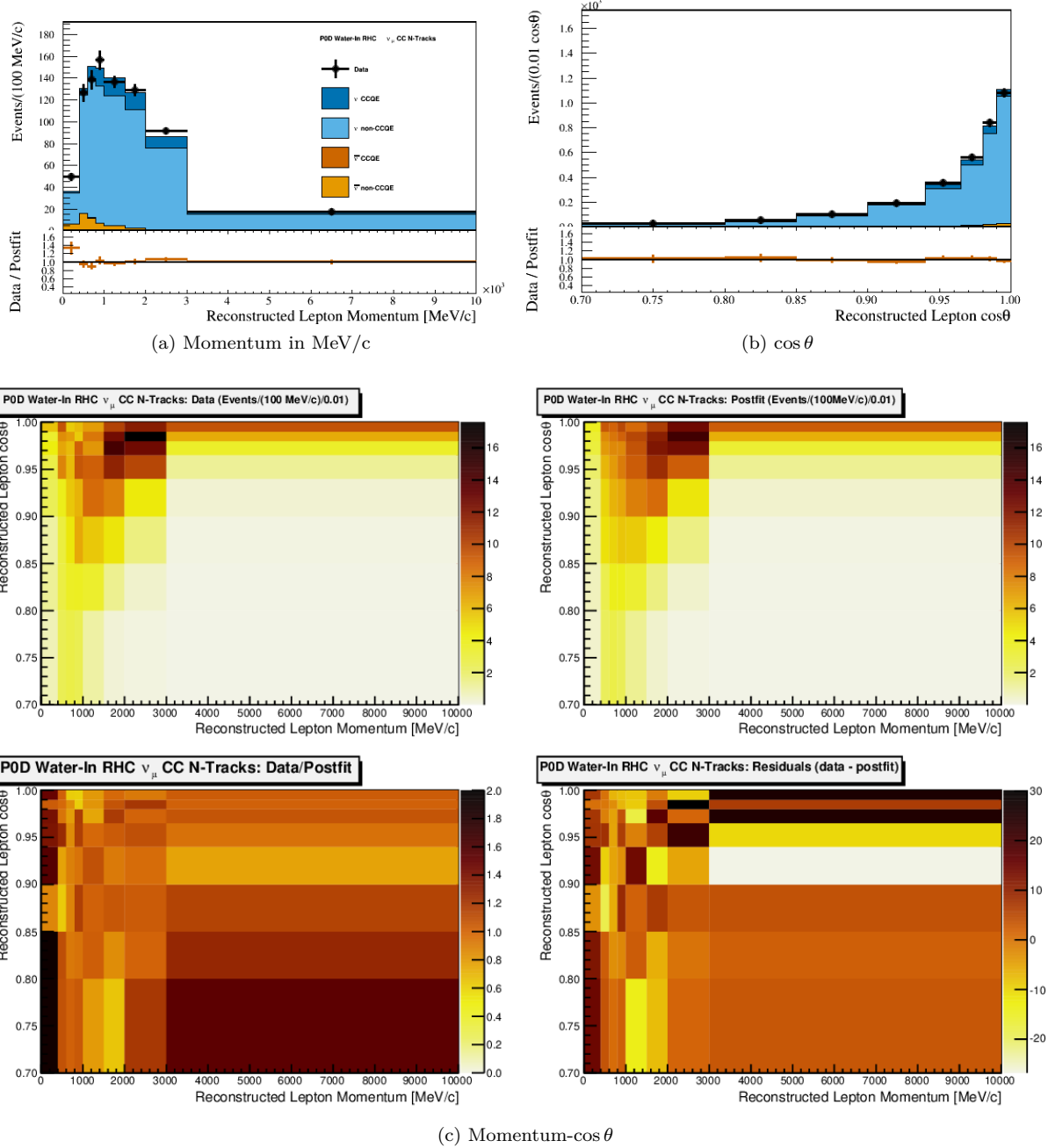


Figure 6.18: Data and postfit for the PØD Water-In  $\nu_\mu$  in RHC Mode CC N-Tracks sample. Sub-figure (a) shows the momentum one-dimensional profile in all but the highest momentum fit bin. Sub-figure (b) shows the  $\cos\theta$  one-dimensional profile in all but the highest angle fit bin. Shown in both (a) and (b) is the ratio between data and the postfit value. Sub-figure (c) shows a grid of two-dimensional data and postfit distributions in the same phase space as (a) and (b). Moving from top-left to bottom-right in (c) is the data, postfit, data to postfit ratio, and data to postfit difference.

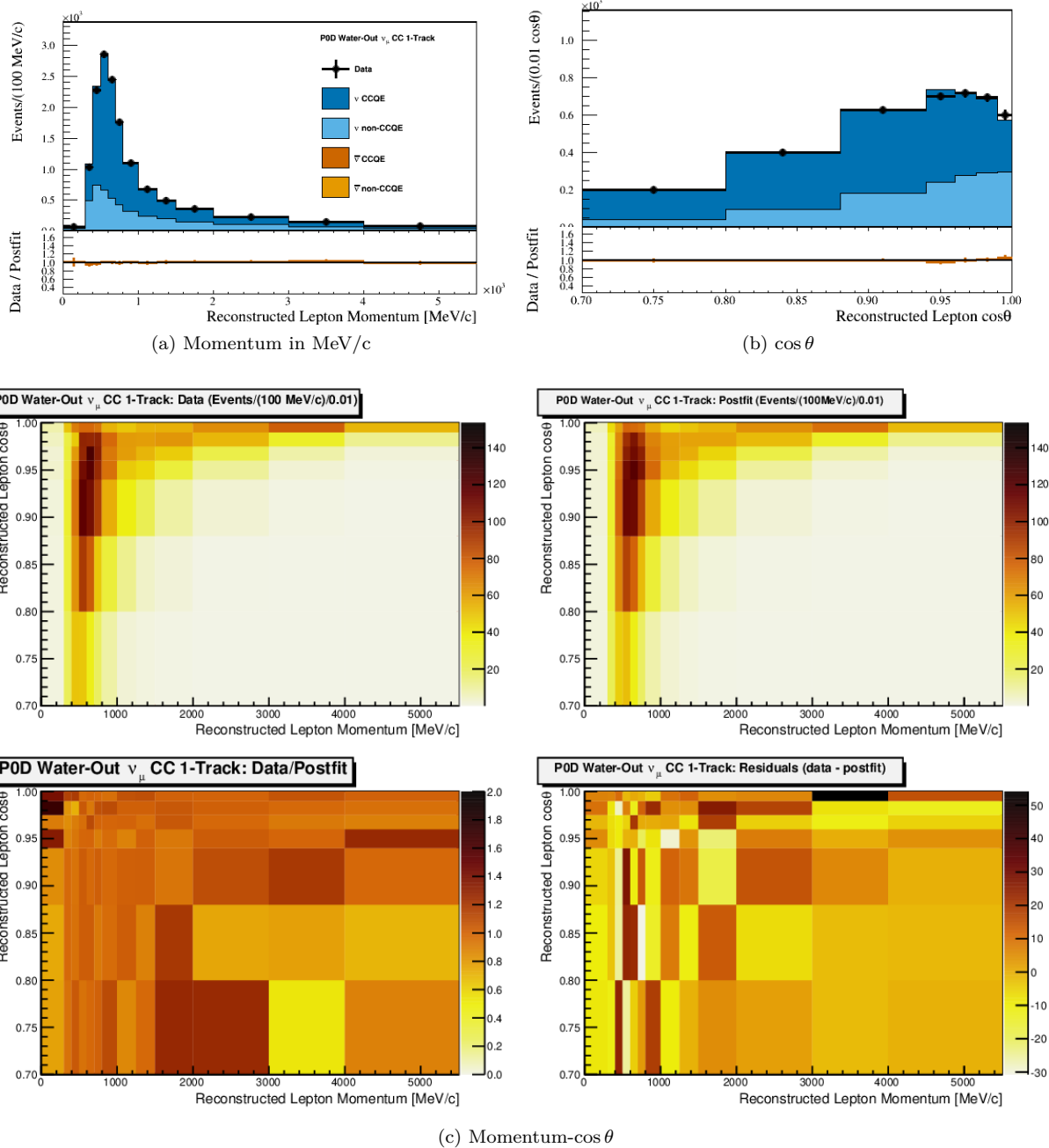


Figure 6.19: Data and postfit for the PØD Water-Out  $\nu_\mu$  in FHC Mode CC 1-Track sample. Sub-figure (a) shows the momentum one-dimensional profile in all but the highest momentum fit bin. Sub-figure (b) shows the  $\cos \theta$  one-dimensional profile in all but the highest angle fit bin. Shown in both (a) and (b) is the ratio between data and the postfit value. Sub-figure (c) shows a grid of two-dimensional data and postfit distributions in the same phase space as (a) and (b). Moving from top-left to bottom-right in (c) is the data, postfit, data to postfit ratio, and data to postfit difference.

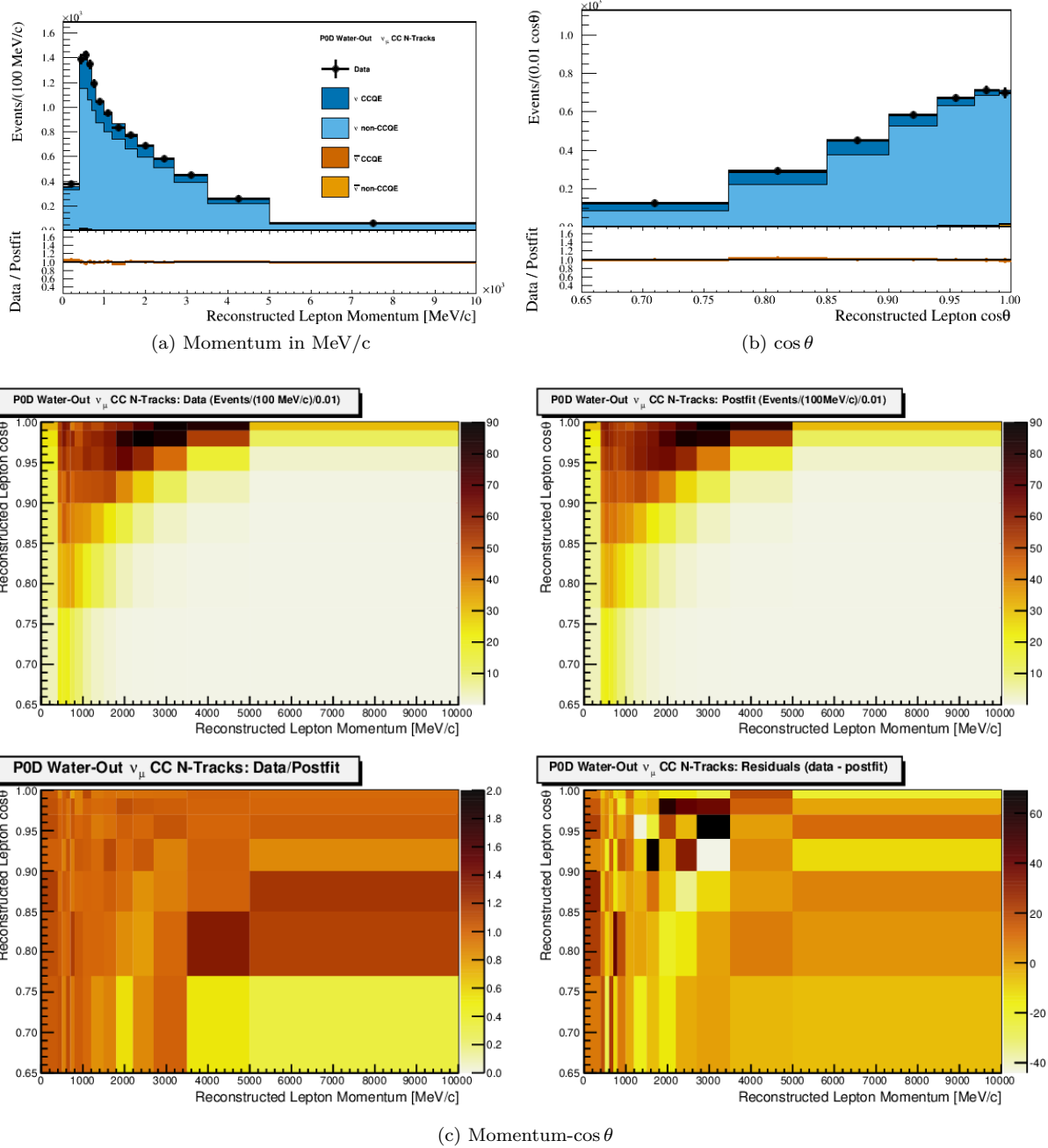


Figure 6.20: Data and postfit for the PØD Water-Out  $\nu_\mu$  in FHC Mode CC N-Tracks sample. Sub-figure (a) shows the momentum one-dimensional profile in all but the highest momentum fit bin. Sub-figure (b) shows the  $\cos \theta$  one-dimensional profile in all but the highest angle fit bin. Shown in both (a) and (b) is the ratio between data and the postfit value. Sub-figure (c) shows a grid of two-dimensional data and postfit distributions in the same phase space as (a) and (b). Moving from top-left to bottom-right in (c) is the data, postfit, data to postfit ratio, and data to postfit difference.

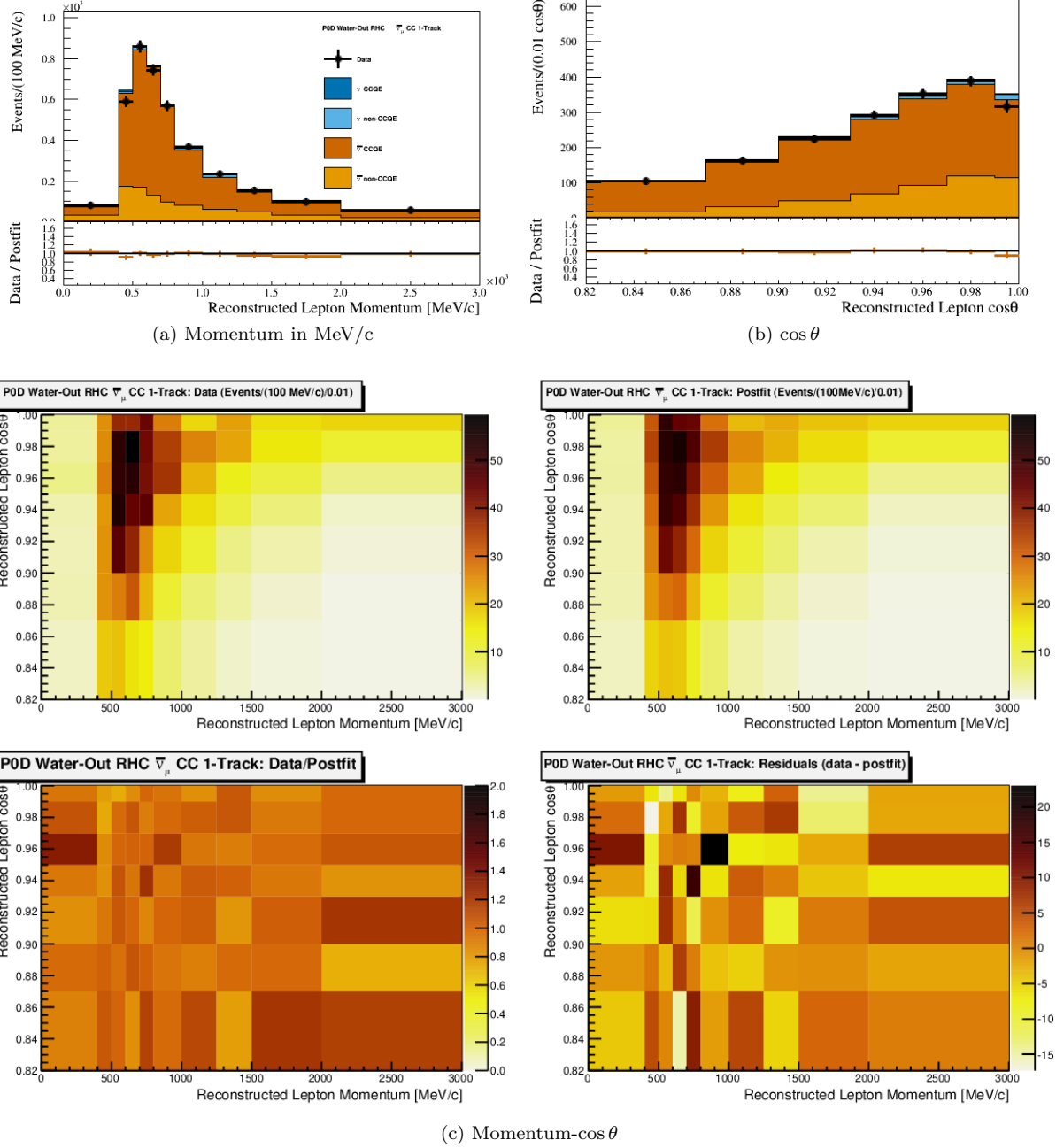


Figure 6.21: Data and postfit for the PØD Water-Out  $\bar{\nu}_\mu$  in RHC Mode CC 1-Track sample. Sub-figure (a) shows the momentum one-dimensional profile in all but the highest momentum fit bin. Sub-figure (b) shows the  $\cos \theta$  one-dimensional profile in all but the highest angle fit bin. Shown in both (a) and (b) is the ratio between data and the postfit value. Sub-figure (c) shows a grid of two-dimensional data and postfit distributions in the same phase space as (a) and (b). Moving from top-left to bottom-right in (c) is the data, postfit, data to postfit ratio, and data to postfit difference.

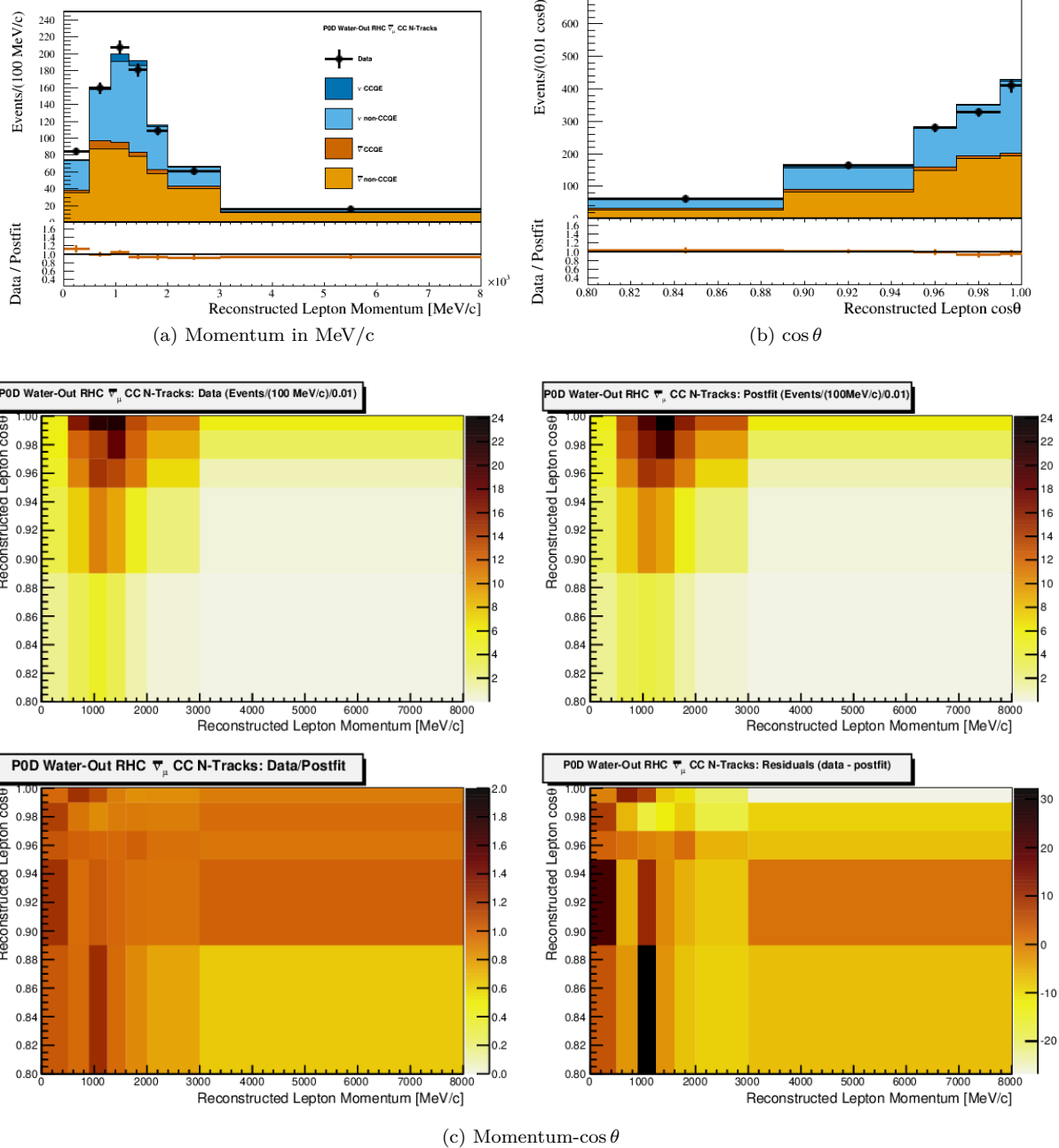


Figure 6.22: Data and postfit for the PØD Water-Out  $\bar{\nu}_\mu$  in RHC Mode CC N-Tracks sample. Sub-figure (a) shows the momentum one-dimensional profile in all but the highest momentum fit bin. Sub-figure (b) shows the  $\cos \theta$  one-dimensional profile in all but the highest angle fit bin. Shown in both (a) and (b) is the ratio between data and the postfit value. Sub-figure (c) shows a grid of two-dimensional data and postfit distributions in the same phase space as (a) and (b). Moving from top-left to bottom-right in (c) is the data, postfit, data to postfit ratio, and data to postfit difference.

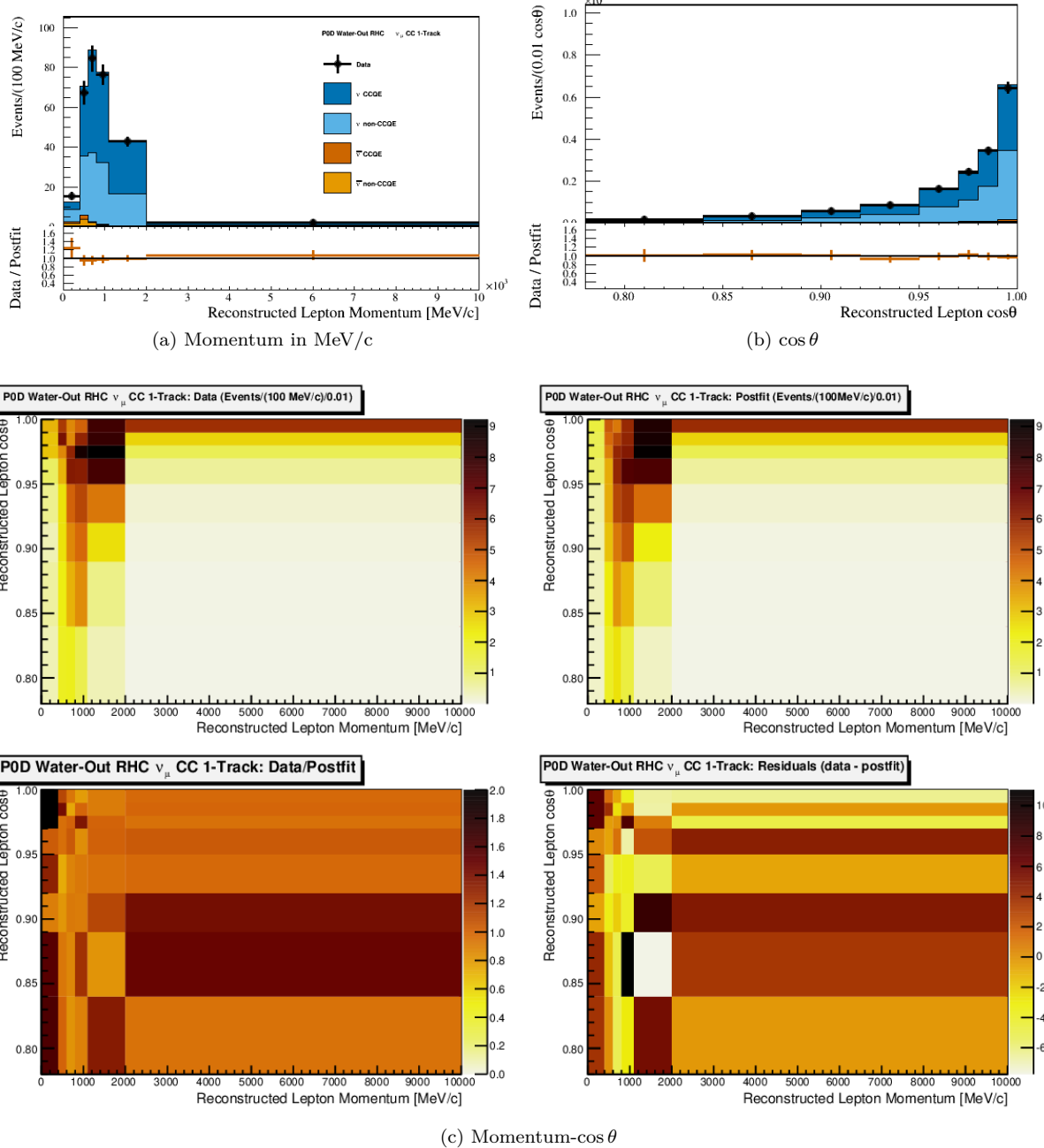


Figure 6.23: Data and postfit for the PØD Water-Out  $\nu_{\mu}$  in RHC Mode CC 1-Track sample. Sub-figure (a) shows the momentum one-dimensional profile in all but the highest momentum fit bin. Sub-figure (b) shows the  $\cos\theta$  one-dimensional profile in all but the highest angle fit bin. Shown in both (a) and (b) is the ratio between data and the postfit value. Sub-figure (c) shows a grid of two-dimensional data and postfit distributions in the same phase space as (a) and (b). Moving from top-left to bottom-right in (c) is the data, postfit, data to postfit ratio, and data to postfit difference.

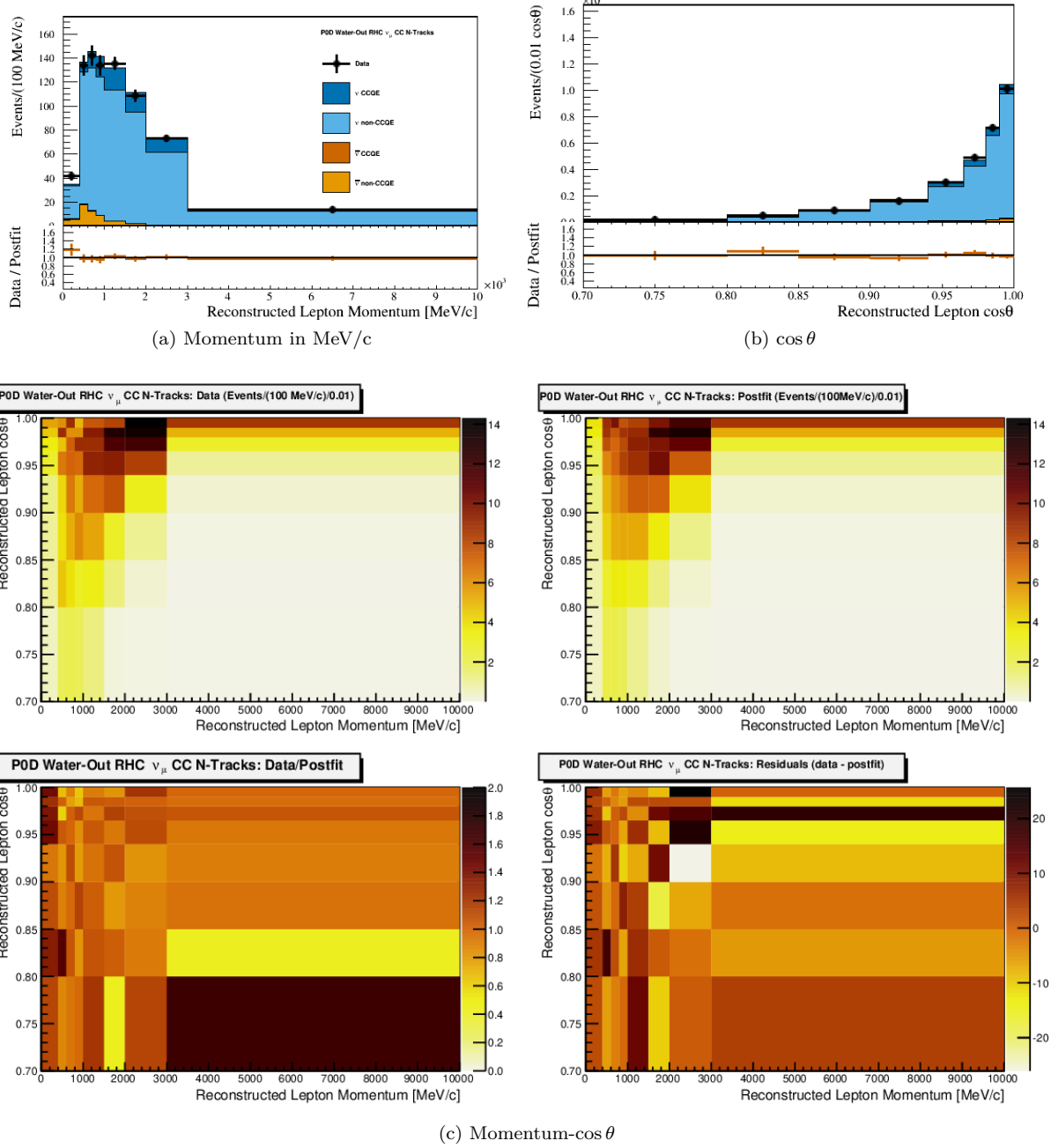


Figure 6.24: Data and postfit for the PØD Water-Out  $\nu_\mu$  in RHC Mode CC N-Tracks sample. Sub-figure (a) shows the momentum one-dimensional profile in all but the highest momentum fit bin. Sub-figure (b) shows the  $\cos \theta$  one-dimensional profile in all but the highest angle fit bin. Shown in both (a) and (b) is the ratio between data and the postfit value. Sub-figure (c) shows a grid of two-dimensional data and postfit distributions in the same phase space as (a) and (b). Moving from top-left to bottom-right in (c) is the data, postfit, data to postfit ratio, and data to postfit difference.

1256 Now that we have examined the postfit samples and seen that the prediction has indeed changed, we can  
1257 proceed to look at the parameter values.

1258 **6.2.2 Parameter Value and Correlation Comparisons**

1259 The postfit parameters from the PØD-only BANFF fit are shown in Figure 6.25 on page 128 through Figure  
1260 6.28 on page 131. A complete listing of the prefit and postfit values is given in Appendix G. Additionally, a  
1261 comparison is made between the PØD-only results with that of the FGD-only results. It must be stated that  
1262 while the PØD-only and FGD-only fits are using the same 2017 canonical cross section parameterization,  
1263 the analyses had different POT exposures. This PØD-only analysis fit uses run periods 2 – 8, or about  
1264  $11.5 \times 10^{20}$  ( $6.23 \times 10^{20}$ ) POT in FHC (RHC) mode. The FGD-only fit uses runs 2 – 6, or about  $5.81 \times 10^{20}$   
1265 ( $2.84 \times 10^{20}$ ) POT in FHC (RHC) modes. So the PØD-only fit has an additional statistical advantage. This  
1266 does not affect the actual fitting procedure since the POT weights scale the MC prediction to the data.

1267 In order to understand how the two analyses compare to each other in terms of sensitivity to the flux  
1268 and cross section parameters, we need to examine each detector’s integrated mass-luminosity. The number  
1269 of incident neutrinos crossing either the FGD or PØD detector is the product of its respective fiducial mass  
1270 and POT exposure. While the PØD has much more mass, the water-in and water-out modes are mutually  
1271 exclusive, resulting in a reduced aggregate POT exposure as compared to each static FGD for each water-in  
1272 and water-out running periods. Also since the FGD2 has a larger water mass fraction compared to the PØD  
1273 water-in mode, the expected number of neutrino-oxygen interaction events are very similar. The comparative  
1274 advantage of the PØD-only data lies in the number of neutrino-carbon events, which is about 10 times greater  
1275 than the FGD. These numbers and more are tabulated in Table 6.1 on page 125.

Table 6.1: Neutrino-nucleon exposure on target elements in the PØD-only and FGD-only analyses. The FGD1 and FGD2 masses were calculated using the following sources[46, 47, 48]. The PØD mass was taken from the following source[49]. The other mass elements include hydrogen, copper, and heavier elements.

Detector	(kg)	Fiducial volume mass			POT ( $10^{20}$ )		kg POT ( $10^{24}$ )	PØD-to-FGD (kg POT)		
		$^{12}\text{C}$ (%)	$^{16}\text{O}$ (%)	other (%)	FHC	RHC		$^{12}\text{C}$	$^{16}\text{O}$	other
PØD Water-out	3570	70	0.67	19.33	7.872	-	2.81	3.99	-	9.21
	FGD1	985	86	3.7	5.81	-	0.572			
PØD Water-In	5470	45	30	25	3.657	-	2.00	10.63	1.43	8.05
	FGD2	972	15	74	5.81	-	0.565			
PØD Water-out	3570	70	0.67	19.33	-	3.382	1.207	3.513	-	8.10
	FGD1	985	86	3.7	-	2.84	0.280			
PØD Water-In	5470	45	30	25	-	2.852	1.56	16.9	2.29	12.8
	FGD2	972	15	74	-	2.84	0.276			

1276 There is good agreement between the PØD-only and FGD-only BANFF flux parameter values. The flux  
1277 parameters in both fits follow the same shape trends, but with the PØD-only fit parameters having a higher  
1278 expectation comparatively. Also, the magnitude of the flux uncertainties is similar between the two, which  
1279 suggests that the two configurations are statistically similar.

1280 If we examine the bin normalization parameters for the PØD-only fit in Figure 6.28 on page 131, they  
1281 are suggesting a reduction in the event rate across most bins. This high flux, low bin normalization result  
1282 is likely due to the anticorrelated relationship between them as indicated in the correlation matrix shown  
1283 in Figure 6.30 on page 133. This has been observed in previous BANFF analyses. Interestingly, the results  
1284 of the principal components analysis on the bin normalizations in Section 4.2.2.4 are observed here as well.  
1285 The analysis predicted most of the parameters would shift in unison, and we see that trend largely replicated  
1286 in the postfit values. This indicates that we can possibly reduce the number of bin normalizations and still  
1287 obtain a similar postfit result.

1288 The cross section parameters are also quite similar between the two fits, with some larger uncertainties in  
1289 the PØD-only result. The CCQE and BeRPA parameters are in very good agreement with both preferring  
1290 a significant increase in the BeRPA  $B$  scale parameter. There is tension in the fits with the  $M_A^{\text{Res}}$  parameter  
1291 which is not currently understood. However, if the difference in the postfit parameters is distributed according  
1292 to a chi-squared distribution, then this deviation is not unexpected. We will explore this idea further with  
1293 a hypothesis test in the next section.

1294 A couple of interesting features are observed in the 2p2h parameters. Firstly is the 2p2h  $\nu$  normalization  
1295 on carbon which is about two-times larger in the PØD-only fit than the FGD-only fit. This normalization  
1296 result is currently an unknown phenomenon. It could be explained by the fact that the PØD has nearly twice  
1297 as much non-carbon and non-oxygen elements, which is mostly brass, by mass fraction as in the FGD (see  
1298 Table 6.1 on page 125). The second feature involves the 2p2h shape parameters, *both of which have postfit*  
1299 *values at the physical limit of +1, or +2 as shown graphically in Figure 6.27 on page 130*. This predicts that  
1300 the 2p2h interaction has no nucleon-nucleon correlation mode and is only due to the pionless-Delta-decay  
1301 mode. This result is an artifact of the cross section parameterization that is also shared with the FGD result.  
1302 This issue has been addressed in the latest cross section parameterization and BANFF analysis[50].

1303 To provide an uncertainty on those shape parameters, even though they are situated at a discontinuity in  
1304 the derivative, a “mirrored” spline was implemented as shown in Figure 6.29 on page 132. The mirrored spline  
1305 was shown by the BANFF group to not affect the postfit results while providing a calculable uncertainty in  
1306 MINUIT for the Hessian matrix[18]. To further investigate the impact of a mirrored spline, the oscillation  
1307 analysis group used the same splines in the Bayesian analysis, which uses a Markov chain Monte Carlo  
1308 method to explore the parameter space. The Bayesian analysis observed some small relative changes in

1309 the 2p2h and  $I_{1/2}$  background normalizations and BeRPA  $E$  root-mean-square using the mirrored spline.  
1310 However, the parameters that received the largest shifts are already poorly constrained by the ND280 data,  
1311 and so they have a minuscule effect on the fit.

1312 The postfit correlations are shown in Figure 6.30 on page 133. The full matrix shows large anticorrelations  
1313 between the systematic parameters sets. Largest in magnitude are the flux and cross section parameters.  
1314 To better see the correlations for those sets, they are zoomed into on Figure 6.31 on page 134. For only the  
1315 cross section parameters, the correlations are shown in Figure 6.32 on page 135.

### 1316 6.2.3 Receiver Operating Characteristic

1317 To demonstrate the differences between the PØD and FGD parameter estimates, receiver operating characteris-  
1318 tic (ROC) curves are provided in Appendix H. The advantage of ROC curves over a p-value calculation  
1319 is that the differences between the two fits can be statistically quantified for all parameters. These curves  
1320 provide an indication of which fit has better constraints in parameter space, suggest the limitation of each  
1321 fit, and provide guidance for future researchers.

## 1322 6.3 Summary

1323 In this chapter, we have explored the postfit results for the PØD-only data set and compared it against  
1324 the FGD-only fit. While the FGD-only data samples have about twice as many more neutrino-oxygen  
1325 events than the PØD-only data, which helps with sensitivity of the oxygen cross section parameters, the  
1326 accumulated neutrino exposures are similar. Moreover, we observe a good level of agreement between the  
1327 two fits with the largest differences observed with less constrained parameters like those that characterize  
1328 the 2p2h interaction. A hypothesis test was performed to quantify if the PØD-only and FGD-only data are  
1329 similar or not. In order to reject the null hypothesis, which is that the two sets are similar, at the 5% level, a  
1330  $\chi^2$  of 96.21 or greater was needed. A chi-squared of 81.41 was obtained, corresponding to a p-value of 28.65,  
1331 which is insufficient to reject the null hypothesis. Therefore, using the BANFF fit method with the current  
1332 PØD samples and cross section parameterization, the ND280 constraint is expected to be largely similar if  
1333 propagated to the next stage in the oscillation analysis. We will examine in the final chapter the differences  
1334 in the predicted neutrino energy spectrum at SK using the PØD-only and FGD-only postfit results.

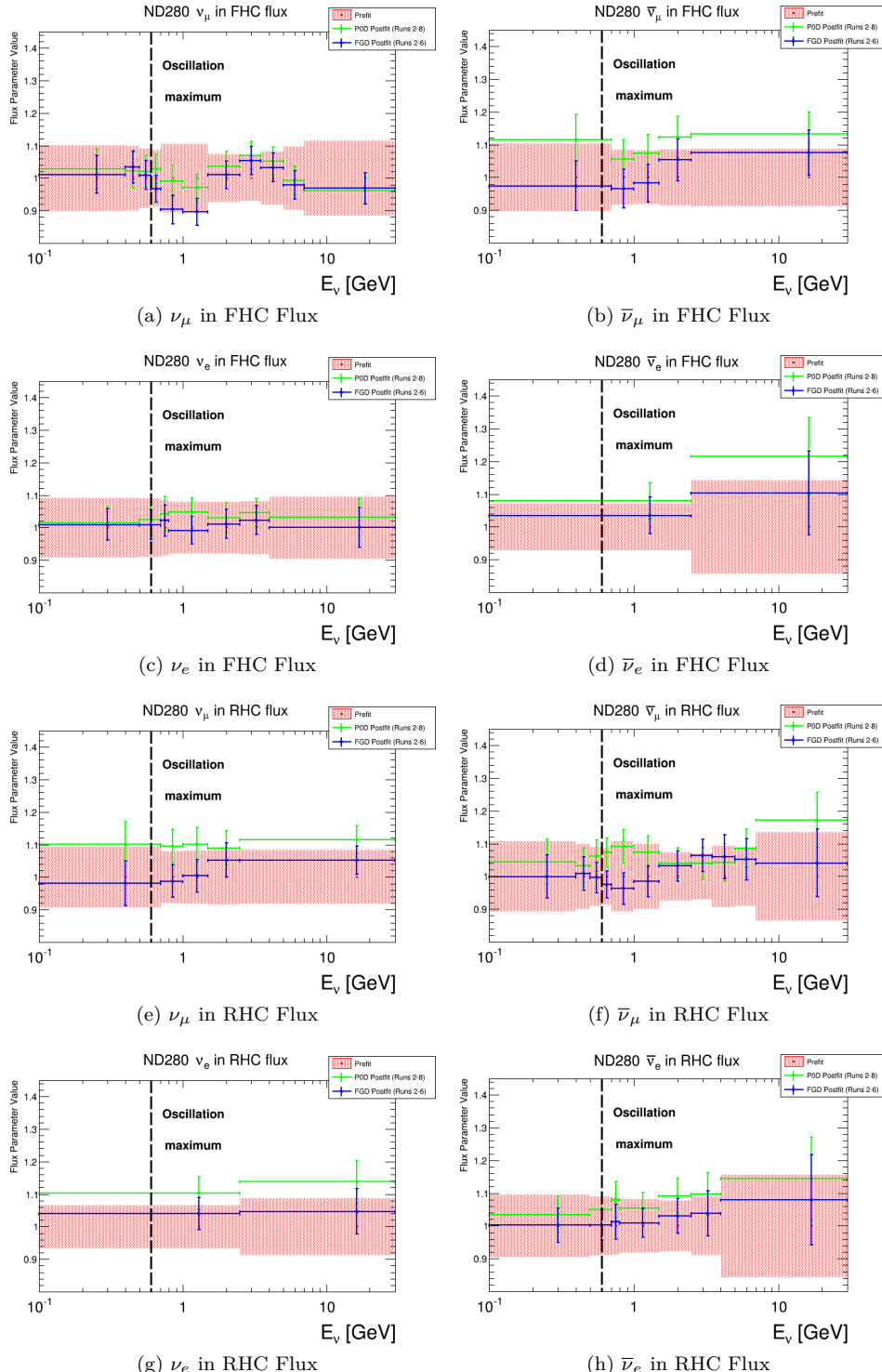


Figure 6.25: Postfit ND280 flux parameters for the PØD-only (green) and FGD-only (blue) BANFF fit as functions of neutrino energy. The energy that maximizes the  $\nu_\mu \rightarrow \nu_e$  oscillation (0.6 GeV) is shown with a dashed, black line.

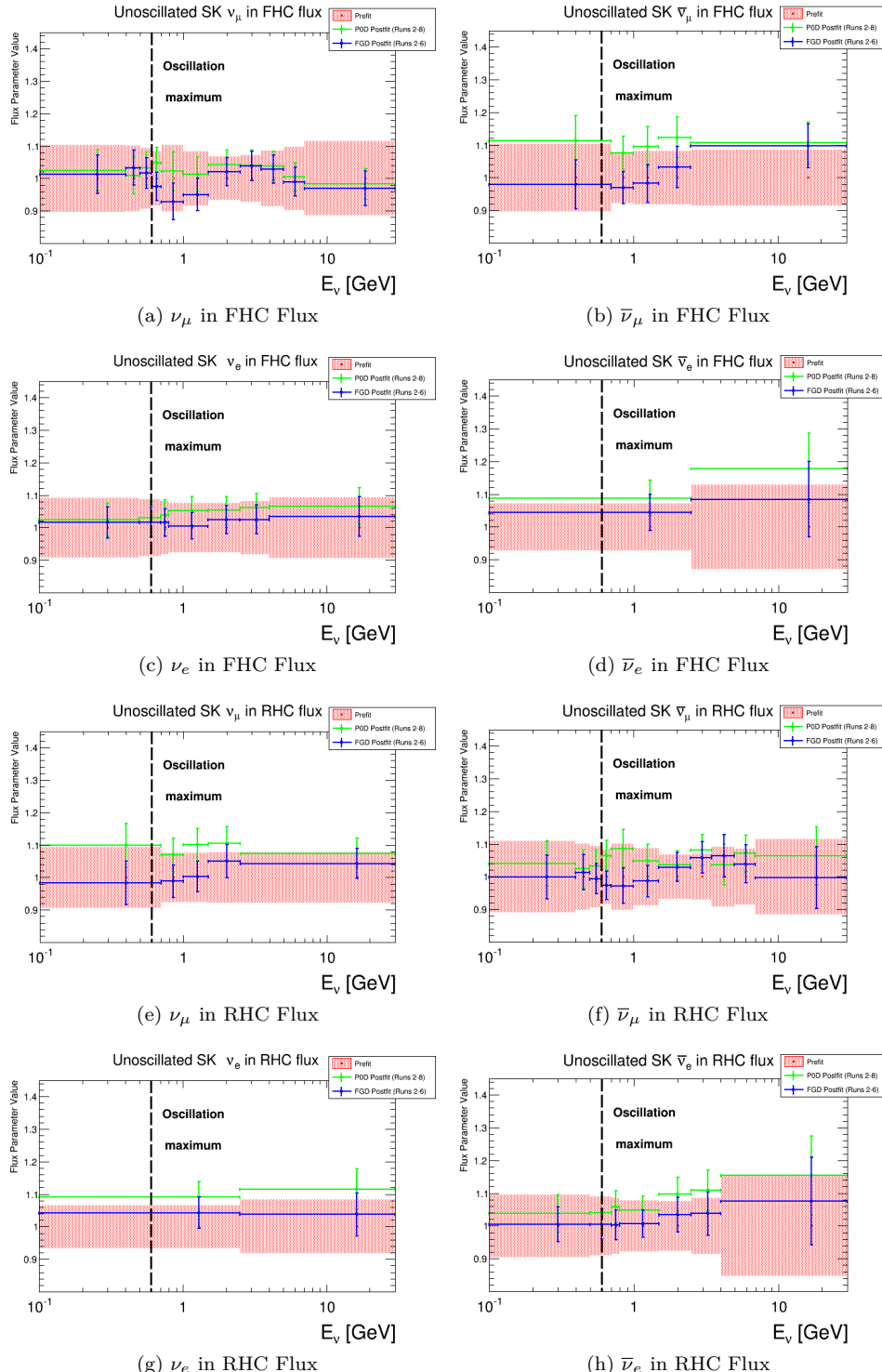


Figure 6.26: Postfit SK flux parameters for the PØD-only (green) and FGD-only (blue) BANFF fit as functions of neutrino energy. The energy that maximizes the  $\nu_\mu \rightarrow \nu_e$  oscillation (0.6 GeV) is shown with a dashed, black line.

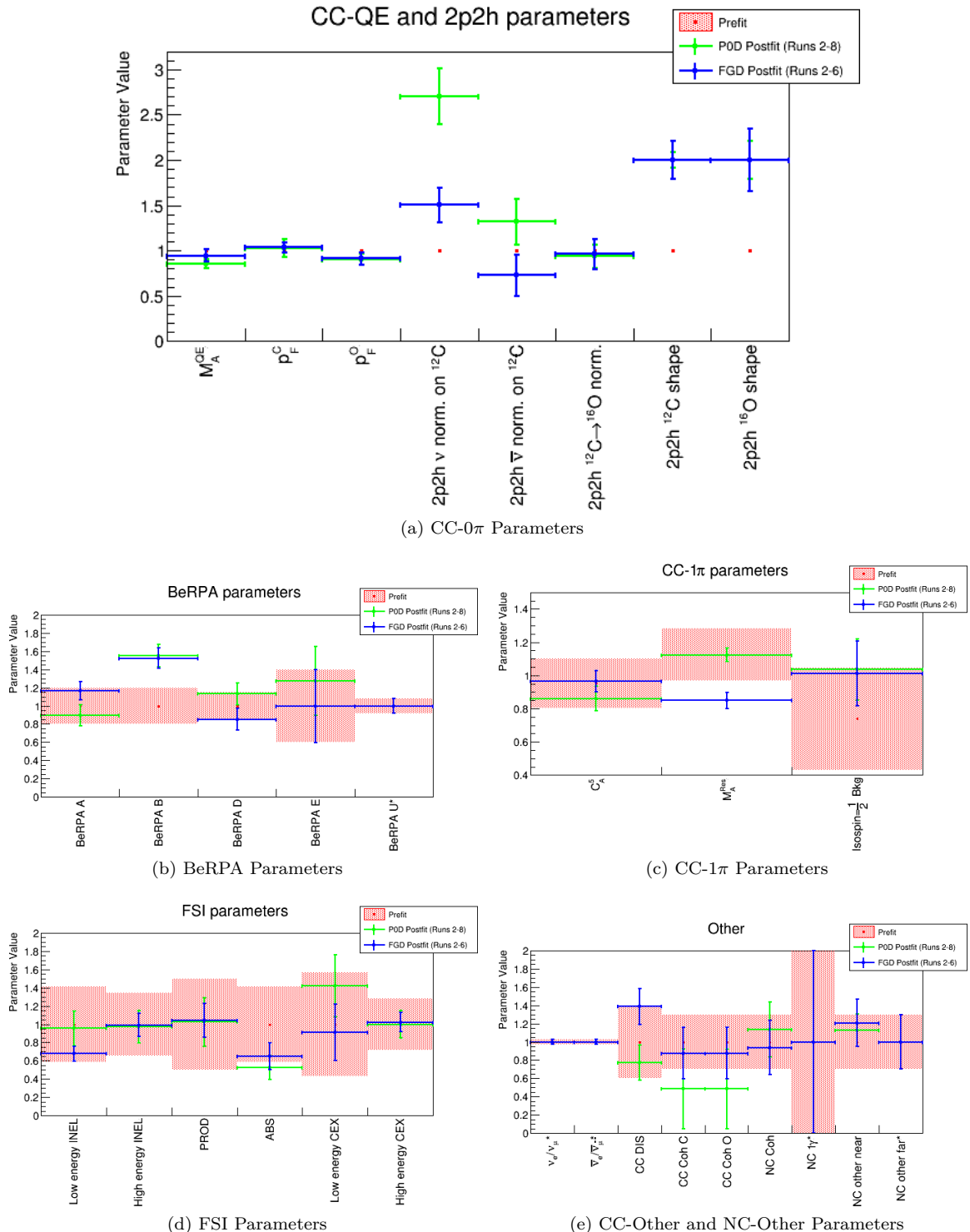


Figure 6.27: Postfit cross section parameters for the PØD-only (green) and FGD-only (blue) BANFF fit. In these figures, all shape and scale factor parameters are adjusted to 1 to provide a consistent graphical representation of all fit parameters. Shape parameters always have a prefit value of 0. Parameters without prefit uncertainties had a flat prior applied to them and an asterisk (\*) represents a fixed parameter.

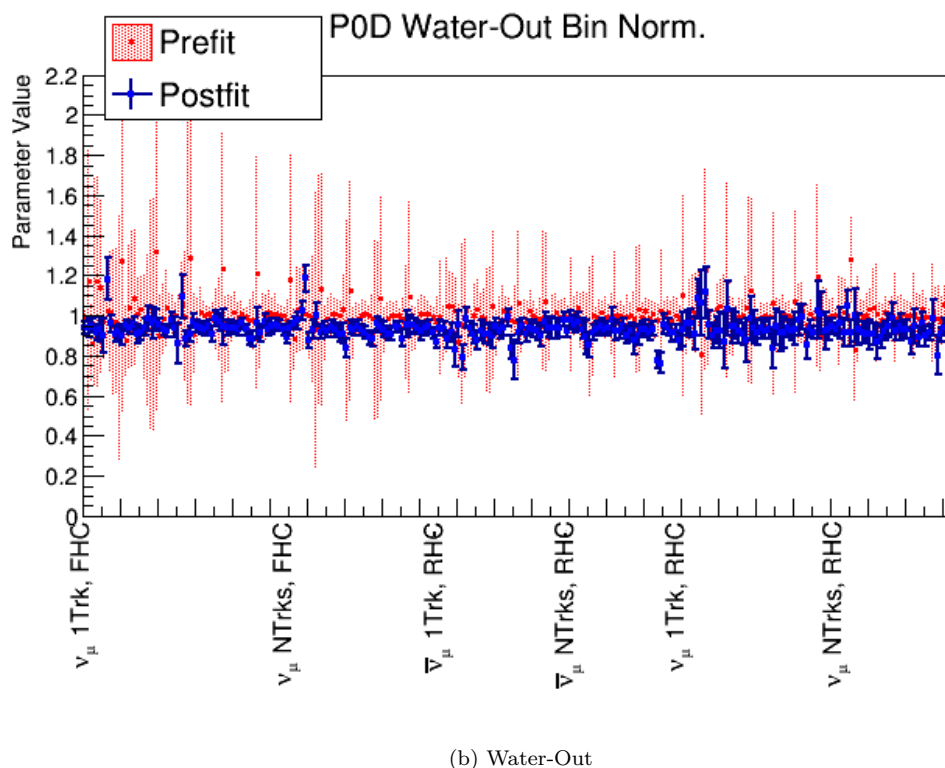
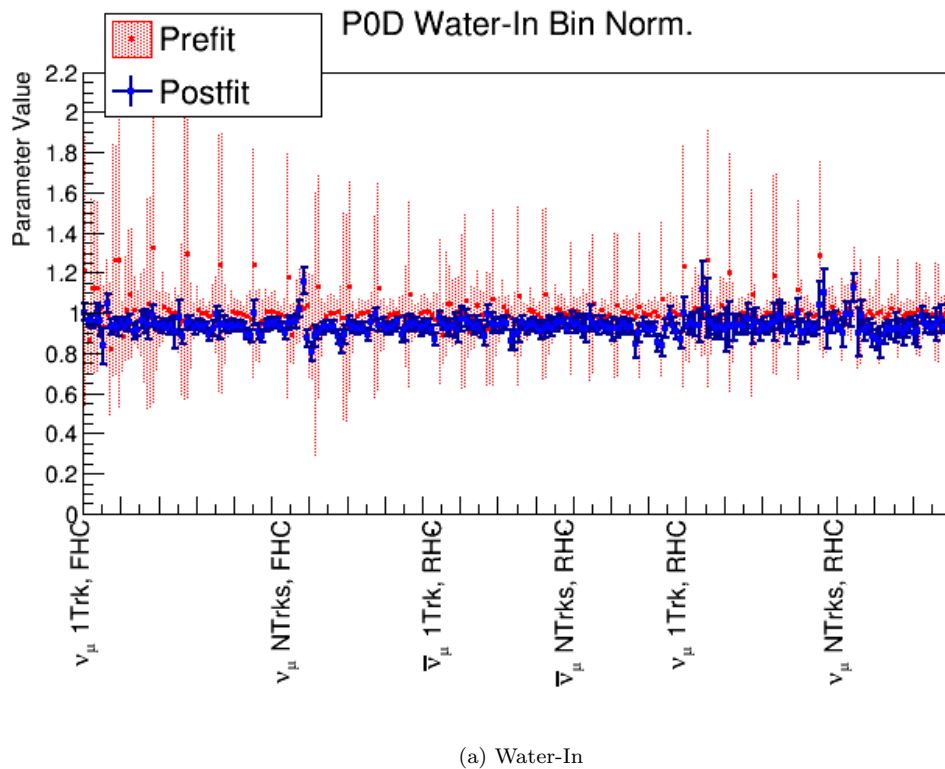


Figure 6.28: Prefit and postfit PØD bin normalization parameters.

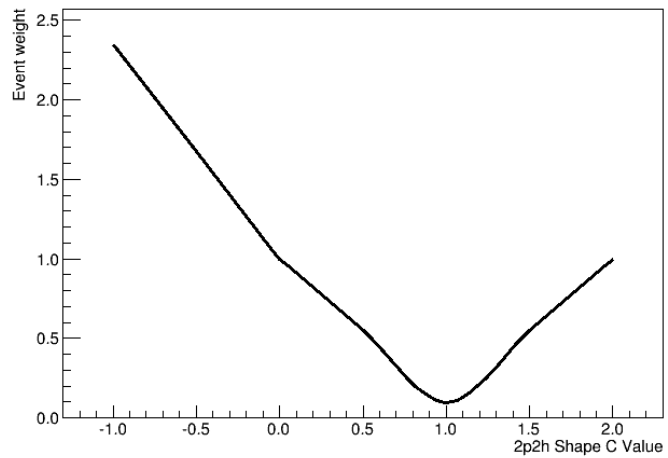


Figure 6.29: The “mirrored” spline for a single event. The spline represents an event weight and variations from the prefit value of 0 alters the event weight. The 2p2h shape splines are mirrored about the value of +1 to provide an uncertainty in the postfit result.

### Postfit Correlation Matrix

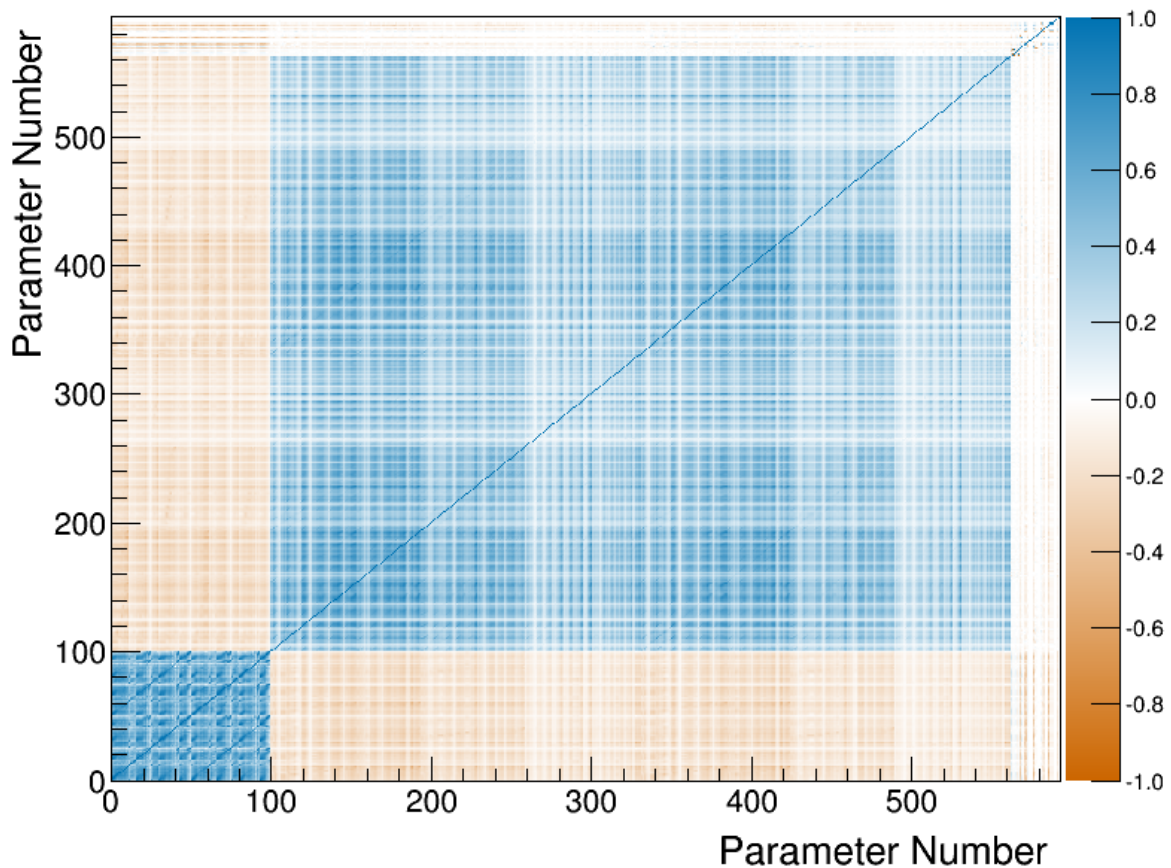
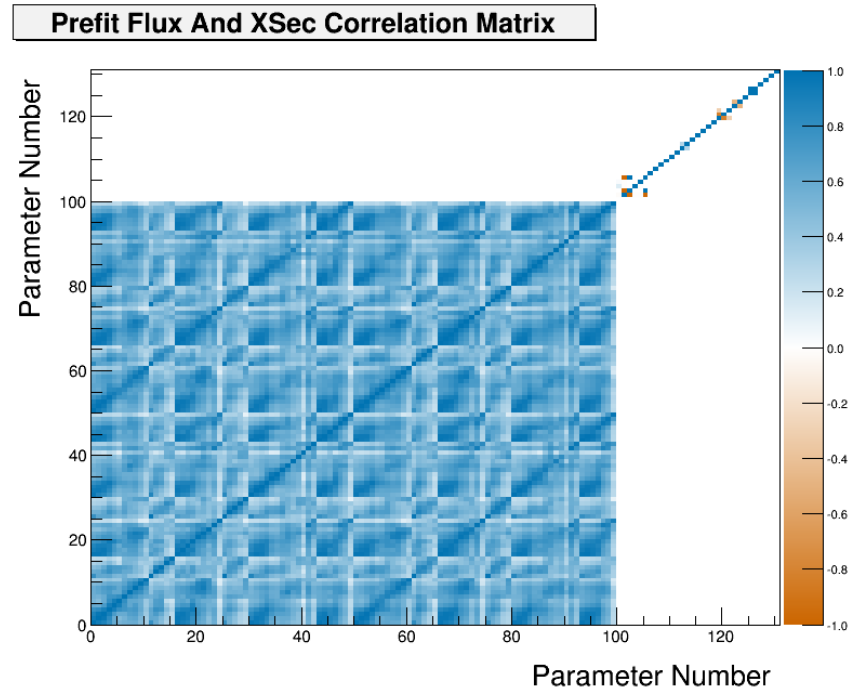
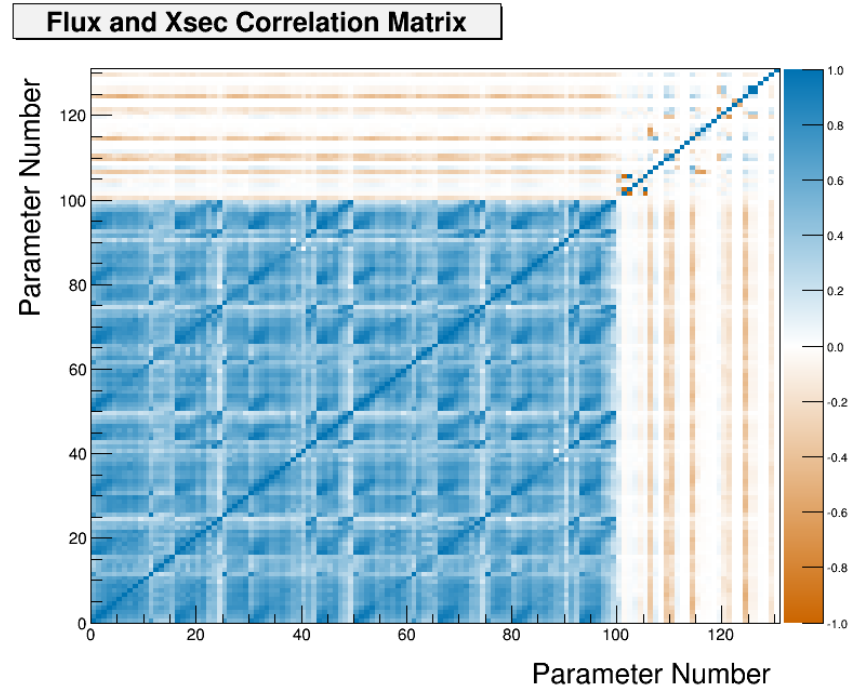


Figure 6.30: Postfit correlation matrix. The first 100 parameters are the flux parameters with the first 50 corresponding to ND280 and the last 50 with Super-K. Between 100 and 561 are the bin normalization parameters. The last 31 are the cross section parameters.



(a) Prefit flux and cross sections correlations



(b) Postfit flux and cross section correlations

Figure 6.31: Prefit and post flux and cross section parameter correlations. In (a) and (b), the prefit and postfit, respectively, correlation matrices for the flux and cross section parameters are shown. The first 50 parameters correspond to the ND280 flux with the last 50 with the SK flux. The final 31 parameters are for the cross section.

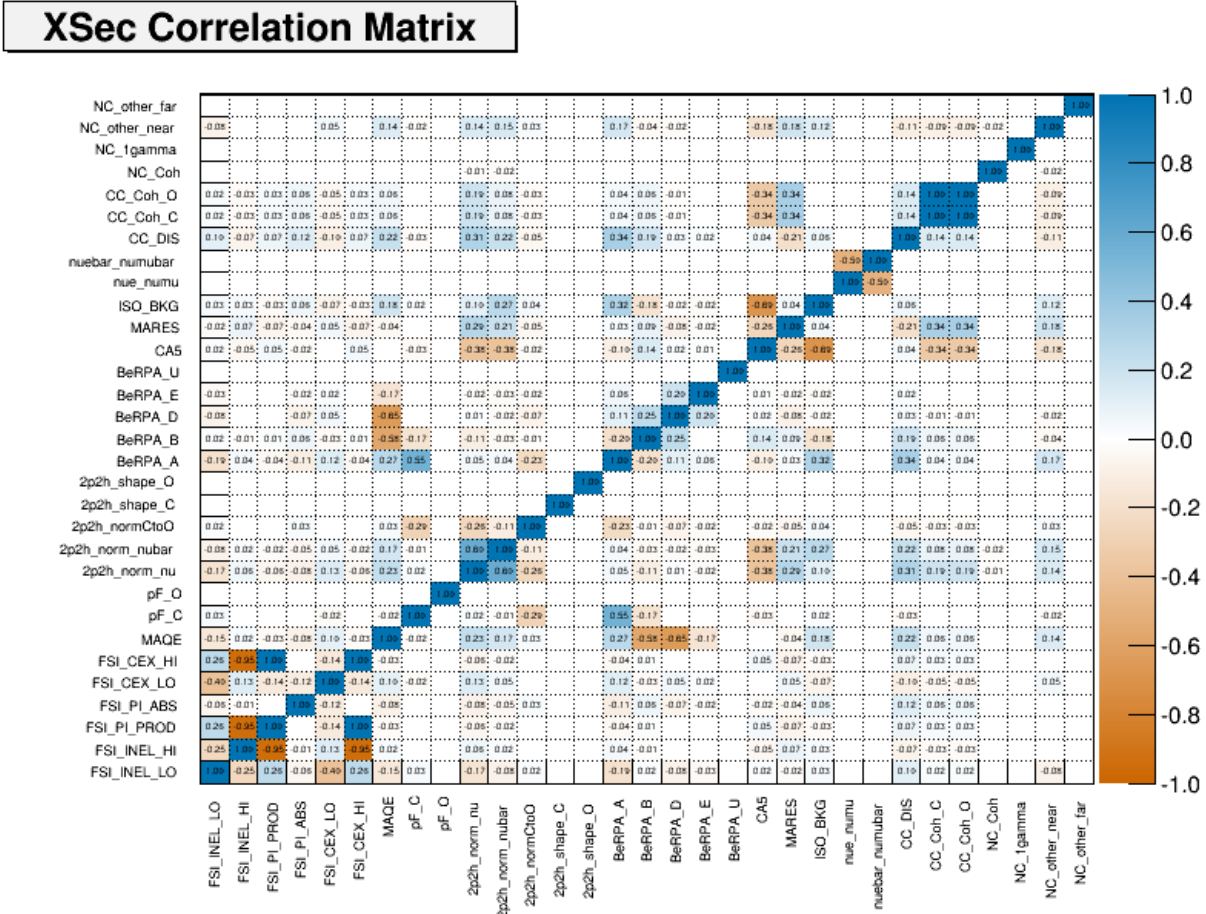


Figure 6.32: Postfit cross section correlation matrix

<sub>1335</sub> **Chapter 7**

<sub>1336</sub> **Discussion**

<sub>1337</sub> This chapter serves to summarize the methods and results shown in this thesis. The Tokai to Kamioka (T2K)  
<sub>1338</sub> experiment is a long baseline, neutrino oscillation experiment designed to observe a  $\nu_\mu$  beam oscillate into  $\nu_e$ .  
<sub>1339</sub> With the aid of the Japan Proton Accelerator Research Complex (J-PARC), a dedicated near detector called  
<sub>1340</sub> ND280 is located downstream of the neutrino production source to observe the beam before oscillations  
<sub>1341</sub> occur. Since the start of data collection, the fine grain detector (FGD) in ND280 has provided constraints on  
<sub>1342</sub> the neutrino flux and neutrino-water interaction modes important to the oscillation analysis. This thesis is  
<sub>1343</sub> an analysis of an independent measurement of the ND280 constraint using a maximum likelihood estimate in  
<sub>1344</sub> the Beam and Near Detector Flux Task Force (BANFF) framework with samples from the pi-zero detector  
<sub>1345</sub> (PØD).

<sub>1346</sub> Analysis samples have been developed with the PØD to capture a wide variety of interaction modes  
<sub>1347</sub> in T2K, importantly interactions classified as charged current quasi-elastic (CCQE) which constitute the  
<sub>1348</sub> highest cross section in the T2K neutrino energy spectrum. While the PØD has a larger volume compared  
<sub>1349</sub> to the FGD, which means it has more neutrino interactions to select, the PØD is less sensitive to non-CCQE  
<sub>1350</sub> interactions like CC single pion production. This limitation is largely due to the design of the detector and  
<sub>1351</sub> sample selection which reduce its  $(p, \cos \theta)$  sensitivity to the lower energy outgoing muons. The systematic  
<sub>1352</sub> uncertainties inherent in the samples were controlled for in a similar manner with previous BANFF analyses.

<sub>1353</sub> The PØD-only data fit shows very good agreement with the FGD-only result using the same flux and  
<sub>1354</sub> cross section parameters. Trends in the postfit parameters like the flux shape and the quantum mechanical  
<sub>1355</sub> correlation affects on the observable cross section were observed in both sets of fits.

<sub>1356</sub> Other topics discussed in this chapter are presented in the following order. First shown is a prediction  
<sub>1357</sub> of the oscillated samples at SK using the ND constraint in Section 7.1. Possible analysis improvements are

Table 7.1: Oscillation parameters used as inputs for studies of simulated data.

Parameter	Value	Units
Mass hierarchy	Normal	
$\Delta m_{21}^2$	7.53	$10^{-5}$ eV $^2/c^4$
$ \Delta m_{32}^2 $	2.509	$10^{-3}$ eV $^2/c^4$
$\sin^2 \theta_{23}$	0.528	1
$\sin^2 2\theta_{12}$	0.846	1
$\sin^2 2\theta_{13}$	0.0857	1
$\delta_{CP}$	-1.601	rad
$e^-$ density	2.6	g/cm $^3$
Baseline length	295	km
$\nu$ -mode luminosity	14.7	$10^{20}$ POT
$\bar{\nu}$ -mode luminosity	7.6	$10^{20}$ POT

discussed in Section 7.2. Finally, the prospect of a joint PØD and FGD fit are discussed in Section ??-Joint::

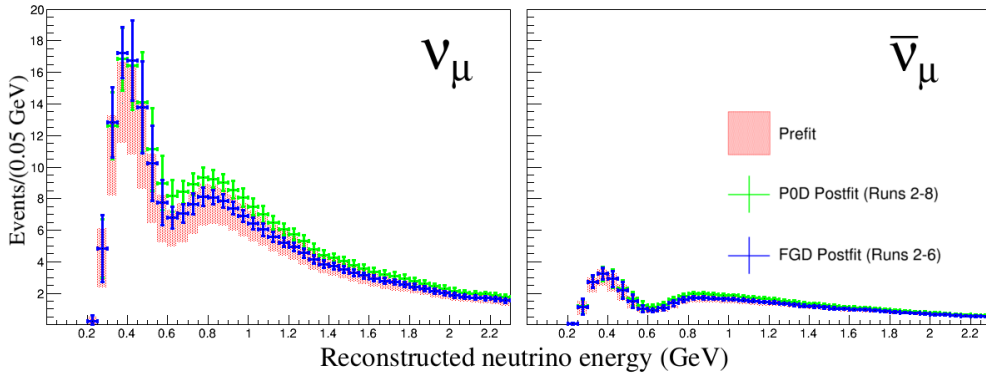
## 7.1 Prediction of the T2K Oscillation Analysis Samples

In this section, we analyze the BANFF fit as the input for the oscillation analysis. We are explicitly NOT performing the oscillation analysis, but we are building a prediction of the oscillated neutrino samples using the frequentist framework described in the 2017 oscillation analysis publication[2]. We then compare the prediction with the observed neutrino energy spectra of the four CCQE-enriched samples at Super-Kamiokande (SK). These samples are the FHC mode ( $\nu$ -mode)  $\nu_\mu$  sample, the RHC mode ( $\bar{\nu}$ -mode)  $\bar{\nu}_\mu$  sample, the  $\nu$ -mode  $\nu_e$  sample, and the  $\bar{\nu}$ -mode  $\bar{\nu}_e$  sample.

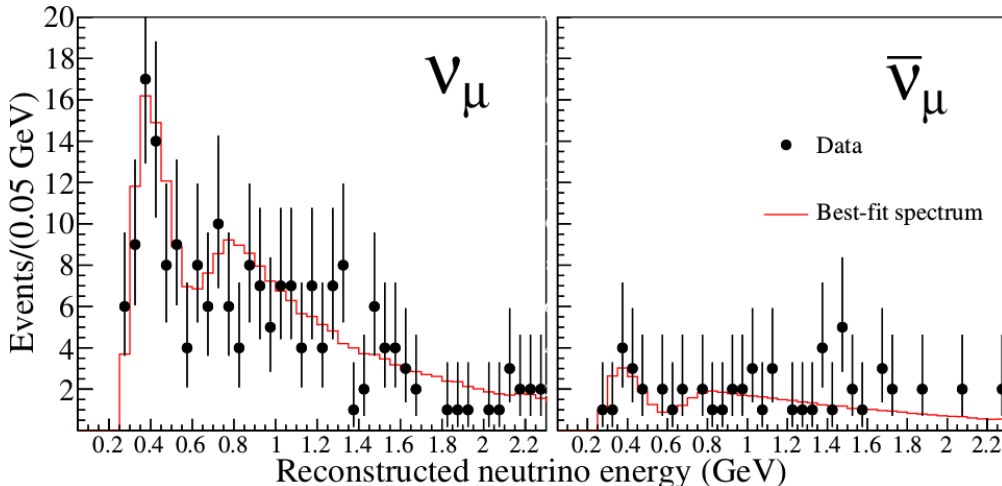
The SK prediction is built with the following ingredients: the flux and cross section parameter estimates from the BANFF fit parameter estimates and covariance matrix, the nominal set of SK detector systematics in the frequentist analysis software, and the full three-flavor oscillation probabilities. The full three-flavor oscillation parameters used are the same as listed in TABLE II in the 2018 CP violation search paper[51], which are shown in Table 7.1 on page 137 for convenience. The observed spectra are also taken from the 2018 CP violation search paper, which had a integrated luminosity of  $2.2 \times 10^{21}$  POT.

The spectra are shown in the following order. First are the of the  $\nu_\mu$  CCQE and  $\bar{\nu}_\mu$  CCQE-enriched samples together shown in Figure 7.1 on page 138. Next is the  $\nu_e$  CCQE-enriched sample shown in Figure 7.2 on page 138. Finally is the  $\bar{\nu}_e$  CCQE-enriched sample shown in Figure 7.3 on page 139. The integrated spectra are tabulated in Table 7.2 on page 139.

We observe that each PØD-only predicted spectrum is systematically higher than each FGD-only predicted spectrum. However, the more interesting differences are the integrated prediction. While the FGD-only prediction has better agreement with both the  $\nu_e$  and  $\nu_\mu$  CCQE samples, the PØD-only prediction is



(a) Prediction



(b) Observed

Figure 7.1: Reconstructed  $\nu_\mu$  (left) and  $\bar{\nu}_\mu$  (right) CCQE-enriched energy distributions at SK. The top figure is the predicted spectra while the bottom is the observed spectra. The observed spectra is taken from the 2018 CP violation search publication[51].

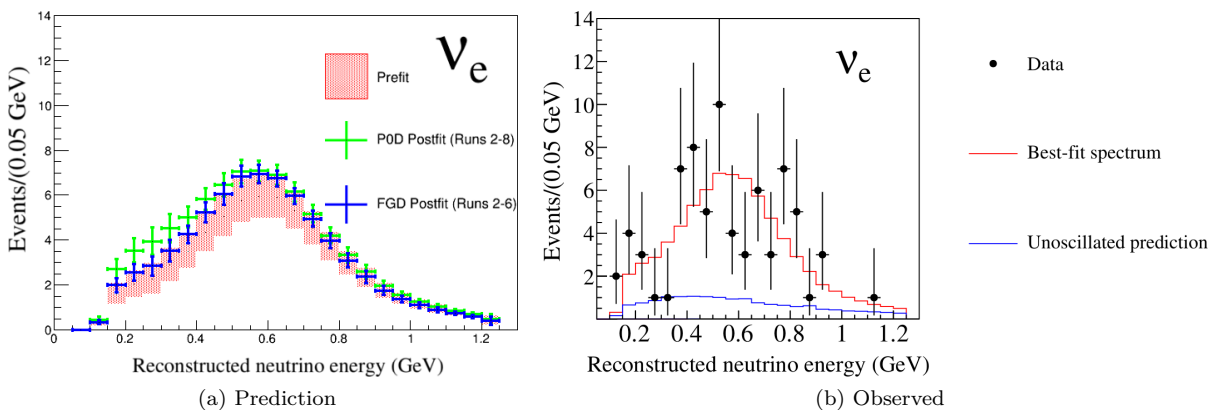


Figure 7.2: Reconstructed  $\nu_e$  CCQE-enriched energy distribution at SK. The observed spectra is taken from the 2018 CP violation search publication[51].

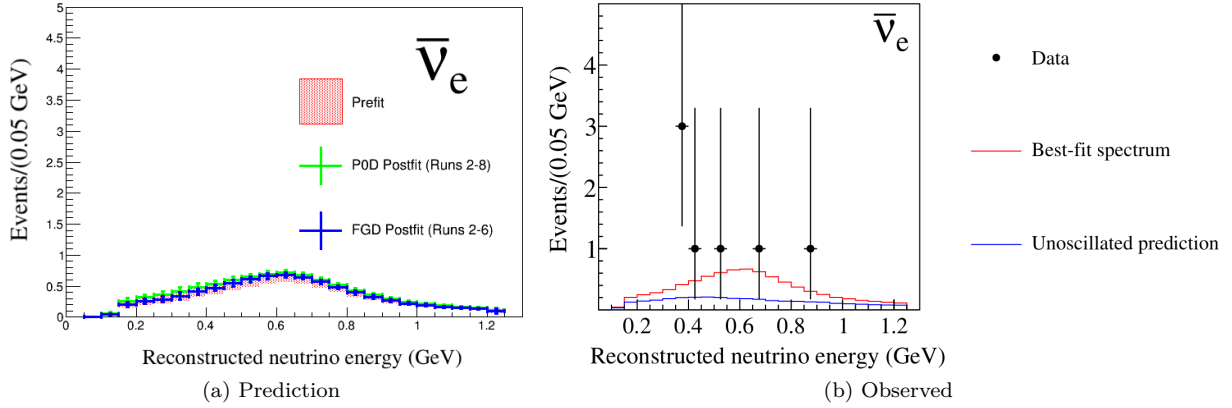


Figure 7.3: Reconstructed  $\bar{\nu}_e$  CCQE-enriched energy distribution at SK. The observed spectra is taken from the 2018 CP violation search publication[51].

Table 7.2: Number of events expected in the SK CCQE-enriched samples.

	Prefit	PØD-only	FGD-only	Observed
$\nu_\mu$ CCQE ( $< 2.3$ GeV)	207.34	252.41	228.07	201
$\bar{\nu}_\mu$ CCQE ( $< 2.3$ GeV)	49.67	58.14	52.47	57
$\nu_e$ CCQE ( $< 1.3$ GeV)	65.61	83.01	74.71	74
$\bar{\nu}_e$ CCQE ( $< 1.3$ GeV)	7.74	9.03	8.15	7

1379 agrees well with the  $\bar{\nu}_\mu$  CCQE sample. It is difficult to judge the agreement of the  $\bar{\nu}_e$  CCQE sample due  
 1380 to small statistics. However, this all suggests that including the PØD data samples can improve the ND  
 1381 constraint in RHC mode.

## 1382 7.2 Analysis Improvements

1383 Looking forward, the PØD-only analysis can be improved significantly. The PØD selections in this thesis  
 1384 are simplistic compared to the recent developments in the T2K experiment. The author was a part of  
 1385 the second generation cross section analysis of single pion production in the PØD, which utilized deep  
 1386 learning techniques, to select a relatively pure CC-1 $\pi$  sample. These details are provided in Appendix ???.  
 1387 Additionally, the PØD  $\bar{\nu}_\mu$  CC-0 $\pi$  analysis[9] was able to achieve a high-purity CCQE-like sample using  
 1388 almost identical cuts as presented in this thesis. However, both the CC-1 $\pi$  and CC-0 $\pi$  analyses use cuts  
 1389 that are not yet available in the BANFF framework due to technical difficulties and lack of expertise in the  
 1390 collaboration.

1391 Also more validation studies could be done to understand the sensitivity of the PØD samples. A test of  
 1392 the biases of the fit parameters requires fitting an ensemble of “fake data” sets, which are variations of the

1393 Asimov set. This all requires significant amount of computational time to complete<sup>1</sup>.

1394 There are other possible improvements to the ND constraint analysis using the methods developed for  
1395 machine learning applications. The following two sections are on topics to improve the BANFF fit analysis  
1396 in its current state. These methods are quite general and rely on the fundamentals of parameter estimation  
1397 techniques in statistics. A section summary is provided to summarize their details.

1398 First is a discussion on applying a different regularization strength. Second is a method to reduce the  
1399 number of effective bin normalization parameters using a different penalty function called the Lasso.

### 1400 7.2.1 Regularization Strength

1401 Recall that the BANFF ND constraint test statistic is defined as

$$\chi_{\text{ND}280}^2 = \chi_{\text{LLR}}^2(\vec{N}^d, \vec{N}^p) + \chi_{\text{Penalty}}^2(\Delta \vec{\gamma})$$

1402 where  $\vec{N}^d$  and  $\vec{N}^p$  are the binned data and prediction measurements, respectively, and  $\Delta \vec{\gamma}$  is the difference  
1403 between postfit and prefit parameter values in the fit. This equation is similar to the general class of  
1404 parameter regression using regularization [16]

$$\hat{\beta} = \underset{f \in \mathcal{F}, \beta \in \mathbb{R}^d}{\operatorname{argmin}} \left\{ L\left(\eta, f\left(\vec{\beta}\right)\right) + \lambda J(f) \right\} , \quad (7.1)$$

1405 where  $L$  is a loss function<sup>2</sup> of measurements  $\eta$ ,  $J(f)$  is a penalty function,  $f(\vec{\beta})$  is a  $d$ -dimensional function  
1406 of  $\vec{\beta}$ ,  $\lambda$  is the regularization parameter, and  $\mathcal{F}$  is a space of function on which  $J(f)$  is defined. In regularized  
1407 regression problems, the penalty term serves to solve an ill posed problem by adding external information.  
1408 Similarly, the regularization parameter controls the importance of the penalty. We recognize that the loss  
1409 function  $L$  is the log-likelihood ratio term  $\chi_{\text{LLR}}^2$ , and penalty term is  $J = \chi_{\text{Penalty}}^2$  with regularization strength  
1410  $\lambda = 1$ .

1411 In defining the BANFF test statistic in Chapter 2, the regularization term  $\lambda$  was set to 1 without  
1412 justification. We can test the effectiveness of this choice using cross-validation. Cross-Validation provides  
1413 an estimate on the prediction error as well as determines the “optimal” choice of regularization. In cross-  
1414 validation, the input data is randomly split into  $K$  equal sized partitions. For the  $k \in K$  data partition, we  
1415 fit the model to the other  $K - 1$  parts of the data and calculate a prediction error  $P$ .

1416 In this verification of the regularization strength, the test statistic is altered to include a regularization  
1417 term

---

<sup>1</sup>Also not to mention the carbon footprint left afterwards.

<sup>2</sup> $L$  is also called an objective function.

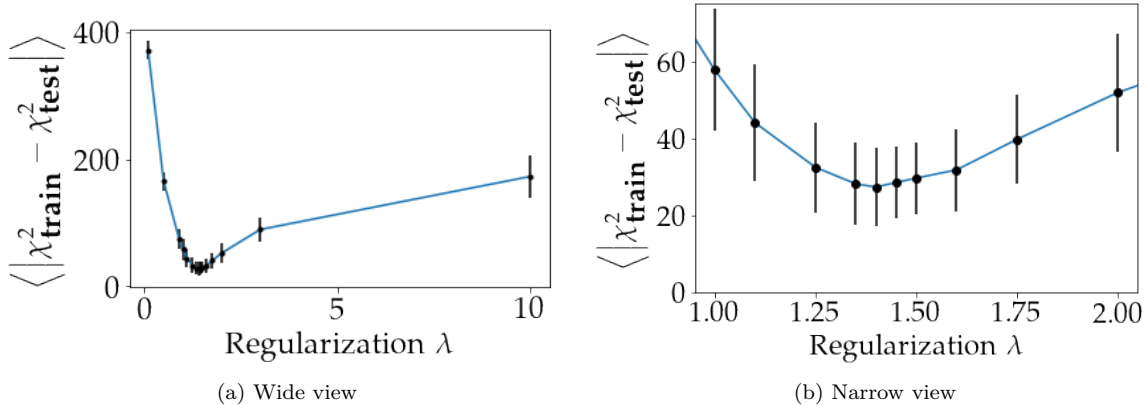


Figure 7.4: Cross-validation curve for the BANFF fit regularization strength. Figure (a) examines the cross-validation error for a wide range of regularization strengths. Figure (b) zooms in on the minimized error. The error bars shown are statistical only.

$$\begin{aligned} \chi^2_{\text{ND280}} &= \chi^2_{\text{LLR}} + \lambda \chi^2_{\text{Penalty}}(\vec{y}) \\ &= \chi^2_{\text{LLR}} + \lambda (\vec{y} - \vec{y}_0)^T V^{-1} (\vec{y} - \vec{y}_0), \end{aligned} \quad (7.2)$$

and the data is split into  $K = 5$  partitions. The prediction error,  $P$ , in this analysis is defined as

$$P_k \left( (\chi^2_{\text{train}})^{-k}, (\chi^2_{\text{test}})^k \right) = \left| (\chi^2_{\text{train}})^{-k} - (\chi^2_{\text{test}})^k \right| \quad (7.3)$$

where  $(\chi^2_{\text{train}})^{-k}$  is the fitted model statistic on all but the  $k$ th partition, and  $(\chi^2_{\text{test}})^k$  is prediction from the fitted model on the  $k$ th partition. This definition of  $P$  is useful since the penalty terms cancel, leaving only the difference in log-likelihood terms. The optimal regularization strength is determined by minimizing the cross-validation error,

$$\begin{aligned} \text{CV}(\lambda) &= \langle |\chi^2_{\text{train}} - \chi^2_{\text{test}}| \rangle \\ &= \frac{1}{5} \sum_{k=1}^5 P_k \left( (\chi^2_{\text{train}})^{-k}, (\chi^2_{\text{test}})^k \right), \end{aligned} \quad (7.4)$$

which is the average prediction error.

Results of the cross-validation are shown in Figure 7.4 on page 141. We see that while the penalty strength of  $\lambda = 1$  nearly minimizes the cross-validation error, slightly larger penalties are preferred. The cross-validation error curve is minimized roughly at  $\lambda = 1.4$ , and it is roughly quadratic in the neighborhood around the minimum. Therefore, a more regularized solution is preferred with the data sample.

Another data fit with  $\lambda = 1.4$  was performed with the following results. The MINUIT optimization routine required 175602 (149661) iterations to find the global minimum at  $\hat{\chi}^2_{\text{ND280}} = 1344.89$  (1412.28) with

1430 the regularized (non-regularized) penalty term. The flux parameters have significantly reduced uncertainties  
 1431 compared to the  $\lambda = 1$  result. The cross section parameters are relatively the same as before except for the  
 1432 CC coherent uncertainties which are much smaller. There was no observed changes in the bin normalization  
 1433 parameters as well. This suggests that the flux covariance matrix input needs to reexamined for future  
 1434 BANFF fit analyses. The postfit parameters are presented in Appendix I.

### 1435 7.2.2 Alternative Penalty

1436 Consider solving the linear regression problem

$$\vec{\eta} = X\vec{\beta} \quad (7.5)$$

1437 where  $X$  is a  $p \times d$  matrix of  $d$  model features from  $p$  measurements,  $\vec{\beta}$  is a vector of regression weights with  
 1438  $p$  rows, and  $\vec{\eta}$  is a response vector. There are many approaches to solving Eqn. (7.5) using Eqn. (7.1). A  
 1439 popular solution is the  $l_2$ -regularization constraint[16]

$$\underset{\vec{\beta} \in \mathbb{R}^d}{\operatorname{argmin}} \left\{ L(\vec{\eta}, \vec{\beta}) + \lambda \sum_i |\beta_i|^2 \right\} \quad (7.6)$$

1440 where the sum of squares of the weights  $\beta_i$  sets the constraint and  $L$  is the loss function. A popular choice  
 1441 of  $L$  is using ordinary least squares

$$L(\vec{\eta}, \vec{\beta}) = \sum_j \left| \vec{\eta} - X\vec{\beta} \right|^2,$$

1442 which provides the lowest variance in parameter weights.

1443 With some algebra, we can rewrite the BANFF test statistic Eqn. (2.13) into the form of Eqn. (7.6).  
 1444 We again recognize  $\chi_{\text{LLR}}^2$  is the loss function  $L$  which leaves the penalty term to be tackled. The (inverse)  
 1445 covariance matrix is symmetric and real and can be decomposed as

$$V^{-1} = U^T \Lambda U$$

1446 where  $U$  and  $\Lambda$  are the matrix of the eigenvectors and eigenvalues, respectively, of  $V^{-1}$ . Since the eigenvalues  
 1447 are real and positive, the matrix  $\Lambda$  can be expressed as the square of a diagonal matrix  $\Gamma$

$$\Lambda = \Gamma^2.$$

1448 We can now rewrite the penalty term as an inner product of two vectors.

$$\begin{aligned}\chi_{\text{Penalty}}^2 &= (\Delta \vec{y})^T V^{-1} (\Delta \vec{y}) \\ &= (\Delta \vec{y})^T U^T \Gamma^2 U (\Delta \vec{y}) \\ &= (\Gamma U \Delta \vec{y})^T (\Gamma U \Delta \vec{y}).\end{aligned}$$

1449 If we let  $\vec{\psi} = \Gamma U \Delta \vec{y}$ , then the penalty term becomes

$$\chi_{\text{Penalty}}^2 = (\vec{\psi})^T \vec{\psi} = \sum_j |\psi_j|^2$$

1450 and test statistic is now

$$\chi_{\text{ND280}}^2 = \chi_{\text{LLR}}^2(N^d, N^p) + \|\psi\|_2^2 \quad , \quad (7.7)$$

1451 where  $\|\cdot\|_2^2$  is shorthand for the  $l_2$ -regularization constraint sum of squares. We see that the BANFF test  
1452 statistic is indeed a  $l_2$ -regularized solution with  $\Delta \vec{y}$ , recast as  $\vec{\psi}$ , acting as the parameter weight vector and  
1453 has the regularization strength  $\lambda = 1$ .

1454 Consider now another solution to Eqn. (7.5) using the  $l_1$ -regularization constraint or least absolute  
1455 shrinkage and selection operator (Lasso)<sup>3</sup>

$$\underset{\vec{\beta} \in \mathbb{R}^d}{\operatorname{argmin}} \left\{ L(\vec{\eta}, \vec{\beta}) + \lambda \|\beta\|_1 \right\}, \quad (7.8)$$

1456 where  $\|\cdot\|_1$  indicates the sum of absolute values of the parameter weight terms. What is unique about the  
1457 Lasso is its ability to promote model solutions with few nonzero coefficient weights, sometimes called sparse  
1458 solutions. In other words, predictor parameters with no model impact are excluded in the solution using the  
1459  $l_1$ -regularized constraint. Thus the Lasso has the advantage of providing an interpretable model in situations  
1460 with very high parameter spaces. However, the Lasso does not handle highly correlated variables very well.  
1461 This is overcome by combining the Lasso with  $l_2$ -regularization which is called the elastic net constraint

$$\underset{\vec{\beta} \in \mathbb{R}^d}{\operatorname{argmin}} \left\{ L(\vec{\eta}, \vec{\beta}) + \lambda \left( \frac{1}{2} (1 - \alpha) \|\beta_i\|_2^2 + \alpha \|\beta_i\|_1 \right) \right\},$$

1462 where  $\alpha$  is the “budget” between the Lasso and  $l_2$ -regularization. The results of using the Lasso and elastic  
1463 net with highly correlated variables is shown in Figure 7.5 on page 144. The elastic net controls for strong  
1464 within-group correlations and has a unique solution. Further details about the Lasso and elastic net can be

---

<sup>3</sup>The Lasso or  $l_1$ -regularization constraint is commonly employed in parameter estimation problems in linear systems. The Lasso has been shown to work with generalized linear models[52].

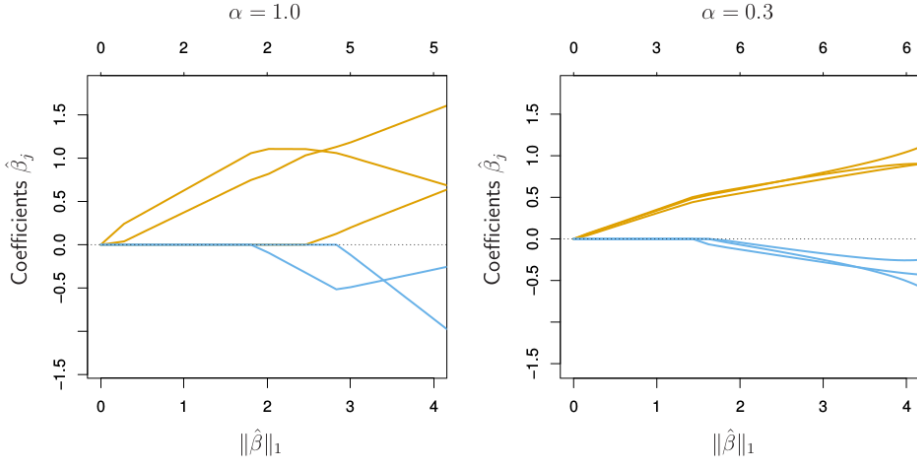


Figure 7.5: The Lasso vs elastic net constraint. Six variables are shown and the highly correlated variables are in groups of three. The Lasso estimate, left, estimate exhibits erratic behavior as the regularization strength  $\lambda$  is varied. The elastic net, right, pulls highly correlated variables together. In both panels, the vertical axis is the magnitude of the parameter weights (coefficients), the bottom horizontal axis is the regularization strength as measured by the estimate  $\|\hat{\beta}\|_1$ , and top horizontal axis is the count of non-zero parameter weights. This figure was taken directly from the following reference[53].

1465 found in the following reference [53].

1466 We can potentially reduce the dimensionality of the ND constraint by utilizing the elastic net. Using the  
1467 elastic net constraint provides a data-driven method to determine the number of important bin normalizations  
1468 in the analysis. The method to define the fit binning described in Chapter 4 would be unchanged. What  
1469 changes is that instead of merging fit bins prior to the fit, the elastic net determines which bin normalizations  
1470 are important or not important. Along with cross-validation, fit bins with minimal to no impact on the fit  
1471 can be excluded or combined with important fit bins. Then the best fit parameters and covariance matrix  
1472 using the current BANFF machinery can still be found.

1473 Another possibility in the future is for the BANFF fit to use the elastic net to directly estimate the  
1474 flux and cross section parameters. The challenge with this approach is that using non-Gaussian priors, the  
1475 covariance matrix is no longer calculable using the Hess matrix. This is a general critique of the BANFF fit  
1476 postfit error estimates since there are non-Gaussian priors for many of the cross section parameters. Instead,  
1477 bootstrap methods could be employed to infer the parameter covariances. This is further discussed in the  
1478 following reference [16].

### 1479 7.2.3 Analysis Improvement Summary

1480 We have explored topics that can potentially improve the BANFF fit analysis. Improved sensitivity to CC- $0\pi$   
1481 and CC- $1\pi$  model parameters using already developed PØD selections is possible if the BANFF software

1482 is updated. We also examined two topics developed in machine learning practices to improve parameter  
 1483 estimation. The first was a study on the strength of the penalty term. It was shown that we can find a  
 1484 tuning, or regularization, parameter for the penalty term that reduces the parameter variance but at cost of  
 1485 some parameter bias. The second topic was a general discussion on using a different BANFF fit test statistic  
 1486 called the Lasso. The Lasso has the attractive feature, without user input, of determining which parameters  
 1487 are unimportant in a model fit. The implication here is that the number bin normalization parameters in  
 1488 the BANFF fit can be effectively shrunk using the data itself.

### 1489 7.3 Future Prospects: Joint PØD+FGD Fit

1490 There are potential improvements in a “joint” PØD+FGD BANFF fit for the T2K experiment. As shown  
 1491 in the previous chapter, the number of neutrino-carbon and neutrino-oxygen events can be significantly  
 1492 increased by including the PØD data. This will enhance the fit’s sensitivity, and possibly improve constraints  
 1493 on poorly constrained parameters like that of the 2p2h interaction. There is an additional observed tension  
 1494 in each of the predicted SK sample spectrum between the PØD-only and FGD-only fits, which needs to be  
 1495 resolved.

1496 However, since the fits were performed on different T2K run periods, an equal POT exposure comparison  
 1497 is useful here. Proposing to run a “joint” PØD+FGD ND constraint using T2K runs 2 - 8, the updated  
 1498 neutrino-nucleus exposures are given in Table 7.3 on page 147. We see that while the number of neutrino-  
 1499 carbon events is still larger in the PØD. However, the PØD has 25% fewer neutrino-oxygen events in FHC  
 1500 mode and 9% more in RHC mode. We can estimate the fractional statistical error ( $\delta N$ ) reduction in a joint  
 1501 fit using the data from Table 7.3 on page 147 assuming the FGD fit is the nominal ND constraint. The  
 1502 fractional errors decrease approximately by

$$\begin{aligned}\delta N_{^{12}C}^{\text{FGD1-FHC}} &= \frac{1}{\sqrt{N_{^{12}C}^{\text{FGD1-FHC}}}} \xrightarrow{+\text{PØD Air}} \frac{1}{\sqrt{(1 + 2.01)N_{^{12}C}^{\text{FGD1-FHC}}}} \sim \frac{1}{\sqrt{3.01}} \approx 0.576 \\ \delta N_{^{16}O}^{\text{FGD2-FHC}} &= \frac{1}{\sqrt{N_{^{16}O}^{\text{FGD2-FHC}}}} \xrightarrow{+\text{PØD Water}} \frac{1}{\sqrt{(1 + 0.72)N_{^{12}C}^{\text{FGD1-FHC}}}} \sim \frac{1}{\sqrt{1.72}} \approx 0.762 \\ \delta N_{^{12}C}^{\text{FGD1-RHC}} &= \frac{1}{\sqrt{N_{^{12}C}^{\text{FGD1-RHC}}}} \xrightarrow{+\text{PØD Air}} \frac{1}{\sqrt{(1 + 1.60)N_{^{12}C}^{\text{FGD1-RHC}}}} \sim \frac{1}{\sqrt{2.60}} \approx 0.620 \\ \delta N_{^{16}O}^{\text{FGD2-RHC}} &= \frac{1}{\sqrt{N_{^{16}O}^{\text{FGD2-RHC}}}} \xrightarrow{+\text{PØD Water}} \frac{1}{\sqrt{(1 + 1.04)N_{^{12}C}^{\text{FGD2-RHC}}}} \sim \frac{1}{\sqrt{2.04}} \approx 0.700,\end{aligned}$$

1503 where combinations of FGD1/2 and FHC/RHC represent the FGD in the different beam modes, and an  
 1504 right-pointing arrow indicates adding the PØD data. These results indicate a fractional statistical error

1505 reductions around  $1/\sqrt{2}$  for both neutrino-oxygen events and also potentially stronger flux constraint from  
1506 higher statistics.

1507 Employing both the FGD and PØD in a joint BANFF fit was attempted, but the fit failed to converge  
1508 due to machine precision limits. Including both detectors with the FGD parameterization described in  
1509 reference [18] more than doubles the number of parameters and events than a single detector-only fit. This  
1510 not only requires more iterations to ensure the test statistic global minimum is found, but also requires more  
1511 calculations per iteration as well. For instance, the required time to ensure the joint PØD+FGD Asimov fit  
1512 started at the global minimum took 10 times larger than the PØD-only Asimov fit. So parameter shrinkage  
1513 must be performed on both analyses if reasonable computational speed and maximum statistical power are  
1514 desired in the BANFF fit. This is further discussed in Appendix Chapter F.

Table 7.3: Neutrino-nucleon exposure on target elements in a joint PØD and FGD analysis using T2K runs 2 - 8.

Detector	POT ( $10^{20}$ )		kg POT ( $10^{24}$ )	PØD-to-FGD (kg POT)		
	FHC	RHC		$^{12}\text{C}$	$^{16}\text{O}$	other
PØD Water-out FGD1	7.872	-	2.81	2.01	-	4.64
	11.529	-	1.14			
PØD Water-In FGD2	3.657	-	2.00	5.36	0.724	4.06
	11.529	-	1.12			
PØD Water-out FGD1	-	3.382	1.207	1.60	-	3.69
	-	6.234	0.614			
PØD Water-In FGD2	-	2.852	1.56	7.72	1.04	5.85
	-	6.234	0.606			

<sub>1515</sub> **Bibliography**

- <sub>1516</sub> [1] K. Abe *et al.*, “Measurements of neutrino oscillation in appearance and disappearance channels by the  
<sub>1517</sub> T2K experiment with  $6.6 \times 10^{20}$  protons on target,” *Phys. Rev. D*, vol. 91, p. 072010, April 2015. 9, 18
- <sub>1518</sub> [2] K. Abe *et al.*, “Measurement of neutrino and antineutrino oscillations by the T2K experiment including  
<sub>1519</sub> a new additional sample of  $\nu_e$  interactions at the far detector,” *Phys. Rev. D*, vol. 96, NOV 21 2017. 9,

- 1520 49, 57, 84, 137
- 1521 [3] S. Baker *et al.*, “Clarification of the use of chi-square and likelihood functions in fits to histograms,”  
1522 *Nucl. Instrum. Meth.*, vol. A221, pp. 437–442, 1983. 11
- 1523 [4] M. Hartz *et al.*, “Constraining the flux and cross section models with data from the ND280 detector for  
1524 the 2014/15 oscillation analysis,” tech. rep., T2K Collaboration, May 2015. T2K-TN-220 v4. 11
- 1525 [5] R. Das, *Measurement of NuMu induced charged current inclusive cross section on water using the near  
1526 detector of the T2K experiment*. PhD thesis, Colorado State University, Fort Collins, Colorado, USA,  
1527 2016. Available at <https://hdl.handle.net/10217/189398>. 16, 18
- 1528 [6] K. Abe *et al.*, “Measurement of  $\nu_\mu$  and  $\bar{\nu}_\mu$  charged current inclusive cross sections and their ratio with  
1529 the T2K off-axis near detector,” *Phys. Rev. D*, vol. 96, Sept. 2017. 16, 18
- 1530 [7] K. Abe *et al.*, “First measurement of the  $\nu_\mu$  charged-current cross section on a water target without  
1531 pions in the final state,” *Phys. Rev. D*, vol. 97, p. 012001, Jan. 2018. 16, 17, 18, 20, 57, 58
- 1532 [8] K. Abe *et al.*, “First measurement of the anti-numu charge current double differential cross section on  
1533 water without pions in the final state,” *Phys. Rev. D*, Forthcoming. 16
- 1534 [9] T. Campbell, *Measurement of the muon anti-neutrino charged current double differential cross section  
1535 with no pions in the final state on water using the pi-zero detector at T2K*. PhD thesis, Colorado State  
1536 University, Fort Collins, Colorado, USA, 2018. Available at <https://hdl.handle.net/10217/189329>. 16,  
1537 17, 21, 139
- 1538 [10] G. Welch and G. Bishop, “An introduction to the Kalman filter,” Tech. Rep. 95041, University of North  
1539 Carolina at Chapel Hill, Chapel Hill, NC 27599-3175, July 2006. 17
- 1540 [11] A. A. G. Soto, *Study of the  $\nu_\mu$  interactions via charged current in the T2K near detector*. PhD thesis,  
1541 Universitat Autònoma de Barcelona, 2017. Available at <http://hdl.handle.net/10803/405705>. 18
- 1542 [12] T. Campbell *et al.*, “Analysis of  $\nu_\mu$  Charged Current Inclusive Events in the PØD in Runs 1+2+3+4,”  
1543 Mar. 2014. T2K-TN-80 v4. 19
- 1544 [13] T. Campbell *et al.*, “The anumu/numu cross sections ratio with the P0D+TPC samples,” 2017. 19, 59
- 1545 [14] S. Agostinelli *et al.*, “GEANT4: A Simulation toolkit,” *Nucl. Instrum. Meth.*, vol. A506, pp. 250–303,  
1546 2003. 24

- 1547 [15] M. Martini *et al.*, “A unified approach for nucleon knock-out, coherent and incoherent pion production  
 1548 in neutrino interactions with nuclei,” *Phys. Rev.*, vol. C80, p. 065501, 2009. 28, 72
- 1549 [16] T. Hastie *et al.*, *The Elements of Statistical Learning: Data Mining, Inference, and Prediction*. Springer  
 1550 Series in Statistics, New York, NY: Springer New York, 2009. 46, 71, 140, 142, 144
- 1551 [17] C. V. C. Wret, *Minimising Systematic Uncertainties in the T2K Experiment Using Near-  
 1552 Detector and External Data.* PhD thesis, Imperial College London, 2019. Available at  
 1553 <https://t2k.org/docs/thesis/097/clarencewretthesis>. 48, 56, 57, 72, 74
- 1554 [18] S. Bienstock *et al.*, “Constraining the Flux and Cross Section Models with Data from the ND280  
 1555 Detector using FGD1 and FGD2 for the 2017 Joint Oscillation Analysis,” 2017. T2K-TN-324. 48, 126,  
 1556 146, 214
- 1557 [19] N. Abgrall *et al.*, “Measurements of  $\pi^\pm$ ,  $k^\pm$ ,  $k_s^0$ ,  $\lambda$  and proton production in proton-carbon interactions  
 1558 at 31 GeV/c with the na61/shine spectrometer at the CERN SPS,” *Eur. Phys. J. C*, vol. 76, p. 84,  
 1559 2016. 48
- 1560 [20] S. Assylbekov *et al.*, “The T2K ND280 off-axis pi-zero detector,” *Nucl. Instrum. Meth.*, vol. A686,  
 1561 pp. 48–63, 2012. 58
- 1562 [21] W. Toki, “Update of P0D Inspection.” Private communication, June 2016. 58
- 1563 [22] T. Yuan *et al.*, “Double differential measurement of the flux averaged  $\nu_\mu$  CC0Pi cross section on water,”  
 1564 Aug. 2016. T2K-TN-258 v4.6.1. 63
- 1565 [23] O. Benhar *et al.*, “Spectral function of finite nuclei and scattering of GeV electrons,” *Nucl. Phys.*,  
 1566 vol. A579, pp. 193–517, 1994. 72
- 1567 [24] L. H. Chan *et al.*, “Nucleon form factors and their interpretation,” *Phys. Rev.*, vol. 141, pp. 1298–1307,  
 1568 Jan. 1966. 72
- 1569 [25] C. H. Llewellyn Smith, “Neutrino reactions at accelerator energies,” *Phys. Rept.*, vol. 3, pp. 261–379,  
 1570 1972. 72
- 1571 [26] R. Smith and E. Moniz, “Neutrino reactions on nuclear targets,” *Nucl. Phys. B*, vol. 43, pp. 605–622,  
 1572 1972. 72
- 1573 [27] K. Niewczas and J. Sobczyk, “Search for nucleon-nucleon correlations in neutrino-argon scattering,”  
 1574 *Phys. Rev.*, vol. C93, no. 3, p. 035502, 2016. 72

- 1575 [28] R. Bradford *et al.*, “A new parameterization of the nucleon elastic form factors,” *Nucl. Phys.*, vol. B159,  
 1576 no. 127, 2006. 72
- 1577 [29] G. Co’, “Random phase approximation and neutrino-nucleus cross sections,” *Acta Phys. Polon.*,  
 1578 vol. B37, pp. 2235–2242, 2006. 72
- 1579 [30] J. Nieves *et al.*, “Inclusive charged-current neutrino-nucleus reactions,” *Phys. Rev.*, vol. C83, p. 045501,  
 1580 2011. 72, 73
- 1581 [31] R. T. Farouki, “The Bernstein polynomial basis: A centennial retrospective,” *Computer Aided Geometric  
 1582 Design*, vol. 29, no. 6, pp. 379–419, 2012. 73
- 1583 [32] K. M. Graczyk *et al.*, “Electroweak form factors of the  $\Delta(1232)$  resonance,” *Phys. Rev. D*, vol. 90,  
 1584 p. 093001, Nov. 2014. 73
- 1585 [33] K. M. Graczyk *et al.*, “ $C_A^5$  axial form factor from bubble chamber experiments,” *Phys. Rev.*, vol. D80,  
 1586 p. 093001, 2009. 73
- 1587 [34] K. M. Graczyk and J. T. Sobczyk, “Form factors in the quark resonance model,” *Phys. Rev. D*, vol. 77,  
 1588 p. 053001, Mar. 2008. 73
- 1589 [35] D. Rein and L. M. Sehgal, “Neutrino-excitation of baryon resonances and single pion production,” *Ann.  
 1590 Phys.*, vol. 133, no. 1, pp. 79–153, 1981. 73
- 1591 [36] K. M. Graczyk and J. Sobczyk, “Lepton mass effects in weak charged current single pion production,”  
 1592 *Phys. Rev. D*, vol. 77, p. 053003, Mar. 2008. 73
- 1593 [37] C. Berger and L. M. Seghal, “Lepton mass effects in single pion production by neutrinos,” *Phys. Rev.  
 1594 D*, vol. 76, p. 113004, Dec. 2007. 73, 74
- 1595 [38] T. Kitagaki *et al.*, “Charged-current exclusive pion production in neutrino-deuterium interactions,”  
 1596 *Phys. Rev. D*, vol. 34, pp. 2554–2565, Nov. 1986. 73
- 1597 [39] G. M. Radecky *et al.*, “Study of single-pion production by weak charged currents in low-energy  $\nu d$   
 1598 interactions,” *Phys. Rev. D*, vol. 25, pp. 1161–1173, Mar. 1982. 73
- 1599 [40] K. Abe *et al.*, “Measurement of coherent  $\pi^+$  production in low energy neutrino-carbon scattering,”  
 1600 *Phys. Rev. Lett.*, vol. 117, NOV 4 2016. 74
- 1601 [41] D. Rein and L. M. Sehgal, “Coherent  $\pi^0$  production in neutrino reactions,” *Nucl. Phys. B*, vol. 223,  
 1602 no. 1, pp. 29–44, 1983. 74

- 1603 [42] T. Golan *et al.*, “Final state interactions effects in neutrino-nucleus interactions,” *Phys. Rev. C*, vol. 86,  
1604 p. 015505, 2012. 74
- 1605 [43] L. Salcedo *et al.*, “Computer simulation of inclusive pion nuclear reactions,” *Nucl. Phys. A*, vol. 484,  
1606 no. 3, pp. 557–592, 1988. 74
- 1607 [44] G. Rowe *et al.*, “Energy-dependent phase shift analysis of pion-nucleon scattering below 400 MeV,”  
1608 *Phys. Rev. C*, vol. 18, pp. 584–589, July 1978. 74
- 1609 [45] G. Cowan *et al.*, “Asymptotic formulae for likelihood-based tests of new physics,” *Eur. Phys. J.*, vol. C71,  
1610 p. 1554, 2011. [Erratum: Eur. Phys. J.C73,2501(2013)]. 79
- 1611 [46] P. A. Amaudruz *et al.*, “The T2K fine grain detectors,” *Nucl. Instrum. Meth. A*, vol. A696, pp. 1–31,  
1612 2012. 125
- 1613 [47] A. Longhin *et al.*, “Measurement of the inclusive charged-current numu cross section in plastic using  
1614 the ND280 tracker Run 5c data,” tech. rep., T2K Collaboration, 2016. T2K-TN-249v8. 125
- 1615 [48] F. Lodovico and P. Martins, “Measurement of the charged current coherent pion production cross-section  
1616 on carbon and oxygen using the ND280 tracker,” tech. rep., T2K Collaboration, 2017. T2K-TN-290.  
1617 125
- 1618 [49] J. Schwehr, *Measurement of the Differential Charged Current Single Pion Cross Section Using Muon  
1619 Momentum and Muon Angle In the pi-ero detector of the T2K Experiment*. PhD thesis, Colorado State  
1620 University, Fort Collins, Colorado, 2018. Available at <https://hdl.handle.net/10217/189398>. 125
- 1621 [50] J. A. Morrison, *Effect of New Samples in the T2K Off-Axis Near Detector for the T2K Oscilla-  
1622 tion Analysis*. PhD thesis, Michigan State University, East Lansing, Michigan, 2019. Available at  
1623 <https://doi.org/10.25335/hy4e-wy68>. 126
- 1624 [51] K. Abe *et al.*, “Search for CP violation in neutrino and antineutrino oscillations by the T2K experiment  
1625 with  $2.2 \times 10^{21}$  protons on target,” *Phys. Rev. Lett.*, vol. 121, no. 17, p. 171802, 2018. 137, 138, 139
- 1626 [52] J. Friedman *et al.*, “Regularization paths for generalized linear models via coordinate descent,” *Journal  
1627 of Statistical Software, Articles*, vol. 33, no. 1, pp. 1–22, 2010. 143
- 1628 [53] T. Hastie *et al.*, *Statistical Learning with Sparsity: The Lasso and Generalizations*. Chapman and  
1629 Hall/CRC monographs on statistics and applied probability, Boca Raton: CRC Press, Taylor and  
1630 Francis Group, 2015. 144

<sub>1631</sub> [54] R. Brun and F. Rademakers, “ROOT - An object oriented data analysis framework,” *Nucl. Instrum.*

<sub>1632</sub> *Meth. A*, vol. 389, no. 1, pp. 81 – 86, 1997. See also <http://root.cern.ch/>. 239

<sub>1633</sub> **Appendix A**

<sub>1634</sub> **The PØD-Only Bin Normalization Parameters**

<sub>1636</sub> The observable normalizations used in the PØD-only BANFF fit are tabulated here. In Table A.1 on page  
<sub>1637</sub> 154, FHC mode is assumed unless RHC mode is specified and the initialisms “1-Trk”, “N-Trks”, “Wtr”, and  
<sub>1638</sub> “Air” represent the 1-Track selection, N-Tracks selection, PØD water-in mode, and PØD water-out mode,  
<sub>1639</sub> respectively.

---

Table A.1: Observable normalization fit bins.

Fit Index	Sample	p [GeV/c]	$\cos\theta$	Prefit
100	$\nu_\mu$ 1-Trk Wtr	$0 \leq p < 0.40$	$-1 \leq \cos\theta < 0.70$	$1.21 \pm 0.67$
101		$0.40 \leq p < 0.60$	$-1 \leq \cos\theta < 0.70$	$0.87 \pm 0.18$
102		$0.60 \leq p < 0.80$	$-1 \leq \cos\theta < 0.70$	$1.12 \pm 0.44$
103		$0.80 \leq p < 1.25$	$-1 \leq \cos\theta < 0.70$	$1.13 \pm 0.43$
104		$1.25 \leq p < 2.00$	$-1 \leq \cos\theta < 0.70$	$1.02 \pm 0.17$
105		$2.00 \leq p < 3.00$	$-1 \leq \cos\theta < 0.70$	$0.93 \pm 0.20$
106		$3.00 \leq p < 4.00$	$-1 \leq \cos\theta < 0.70$	$1.00 \pm 0.28$
107		$4.00 \leq p < 5.50$	$-1 \leq \cos\theta < 0.70$	$0.82 \pm 0.33$
108		$5.50 \leq p < 30$	$-1 \leq \cos\theta < 0.70$	$1.26 \pm 0.58$
109		$0 \leq p < 0.40$	$0.70 \leq \cos\theta < 0.80$	$1.27 \pm 0.74$
110	$\nu_\mu$ 1-Trk Wtr	$0.40 \leq p < 0.60$	$0.70 \leq \cos\theta < 0.80$	$0.89 \pm 0.18$
111		$0.60 \leq p < 0.80$	$0.70 \leq \cos\theta < 0.80$	$1.02 \pm 0.27$

Fit Index	Sample	p [GeV/c]	$\cos\theta$	Prefit
112		$0.80 \leq p < 1.25$	$0.70 \leq \cos\theta < 0.80$	$1.09 \pm 0.33$
113		$1.25 \leq p < 2.00$	$0.70 \leq \cos\theta < 0.80$	$1.02 \pm 0.17$
114		$2.00 \leq p < 3.00$	$0.70 \leq \cos\theta < 0.80$	$0.96 \pm 0.15$
115		$3.00 \leq p < 4.00$	$0.70 \leq \cos\theta < 0.80$	$0.99 \pm 0.21$
116		$4.00 \leq p < 5.50$	$0.70 \leq \cos\theta < 0.80$	$0.94 \pm 0.29$
117		$5.50 \leq p < 30$	$0.70 \leq \cos\theta < 0.80$	$1.05 \pm 0.53$
118		$0 \leq p < 0.40$	$0.80 \leq \cos\theta < 0.94$	$1.33 \pm 0.78$
119		$0.40 \leq p < 0.60$	$0.80 \leq \cos\theta < 0.94$	$0.91 \pm 0.21$
120	$\nu_\mu$ 1-Trk Wtr	$0.60 \leq p < 0.80$	$0.80 \leq \cos\theta < 0.94$	$0.97 \pm 0.14$
121		$0.80 \leq p < 1.25$	$0.80 \leq \cos\theta < 0.94$	$1.03 \pm 0.17$
122		$1.25 \leq p < 2.00$	$0.80 \leq \cos\theta < 0.94$	$1.01 \pm 0.09$
123		$2.00 \leq p < 3.00$	$0.80 \leq \cos\theta < 0.94$	$1.00 \pm 0.05$
124		$3.00 \leq p < 4.00$	$0.80 \leq \cos\theta < 0.94$	$1.00 \pm 0.12$
125		$4.00 \leq p < 5.50$	$0.80 \leq \cos\theta < 0.94$	$0.95 \pm 0.15$
126		$5.50 \leq p < 30$	$0.80 \leq \cos\theta < 0.94$	$0.96 \pm 0.38$
127		$0 \leq p < 0.40$	$0.94 \leq \cos\theta < 0.97$	$1.29 \pm 0.73$
128		$0.40 \leq p < 0.60$	$0.94 \leq \cos\theta < 0.97$	$0.93 \pm 0.22$
129		$0.60 \leq p < 0.80$	$0.94 \leq \cos\theta < 0.97$	$0.96 \pm 0.09$
130	$\nu_\mu$ 1-Trk Wtr	$0.80 \leq p < 1.25$	$0.94 \leq \cos\theta < 0.97$	$1.02 \pm 0.11$
131		$1.25 \leq p < 2.00$	$0.94 \leq \cos\theta < 0.97$	$1.00 \pm 0.07$
132		$2.00 \leq p < 3.00$	$0.94 \leq \cos\theta < 0.97$	$1.00 \pm 0.03$
133		$3.00 \leq p < 4.00$	$0.94 \leq \cos\theta < 0.97$	$0.99 \pm 0.08$
134		$4.00 \leq p < 5.50$	$0.94 \leq \cos\theta < 0.97$	$1.00 \pm 0.14$
135		$5.50 \leq p < 30$	$0.94 \leq \cos\theta < 0.97$	$0.99 \pm 0.20$
136		$0 \leq p < 0.40$	$0.97 \leq \cos\theta < 0.99$	$1.25 \pm 0.65$
137		$0.40 \leq p < 0.60$	$0.97 \leq \cos\theta < 0.99$	$0.94 \pm 0.20$
138		$0.60 \leq p < 0.80$	$0.97 \leq \cos\theta < 0.99$	$0.95 \pm 0.08$
139		$0.80 \leq p < 1.25$	$0.97 \leq \cos\theta < 0.99$	$1.01 \pm 0.11$
140	$\nu_\mu$ 1-Trk Wtr	$1.25 \leq p < 2.00$	$0.97 \leq \cos\theta < 0.99$	$1.00 \pm 0.07$
141		$2.00 \leq p < 3.00$	$0.97 \leq \cos\theta < 0.99$	$1.00 \pm 0.06$
142		$3.00 \leq p < 4.00$	$0.97 \leq \cos\theta < 0.99$	$1.00 \pm 0.03$

Fit Index	Sample	$p$ [GeV/c]	$\cos\theta$	Prefit
143		$4.00 \leq p < 5.50$	$0.97 \leq \cos\theta < 0.99$	$0.98 \pm 0.10$
144		$5.50 \leq p < 30$	$0.97 \leq \cos\theta < 0.99$	$0.97 \pm 0.14$
145		$0 \leq p < 0.40$	$0.99 \leq \cos\theta < 1$	$1.25 \pm 0.58$
146		$0.40 \leq p < 0.60$	$0.99 \leq \cos\theta < 1$	$0.93 \pm 0.18$
147		$0.60 \leq p < 0.80$	$0.99 \leq \cos\theta < 1$	$0.96 \pm 0.11$
148		$0.80 \leq p < 1.25$	$0.99 \leq \cos\theta < 1$	$1.01 \pm 0.11$
149		$1.25 \leq p < 2.00$	$0.99 \leq \cos\theta < 1$	$1.01 \pm 0.08$
150	$\nu_\mu$ 1-Trk Wtr	$2.00 \leq p < 3.00$	$0.99 \leq \cos\theta < 1$	$1.01 \pm 0.10$
151		$3.00 \leq p < 4.00$	$0.99 \leq \cos\theta < 1$	$1.00 \pm 0.06$
152		$4.00 \leq p < 5.50$	$0.99 \leq \cos\theta < 1$	$1.00 \pm 0.05$
153		$5.50 \leq p < 30$	$0.99 \leq \cos\theta < 1$	$0.98 \pm 0.10$
154	$\nu_\mu$ N-Trks Wtr	$0 \leq p < 0.40$	$-1 \leq \cos\theta < 0.77$	$1.18 \pm 0.61$
155		$0.40 \leq p < 0.60$	$-1 \leq \cos\theta < 0.77$	$0.89 \pm 0.15$
156		$0.60 \leq p < 0.80$	$-1 \leq \cos\theta < 0.77$	$1.01 \pm 0.16$
157		$0.80 \leq p < 1.20$	$-1 \leq \cos\theta < 0.77$	$1.03 \pm 0.19$
158		$1.20 \leq p < 2.20$	$-1 \leq \cos\theta < 0.77$	$1.02 \pm 0.15$
159		$2.20 \leq p < 3.50$	$-1 \leq \cos\theta < 0.77$	$1.04 \pm 0.16$
160	$\nu_\mu$ N-Trks Wtr	$3.50 \leq p < 10.0$	$-1 \leq \cos\theta < 0.77$	$0.93 \pm 0.26$
161		$10.0 \leq p < 30$	$-1 \leq \cos\theta < 0.77$	$0.94 \pm 0.67$
162		$0 \leq p < 0.40$	$0.77 \leq \cos\theta < 0.85$	$1.13 \pm 0.56$
163		$0.40 \leq p < 0.60$	$0.77 \leq \cos\theta < 0.85$	$0.92 \pm 0.15$
164		$0.60 \leq p < 0.80$	$0.77 \leq \cos\theta < 0.85$	$0.98 \pm 0.07$
165		$0.80 \leq p < 1.20$	$0.77 \leq \cos\theta < 0.85$	$1.00 \pm 0.09$
166		$1.20 \leq p < 2.20$	$0.77 \leq \cos\theta < 0.85$	$1.01 \pm 0.08$
167		$2.20 \leq p < 3.50$	$0.77 \leq \cos\theta < 0.85$	$1.01 \pm 0.06$
168		$3.50 \leq p < 10.0$	$0.77 \leq \cos\theta < 0.85$	$0.98 \pm 0.16$
169		$10.0 \leq p < 30$	$0.77 \leq \cos\theta < 0.85$	$0.98 \pm 0.52$
170	$\nu_\mu$ N-Trks Wtr	$0 \leq p < 0.40$	$0.85 \leq \cos\theta < 0.90$	$1.13 \pm 0.53$
171		$0.40 \leq p < 0.60$	$0.85 \leq \cos\theta < 0.90$	$0.92 \pm 0.14$
172		$0.60 \leq p < 0.80$	$0.85 \leq \cos\theta < 0.90$	$0.98 \pm 0.05$
173		$0.80 \leq p < 1.20$	$0.85 \leq \cos\theta < 0.90$	$1.00 \pm 0.07$

Fit Index	Sample	p [GeV/c]	$\cos\theta$	Prefit
174		$1.20 \leq p < 2.20$	$0.85 \leq \cos\theta < 0.90$	$1.00 \pm 0.06$
175		$2.20 \leq p < 3.50$	$0.85 \leq \cos\theta < 0.90$	$1.01 \pm 0.05$
176		$3.50 \leq p < 10.0$	$0.85 \leq \cos\theta < 0.90$	$0.99 \pm 0.12$
177		$10.0 \leq p < 30$	$0.85 \leq \cos\theta < 0.90$	$1.03 \pm 0.46$
178		$0 \leq p < 0.40$	$0.90 \leq \cos\theta < 0.97$	$1.13 \pm 0.52$
179		$0.40 \leq p < 0.60$	$0.90 \leq \cos\theta < 0.97$	$0.94 \pm 0.13$
180	$\nu_\mu$ N-Trks Wtr	$0.60 \leq p < 0.80$	$0.90 \leq \cos\theta < 0.97$	$0.97 \pm 0.06$
181		$0.80 \leq p < 1.20$	$0.90 \leq \cos\theta < 0.97$	$0.99 \pm 0.08$
182		$1.20 \leq p < 2.20$	$0.90 \leq \cos\theta < 0.97$	$1.00 \pm 0.07$
183		$2.20 \leq p < 3.50$	$0.90 \leq \cos\theta < 0.97$	$1.00 \pm 0.03$
184		$3.50 \leq p < 10.0$	$0.90 \leq \cos\theta < 0.97$	$0.99 \pm 0.10$
185		$10.0 \leq p < 30$	$0.90 \leq \cos\theta < 0.97$	$0.98 \pm 0.25$
186		$0 \leq p < 0.40$	$0.97 \leq \cos\theta < 1$	$1.09 \pm 0.47$
187		$0.40 \leq p < 0.60$	$0.97 \leq \cos\theta < 1$	$0.96 \pm 0.11$
188		$0.60 \leq p < 0.80$	$0.97 \leq \cos\theta < 1$	$0.96 \pm 0.09$
189		$0.80 \leq p < 1.20$	$0.97 \leq \cos\theta < 1$	$1.00 \pm 0.09$
190	$\nu_\mu$ N-Trks Wtr	$1.20 \leq p < 2.20$	$0.97 \leq \cos\theta < 1$	$1.01 \pm 0.09$
191		$2.20 \leq p < 3.50$	$0.97 \leq \cos\theta < 1$	$1.01 \pm 0.08$
192		$3.50 \leq p < 10.0$	$0.97 \leq \cos\theta < 1$	$0.99 \pm 0.05$
193		$10.0 \leq p < 30$	$0.97 \leq \cos\theta < 1$	$0.97 \pm 0.13$
194	$\bar{\nu}_\mu$ RHC 1-Trk Wtr	$0 \leq p < 0.50$	$-1 \leq \cos\theta < 0.82$	$1.00 \pm 0.36$
195		$0.50 \leq p < 0.60$	$-1 \leq \cos\theta < 0.82$	$0.90 \pm 0.15$
196		$0.60 \leq p < 0.80$	$-1 \leq \cos\theta < 0.82$	$1.05 \pm 0.26$
197		$0.80 \leq p < 1.25$	$-1 \leq \cos\theta < 0.82$	$1.04 \pm 0.20$
198		$1.25 \leq p < 2.00$	$-1 \leq \cos\theta < 0.82$	$1.00 \pm 0.17$
199		$2.00 \leq p < 3.00$	$-1 \leq \cos\theta < 0.82$	$1.01 \pm 0.17$
200	$\bar{\nu}_\mu$ RHC 1-Trk Wtr	$3.00 \leq p < 30$	$-1 \leq \cos\theta < 0.82$	$1.00 \pm 0.39$
201		$0 \leq p < 0.50$	$0.82 \leq \cos\theta < 0.90$	$1.06 \pm 0.43$
202		$0.50 \leq p < 0.60$	$0.82 \leq \cos\theta < 0.90$	$0.91 \pm 0.13$
203		$0.60 \leq p < 0.80$	$0.82 \leq \cos\theta < 0.90$	$0.97 \pm 0.16$
204		$0.80 \leq p < 1.25$	$0.82 \leq \cos\theta < 0.90$	$1.04 \pm 0.17$

Fit Index	Sample	p [GeV/c]	$\cos\theta$	Prefit
205		$1.25 \leq p < 2.00$	$0.82 \leq \cos\theta < 0.90$	$1.00 \pm 0.11$
206		$2.00 \leq p < 3.00$	$0.82 \leq \cos\theta < 0.90$	$0.99 \pm 0.11$
207		$3.00 \leq p < 30$	$0.82 \leq \cos\theta < 0.90$	$0.92 \pm 0.28$
208		$0 \leq p < 0.50$	$0.90 \leq \cos\theta < 0.95$	$1.07 \pm 0.44$
209		$0.50 \leq p < 0.60$	$0.90 \leq \cos\theta < 0.95$	$0.93 \pm 0.14$
210	$\bar{\nu}_\mu$ RHC 1-Trk Wtr	$0.60 \leq p < 0.80$	$0.90 \leq \cos\theta < 0.95$	$0.96 \pm 0.11$
211		$0.80 \leq p < 1.25$	$0.90 \leq \cos\theta < 0.95$	$1.03 \pm 0.14$
212		$1.25 \leq p < 2.00$	$0.90 \leq \cos\theta < 0.95$	$1.01 \pm 0.08$
213		$2.00 \leq p < 3.00$	$0.90 \leq \cos\theta < 0.95$	$0.98 \pm 0.06$
214		$3.00 \leq p < 30$	$0.90 \leq \cos\theta < 0.95$	$0.95 \pm 0.17$
215		$0 \leq p < 0.50$	$0.95 \leq \cos\theta < 0.99$	$1.08 \pm 0.45$
216		$0.50 \leq p < 0.60$	$0.95 \leq \cos\theta < 0.99$	$0.93 \pm 0.16$
217		$0.60 \leq p < 0.80$	$0.95 \leq \cos\theta < 0.99$	$0.96 \pm 0.09$
218		$0.80 \leq p < 1.25$	$0.95 \leq \cos\theta < 0.99$	$1.02 \pm 0.12$
219		$1.25 \leq p < 2.00$	$0.95 \leq \cos\theta < 0.99$	$1.01 \pm 0.07$
220	$\bar{\nu}_\mu$ RHC 1-Trk Wtr	$2.00 \leq p < 3.00$	$0.95 \leq \cos\theta < 0.99$	$1.00 \pm 0.04$
221		$3.00 \leq p < 30$	$0.95 \leq \cos\theta < 0.99$	$0.98 \pm 0.09$
222		$0 \leq p < 0.50$	$0.99 \leq \cos\theta < 1$	$1.09 \pm 0.43$
223		$0.50 \leq p < 0.60$	$0.99 \leq \cos\theta < 1$	$0.94 \pm 0.15$
224		$0.60 \leq p < 0.80$	$0.99 \leq \cos\theta < 1$	$0.93 \pm 0.10$
225		$0.80 \leq p < 1.25$	$0.99 \leq \cos\theta < 1$	$1.02 \pm 0.12$
226		$1.25 \leq p < 2.00$	$0.99 \leq \cos\theta < 1$	$1.01 \pm 0.08$
227		$2.00 \leq p < 3.00$	$0.99 \leq \cos\theta < 1$	$1.00 \pm 0.07$
228		$3.00 \leq p < 30$	$0.99 \leq \cos\theta < 1$	$0.99 \pm 0.05$
229	$\bar{\nu}_\mu$ RHC N-Trks Wtr	$0 \leq p < 0.50$	$-1 \leq \cos\theta < 0.89$	$1.02 \pm 0.34$
230		$0.50 \leq p < 0.90$	$-1 \leq \cos\theta < 0.89$	$1.00 \pm 0.09$
231		$0.90 \leq p < 1.25$	$-1 \leq \cos\theta < 0.89$	$1.01 \pm 0.07$
232		$1.25 \leq p < 1.60$	$-1 \leq \cos\theta < 0.89$	$0.99 \pm 0.13$
233		$1.60 \leq p < 3.00$	$-1 \leq \cos\theta < 0.89$	$0.99 \pm 0.11$
234		$3.00 \leq p < 30$	$-1 \leq \cos\theta < 0.89$	$0.98 \pm 0.33$
235		$0 \leq p < 0.50$	$0.89 \leq \cos\theta < 0.95$	$1.05 \pm 0.34$

Fit Index	Sample	$p$ [GeV/c]	$\cos\theta$	Prefit
236		$0.50 \leq p < 0.90$	$0.89 \leq \cos\theta < 0.95$	$0.97 \pm 0.05$
237		$0.90 \leq p < 1.25$	$0.89 \leq \cos\theta < 0.95$	$1.02 \pm 0.06$
238		$1.25 \leq p < 1.60$	$0.89 \leq \cos\theta < 0.95$	$0.98 \pm 0.09$
239		$1.60 \leq p < 3.00$	$0.89 \leq \cos\theta < 0.95$	$0.99 \pm 0.06$
240	$\bar{\nu}_\mu$ RHC N-Trks Wtr	$3.00 \leq p < 30$	$0.89 \leq \cos\theta < 0.95$	$0.98 \pm 0.14$
241		$0 \leq p < 0.50$	$0.95 \leq \cos\theta < 0.97$	$1.04 \pm 0.36$
242		$0.50 \leq p < 0.90$	$0.95 \leq \cos\theta < 0.97$	$0.97 \pm 0.05$
243		$0.90 \leq p < 1.25$	$0.95 \leq \cos\theta < 0.97$	$1.01 \pm 0.05$
244		$1.25 \leq p < 1.60$	$0.95 \leq \cos\theta < 0.97$	$1.00 \pm 0.09$
245		$1.60 \leq p < 3.00$	$0.95 \leq \cos\theta < 0.97$	$1.01 \pm 0.06$
246		$3.00 \leq p < 30$	$0.95 \leq \cos\theta < 0.97$	$0.98 \pm 0.12$
247		$0 \leq p < 0.50$	$0.97 \leq \cos\theta < 0.99$	$1.03 \pm 0.37$
248		$0.50 \leq p < 0.90$	$0.97 \leq \cos\theta < 0.99$	$1.01 \pm 0.05$
249		$0.90 \leq p < 1.25$	$0.97 \leq \cos\theta < 0.99$	$1.00 \pm 0.05$
250	$\bar{\nu}_\mu$ RHC N-Trks Wtr	$1.25 \leq p < 1.60$	$0.97 \leq \cos\theta < 0.99$	$0.99 \pm 0.07$
251		$1.60 \leq p < 3.00$	$0.97 \leq \cos\theta < 0.99$	$1.01 \pm 0.07$
252		$3.00 \leq p < 30$	$0.97 \leq \cos\theta < 0.99$	$0.99 \pm 0.07$
253		$0 \leq p < 0.50$	$0.99 \leq \cos\theta < 1$	$1.07 \pm 0.39$
254		$0.50 \leq p < 0.90$	$0.99 \leq \cos\theta < 1$	$0.98 \pm 0.07$
255		$0.90 \leq p < 1.25$	$0.99 \leq \cos\theta < 1$	$1.02 \pm 0.08$
256		$1.25 \leq p < 1.60$	$0.99 \leq \cos\theta < 1$	$1.01 \pm 0.08$
257		$1.60 \leq p < 3.00$	$0.99 \leq \cos\theta < 1$	$0.99 \pm 0.09$
258		$3.00 \leq p < 30$	$0.99 \leq \cos\theta < 1$	$0.99 \pm 0.06$
259	$\nu_\mu$ RHC 1-Trk Wtr	$0 \leq p < 0.40$	$-1 \leq \cos\theta < 0.78$	$1.24 \pm 0.60$
260		$0.40 \leq p < 0.60$	$-1 \leq \cos\theta < 0.78$	$0.91 \pm 0.16$
261		$0.60 \leq p < 0.80$	$-1 \leq \cos\theta < 0.78$	$1.00 \pm 0.13$
262		$0.80 \leq p < 1.10$	$-1 \leq \cos\theta < 0.78$	$1.02 \pm 0.21$
263		$1.10 \leq p < 2.00$	$-1 \leq \cos\theta < 0.78$	$1.03 \pm 0.17$
264		$2.00 \leq p < 10.0$	$-1 \leq \cos\theta < 0.78$	$0.99 \pm 0.21$
265		$0 \leq p < 0.40$	$0.78 \leq \cos\theta < 0.84$	$1.27 \pm 0.64$
266		$0.40 \leq p < 0.60$	$0.78 \leq \cos\theta < 0.84$	$0.95 \pm 0.16$

Fit Index	Sample	p [GeV/c]	$\cos\theta$	Prefit
267		$0.60 \leq p < 0.80$	$0.78 \leq \cos\theta < 0.84$	$0.99 \pm 0.06$
268		$0.80 \leq p < 1.10$	$0.78 \leq \cos\theta < 0.84$	$0.98 \pm 0.11$
269		$1.10 \leq p < 2.00$	$0.78 \leq \cos\theta < 0.84$	$1.04 \pm 0.14$
270	$\nu_\mu$ RHC 1-Trk Wtr	$2.00 \leq p < 10.0$	$0.78 \leq \cos\theta < 0.84$	$0.99 \pm 0.16$
271		$0 \leq p < 0.40$	$0.84 \leq \cos\theta < 0.92$	$1.20 \pm 0.60$
272		$0.40 \leq p < 0.60$	$0.84 \leq \cos\theta < 0.92$	$0.95 \pm 0.20$
273		$0.60 \leq p < 0.80$	$0.84 \leq \cos\theta < 0.92$	$0.97 \pm 0.07$
274		$0.80 \leq p < 1.10$	$0.84 \leq \cos\theta < 0.92$	$1.00 \pm 0.08$
275		$1.10 \leq p < 2.00$	$0.84 \leq \cos\theta < 0.92$	$1.00 \pm 0.08$
276		$2.00 \leq p < 10.0$	$0.84 \leq \cos\theta < 0.92$	$1.00 \pm 0.10$
277		$0 \leq p < 0.40$	$0.92 \leq \cos\theta < 0.95$	$1.10 \pm 0.52$
278		$0.40 \leq p < 0.60$	$0.92 \leq \cos\theta < 0.95$	$0.99 \pm 0.16$
279		$0.60 \leq p < 0.80$	$0.92 \leq \cos\theta < 0.95$	$0.95 \pm 0.06$
280	$\nu_\mu$ RHC 1-Trk Wtr	$0.80 \leq p < 1.10$	$0.92 \leq \cos\theta < 0.95$	$0.99 \pm 0.04$
281		$1.10 \leq p < 2.00$	$0.92 \leq \cos\theta < 0.95$	$1.00 \pm 0.07$
282		$2.00 \leq p < 10.0$	$0.92 \leq \cos\theta < 0.95$	$1.00 \pm 0.06$
283		$0 \leq p < 0.40$	$0.95 \leq \cos\theta < 0.98$	$1.19 \pm 0.50$
284		$0.40 \leq p < 0.60$	$0.95 \leq \cos\theta < 0.98$	$0.98 \pm 0.15$
285		$0.60 \leq p < 0.80$	$0.95 \leq \cos\theta < 0.98$	$0.96 \pm 0.09$
286		$0.80 \leq p < 1.10$	$0.95 \leq \cos\theta < 0.98$	$0.99 \pm 0.07$
287		$1.10 \leq p < 2.00$	$0.95 \leq \cos\theta < 0.98$	$1.00 \pm 0.06$
288		$2.00 \leq p < 10.0$	$0.95 \leq \cos\theta < 0.98$	$1.00 \pm 0.04$
289		$0 \leq p < 0.40$	$0.98 \leq \cos\theta < 0.99$	$1.12 \pm 0.46$
290	$\nu_\mu$ RHC 1-Trk Wtr	$0.40 \leq p < 0.60$	$0.98 \leq \cos\theta < 0.99$	$1.01 \pm 0.15$
291		$0.60 \leq p < 0.80$	$0.98 \leq \cos\theta < 0.99$	$0.98 \pm 0.09$
292		$0.80 \leq p < 1.10$	$0.98 \leq \cos\theta < 0.99$	$1.00 \pm 0.09$
293		$1.10 \leq p < 2.00$	$0.98 \leq \cos\theta < 0.99$	$0.98 \pm 0.07$
294		$2.00 \leq p < 10.0$	$0.98 \leq \cos\theta < 0.99$	$1.00 \pm 0.03$
295		$0 \leq p < 0.40$	$0.99 \leq \cos\theta < 1$	$1.29 \pm 0.47$
296		$0.40 \leq p < 0.60$	$0.99 \leq \cos\theta < 1$	$0.98 \pm 0.20$
297		$0.60 \leq p < 0.80$	$0.99 \leq \cos\theta < 1$	$0.95 \pm 0.16$

Fit Index	Sample	p [GeV/c]	$\cos\theta$	Prefit
298		$0.80 \leq p < 1.10$	$0.99 \leq \cos\theta < 1$	$1.03 \pm 0.10$
299		$1.10 \leq p < 2.00$	$0.99 \leq \cos\theta < 1$	$1.01 \pm 0.08$
300	$\nu_\mu$ RHC 1-Trk Wtr	$2.00 \leq p < 10.0$	$0.99 \leq \cos\theta < 1$	$1.00 \pm 0.03$
301	$\nu_\mu$ RHC N-Trks Wtr	$0 \leq p < 0.60$	$-1 \leq \cos\theta < 0.70$	$0.97 \pm 0.21$
302		$0.60 \leq p < 1.00$	$-1 \leq \cos\theta < 0.70$	$1.01 \pm 0.13$
303		$1.00 \leq p < 1.50$	$-1 \leq \cos\theta < 0.70$	$1.01 \pm 0.15$
304		$1.50 \leq p < 2.00$	$-1 \leq \cos\theta < 0.70$	$1.15 \pm 0.19$
305		$2.00 \leq p < 10.0$	$-1 \leq \cos\theta < 0.70$	$0.95 \pm 0.23$
306		$0 \leq p < 0.60$	$0.70 \leq \cos\theta < 0.80$	$1.00 \pm 0.26$
307		$0.60 \leq p < 1.00$	$0.70 \leq \cos\theta < 0.80$	$0.99 \pm 0.08$
308		$1.00 \leq p < 1.50$	$0.70 \leq \cos\theta < 0.80$	$1.01 \pm 0.11$
309		$1.50 \leq p < 2.00$	$0.70 \leq \cos\theta < 0.80$	$0.98 \pm 0.09$
310	$\nu_\mu$ RHC N-Trks Wtr	$2.00 \leq p < 10.0$	$0.70 \leq \cos\theta < 0.80$	$1.00 \pm 0.16$
311		$0 \leq p < 0.60$	$0.80 \leq \cos\theta < 0.85$	$1.01 \pm 0.28$
312		$0.60 \leq p < 1.00$	$0.80 \leq \cos\theta < 0.85$	$0.98 \pm 0.06$
313		$1.00 \leq p < 1.50$	$0.80 \leq \cos\theta < 0.85$	$1.00 \pm 0.08$
314		$1.50 \leq p < 2.00$	$0.80 \leq \cos\theta < 0.85$	$1.02 \pm 0.08$
315		$2.00 \leq p < 10.0$	$0.80 \leq \cos\theta < 0.85$	$0.98 \pm 0.11$
316		$0 \leq p < 0.60$	$0.85 \leq \cos\theta < 0.98$	$1.02 \pm 0.25$
317		$0.60 \leq p < 1.00$	$0.85 \leq \cos\theta < 0.98$	$0.98 \pm 0.07$
318		$1.00 \leq p < 1.50$	$0.85 \leq \cos\theta < 0.98$	$1.00 \pm 0.07$
319		$1.50 \leq p < 2.00$	$0.85 \leq \cos\theta < 0.98$	$1.00 \pm 0.07$
320	$\nu_\mu$ RHC N-Trks Wtr	$2.00 \leq p < 10.0$	$0.85 \leq \cos\theta < 0.98$	$1.00 \pm 0.06$
321		$0 \leq p < 0.60$	$0.98 \leq \cos\theta < 0.99$	$1.02 \pm 0.24$
322		$0.60 \leq p < 1.00$	$0.98 \leq \cos\theta < 0.99$	$0.96 \pm 0.10$
323		$1.00 \leq p < 1.50$	$0.98 \leq \cos\theta < 0.99$	$1.01 \pm 0.09$
324		$1.50 \leq p < 2.00$	$0.98 \leq \cos\theta < 0.99$	$0.99 \pm 0.09$
325		$2.00 \leq p < 10.0$	$0.98 \leq \cos\theta < 0.99$	$0.99 \pm 0.04$
326		$0 \leq p < 0.60$	$0.99 \leq \cos\theta < 1$	$1.00 \pm 0.25$
327		$0.60 \leq p < 1.00$	$0.99 \leq \cos\theta < 1$	$0.98 \pm 0.11$
328		$1.00 \leq p < 1.50$	$0.99 \leq \cos\theta < 1$	$1.00 \pm 0.09$

Fit Index	Sample	$p$ [GeV/c]	$\cos\theta$	Prefit
329		$1.50 \leq p < 2.00$	$0.99 \leq \cos\theta < 1$	$1.01 \pm 0.10$
330	$\nu_\mu$ RHC N-Trks Wtr	$2.00 \leq p < 10.0$	$0.99 \leq \cos\theta < 1$	$1.00 \pm 0.04$
331	$\nu_\mu$ 1-Trk Air	$0 \leq p < 0.40$	$-1 \leq \cos\theta < 0.70$	$1.17 \pm 0.66$
332		$0.40 \leq p < 0.60$	$-1 \leq \cos\theta < 0.70$	$0.86 \pm 0.19$
333		$0.60 \leq p < 0.80$	$-1 \leq \cos\theta < 0.70$	$1.17 \pm 0.53$
334		$0.80 \leq p < 1.25$	$-1 \leq \cos\theta < 0.70$	$1.15 \pm 0.44$
335		$1.25 \leq p < 2.00$	$-1 \leq \cos\theta < 0.70$	$0.97 \pm 0.19$
336		$2.00 \leq p < 3.00$	$-1 \leq \cos\theta < 0.70$	$1.02 \pm 0.19$
337		$3.00 \leq p < 4.00$	$-1 \leq \cos\theta < 0.70$	$1.02 \pm 0.31$
338		$4.00 \leq p < 5.50$	$-1 \leq \cos\theta < 0.70$	$0.97 \pm 0.37$
339		$5.50 \leq p < 30$	$-1 \leq \cos\theta < 0.70$	$0.88 \pm 0.62$
340	$\nu_\mu$ 1-Trk Air	$0 \leq p < 0.40$	$0.70 \leq \cos\theta < 0.80$	$1.27 \pm 0.75$
341		$0.40 \leq p < 0.60$	$0.70 \leq \cos\theta < 0.80$	$0.87 \pm 0.17$
342		$0.60 \leq p < 0.80$	$0.70 \leq \cos\theta < 0.80$	$1.04 \pm 0.31$
343		$0.80 \leq p < 1.25$	$0.70 \leq \cos\theta < 0.80$	$1.09 \pm 0.34$
344		$1.25 \leq p < 2.00$	$0.70 \leq \cos\theta < 0.80$	$1.01 \pm 0.18$
345		$2.00 \leq p < 3.00$	$0.70 \leq \cos\theta < 0.80$	$1.03 \pm 0.17$
346		$3.00 \leq p < 4.00$	$0.70 \leq \cos\theta < 0.80$	$0.94 \pm 0.27$
347		$4.00 \leq p < 5.50$	$0.70 \leq \cos\theta < 0.80$	$0.93 \pm 0.38$
348		$5.50 \leq p < 30$	$0.70 \leq \cos\theta < 0.80$	$1.00 \pm 0.58$
349		$0 \leq p < 0.40$	$0.80 \leq \cos\theta < 0.94$	$1.32 \pm 0.79$
350	$\nu_\mu$ 1-Trk Air	$0.40 \leq p < 0.60$	$0.80 \leq \cos\theta < 0.94$	$0.90 \pm 0.20$
351		$0.60 \leq p < 0.80$	$0.80 \leq \cos\theta < 0.94$	$0.98 \pm 0.17$
352		$0.80 \leq p < 1.25$	$0.80 \leq \cos\theta < 0.94$	$1.04 \pm 0.19$
353		$1.25 \leq p < 2.00$	$0.80 \leq \cos\theta < 0.94$	$1.01 \pm 0.10$
354		$2.00 \leq p < 3.00$	$0.80 \leq \cos\theta < 0.94$	$1.00 \pm 0.07$
355		$3.00 \leq p < 4.00$	$0.80 \leq \cos\theta < 0.94$	$0.97 \pm 0.14$
356		$4.00 \leq p < 5.50$	$0.80 \leq \cos\theta < 0.94$	$1.06 \pm 0.22$
357		$5.50 \leq p < 30$	$0.80 \leq \cos\theta < 0.94$	$1.00 \pm 0.33$
358		$0 \leq p < 0.40$	$0.94 \leq \cos\theta < 0.97$	$1.29 \pm 0.73$
359		$0.40 \leq p < 0.60$	$0.94 \leq \cos\theta < 0.97$	$0.91 \pm 0.20$

<b>Fit Index</b>	<b>Sample</b>	<b>p [GeV/c]</b>	<b>cosθ</b>	<b>Prefit</b>
360	$\nu_\mu$ 1-Trk Air	$0.60 \leq p < 0.80$	$0.94 \leq \cos \theta < 0.97$	$0.97 \pm 0.11$
361		$0.80 \leq p < 1.25$	$0.94 \leq \cos \theta < 0.97$	$1.02 \pm 0.12$
362		$1.25 \leq p < 2.00$	$0.94 \leq \cos \theta < 0.97$	$1.00 \pm 0.07$
363		$2.00 \leq p < 3.00$	$0.94 \leq \cos \theta < 0.97$	$1.01 \pm 0.04$
364		$3.00 \leq p < 4.00$	$0.94 \leq \cos \theta < 0.97$	$0.98 \pm 0.09$
365		$4.00 \leq p < 5.50$	$0.94 \leq \cos \theta < 0.97$	$0.98 \pm 0.15$
366		$5.50 \leq p < 30$	$0.94 \leq \cos \theta < 0.97$	$0.98 \pm 0.21$
367		$0 \leq p < 0.40$	$0.97 \leq \cos \theta < 0.99$	$1.23 \pm 0.68$
368		$0.40 \leq p < 0.60$	$0.97 \leq \cos \theta < 0.99$	$0.91 \pm 0.20$
369		$0.60 \leq p < 0.80$	$0.97 \leq \cos \theta < 0.99$	$0.98 \pm 0.12$
370	$\nu_\mu$ 1-Trk Air	$0.80 \leq p < 1.25$	$0.97 \leq \cos \theta < 0.99$	$1.02 \pm 0.11$
371		$1.25 \leq p < 2.00$	$0.97 \leq \cos \theta < 0.99$	$0.99 \pm 0.08$
372		$2.00 \leq p < 3.00$	$0.97 \leq \cos \theta < 0.99$	$1.01 \pm 0.06$
373		$3.00 \leq p < 4.00$	$0.97 \leq \cos \theta < 0.99$	$1.00 \pm 0.04$
374		$4.00 \leq p < 5.50$	$0.97 \leq \cos \theta < 0.99$	$0.98 \pm 0.11$
375		$5.50 \leq p < 30$	$0.97 \leq \cos \theta < 0.99$	$0.98 \pm 0.15$
376		$0 \leq p < 0.40$	$0.99 \leq \cos \theta < 1$	$1.21 \pm 0.58$
377		$0.40 \leq p < 0.60$	$0.99 \leq \cos \theta < 1$	$0.90 \pm 0.16$
378		$0.60 \leq p < 0.80$	$0.99 \leq \cos \theta < 1$	$0.99 \pm 0.12$
379		$0.80 \leq p < 1.25$	$0.99 \leq \cos \theta < 1$	$1.02 \pm 0.12$
380	$\nu_\mu$ 1-Trk Air	$1.25 \leq p < 2.00$	$0.99 \leq \cos \theta < 1$	$1.01 \pm 0.09$
381		$2.00 \leq p < 3.00$	$0.99 \leq \cos \theta < 1$	$1.01 \pm 0.10$
382		$3.00 \leq p < 4.00$	$0.99 \leq \cos \theta < 1$	$1.00 \pm 0.06$
383		$4.00 \leq p < 5.50$	$0.99 \leq \cos \theta < 1$	$1.00 \pm 0.05$
384		$5.50 \leq p < 30$	$0.99 \leq \cos \theta < 1$	$0.98 \pm 0.10$
385	$\nu_\mu$ N-Trks Air	$0 \leq p < 0.40$	$-1 \leq \cos \theta < 0.77$	$1.18 \pm 0.62$
386		$0.40 \leq p < 0.60$	$-1 \leq \cos \theta < 0.77$	$0.88 \pm 0.15$
387		$0.60 \leq p < 0.80$	$-1 \leq \cos \theta < 0.77$	$1.03 \pm 0.21$
388		$0.80 \leq p < 1.20$	$-1 \leq \cos \theta < 0.77$	$1.03 \pm 0.21$
389		$1.20 \leq p < 2.20$	$-1 \leq \cos \theta < 0.77$	$1.01 \pm 0.16$
390	$\nu_\mu$ N-Trks Air	$2.20 \leq p < 3.50$	$-1 \leq \cos \theta < 0.77$	$1.00 \pm 0.22$

Fit Index	Sample	p [GeV/c]	$\cos\theta$	Prefit
391		$3.50 \leq p < 10.0$	$-1 \leq \cos\theta < 0.77$	$0.99 \pm 0.32$
392		$10.0 \leq p < 30$	$-1 \leq \cos\theta < 0.77$	$0.93 \pm 0.69$
393		$0 \leq p < 0.40$	$0.77 \leq \cos\theta < 0.85$	$1.13 \pm 0.58$
394		$0.40 \leq p < 0.60$	$0.77 \leq \cos\theta < 0.85$	$0.91 \pm 0.14$
395		$0.60 \leq p < 0.80$	$0.77 \leq \cos\theta < 0.85$	$0.99 \pm 0.10$
396		$0.80 \leq p < 1.20$	$0.77 \leq \cos\theta < 0.85$	$1.01 \pm 0.11$
397		$1.20 \leq p < 2.20$	$0.77 \leq \cos\theta < 0.85$	$1.01 \pm 0.08$
398		$2.20 \leq p < 3.50$	$0.77 \leq \cos\theta < 0.85$	$1.00 \pm 0.08$
399		$3.50 \leq p < 10.0$	$0.77 \leq \cos\theta < 0.85$	$1.03 \pm 0.18$
400	$\nu_\mu$ N-Trks Air	$10.0 \leq p < 30$	$0.77 \leq \cos\theta < 0.85$	$0.97 \pm 0.51$
401		$0 \leq p < 0.40$	$0.85 \leq \cos\theta < 0.90$	$1.12 \pm 0.55$
402		$0.40 \leq p < 0.60$	$0.85 \leq \cos\theta < 0.90$	$0.92 \pm 0.13$
403		$0.60 \leq p < 0.80$	$0.85 \leq \cos\theta < 0.90$	$0.99 \pm 0.08$
404		$0.80 \leq p < 1.20$	$0.85 \leq \cos\theta < 0.90$	$1.00 \pm 0.08$
405		$1.20 \leq p < 2.20$	$0.85 \leq \cos\theta < 0.90$	$1.01 \pm 0.07$
406		$2.20 \leq p < 3.50$	$0.85 \leq \cos\theta < 0.90$	$1.00 \pm 0.06$
407		$3.50 \leq p < 10.0$	$0.85 \leq \cos\theta < 0.90$	$0.98 \pm 0.13$
408		$10.0 \leq p < 30$	$0.85 \leq \cos\theta < 0.90$	$0.93 \pm 0.45$
409		$0 \leq p < 0.40$	$0.90 \leq \cos\theta < 0.97$	$1.09 \pm 0.51$
410	$\nu_\mu$ N-Trks Air	$0.40 \leq p < 0.60$	$0.90 \leq \cos\theta < 0.97$	$0.93 \pm 0.11$
411		$0.60 \leq p < 0.80$	$0.90 \leq \cos\theta < 0.97$	$0.99 \pm 0.08$
412		$0.80 \leq p < 1.20$	$0.90 \leq \cos\theta < 0.97$	$1.00 \pm 0.08$
413		$1.20 \leq p < 2.20$	$0.90 \leq \cos\theta < 0.97$	$1.00 \pm 0.07$
414		$2.20 \leq p < 3.50$	$0.90 \leq \cos\theta < 0.97$	$1.00 \pm 0.03$
415		$3.50 \leq p < 10.0$	$0.90 \leq \cos\theta < 0.97$	$0.99 \pm 0.10$
416		$10.0 \leq p < 30$	$0.90 \leq \cos\theta < 0.97$	$0.97 \pm 0.28$
417		$0 \leq p < 0.40$	$0.97 \leq \cos\theta < 1$	$1.09 \pm 0.48$
418		$0.40 \leq p < 0.60$	$0.97 \leq \cos\theta < 1$	$0.94 \pm 0.12$
419		$0.60 \leq p < 0.80$	$0.97 \leq \cos\theta < 1$	$0.98 \pm 0.11$
420	$\nu_\mu$ N-Trks Air	$0.80 \leq p < 1.20$	$0.97 \leq \cos\theta < 1$	$1.01 \pm 0.10$
421		$1.20 \leq p < 2.20$	$0.97 \leq \cos\theta < 1$	$1.01 \pm 0.09$

Fit Index	Sample	$p$ [GeV/c]	$\cos\theta$	Prefit
422		$2.20 \leq p < 3.50$	$0.97 \leq \cos\theta < 1$	$1.01 \pm 0.07$
423		$3.50 \leq p < 10.0$	$0.97 \leq \cos\theta < 1$	$0.99 \pm 0.06$
424		$10.0 \leq p < 30$	$0.97 \leq \cos\theta < 1$	$0.97 \pm 0.13$
425	$\bar{\nu}_\mu$ RHC 1-Trk Air	$0 \leq p < 0.50$	$-1 \leq \cos\theta < 0.82$	$0.99 \pm 0.29$
426		$0.50 \leq p < 0.60$	$-1 \leq \cos\theta < 0.82$	$0.92 \pm 0.14$
427		$0.60 \leq p < 0.80$	$-1 \leq \cos\theta < 0.82$	$1.05 \pm 0.24$
428		$0.80 \leq p < 1.25$	$-1 \leq \cos\theta < 0.82$	$1.05 \pm 0.18$
429		$1.25 \leq p < 2.00$	$-1 \leq \cos\theta < 0.82$	$1.02 \pm 0.17$
430	$\bar{\nu}_\mu$ RHC 1-Trk Air	$2.00 \leq p < 3.00$	$-1 \leq \cos\theta < 0.82$	$0.87 \pm 0.19$
431		$3.00 \leq p < 30$	$-1 \leq \cos\theta < 0.82$	$0.96 \pm 0.41$
432		$0 \leq p < 0.50$	$0.82 \leq \cos\theta < 0.90$	$1.03 \pm 0.35$
433		$0.50 \leq p < 0.60$	$0.82 \leq \cos\theta < 0.90$	$0.91 \pm 0.12$
434		$0.60 \leq p < 0.80$	$0.82 \leq \cos\theta < 0.90$	$1.00 \pm 0.16$
435		$0.80 \leq p < 1.25$	$0.82 \leq \cos\theta < 0.90$	$1.03 \pm 0.15$
436		$1.25 \leq p < 2.00$	$0.82 \leq \cos\theta < 0.90$	$0.99 \pm 0.12$
437		$2.00 \leq p < 3.00$	$0.82 \leq \cos\theta < 0.90$	$0.99 \pm 0.15$
438		$3.00 \leq p < 30$	$0.82 \leq \cos\theta < 0.90$	$0.93 \pm 0.31$
439		$0 \leq p < 0.50$	$0.90 \leq \cos\theta < 0.95$	$1.05 \pm 0.37$
440	$\bar{\nu}_\mu$ RHC 1-Trk Air	$0.50 \leq p < 0.60$	$0.90 \leq \cos\theta < 0.95$	$0.92 \pm 0.11$
441		$0.60 \leq p < 0.80$	$0.90 \leq \cos\theta < 0.95$	$0.98 \pm 0.12$
442		$0.80 \leq p < 1.25$	$0.90 \leq \cos\theta < 0.95$	$1.03 \pm 0.12$
443		$1.25 \leq p < 2.00$	$0.90 \leq \cos\theta < 0.95$	$1.02 \pm 0.08$
444		$2.00 \leq p < 3.00$	$0.90 \leq \cos\theta < 0.95$	$0.97 \pm 0.08$
445		$3.00 \leq p < 30$	$0.90 \leq \cos\theta < 0.95$	$0.97 \pm 0.19$
446		$0 \leq p < 0.50$	$0.95 \leq \cos\theta < 0.99$	$1.06 \pm 0.37$
447		$0.50 \leq p < 0.60$	$0.95 \leq \cos\theta < 0.99$	$0.93 \pm 0.12$
448		$0.60 \leq p < 0.80$	$0.95 \leq \cos\theta < 0.99$	$0.97 \pm 0.11$
449		$0.80 \leq p < 1.25$	$0.95 \leq \cos\theta < 0.99$	$1.02 \pm 0.10$
450	$\bar{\nu}_\mu$ RHC 1-Trk Air	$1.25 \leq p < 2.00$	$0.95 \leq \cos\theta < 0.99$	$1.00 \pm 0.07$
451		$2.00 \leq p < 3.00$	$0.95 \leq \cos\theta < 0.99$	$0.99 \pm 0.04$
452		$3.00 \leq p < 30$	$0.95 \leq \cos\theta < 0.99$	$0.99 \pm 0.10$

Fit Index	Sample	$p$ [GeV/c]	$\cos\theta$	Prefit
453		$0 \leq p < 0.50$	$0.99 \leq \cos\theta < 1$	$1.07 \pm 0.35$
454		$0.50 \leq p < 0.60$	$0.99 \leq \cos\theta < 1$	$0.89 \pm 0.12$
455		$0.60 \leq p < 0.80$	$0.99 \leq \cos\theta < 1$	$0.99 \pm 0.11$
456		$0.80 \leq p < 1.25$	$0.99 \leq \cos\theta < 1$	$1.02 \pm 0.11$
457		$1.25 \leq p < 2.00$	$0.99 \leq \cos\theta < 1$	$0.99 \pm 0.09$
458		$2.00 \leq p < 3.00$	$0.99 \leq \cos\theta < 1$	$1.01 \pm 0.07$
459		$3.00 \leq p < 30$	$0.99 \leq \cos\theta < 1$	$0.99 \pm 0.06$
460	$\bar{\nu}_\mu$ RHC N-Trks Air	$0 \leq p < 0.50$	$-1 \leq \cos\theta < 0.89$	$1.00 \pm 0.29$
461		$0.50 \leq p < 0.90$	$-1 \leq \cos\theta < 0.89$	$1.00 \pm 0.10$
462		$0.90 \leq p < 1.25$	$-1 \leq \cos\theta < 0.89$	$1.04 \pm 0.09$
463		$1.25 \leq p < 1.60$	$-1 \leq \cos\theta < 0.89$	$0.98 \pm 0.14$
464		$1.60 \leq p < 3.00$	$-1 \leq \cos\theta < 0.89$	$0.98 \pm 0.13$
465		$3.00 \leq p < 30$	$-1 \leq \cos\theta < 0.89$	$0.92 \pm 0.33$
466		$0 \leq p < 0.50$	$0.89 \leq \cos\theta < 0.95$	$1.00 \pm 0.31$
467		$0.50 \leq p < 0.90$	$0.89 \leq \cos\theta < 0.95$	$0.99 \pm 0.06$
468		$0.90 \leq p < 1.25$	$0.89 \leq \cos\theta < 0.95$	$1.02 \pm 0.06$
469		$1.25 \leq p < 1.60$	$0.89 \leq \cos\theta < 0.95$	$0.99 \pm 0.11$
470	$\bar{\nu}_\mu$ RHC N-Trks Air	$1.60 \leq p < 3.00$	$0.89 \leq \cos\theta < 0.95$	$0.99 \pm 0.06$
471		$3.00 \leq p < 30$	$0.89 \leq \cos\theta < 0.95$	$0.96 \pm 0.16$
472		$0 \leq p < 0.50$	$0.95 \leq \cos\theta < 0.97$	$1.00 \pm 0.32$
473		$0.50 \leq p < 0.90$	$0.95 \leq \cos\theta < 0.97$	$1.00 \pm 0.07$
474		$0.90 \leq p < 1.25$	$0.95 \leq \cos\theta < 0.97$	$1.00 \pm 0.06$
475		$1.25 \leq p < 1.60$	$0.95 \leq \cos\theta < 0.97$	$1.00 \pm 0.11$
476		$1.60 \leq p < 3.00$	$0.95 \leq \cos\theta < 0.97$	$1.00 \pm 0.06$
477		$3.00 \leq p < 30$	$0.95 \leq \cos\theta < 0.97$	$0.99 \pm 0.13$
478		$0 \leq p < 0.50$	$0.97 \leq \cos\theta < 0.99$	$1.03 \pm 0.32$
479		$0.50 \leq p < 0.90$	$0.97 \leq \cos\theta < 0.99$	$0.99 \pm 0.07$
480	$\bar{\nu}_\mu$ RHC N-Trks Air	$0.90 \leq p < 1.25$	$0.97 \leq \cos\theta < 0.99$	$1.02 \pm 0.07$
481		$1.25 \leq p < 1.60$	$0.97 \leq \cos\theta < 0.99$	$0.99 \pm 0.10$
482		$1.60 \leq p < 3.00$	$0.97 \leq \cos\theta < 0.99$	$1.01 \pm 0.08$
483		$3.00 \leq p < 30$	$0.97 \leq \cos\theta < 0.99$	$0.98 \pm 0.09$

Fit Index	Sample	$p$ [GeV/c]	$\cos\theta$	Prefit
484		$0 \leq p < 0.50$	$0.99 \leq \cos\theta < 1$	$1.02 \pm 0.31$
485		$0.50 \leq p < 0.90$	$0.99 \leq \cos\theta < 1$	$1.01 \pm 0.07$
486		$0.90 \leq p < 1.25$	$0.99 \leq \cos\theta < 1$	$1.02 \pm 0.08$
487		$1.25 \leq p < 1.60$	$0.99 \leq \cos\theta < 1$	$0.98 \pm 0.10$
488		$1.60 \leq p < 3.00$	$0.99 \leq \cos\theta < 1$	$1.00 \pm 0.09$
489		$3.00 \leq p < 30$	$0.99 \leq \cos\theta < 1$	$0.99 \pm 0.07$
490	$\nu_\mu$ RHC 1-Trk Air	$0 \leq p < 0.40$	$-1 \leq \cos\theta < 0.78$	$1.10 \pm 0.50$
491		$0.40 \leq p < 0.60$	$-1 \leq \cos\theta < 0.78$	$0.92 \pm 0.12$
492		$0.60 \leq p < 0.80$	$-1 \leq \cos\theta < 0.78$	$1.03 \pm 0.16$
493		$0.80 \leq p < 1.10$	$-1 \leq \cos\theta < 0.78$	$1.02 \pm 0.20$
494		$1.10 \leq p < 2.00$	$-1 \leq \cos\theta < 0.78$	$1.08 \pm 0.14$
495		$2.00 \leq p < 10.0$	$-1 \leq \cos\theta < 0.78$	$0.81 \pm 0.31$
496		$0 \leq p < 0.40$	$0.78 \leq \cos\theta < 0.84$	$1.23 \pm 0.50$
497		$0.40 \leq p < 0.60$	$0.78 \leq \cos\theta < 0.84$	$0.93 \pm 0.18$
498		$0.60 \leq p < 0.80$	$0.78 \leq \cos\theta < 0.84$	$0.93 \pm 0.09$
499		$0.80 \leq p < 1.10$	$0.78 \leq \cos\theta < 0.84$	$1.03 \pm 0.12$
500	$\nu_\mu$ RHC 1-Trk Air	$1.10 \leq p < 2.00$	$0.78 \leq \cos\theta < 0.84$	$1.05 \pm 0.14$
501		$2.00 \leq p < 10.0$	$0.78 \leq \cos\theta < 0.84$	$1.00 \pm 0.21$
502		$0 \leq p < 0.40$	$0.84 \leq \cos\theta < 0.92$	$1.17 \pm 0.49$
503		$0.40 \leq p < 0.60$	$0.84 \leq \cos\theta < 0.92$	$0.95 \pm 0.15$
504		$0.60 \leq p < 0.80$	$0.84 \leq \cos\theta < 0.92$	$0.97 \pm 0.08$
505		$0.80 \leq p < 1.10$	$0.84 \leq \cos\theta < 0.92$	$1.00 \pm 0.10$
506		$1.10 \leq p < 2.00$	$0.84 \leq \cos\theta < 0.92$	$1.00 \pm 0.08$
507		$2.00 \leq p < 10.0$	$0.84 \leq \cos\theta < 0.92$	$1.04 \pm 0.16$
508		$0 \leq p < 0.40$	$0.92 \leq \cos\theta < 0.95$	$1.13 \pm 0.47$
509		$0.40 \leq p < 0.60$	$0.92 \leq \cos\theta < 0.95$	$0.99 \pm 0.13$
510	$\nu_\mu$ RHC 1-Trk Air	$0.60 \leq p < 0.80$	$0.92 \leq \cos\theta < 0.95$	$0.94 \pm 0.09$
511		$0.80 \leq p < 1.10$	$0.92 \leq \cos\theta < 0.95$	$0.99 \pm 0.07$
512		$1.10 \leq p < 2.00$	$0.92 \leq \cos\theta < 0.95$	$1.00 \pm 0.06$
513		$2.00 \leq p < 10.0$	$0.92 \leq \cos\theta < 0.95$	$0.99 \pm 0.08$
514		$0 \leq p < 0.40$	$0.95 \leq \cos\theta < 0.98$	$1.06 \pm 0.46$

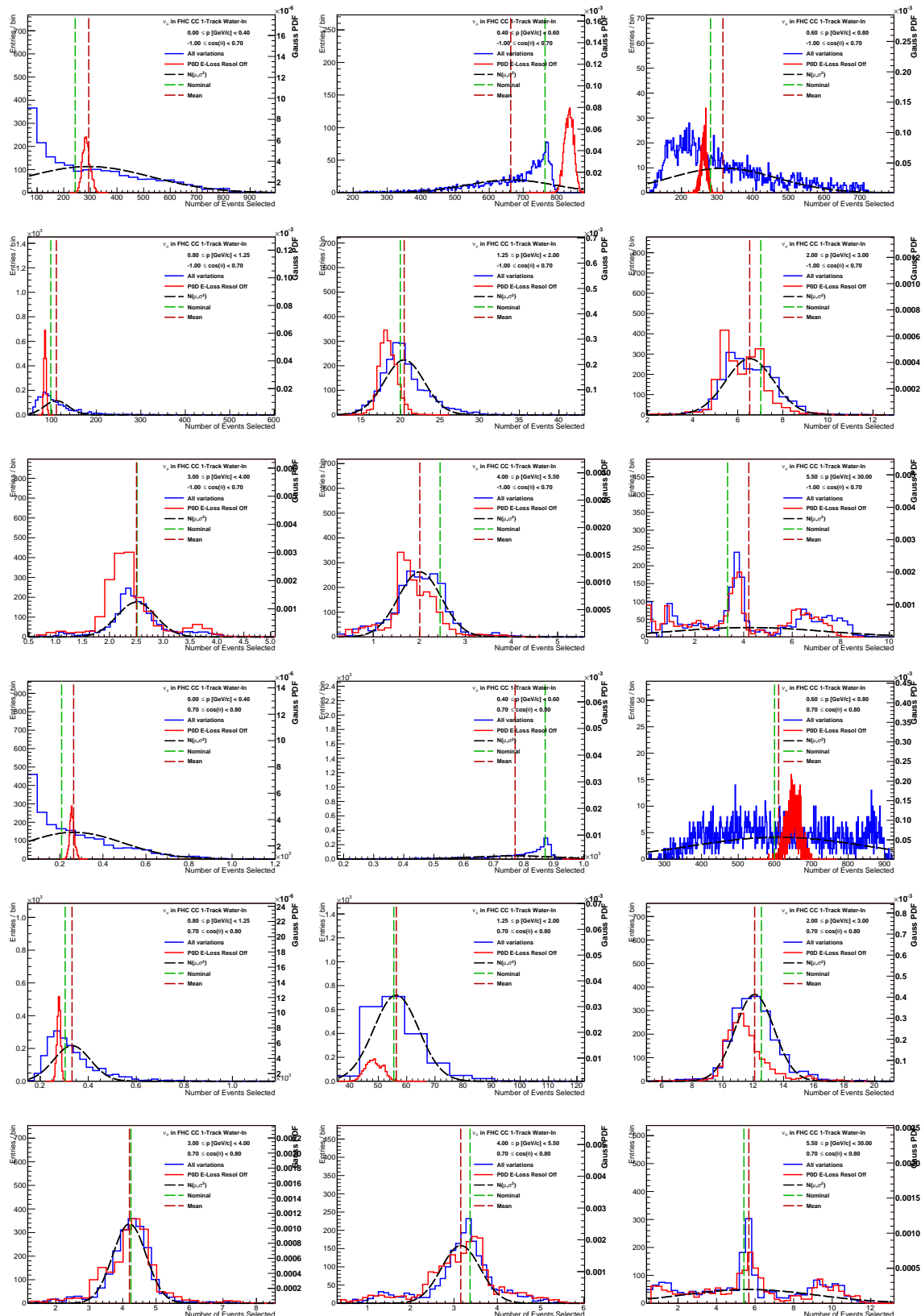
Fit Index	Sample	$p$ [GeV/c]	$\cos\theta$	Prefit
515		$0.40 \leq p < 0.60$	$0.95 \leq \cos\theta < 0.98$	$0.95 \pm 0.14$
516		$0.60 \leq p < 0.80$	$0.95 \leq \cos\theta < 0.98$	$0.97 \pm 0.11$
517		$0.80 \leq p < 1.10$	$0.95 \leq \cos\theta < 0.98$	$1.01 \pm 0.10$
518		$1.10 \leq p < 2.00$	$0.95 \leq \cos\theta < 0.98$	$1.00 \pm 0.07$
519		$2.00 \leq p < 10.0$	$0.95 \leq \cos\theta < 0.98$	$0.99 \pm 0.06$
520	$\nu_\mu$ RHC 1-Trk Air	$0 \leq p < 0.40$	$0.98 \leq \cos\theta < 0.99$	$1.07 \pm 0.46$
521		$0.40 \leq p < 0.60$	$0.98 \leq \cos\theta < 0.99$	$1.00 \pm 0.15$
522		$0.60 \leq p < 0.80$	$0.98 \leq \cos\theta < 0.99$	$1.02 \pm 0.16$
523		$0.80 \leq p < 1.10$	$0.98 \leq \cos\theta < 0.99$	$0.96 \pm 0.10$
524		$1.10 \leq p < 2.00$	$0.98 \leq \cos\theta < 0.99$	$1.01 \pm 0.08$
525		$2.00 \leq p < 10.0$	$0.98 \leq \cos\theta < 0.99$	$0.99 \pm 0.04$
526		$0 \leq p < 0.40$	$0.99 \leq \cos\theta < 1$	$1.19 \pm 0.46$
527		$0.40 \leq p < 0.60$	$0.99 \leq \cos\theta < 1$	$0.89 \pm 0.17$
528		$0.60 \leq p < 0.80$	$0.99 \leq \cos\theta < 1$	$0.99 \pm 0.15$
529		$0.80 \leq p < 1.10$	$0.99 \leq \cos\theta < 1$	$0.99 \pm 0.10$
530	$\nu_\mu$ RHC 1-Trk Air	$1.10 \leq p < 2.00$	$0.99 \leq \cos\theta < 1$	$1.00 \pm 0.09$
531		$2.00 \leq p < 10.0$	$0.99 \leq \cos\theta < 1$	$1.00 \pm 0.03$
532	$\nu_\mu$ RHC N-Trks Air	$0 \leq p < 0.60$	$-1 \leq \cos\theta < 0.70$	$0.97 \pm 0.22$
533		$0.60 \leq p < 1.00$	$-1 \leq \cos\theta < 0.70$	$1.02 \pm 0.17$
534		$1.00 \leq p < 1.50$	$-1 \leq \cos\theta < 0.70$	$1.00 \pm 0.14$
535		$1.50 \leq p < 2.00$	$-1 \leq \cos\theta < 0.70$	$1.28 \pm 0.22$
536		$2.00 \leq p < 10.0$	$-1 \leq \cos\theta < 0.70$	$0.83 \pm 0.25$
537		$0 \leq p < 0.60$	$0.70 \leq \cos\theta < 0.80$	$0.98 \pm 0.22$
538		$0.60 \leq p < 1.00$	$0.70 \leq \cos\theta < 0.80$	$0.99 \pm 0.09$
539		$1.00 \leq p < 1.50$	$0.70 \leq \cos\theta < 0.80$	$1.00 \pm 0.11$
540	$\nu_\mu$ RHC N-Trks Air	$1.50 \leq p < 2.00$	$0.70 \leq \cos\theta < 0.80$	$1.03 \pm 0.11$
541		$2.00 \leq p < 10.0$	$0.70 \leq \cos\theta < 0.80$	$1.04 \pm 0.20$
542		$0 \leq p < 0.60$	$0.80 \leq \cos\theta < 0.85$	$1.01 \pm 0.25$
543		$0.60 \leq p < 1.00$	$0.80 \leq \cos\theta < 0.85$	$0.98 \pm 0.08$
544		$1.00 \leq p < 1.50$	$0.80 \leq \cos\theta < 0.85$	$1.01 \pm 0.08$
545		$1.50 \leq p < 2.00$	$0.80 \leq \cos\theta < 0.85$	$1.00 \pm 0.08$

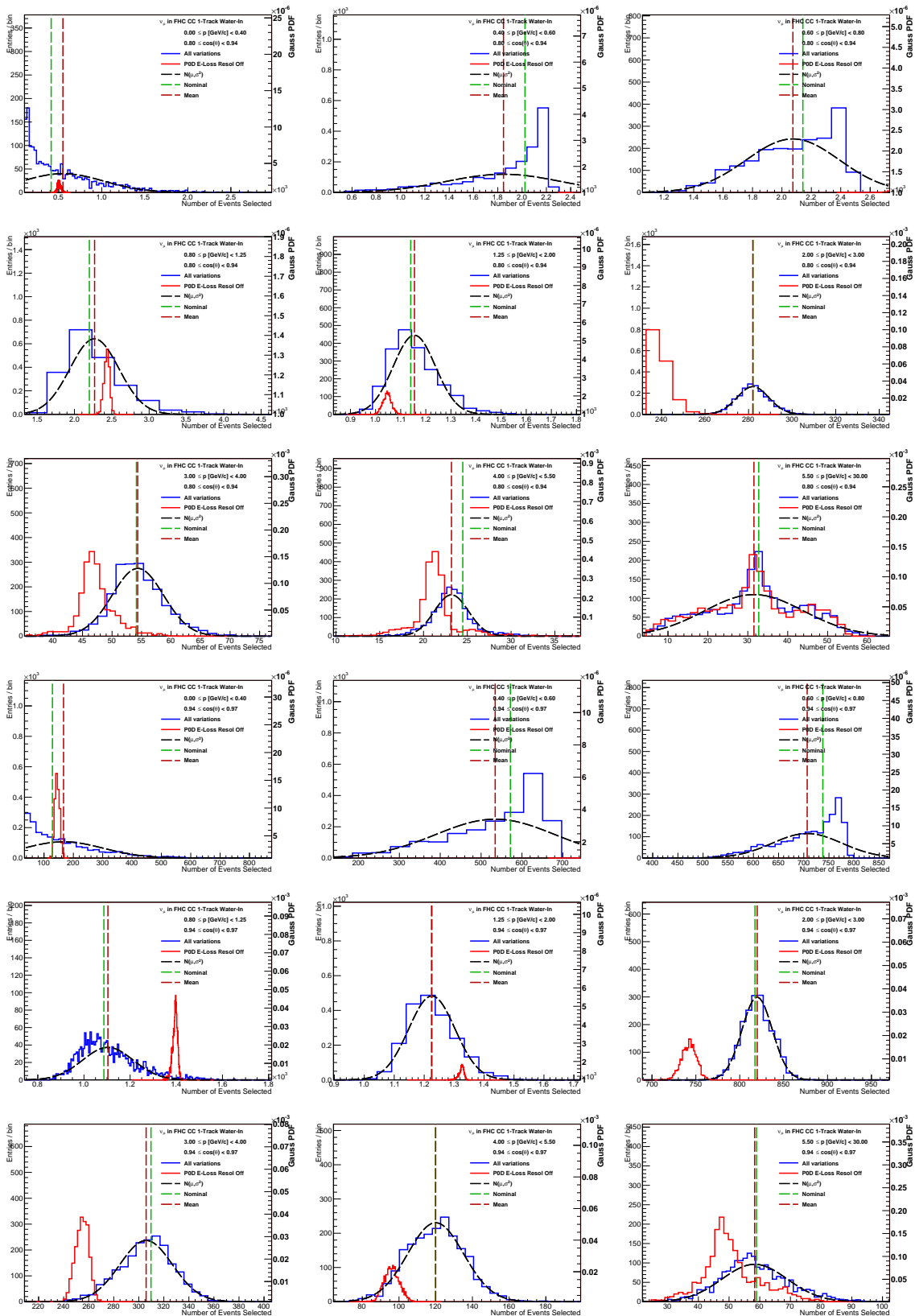
<b>Fit Index</b>	<b>Sample</b>	<b>p [GeV/c]</b>	<b>cosθ</b>	<b>Prefit</b>
546		$2.00 \leq p < 10.0$	$0.80 \leq \cos \theta < 0.85$	$0.99 \pm 0.12$
547		$0 \leq p < 0.60$	$0.85 \leq \cos \theta < 0.98$	$0.99 \pm 0.22$
548		$0.60 \leq p < 1.00$	$0.85 \leq \cos \theta < 0.98$	$1.00 \pm 0.10$
549		$1.00 \leq p < 1.50$	$0.85 \leq \cos \theta < 0.98$	$1.01 \pm 0.07$
550	$\nu_\mu$ RHC N-Trks Air	$1.50 \leq p < 2.00$	$0.85 \leq \cos \theta < 0.98$	$1.00 \pm 0.07$
551		$2.00 \leq p < 10.0$	$0.85 \leq \cos \theta < 0.98$	$1.00 \pm 0.07$
552		$0 \leq p < 0.60$	$0.98 \leq \cos \theta < 0.99$	$1.00 \pm 0.22$
553		$0.60 \leq p < 1.00$	$0.98 \leq \cos \theta < 0.99$	$0.99 \pm 0.12$
554		$1.00 \leq p < 1.50$	$0.98 \leq \cos \theta < 0.99$	$1.04 \pm 0.10$
555		$1.50 \leq p < 2.00$	$0.98 \leq \cos \theta < 0.99$	$0.99 \pm 0.10$
556		$2.00 \leq p < 10.0$	$0.98 \leq \cos \theta < 0.99$	$0.99 \pm 0.04$
557		$0 \leq p < 0.60$	$0.99 \leq \cos \theta < 1$	$1.01 \pm 0.24$
558		$0.60 \leq p < 1.00$	$0.99 \leq \cos \theta < 1$	$0.99 \pm 0.16$
559		$1.00 \leq p < 1.50$	$0.99 \leq \cos \theta < 1$	$0.97 \pm 0.12$
560	$\nu_\mu$ RHC N-Trks Air	$1.50 \leq p < 2.00$	$0.99 \leq \cos \theta < 1$	$1.06 \pm 0.10$
561		$2.00 \leq p < 10.0$	$0.99 \leq \cos \theta < 1$	$1.00 \pm 0.04$

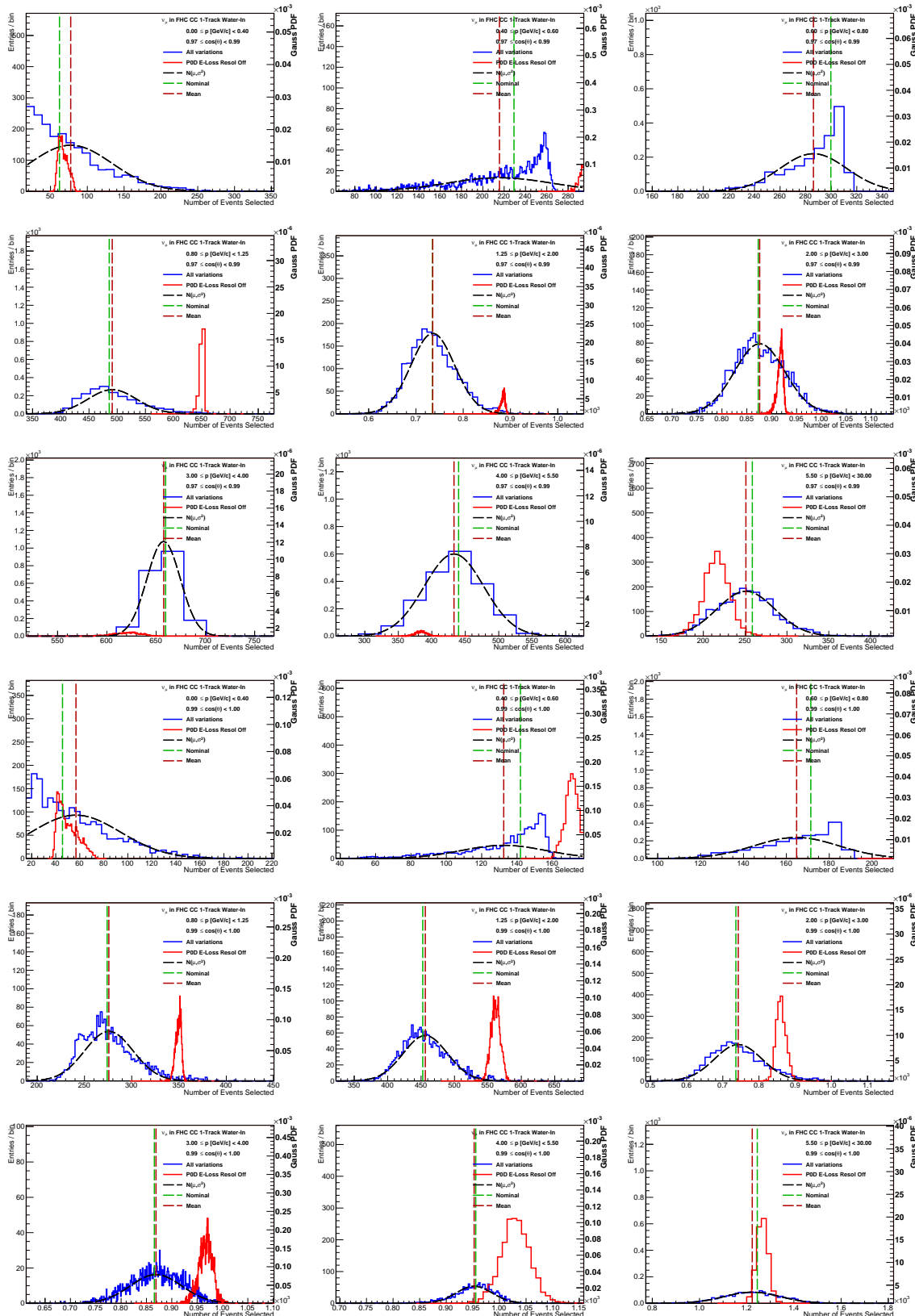
<sub>1640</sub> **Appendix B**

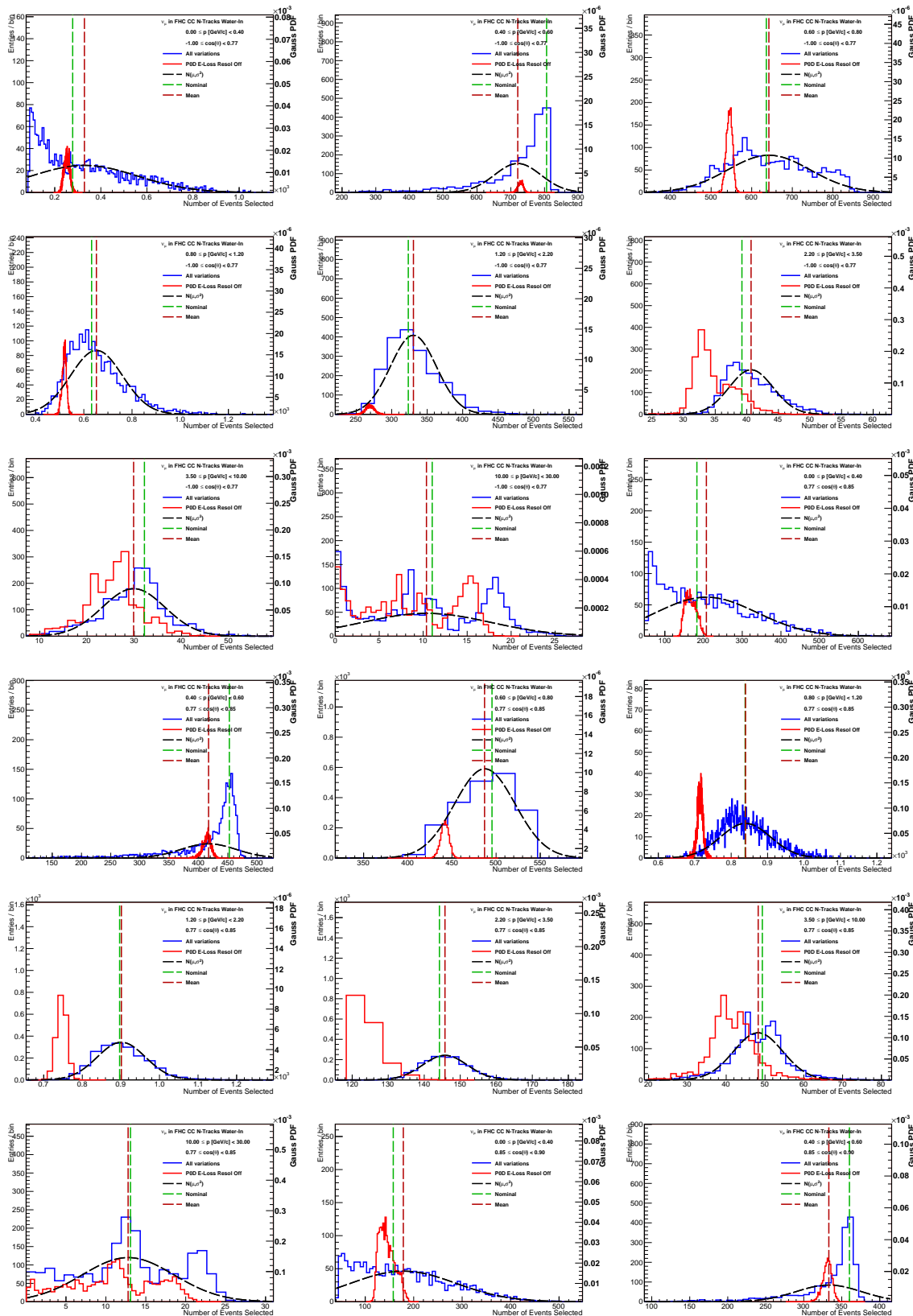
<sub>1641</sub> **Toy Experiment Variations**

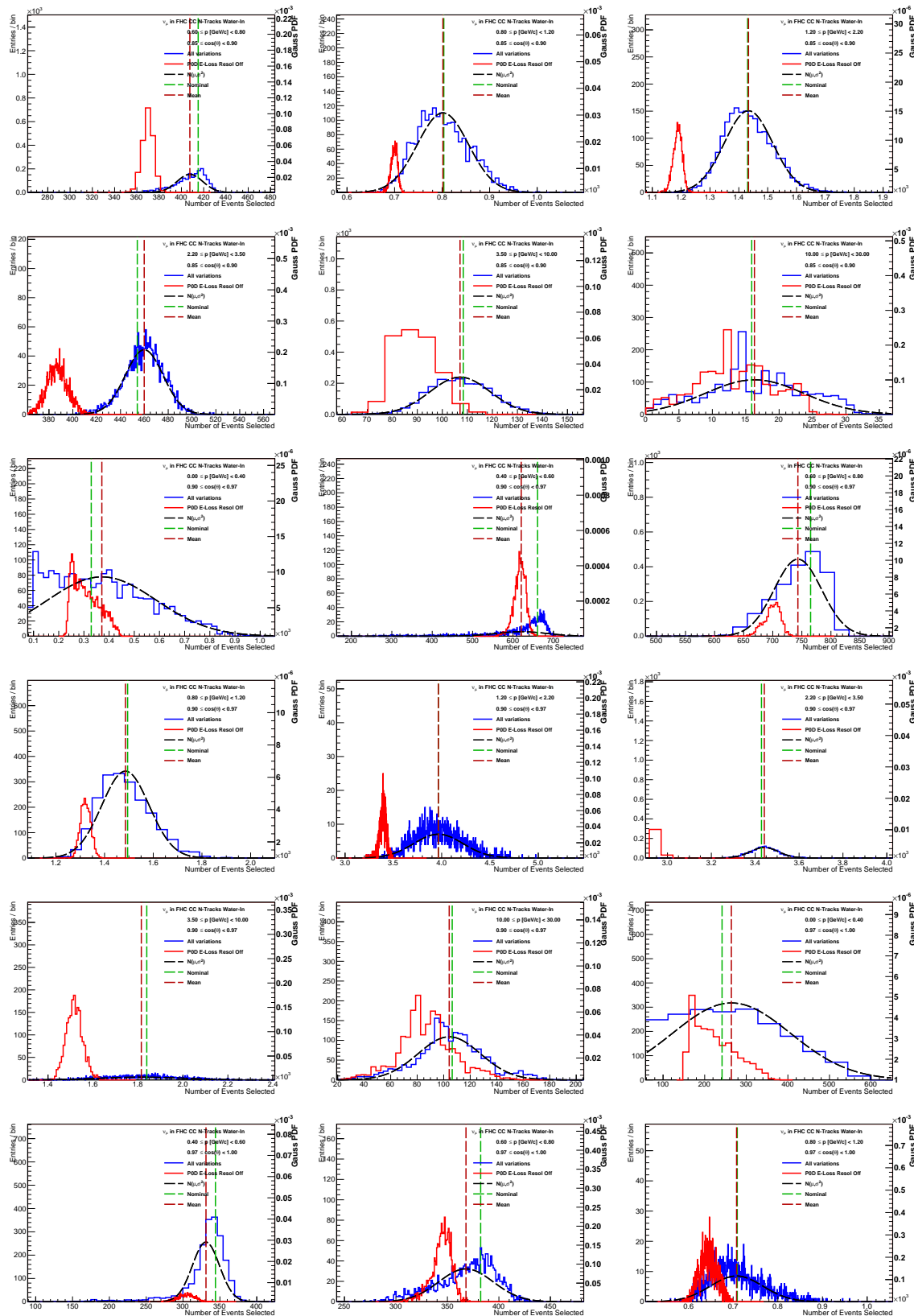
<sub>1642</sub> In this appendix is the collection of all toy experiments used to make observable normalization parameters  
<sub>1643</sub> and detector covariance matrix. Each of the observable bin relevant samples and  $(p, \cos \theta)$  edges are listed  
<sub>1644</sub> in the plots. The nominal MC (Nominal) predicted value and varied mean are shown as differently dashed  
<sub>1645</sub> lines. A normal curve, whose variance was extracted from the covariance matrix itself, is shown to illustrate  
<sub>1646</sub> the estimate on the bin normalization uncertainty. In addition, toy experiment variations with the PØD  
<sub>1647</sub> energy loss resolution off (E-Loss Resol Off) is shown to demonstrate the absence of the energy correction  
<sub>1648</sub> and its affect on when not varied.

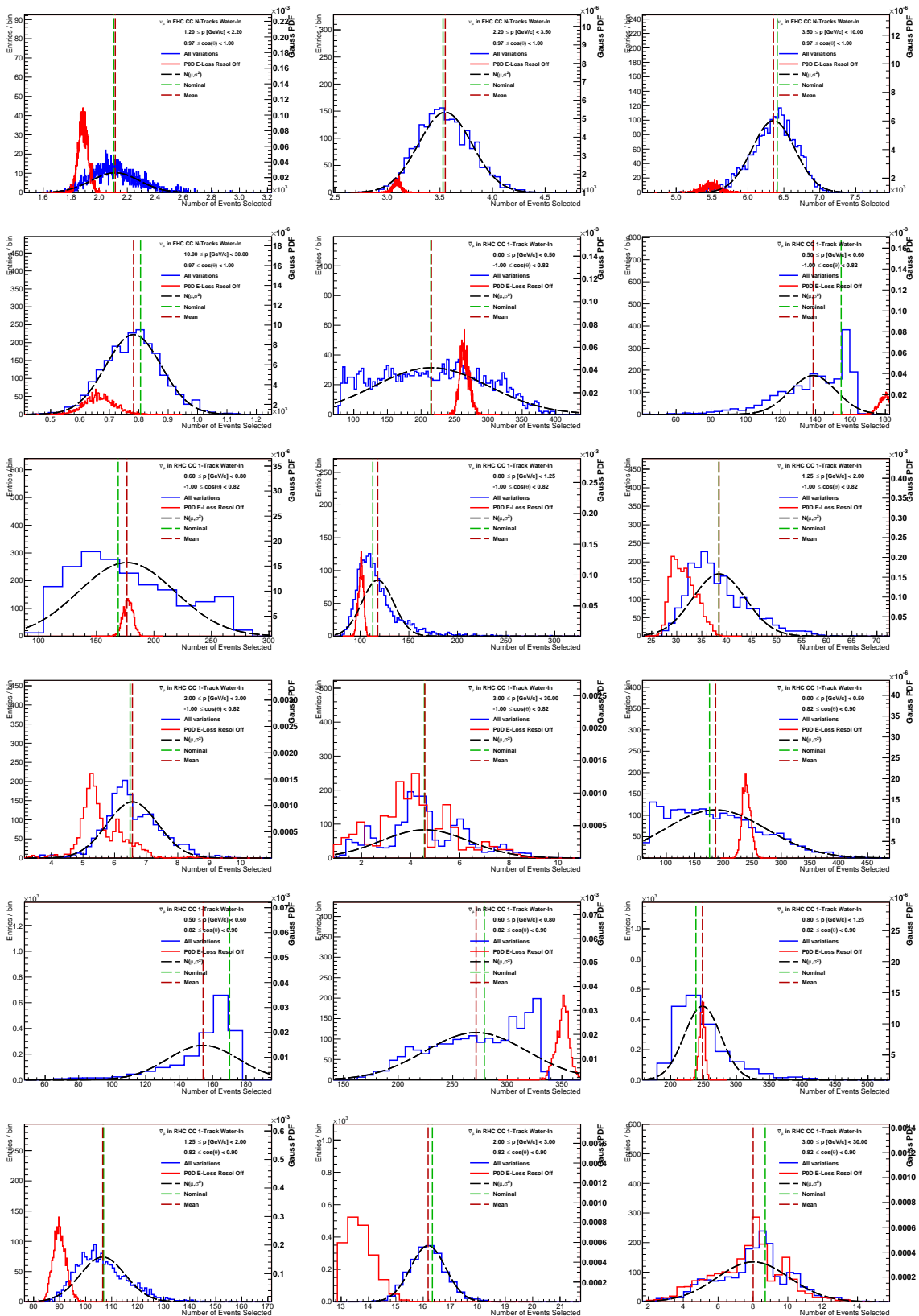


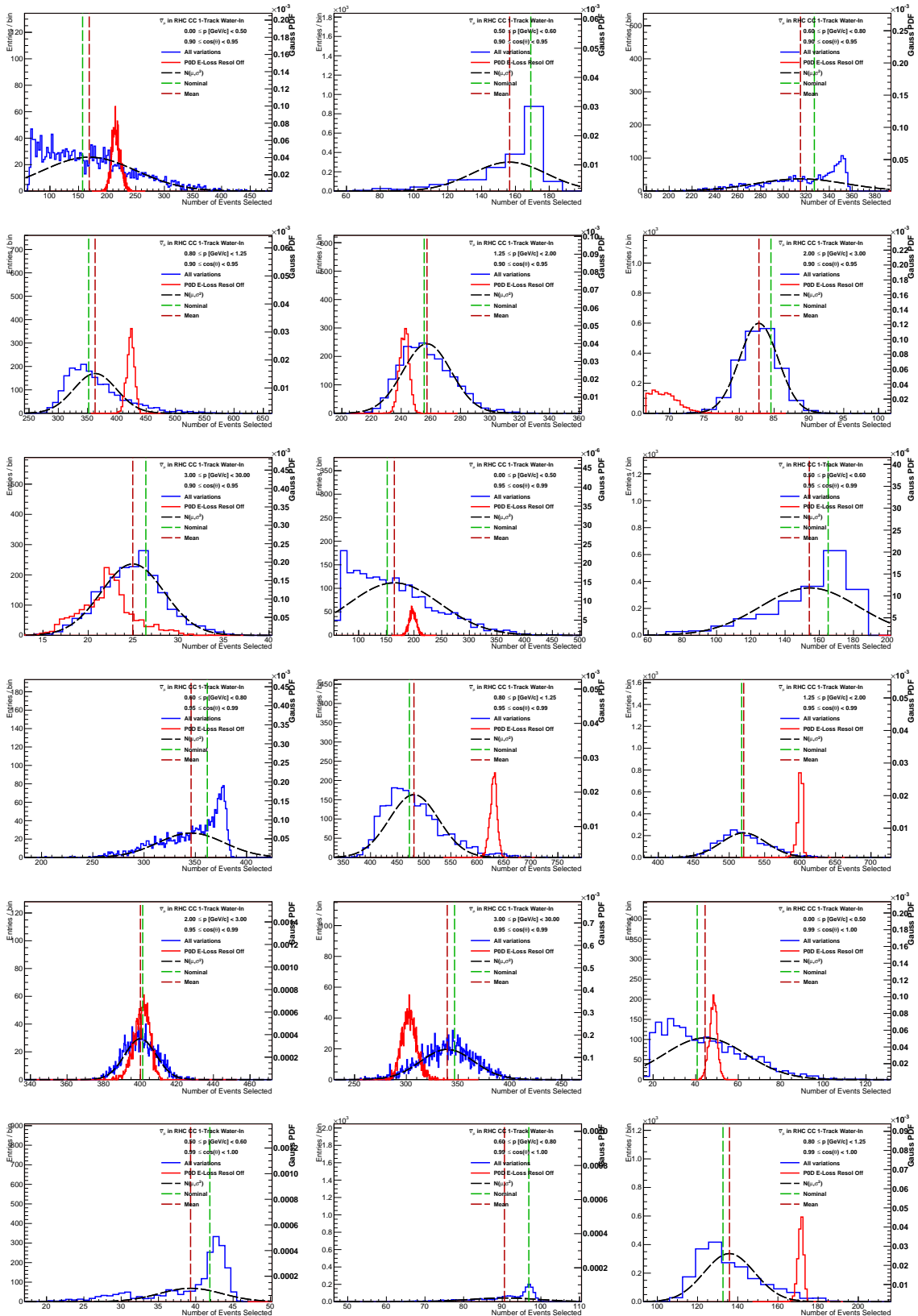


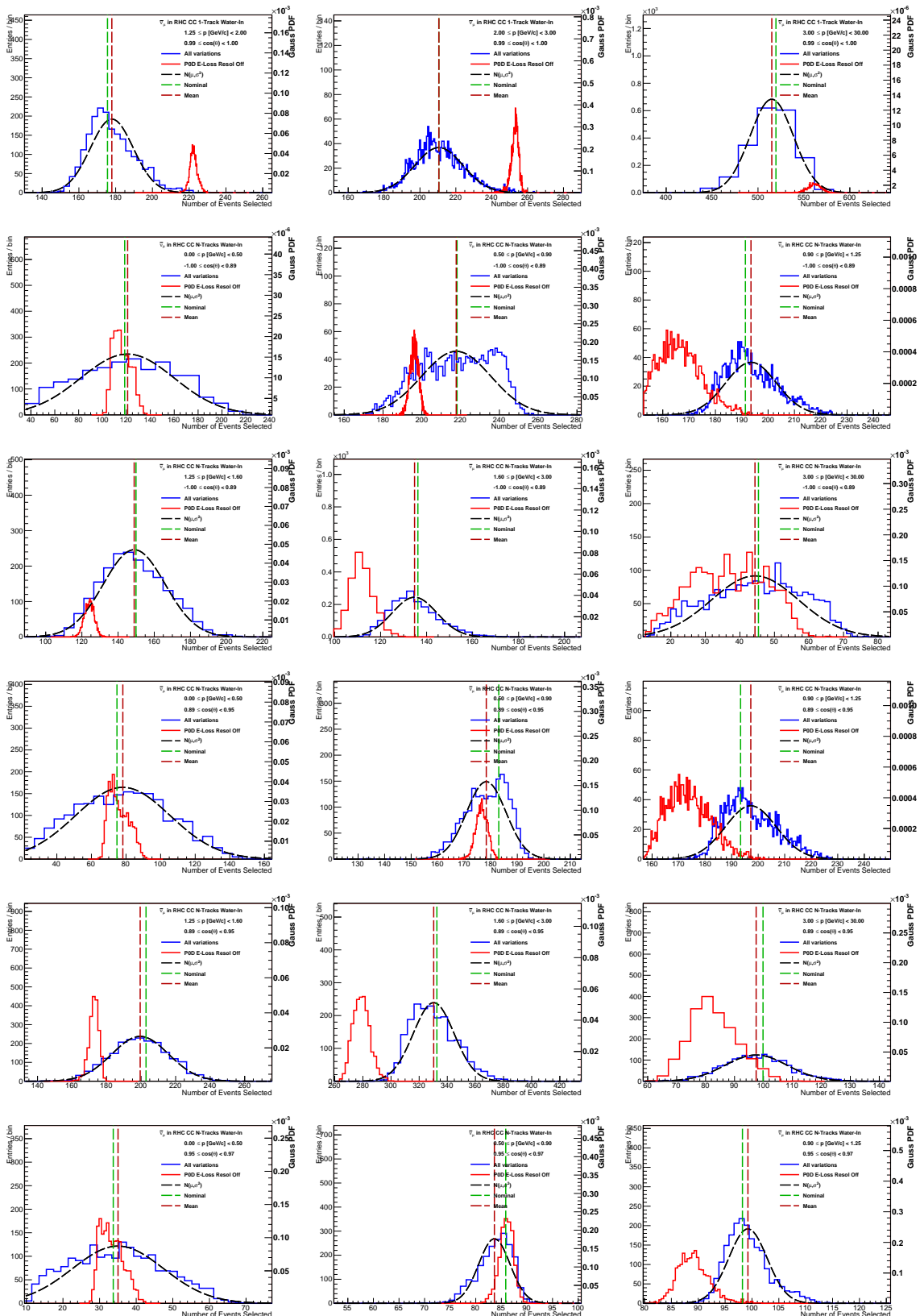


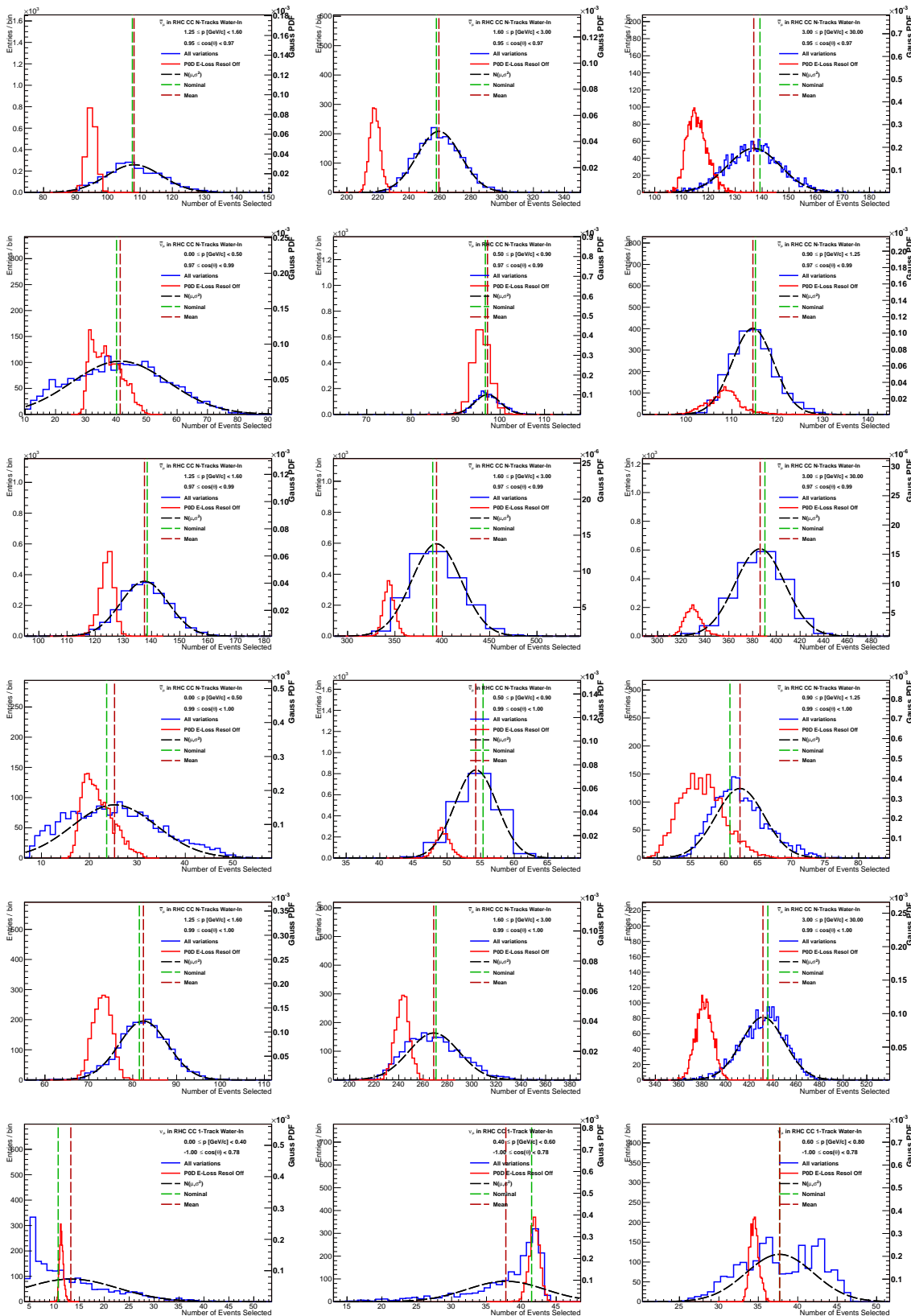


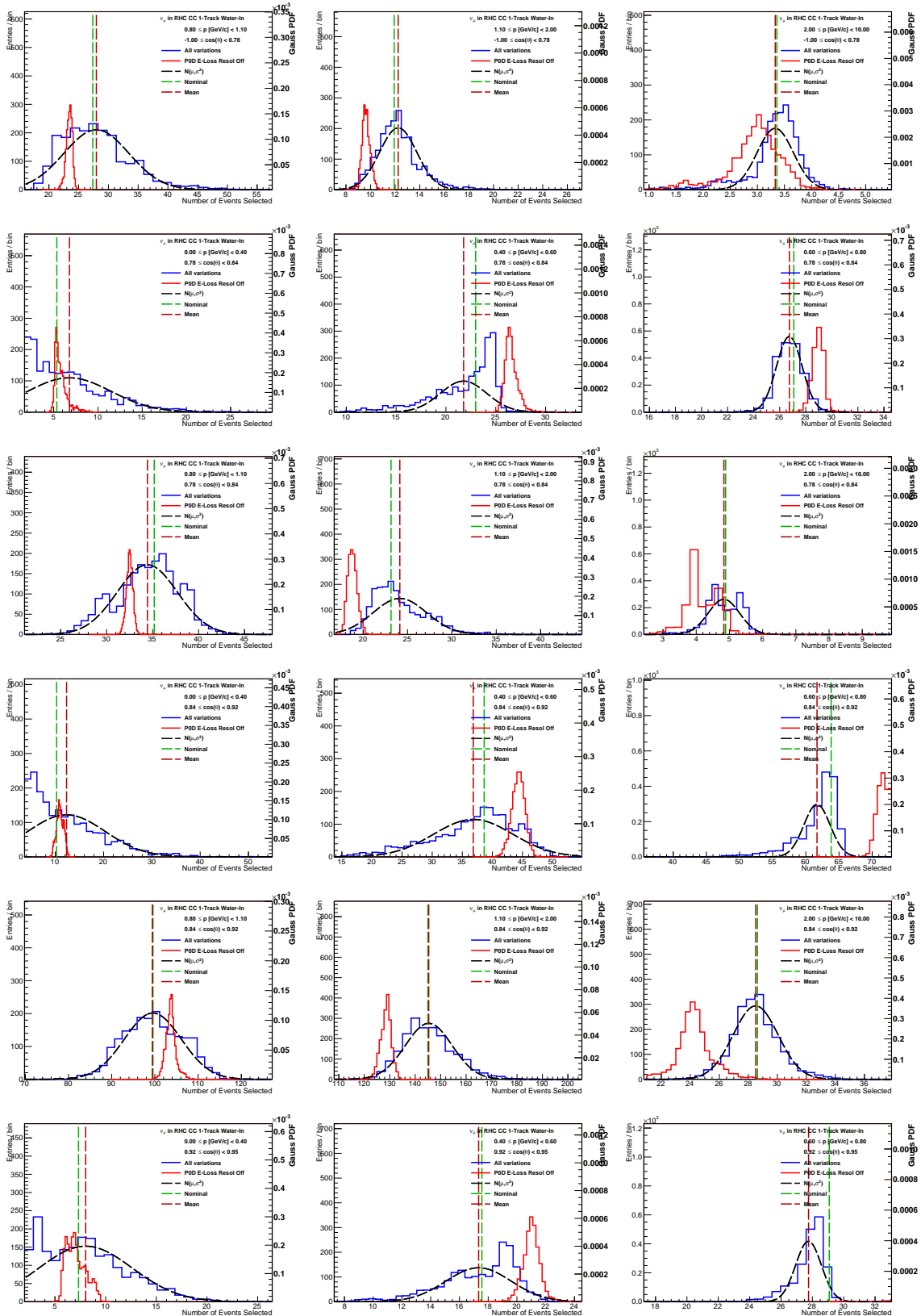


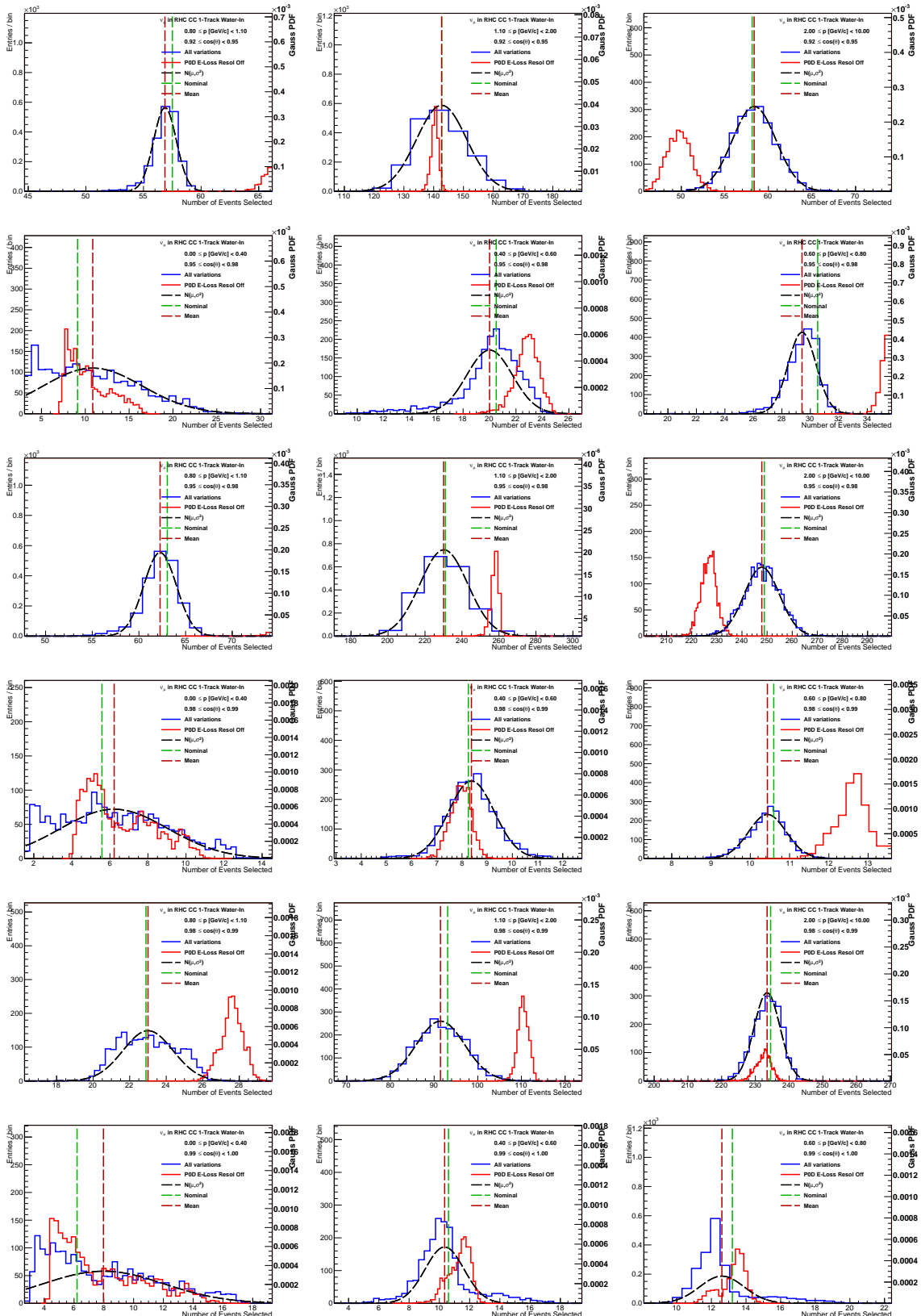


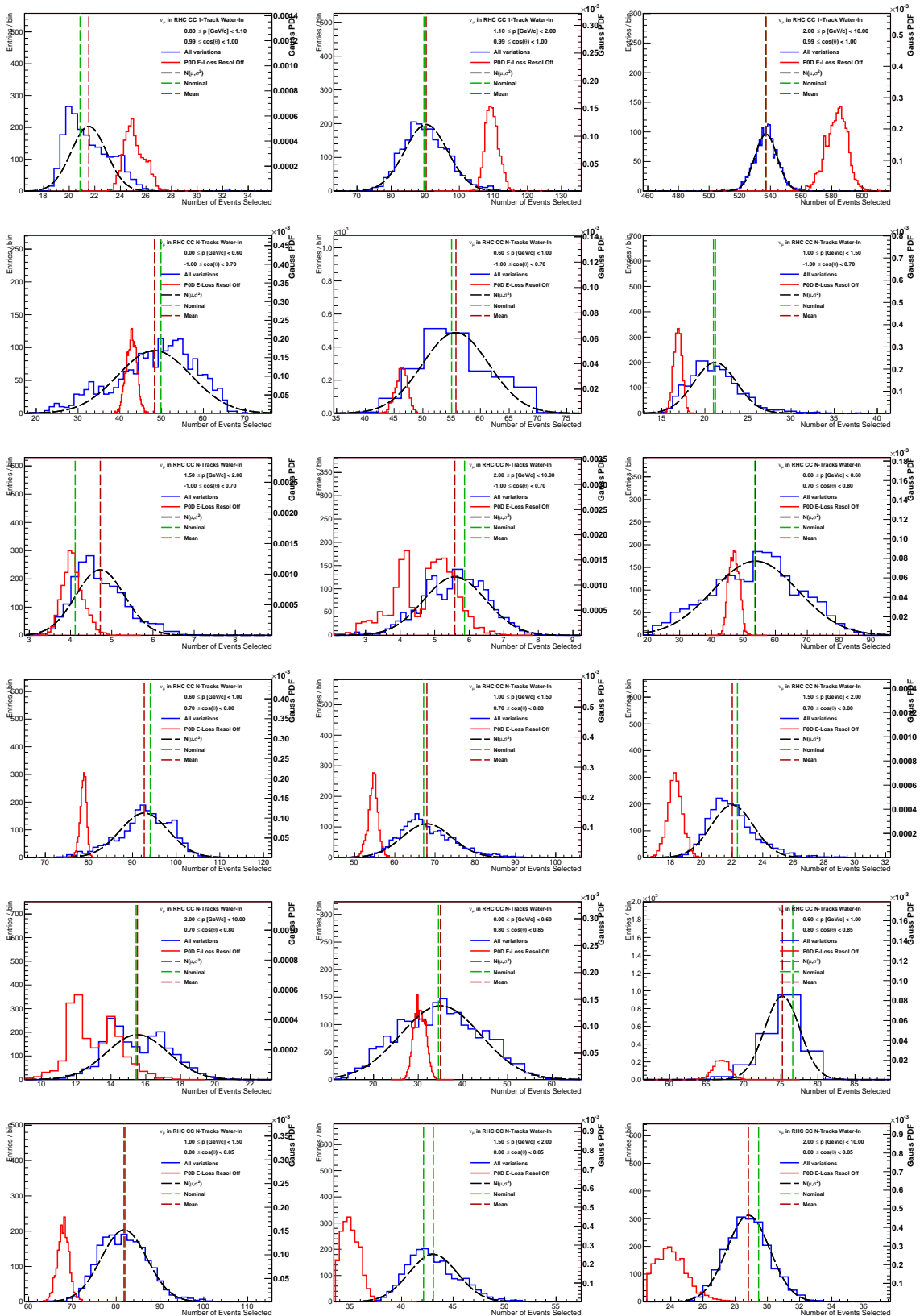


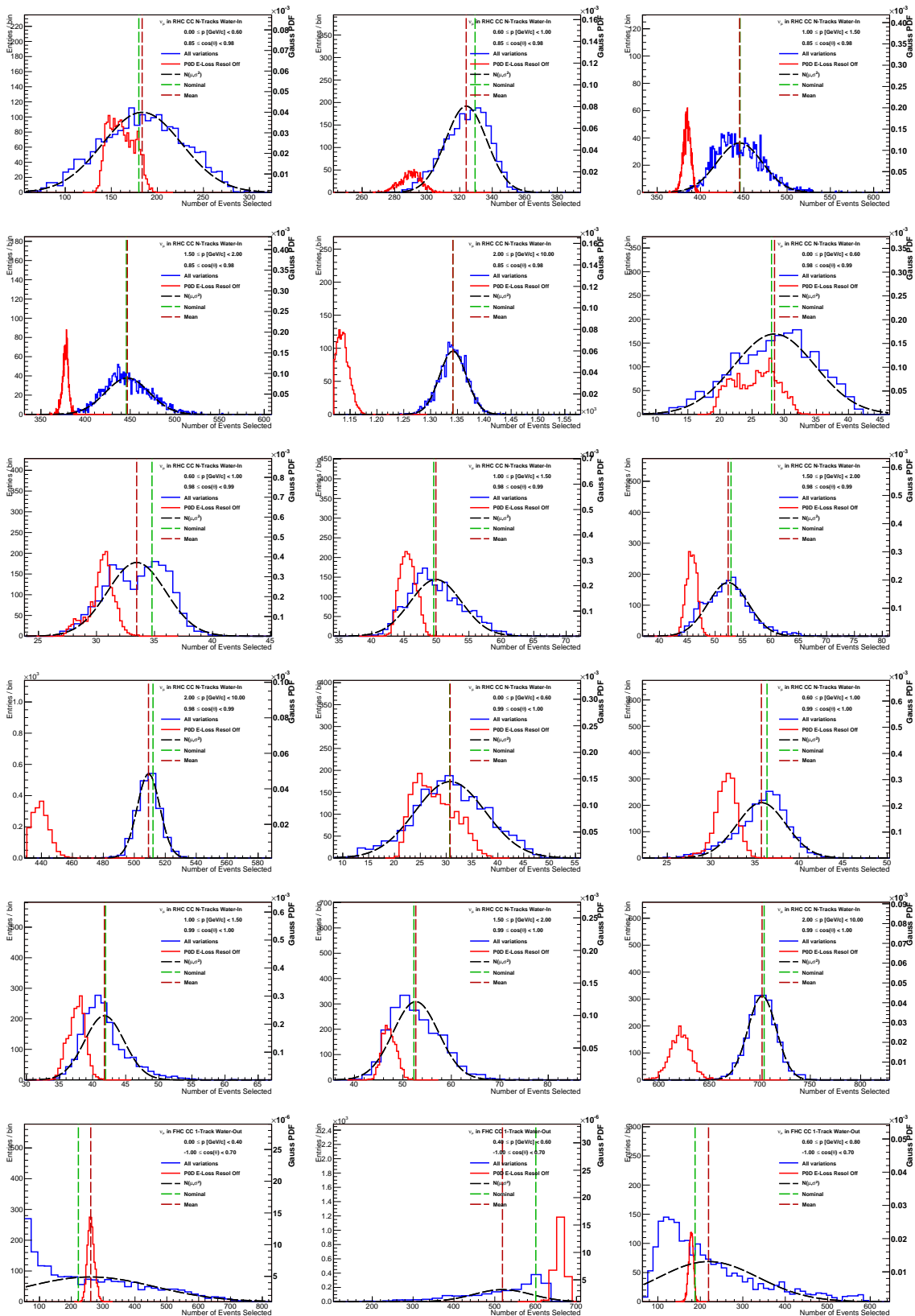


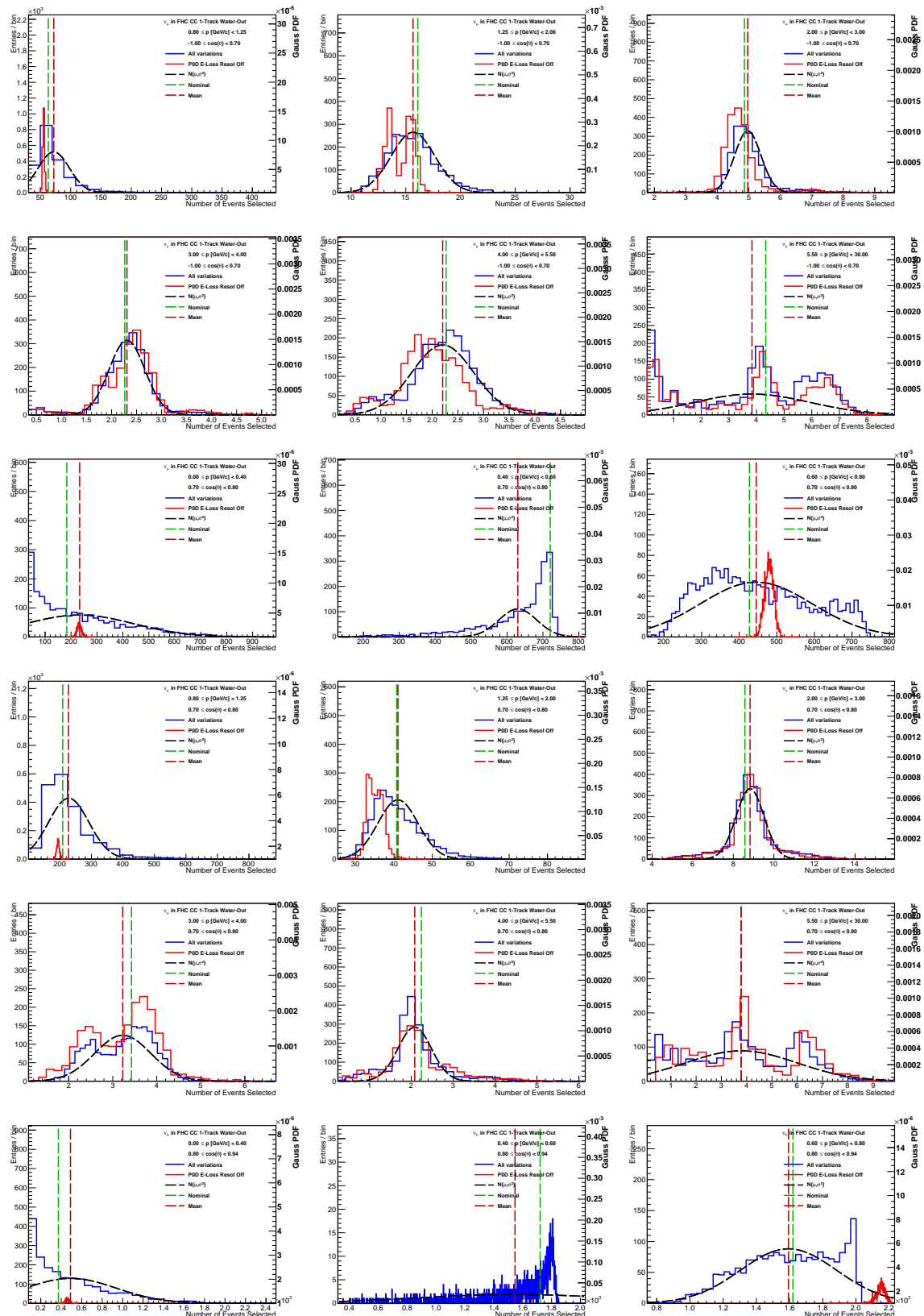


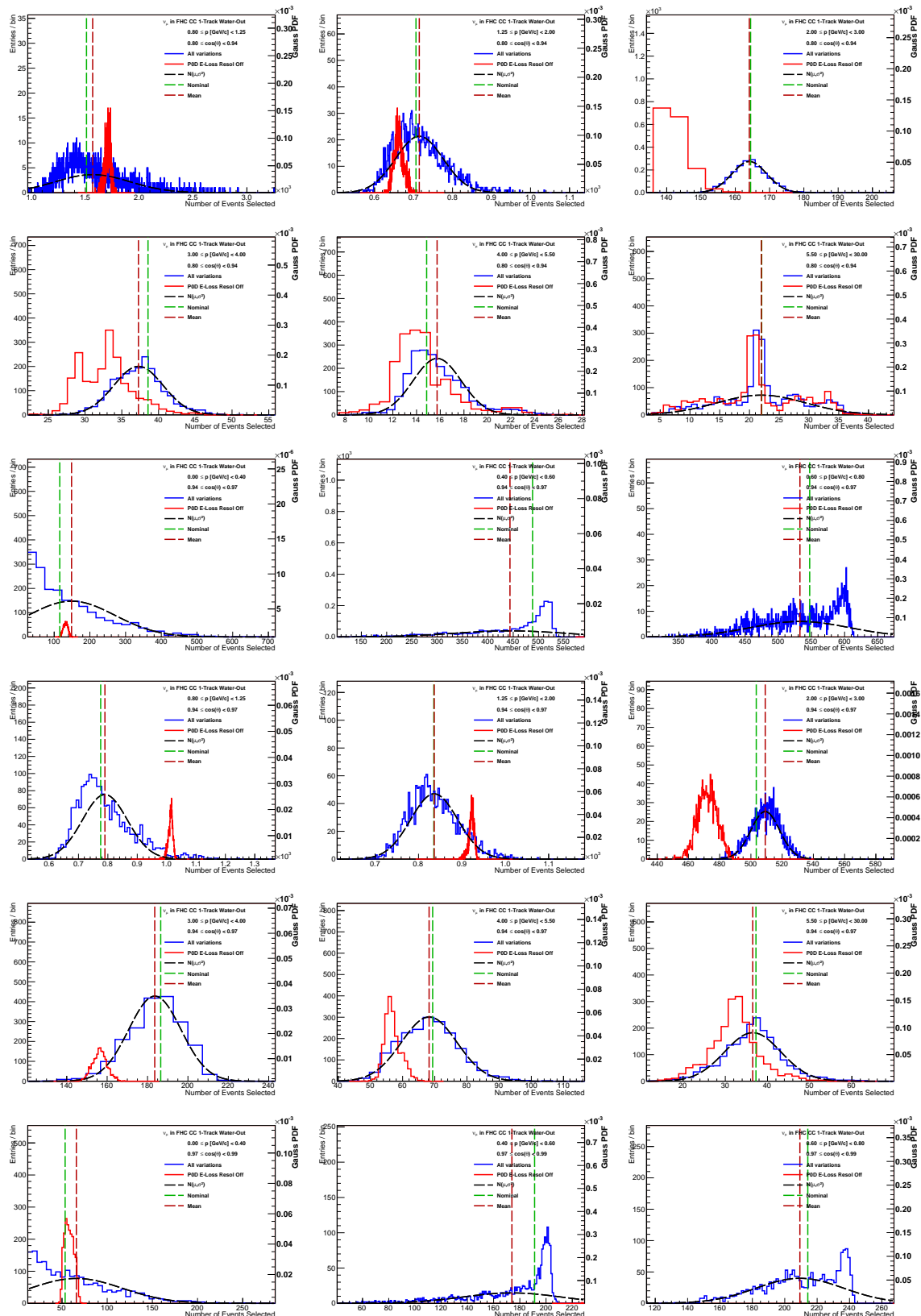


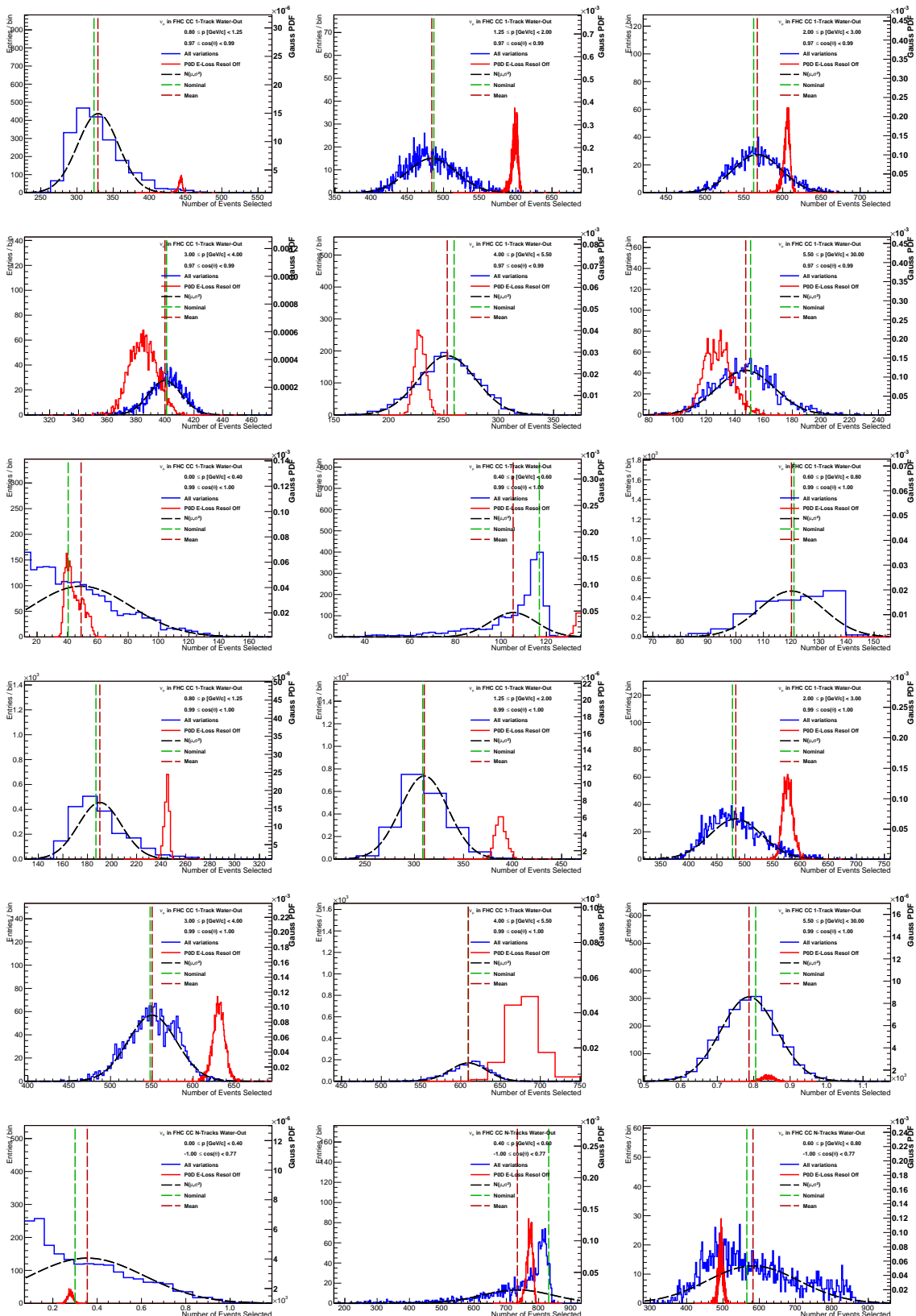


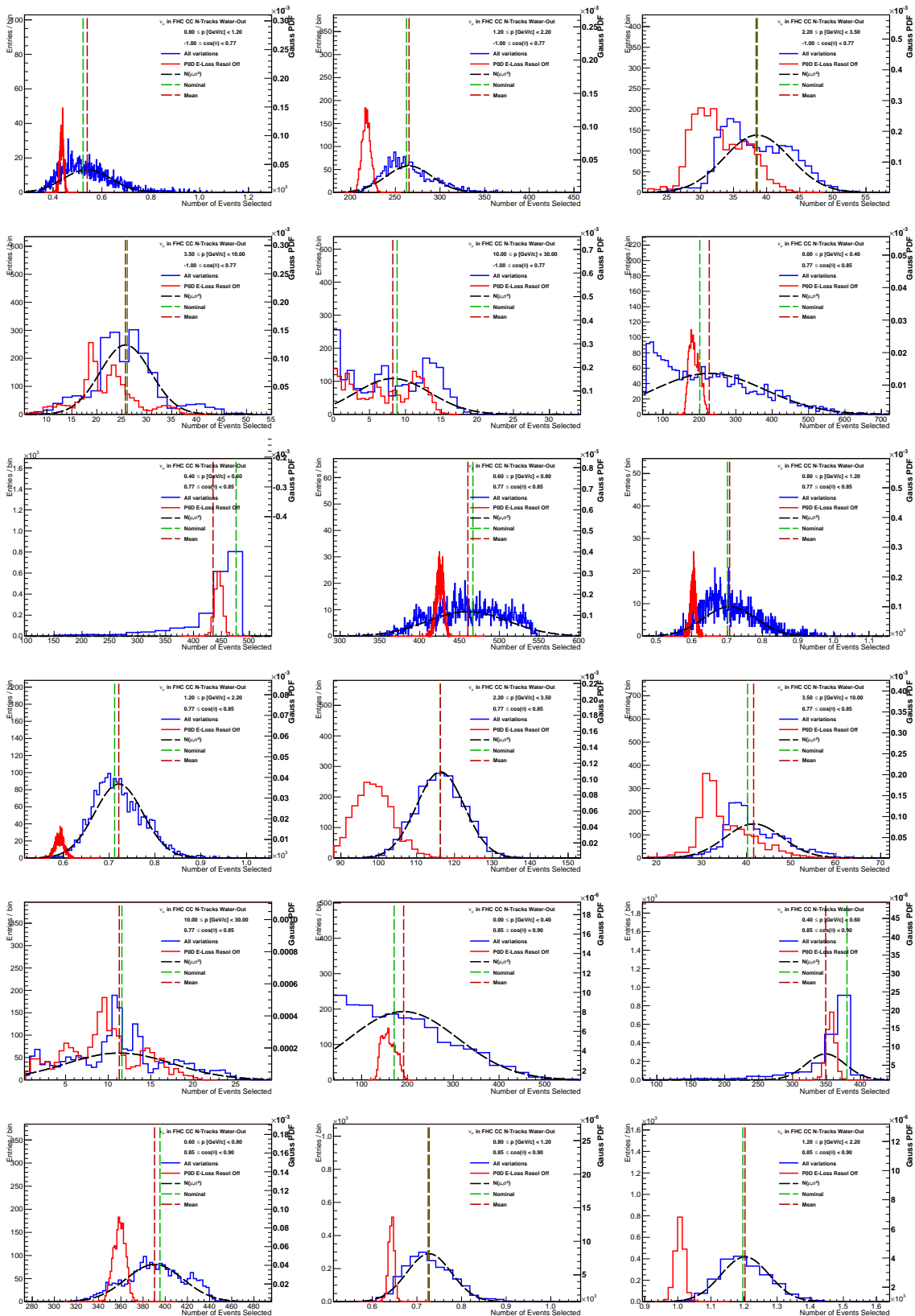


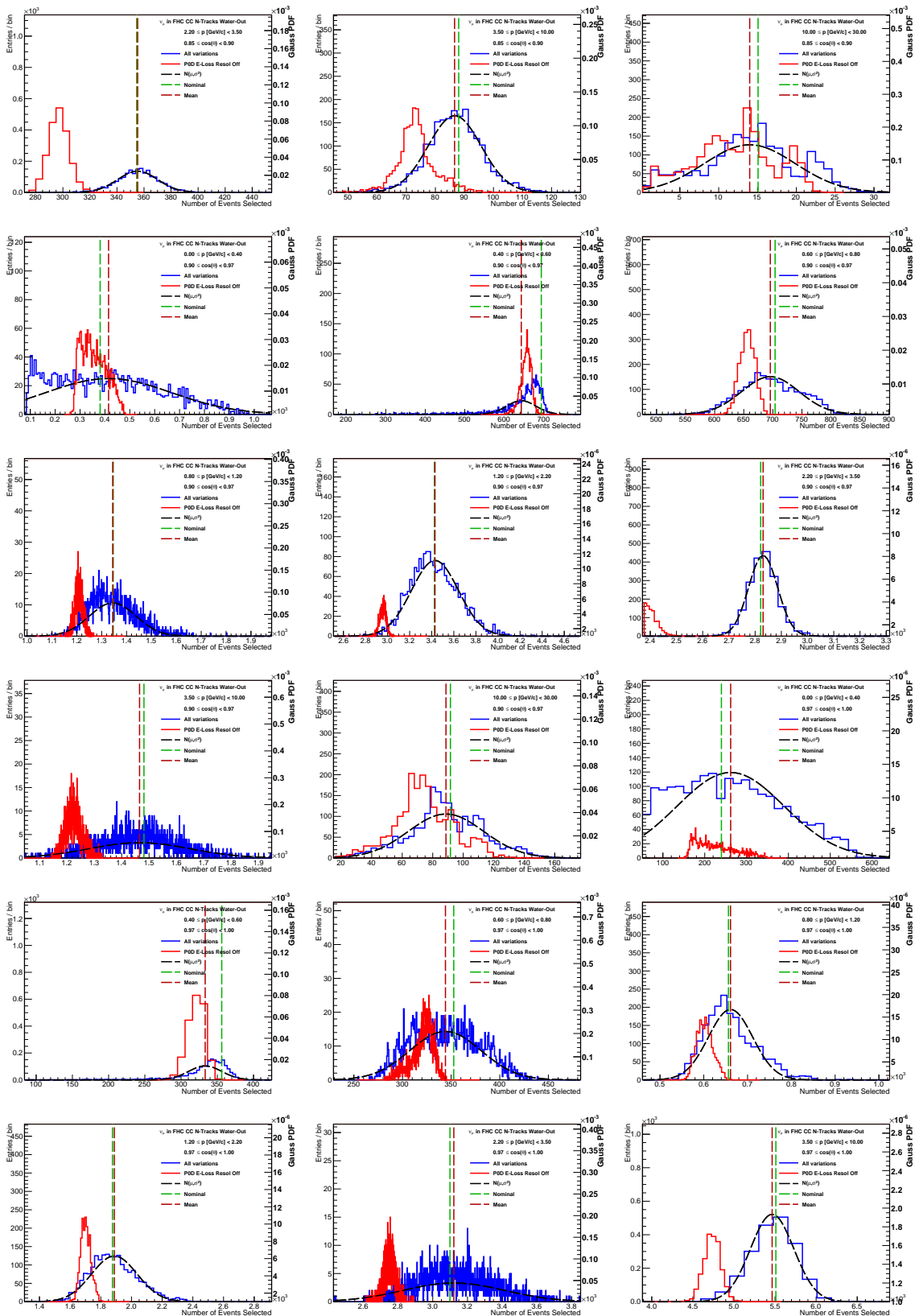


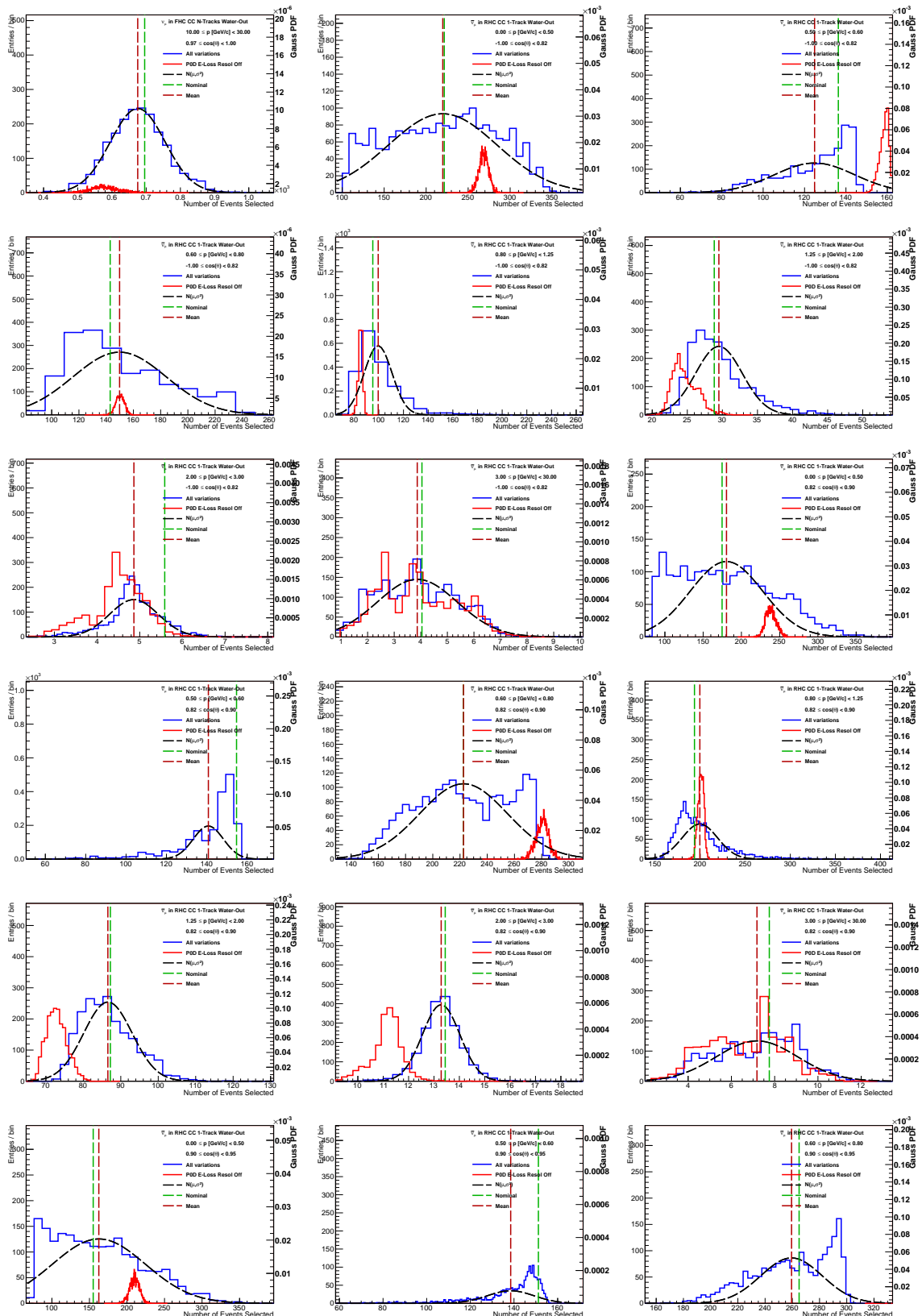


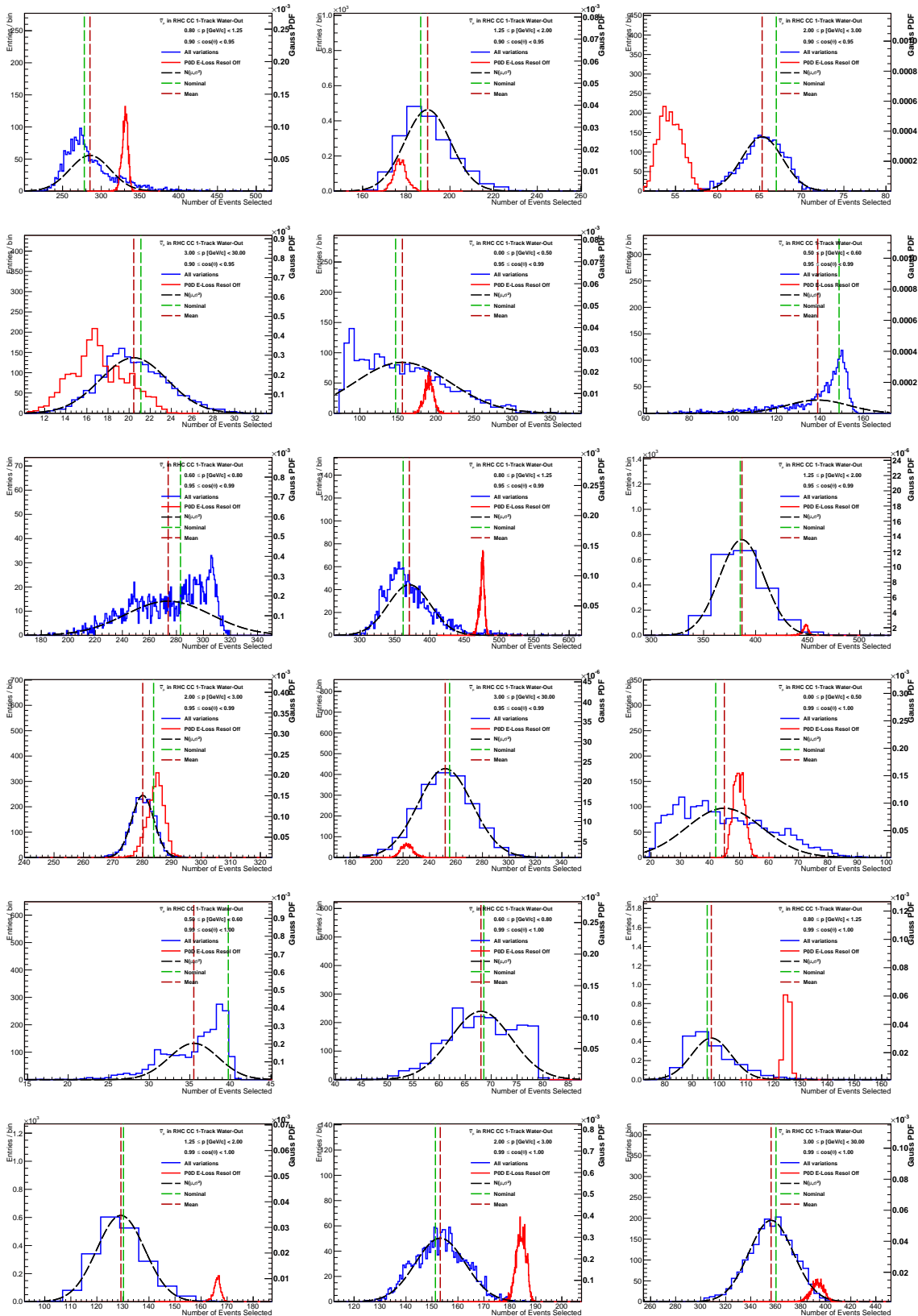


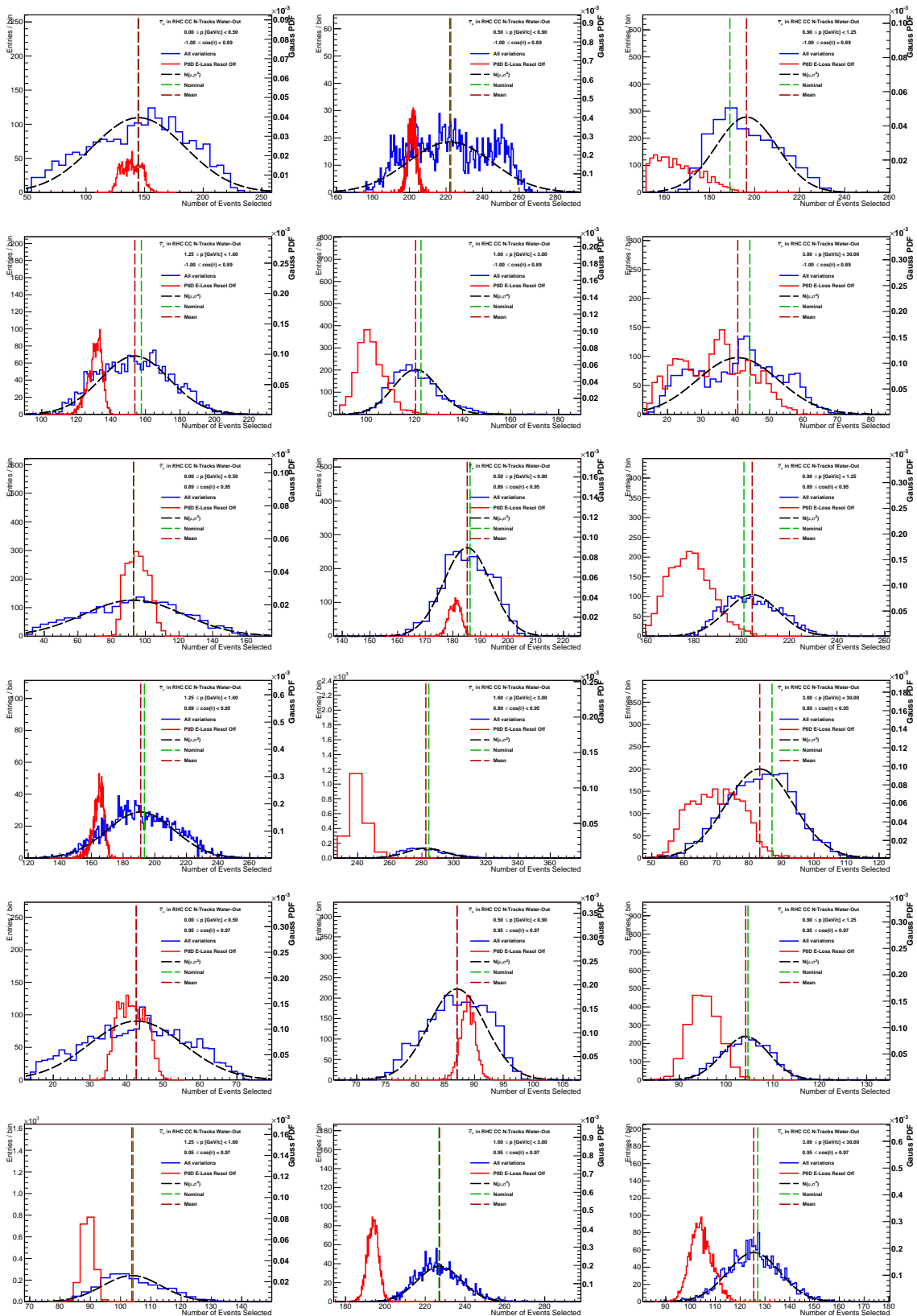


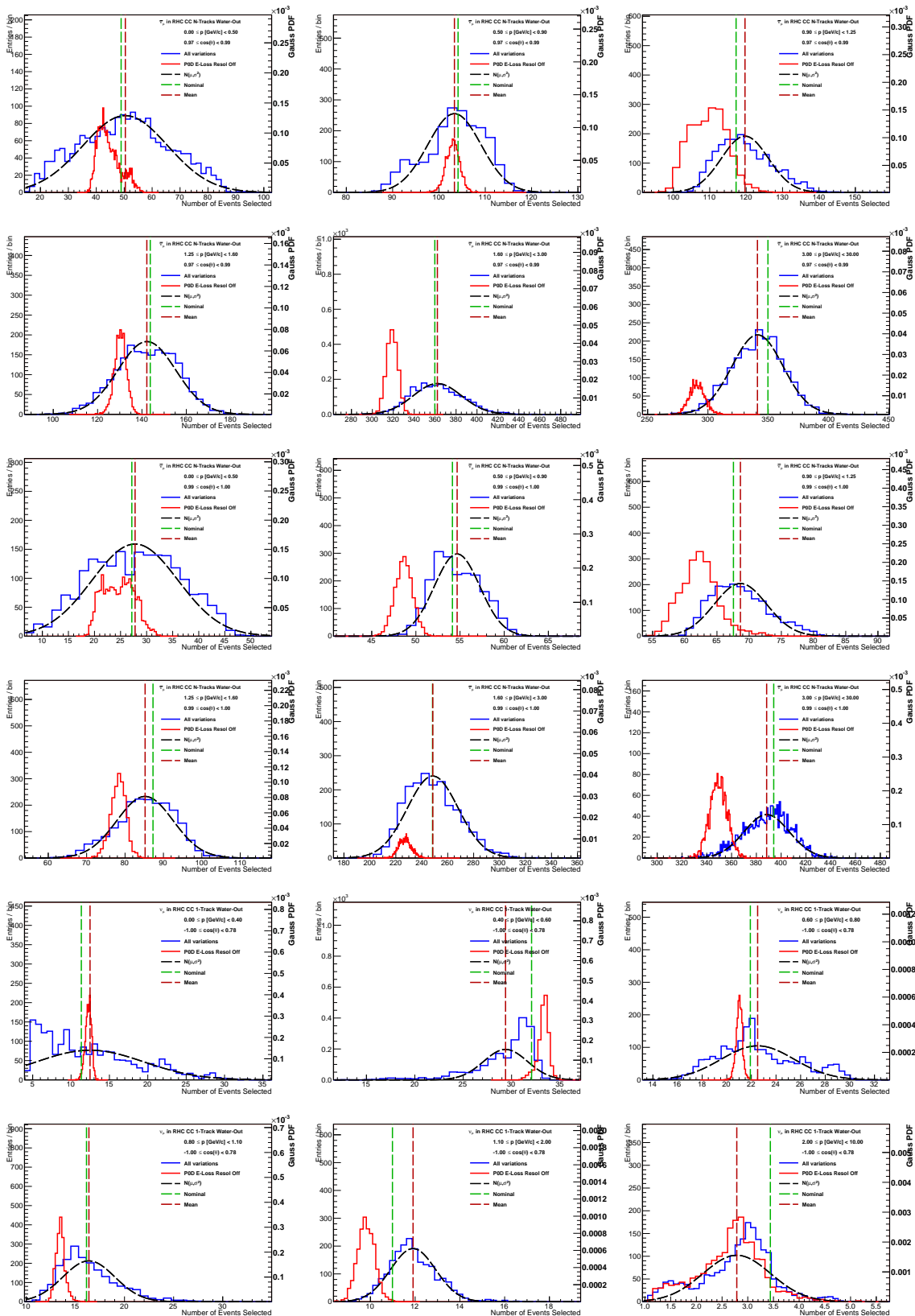


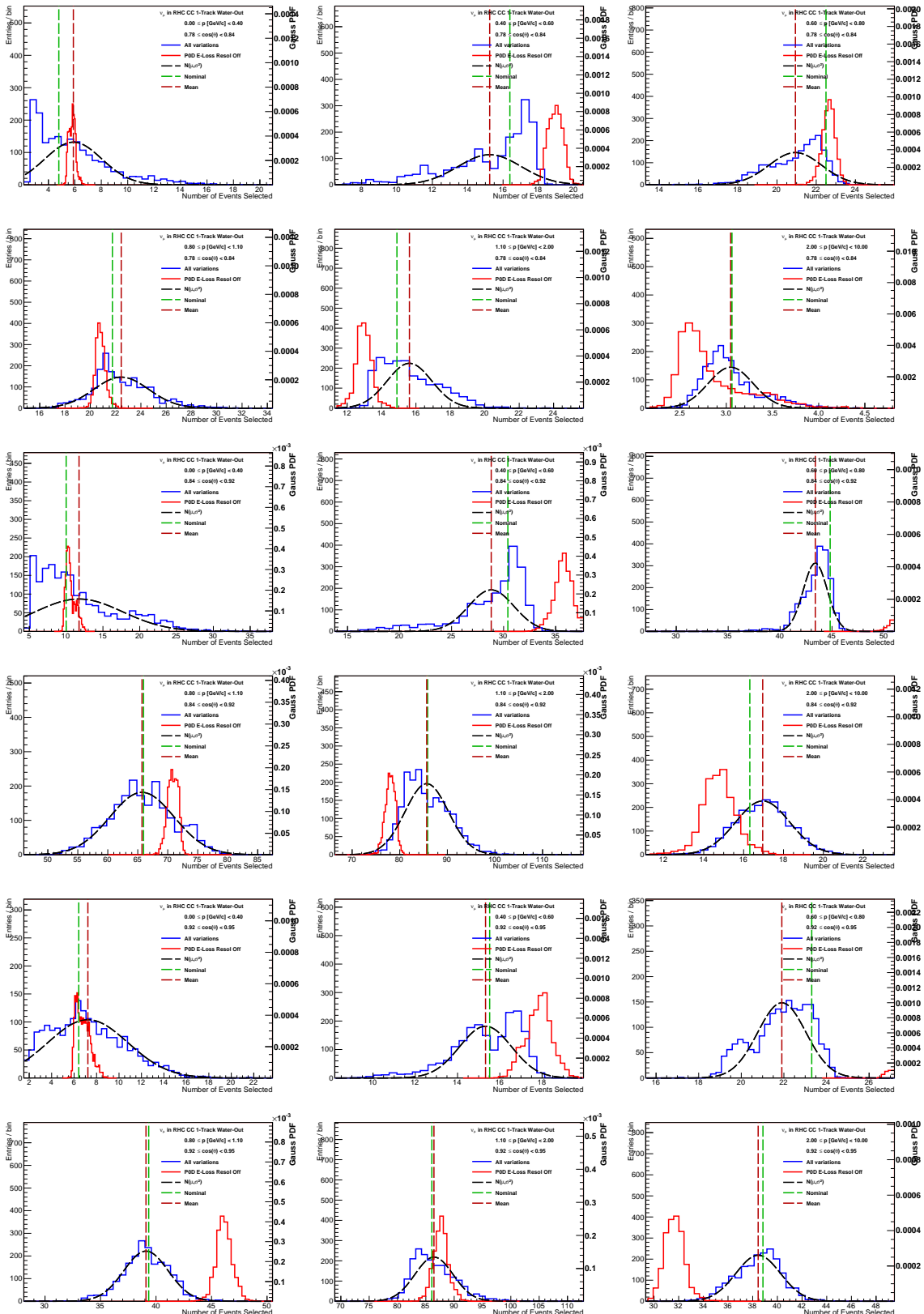


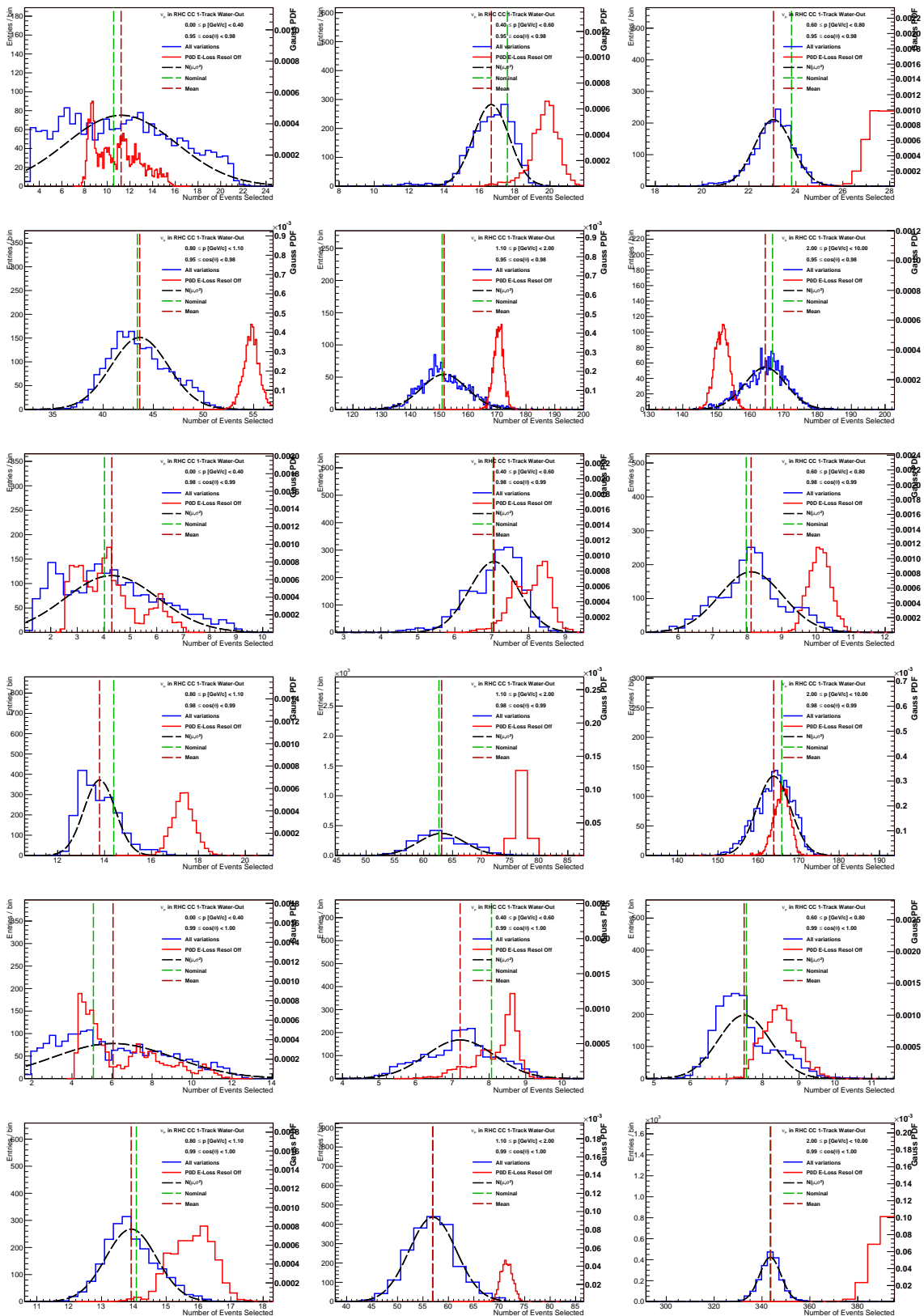


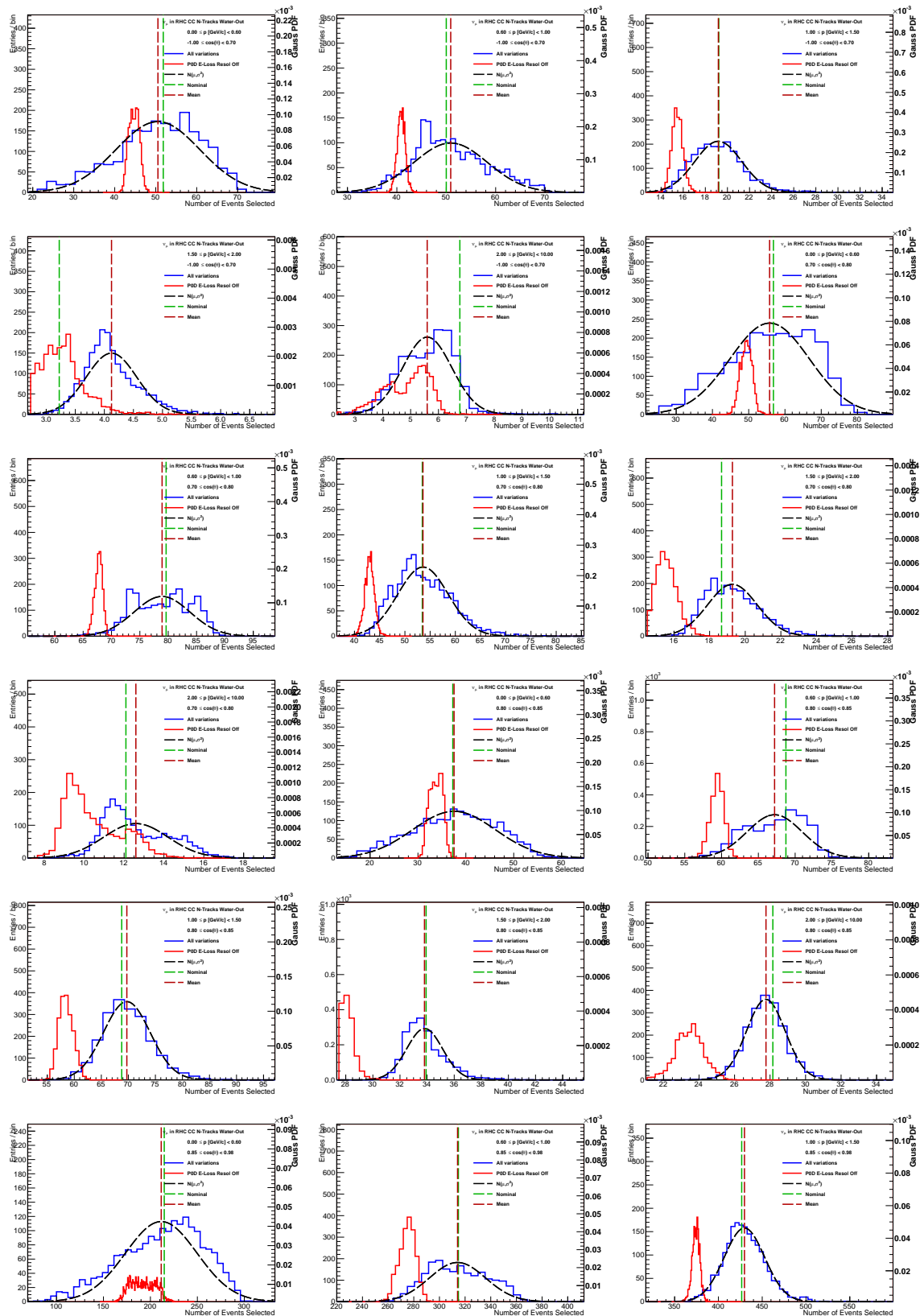


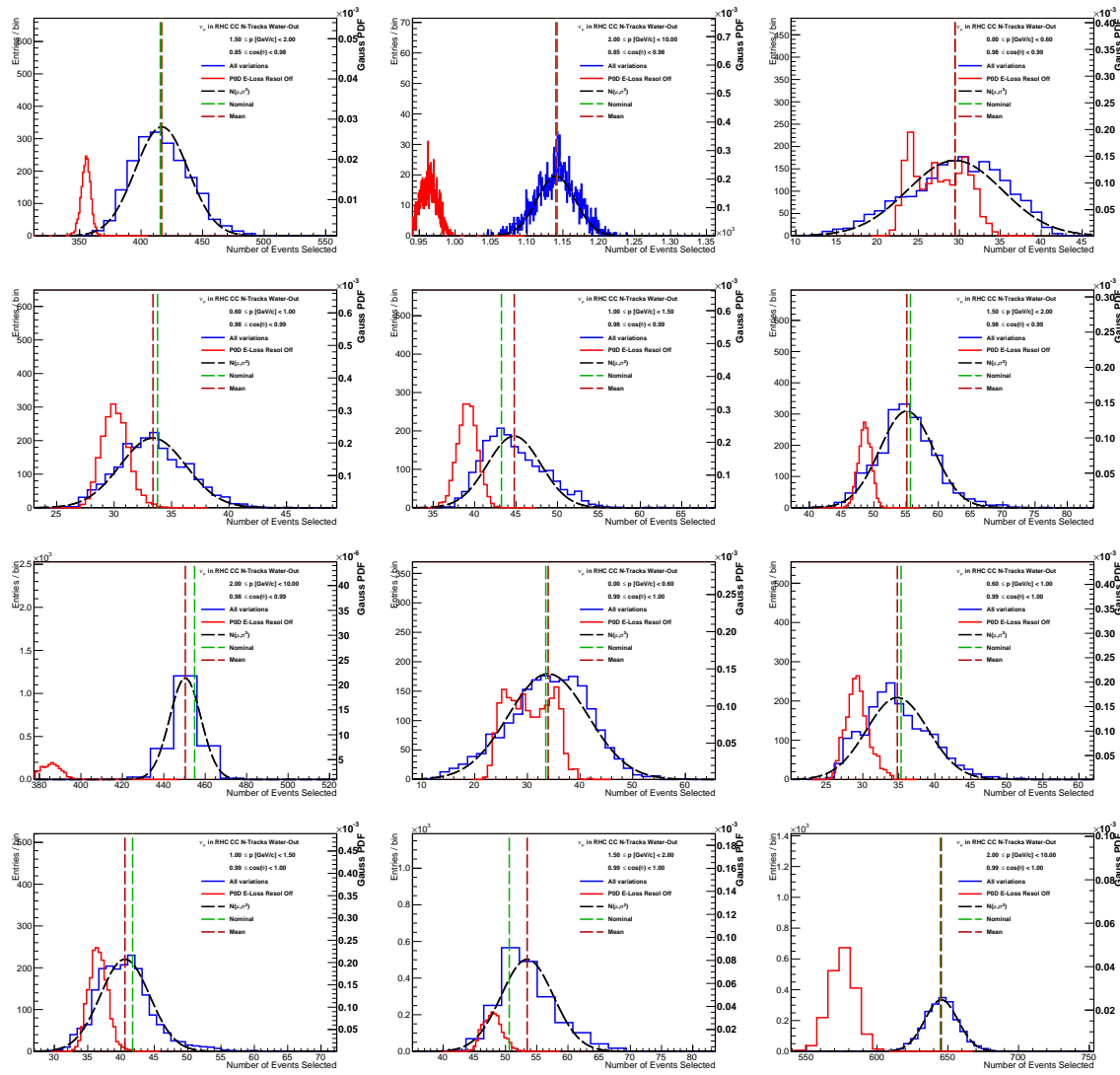












<sub>1675</sub> **Appendix C**

<sub>1676</sub> **Variations of the Cross Section**

<sub>1677</sub> **Parameters**

<sub>1678</sub> This appendix is a tabulation of variations of the cross section parameters and their uncorrelated affect on  
<sub>1679</sub> the analysis samples. The variations are shown in Table C.1. Note that the “nominal” column refers to all  
<sub>1680</sub> weighted events in the sample. When a “ $\pm 1\sigma$ ” variation is applied, the corresponding fractional change is  
<sub>1681</sub> reported.

Table C.1: Event rate variations per cross section parameter variation.

Parameter	$1\sigma$ value	Sample	$-1\sigma$ (%)	nominal	$+1\sigma$ (%)
<b>562 : FSI Low energy INEL</b>	<b>0.41</b>	$\nu_\mu$ 1-Trk Wtr	-0.9	27316.74	0.7
		$\nu_\mu$ N-Trks	0.7	30904.32	-0.5
		$\bar{\nu}_\mu$ RHC 1-Trk	-0.5	8414.09	0.4
		$\bar{\nu}_\mu$ RHC N-Trks	1.0	4724.34	-0.7
		$\nu_\mu$ RHC 1-Trk	-1.2	3022.10	0.9
		$\nu_\mu$ RHC N-Trks	0.5	4928.38	-0.4
		$\nu_\mu$ 1-Trk Air	-0.9	23605.76	0.7
		$\nu_\mu$ N-Trks	0.5	32304.13	-0.4
		$\bar{\nu}_\mu$ RHC 1-Trk	-0.6	6767.65	0.5
		$\bar{\nu}_\mu$ RHC N-Trks	0.8	4544.65	-0.6
		$\nu_\mu$ RHC 1-Trk	-1.5	2067.37	1.4
		$\nu_\mu$ RHC N-Trks	0.6	4568.13	-0.7
<b>563 : FSI High energy INEL</b>	<b>0.34</b>	$\nu_\mu$ 1-Trk Wtr	-0.2	27316.74	0.2
		$\nu_\mu$ N-Trks	-0.1	30904.32	0.2
		$\bar{\nu}_\mu$ RHC 1-Trk	-0.1	8414.09	0.1
		$\bar{\nu}_\mu$ RHC N-Trks	-0.0	4724.34	0.1
		$\nu_\mu$ RHC 1-Trk	-0.4	3022.10	0.4
		$\nu_\mu$ RHC N-Trks	-0.1	4928.38	0.1
		$\nu_\mu$ 1-Trk Air	-0.2	23605.76	0.1
		$\nu_\mu$ N-Trks	-0.2	32304.13	0.2
		$\bar{\nu}_\mu$ RHC 1-Trk	-0.1	6767.65	0.1
		$\bar{\nu}_\mu$ RHC N-Trks	-0.1	4544.65	0.1
		$\nu_\mu$ RHC 1-Trk	-0.2	2067.37	0.2
		$\nu_\mu$ RHC N-Trks	-0.1	4568.13	0.2

Parameter	$1\sigma$ value	Sample	$-1\sigma$ (%)	nominal	$+1\sigma$ (%)
<b>564 : FSI PROD</b>	<b>0.50</b>	$\nu_\mu$ 1-Trk Wtr	-0.1	27316.74	0.1
		$\nu_\mu$ N-Trks	-0.0	30904.32	0.1
		$\bar{\nu}_\mu$ RHC 1-Trk	-0.0	8414.09	0.0
		$\bar{\nu}_\mu$ RHC N-Trks	0.1	4724.34	-0.0
		$\nu_\mu$ RHC 1-Trk	-0.1	3022.10	0.1
		$\nu_\mu$ RHC N-Trks	-0.1	4928.38	0.1
		$\nu_\mu$ 1-Trk Air	-0.0	23605.76	0.1
		$\nu_\mu$ N-Trks	-0.1	32304.13	0.1
		$\bar{\nu}_\mu$ RHC 1-Trk	-0.0	6767.65	0.0
		$\bar{\nu}_\mu$ RHC N-Trks	0.2	4544.65	-0.1
<b>565 : FSI ABS</b>	<b>0.41</b>	$\nu_\mu$ RHC 1-Trk	-0.1	2067.37	0.1
		$\nu_\mu$ RHC N-Trks	-0.1	4568.13	0.1
		$\nu_\mu$ 1-Trk Wtr	-0.7	27316.74	0.5
		$\nu_\mu$ N-Trks	0.6	30904.32	-0.5
		$\bar{\nu}_\mu$ RHC 1-Trk	-0.6	8414.09	0.5
		$\bar{\nu}_\mu$ RHC N-Trks	1.0	4724.34	-0.8
		$\nu_\mu$ RHC 1-Trk	-1.0	3022.10	0.8
		$\nu_\mu$ RHC N-Trks	0.5	4928.38	-0.4
		$\nu_\mu$ 1-Trk Air	-0.7	23605.76	0.6
		$\nu_\mu$ N-Trks	0.6	32304.13	-0.4

Parameter	$1\sigma$ value	Sample	$-1\sigma$ (%)	nominal	$+1\sigma$ (%)
<b>566 : FSI Low energy CEX</b>	<b>0.57</b>	$\nu_\mu$ 1-Trk Wtr	0.3	27316.74	-0.2
		$\nu_\mu$ N-Trks	-0.3	30904.32	0.2
		$\bar{\nu}_\mu$ RHC 1-Trk	0.2	8414.09	-0.1
		$\bar{\nu}_\mu$ RHC N-Trks	-0.2	4724.34	0.2
		$\nu_\mu$ RHC 1-Trk	0.4	3022.10	-0.3
		$\nu_\mu$ RHC N-Trks	-0.3	4928.38	0.2
		$\nu_\mu$ 1-Trk Air	0.3	23605.76	-0.2
		$\nu_\mu$ N-Trks	-0.3	32304.13	0.2
		$\bar{\nu}_\mu$ RHC 1-Trk	0.2	6767.65	-0.1
		$\bar{\nu}_\mu$ RHC N-Trks	-0.3	4544.65	0.3
		$\nu_\mu$ RHC 1-Trk	0.2	2067.37	-0.2
		$\nu_\mu$ RHC N-Trks	-0.1	4568.13	0.1
<b>567 : FSI High energy CEX</b>	<b>0.28</b>	$\nu_\mu$ 1-Trk Wtr	-0.0	27316.74	0.0
		$\nu_\mu$ N-Trks	-0.0	30904.32	0.0
		$\bar{\nu}_\mu$ RHC 1-Trk	-0.0	8414.09	0.0
		$\bar{\nu}_\mu$ RHC N-Trks	0.0	4724.34	-0.0
		$\nu_\mu$ RHC 1-Trk	-0.1	3022.10	0.1
		$\nu_\mu$ RHC N-Trks	-0.0	4928.38	0.0
		$\nu_\mu$ 1-Trk Air	-0.0	23605.76	0.0
		$\nu_\mu$ N-Trks	-0.1	32304.13	0.1
		$\bar{\nu}_\mu$ RHC 1-Trk	-0.0	6767.65	0.0
		$\bar{\nu}_\mu$ RHC N-Trks	0.0	4544.65	-0.0
		$\nu_\mu$ RHC 1-Trk	-0.0	2067.37	0.0
		$\nu_\mu$ RHC N-Trks	-0.0	4568.13	0.0

Parameter	$1\sigma$ value	Sample	$-1\sigma$ (%)	nominal	$+1\sigma$ (%)
<b>568 : <math>M_A^{QE}</math></b>	<b>0.03</b>	$\nu_\mu$ 1-Trk Wtr	-0.8	27316.74	0.8
		$\nu_\mu$ N-Trks	-0.4	30904.32	0.4
		$\bar{\nu}_\mu$ RHC 1-Trk	-0.7	8414.09	0.7
		$\bar{\nu}_\mu$ RHC N-Trks	-0.2	4724.34	0.3
		$\nu_\mu$ RHC 1-Trk	-0.9	3022.10	0.9
		$\nu_\mu$ RHC N-Trks	-0.4	4928.38	0.4
		$\nu_\mu$ 1-Trk Air	-0.8	23605.76	0.8
		$\nu_\mu$ N-Trks	-0.5	32304.13	0.5
		$\bar{\nu}_\mu$ RHC 1-Trk	-0.7	6767.65	0.7
		$\bar{\nu}_\mu$ RHC N-Trks	-0.2	4544.65	0.3
		$\nu_\mu$ RHC 1-Trk	-0.9	2067.37	0.9
		$\nu_\mu$ RHC N-Trks	-0.4	4568.13	0.4
<b>569 : <math>p_F^C</math></b>	<b>0.06</b>	$\nu_\mu$ 1-Trk Wtr	0.8	27316.74	-0.7
		$\nu_\mu$ N-Trks	0.0	30904.32	-0.0
		$\bar{\nu}_\mu$ RHC 1-Trk	0.7	8414.09	-0.7
		$\bar{\nu}_\mu$ RHC N-Trks	0.0	4724.34	-0.0
		$\nu_\mu$ RHC 1-Trk	0.4	3022.10	-0.4
		$\nu_\mu$ RHC N-Trks	0.0	4928.38	-0.0
		$\nu_\mu$ 1-Trk Air	1.1	23605.76	-1.0
		$\nu_\mu$ N-Trks	0.0	32304.13	-0.0
		$\bar{\nu}_\mu$ RHC 1-Trk	1.2	6767.65	-1.1
		$\bar{\nu}_\mu$ RHC N-Trks	0.0	4544.65	-0.0
		$\nu_\mu$ RHC 1-Trk	0.7	2067.37	-0.7
		$\nu_\mu$ RHC N-Trks	0.0	4568.13	-0.0

Parameter	$1\sigma$ value	Sample	$-1\sigma$ (%)	nominal	$+1\sigma$ (%)
<b>570 : <math>p_F^O</math></b>	<b>0.06</b>	$\nu_\mu$ 1-Trk Wtr	0.4	27316.74	-0.4
		$\nu_\mu$ N-Trks	0.0	30904.32	-0.0
		$\bar{\nu}_\mu$ RHC 1-Trk	0.5	8414.09	-0.5
		$\bar{\nu}_\mu$ RHC N-Trks	0.0	4724.34	-0.0
		$\nu_\mu$ RHC 1-Trk	0.3	3022.10	-0.3
		$\nu_\mu$ RHC N-Trks	0.0	4928.38	-0.0
		$\nu_\mu$ 1-Trk Air	0.0	23605.76	-0.0
		$\nu_\mu$ N-Trks	0.0	32304.13	-0.0
		$\bar{\nu}_\mu$ RHC 1-Trk	0.0	6767.65	-0.0
		$\bar{\nu}_\mu$ RHC N-Trks	-0.0	4544.65	-0.0
		$\nu_\mu$ RHC 1-Trk	-0.0	2067.37	0.0
		$\nu_\mu$ RHC N-Trks	0.0	4568.13	-0.0
		$\nu_\mu$ 1-Trk Wtr	-8.9	27316.74	8.9
<b>571 : 2p2h <math>\nu</math> norm. on <math>^{12}\text{C}</math></b>	<b>1.00</b>	$\nu_\mu$ N-Trks	-3.0	30904.32	3.0
		$\bar{\nu}_\mu$ RHC 1-Trk	-0.1	8414.09	0.1
		$\bar{\nu}_\mu$ RHC N-Trks	-0.2	4724.34	0.2
		$\nu_\mu$ RHC 1-Trk	-9.0	3022.10	9.0
		$\nu_\mu$ RHC N-Trks	-2.6	4928.38	2.6
		$\nu_\mu$ 1-Trk Air	-8.1	23605.76	8.1
		$\nu_\mu$ N-Trks	-3.3	32304.13	3.3
		$\bar{\nu}_\mu$ RHC 1-Trk	-0.1	6767.65	0.1
		$\bar{\nu}_\mu$ RHC N-Trks	-0.2	4544.65	0.2
		$\nu_\mu$ RHC 1-Trk	-8.6	2067.37	8.6
		$\nu_\mu$ RHC N-Trks	-2.8	4568.13	2.8

Parameter	$1\sigma$ value	Sample	$-1\sigma$ (%)	nominal	$+1\sigma$ (%)
<b>572 : 2p2h <math>\bar{\nu}</math> norm. on <math>^{12}\text{C}</math></b>	<b>1.00</b>	$\nu_\mu$ 1-Trk Wtr	-0.0	27316.74	0.0
		$\nu_\mu$ N-Trks	-0.0	30904.32	0.0
		$\bar{\nu}_\mu$ RHC 1-Trk	-9.3	8414.09	9.3
		$\bar{\nu}_\mu$ RHC N-Trks	-2.1	4724.34	2.1
		$\nu_\mu$ RHC 1-Trk	-0.2	3022.10	0.2
		$\nu_\mu$ RHC N-Trks	-0.0	4928.38	0.0
		$\nu_\mu$ 1-Trk Air	-0.0	23605.76	0.0
		$\nu_\mu$ N-Trks	-0.0	32304.13	0.0
		$\bar{\nu}_\mu$ RHC 1-Trk	-8.9	6767.65	8.9
		$\bar{\nu}_\mu$ RHC N-Trks	-2.2	4544.65	2.2
		$\nu_\mu$ RHC 1-Trk	-0.3	2067.37	0.3
		$\nu_\mu$ RHC N-Trks	-0.0	4568.13	0.0
<b>573 : 2p2h <math>^{12}\text{C} \rightarrow ^{16}\text{O}</math> norm.</b>	<b>0.20</b>	$\nu_\mu$ 1-Trk Wtr	-0.6	27316.74	0.6
		$\nu_\mu$ N-Trks	-0.2	30904.32	0.2
		$\bar{\nu}_\mu$ RHC 1-Trk	-0.8	8414.09	0.8
		$\bar{\nu}_\mu$ RHC N-Trks	-0.2	4724.34	0.2
		$\nu_\mu$ RHC 1-Trk	-0.8	3022.10	0.8
		$\nu_\mu$ RHC N-Trks	-0.2	4928.38	0.2
		$\nu_\mu$ 1-Trk Air	-0.0	23605.76	0.0
		$\nu_\mu$ N-Trks	-0.0	32304.13	0.0
		$\bar{\nu}_\mu$ RHC 1-Trk	-0.0	6767.65	0.0
		$\bar{\nu}_\mu$ RHC N-Trks	-0.0	4544.65	0.0
		$\nu_\mu$ RHC 1-Trk	-0.0	2067.37	0.0
		$\nu_\mu$ RHC N-Trks	-0.0	4568.13	0.0

Parameter	$1\sigma$ value	Sample	$-1\sigma$ (%)	nominal	$+1\sigma$ (%)
<b>574 : 2p2h <math>^{12}\text{C}</math> shape location</b>	<b>2.00</b>	$\nu_\mu$ 1-Trk Wtr	3.8	27316.74	0.0
		$\nu_\mu$ N-Trks	-1.1	30904.32	0.0
		$\bar{\nu}_\mu$ RHC 1-Trk	0.2	8414.09	0.0
		$\bar{\nu}_\mu$ RHC N-Trks	-0.8	4724.34	0.0
		$\nu_\mu$ RHC 1-Trk	4.3	3022.10	0.0
		$\nu_\mu$ RHC N-Trks	-0.8	4928.38	0.0
		$\nu_\mu$ 1-Trk Air	5.7	23605.76	0.0
		$\nu_\mu$ N-Trks	-1.5	32304.13	0.0
		$\bar{\nu}_\mu$ RHC 1-Trk	0.2	6767.65	0.0
		$\bar{\nu}_\mu$ RHC N-Trks	-1.1	4544.65	0.0
<b>575 : 2p2h <math>^{16}\text{O}</math> shape location</b>	<b>2.00</b>	$\nu_\mu$ RHC 1-Trk	8.1	2067.37	0.0
		$\nu_\mu$ RHC N-Trks	-1.4	4568.13	0.0
		$\nu_\mu$ 1-Trk Wtr	2.1	27316.74	0.0
		$\nu_\mu$ N-Trks	-0.5	30904.32	0.0
		$\bar{\nu}_\mu$ RHC 1-Trk	0.1	8414.09	0.0
		$\bar{\nu}_\mu$ RHC N-Trks	-0.5	4724.34	0.0
		$\nu_\mu$ RHC 1-Trk	3.2	3022.10	0.0
		$\nu_\mu$ RHC N-Trks	-0.6	4928.38	0.0
		$\nu_\mu$ 1-Trk Air	0.0	23605.76	0.0
		$\nu_\mu$ N-Trks	-0.0	32304.13	0.0

Parameter	$1\sigma$ value	Sample	$-1\sigma$ (%)	nominal	$+1\sigma$ (%)
<b>576 : BeRPA A scale</b>	<b>0.12</b>	$\nu_\mu$ 1-Trk Wtr	-5.1	27316.74	5.1
		$\nu_\mu$ N-Trks	-0.3	30904.32	0.3
		$\bar{\nu}_\mu$ RHC 1-Trk	-4.7	8414.09	4.7
		$\bar{\nu}_\mu$ RHC N-Trks	-0.2	4724.34	0.2
		$\nu_\mu$ RHC 1-Trk	-3.5	3022.10	3.5
		$\nu_\mu$ RHC N-Trks	-0.1	4928.38	0.1
		$\nu_\mu$ 1-Trk Air	-5.1	23605.76	5.1
		$\nu_\mu$ N-Trks	-0.3	32304.13	0.3
		$\bar{\nu}_\mu$ RHC 1-Trk	-4.6	6767.65	4.6
		$\bar{\nu}_\mu$ RHC N-Trks	-0.1	4544.65	0.1
<b>577 : BeRPA B scale</b>	<b>0.21</b>	$\nu_\mu$ RHC 1-Trk	-3.7	2067.37	3.7
		$\nu_\mu$ RHC N-Trks	-0.2	4568.13	0.2
		$\nu_\mu$ 1-Trk Wtr	-3.4	27316.74	3.4
		$\nu_\mu$ N-Trks	-0.6	30904.32	0.6
		$\bar{\nu}_\mu$ RHC 1-Trk	-2.6	8414.09	2.6
		$\bar{\nu}_\mu$ RHC N-Trks	-0.2	4724.34	0.2
		$\nu_\mu$ RHC 1-Trk	-3.1	3022.10	3.1
		$\nu_\mu$ RHC N-Trks	-0.4	4928.38	0.4
		$\nu_\mu$ 1-Trk Air	-3.3	23605.76	3.3
		$\nu_\mu$ N-Trks	-0.6	32304.13	0.6

Parameter	$1\sigma$ value	Sample	$-1\sigma$ (%)	nominal	$+1\sigma$ (%)
<b>578 : BeRPA D scale</b>	<b>0.17</b>	$\nu_\mu$ 1-Trk Wtr	-1.3	27316.74	1.3
		$\nu_\mu$ N-Trks	-1.0	30904.32	1.0
		$\bar{\nu}_\mu$ RHC 1-Trk	-1.0	8414.09	1.0
		$\bar{\nu}_\mu$ RHC N-Trks	-0.5	4724.34	0.5
		$\nu_\mu$ RHC 1-Trk	-1.7	3022.10	1.7
		$\nu_\mu$ RHC N-Trks	-0.9	4928.38	0.9
		$\nu_\mu$ 1-Trk Air	-1.1	23605.76	1.1
		$\nu_\mu$ N-Trks	-0.9	32304.13	0.9
		$\bar{\nu}_\mu$ RHC 1-Trk	-0.9	6767.65	0.9
		$\bar{\nu}_\mu$ RHC N-Trks	-0.4	4544.65	0.4
		$\nu_\mu$ RHC 1-Trk	-1.4	2067.37	1.4
		$\nu_\mu$ RHC N-Trks	-0.9	4568.13	0.9
<b>579 : BeRPA E scale</b>	<b>0.35</b>	$\nu_\mu$ 1-Trk Wtr	-0.1	27316.74	0.1
		$\nu_\mu$ N-Trks	-0.0	30904.32	0.0
		$\bar{\nu}_\mu$ RHC 1-Trk	-0.1	8414.09	0.1
		$\bar{\nu}_\mu$ RHC N-Trks	0.0	4724.34	-0.0
		$\nu_\mu$ RHC 1-Trk	-0.1	3022.10	0.1
		$\nu_\mu$ RHC N-Trks	-0.0	4928.38	0.0
		$\nu_\mu$ 1-Trk Air	-0.1	23605.76	0.1
		$\nu_\mu$ N-Trks	-0.0	32304.13	0.0
		$\bar{\nu}_\mu$ RHC 1-Trk	-0.1	6767.65	0.1
		$\bar{\nu}_\mu$ RHC N-Trks	0.0	4544.65	0.0
		$\nu_\mu$ RHC 1-Trk	-0.1	2067.37	0.1
		$\nu_\mu$ RHC N-Trks	-0.0	4568.13	0.0

Parameter	$1\sigma$ value	Sample	$-1\sigma$ (%)	nominal	$+1\sigma$ (%)
<b>580 : BeRPA U scale*</b>	<b>0.10</b>	$\nu_\mu$ 1-Trk Wtr	0.7	27316.74	-0.7
		$\nu_\mu$ N-Trks	0.1	30904.32	-0.1
		$\bar{\nu}_\mu$ RHC 1-Trk	0.6	8414.09	-0.5
		$\bar{\nu}_\mu$ RHC N-Trks	0.0	4724.34	-0.0
		$\nu_\mu$ RHC 1-Trk	0.7	3022.10	-0.6
		$\nu_\mu$ RHC N-Trks	0.1	4928.38	-0.1
		$\nu_\mu$ 1-Trk Air	0.7	23605.76	-0.6
		$\nu_\mu$ N-Trks	0.1	32304.13	-0.1
		$\bar{\nu}_\mu$ RHC 1-Trk	0.5	6767.65	-0.5
		$\bar{\nu}_\mu$ RHC N-Trks	0.0	4544.65	-0.0
		$\nu_\mu$ RHC 1-Trk	0.7	2067.37	-0.6
		$\nu_\mu$ RHC N-Trks	0.1	4568.13	-0.1
<b>581 : <math>C_A^5</math></b>	<b>0.15</b>	$\nu_\mu$ 1-Trk Wtr	-3.4	27316.74	3.9
		$\nu_\mu$ N-Trks	-4.4	30904.32	5.0
		$\bar{\nu}_\mu$ RHC 1-Trk	-2.7	8414.09	3.4
		$\bar{\nu}_\mu$ RHC N-Trks	-4.7	4724.34	5.8
		$\nu_\mu$ RHC 1-Trk	-4.5	3022.10	5.2
		$\nu_\mu$ RHC N-Trks	-4.1	4928.38	4.7
		$\nu_\mu$ 1-Trk Air	-2.9	23605.76	3.3
		$\nu_\mu$ N-Trks	-4.6	32304.13	5.2
		$\bar{\nu}_\mu$ RHC 1-Trk	-2.5	6767.65	3.1
		$\bar{\nu}_\mu$ RHC N-Trks	-4.9	4544.65	6.1
		$\nu_\mu$ RHC 1-Trk	-3.8	2067.37	4.4
		$\nu_\mu$ RHC N-Trks	-4.3	4568.13	5.0

Parameter	$1\sigma$ value	Sample	$-1\sigma$ (%)	nominal	$+1\sigma$ (%)
<b>582 : <math>M_A^{\text{RES}}</math></b>	<b>0.16</b>	$\nu_\mu$ 1-Trk Wtr	-2.1	27316.74	1.9
		$\nu_\mu$ N-Trks	-4.8	30904.32	5.1
		$\bar{\nu}_\mu$ RHC 1-Trk	-1.6	8414.09	1.6
		$\bar{\nu}_\mu$ RHC N-Trks	-4.8	4724.34	5.8
		$\nu_\mu$ RHC 1-Trk	-3.1	3022.10	2.9
		$\nu_\mu$ RHC N-Trks	-4.8	4928.38	5.3
		$\nu_\mu$ 1-Trk Air	-1.7	23605.76	1.5
		$\nu_\mu$ N-Trks	-4.6	32304.13	4.9
		$\bar{\nu}_\mu$ RHC 1-Trk	-1.4	6767.65	1.5
		$\bar{\nu}_\mu$ RHC N-Trks	-4.8	4544.65	5.9
		$\nu_\mu$ RHC 1-Trk	-2.5	2067.37	2.3
		$\nu_\mu$ RHC N-Trks	-4.7	4568.13	5.2
<b>583 : I=<math>^{1/2}</math> bkg. norm.</b>	<b>0.31</b>	$\nu_\mu$ 1-Trk Wtr	-1.1	27316.74	1.8
		$\nu_\mu$ N-Trks	-2.4	30904.32	3.7
		$\bar{\nu}_\mu$ RHC 1-Trk	-0.8	8414.09	1.3
		$\bar{\nu}_\mu$ RHC N-Trks	-3.1	4724.34	4.8
		$\nu_\mu$ RHC 1-Trk	-1.7	3022.10	2.5
		$\nu_\mu$ RHC N-Trks	-2.5	4928.38	3.8
		$\nu_\mu$ 1-Trk Air	-1.1	23605.76	1.6
		$\nu_\mu$ N-Trks	-2.4	32304.13	3.6
		$\bar{\nu}_\mu$ RHC 1-Trk	-0.7	6767.65	1.1
		$\bar{\nu}_\mu$ RHC N-Trks	-3.0	4544.65	4.5
		$\nu_\mu$ RHC 1-Trk	-1.6	2067.37	2.4
		$\nu_\mu$ RHC N-Trks	-2.4	4568.13	3.7

Parameter	$1\sigma$ value	Sample	$-1\sigma$ (%)	nominal	$+1\sigma$ (%)
<b>584 : CC-<math>\nu_e/\nu_\mu^*</math></b>	<b>0.03</b>	$\nu_\mu$ 1-Trk Wtr	0.0	27316.74	0.0
		$\nu_\mu$ N-Trks	0.0	30904.32	0.0
		$\bar{\nu}_\mu$ RHC 1-Trk	0.0	8414.09	0.0
		$\bar{\nu}_\mu$ RHC N-Trks	0.0	4724.34	0.0
		$\nu_\mu$ RHC 1-Trk	0.0	3022.10	0.0
		$\nu_\mu$ RHC N-Trks	0.0	4928.38	0.0
		$\nu_\mu$ 1-Trk Air	0.0	23605.76	0.0
		$\nu_\mu$ N-Trks	0.0	32304.13	0.0
		$\bar{\nu}_\mu$ RHC 1-Trk	0.0	6767.65	0.0
		$\bar{\nu}_\mu$ RHC N-Trks	0.0	4544.65	0.0
<b>585 : CC-<math>\bar{\nu}_e/\bar{\nu}_\mu^*</math></b>	<b>0.03</b>	$\nu_\mu$ RHC 1-Trk	0.0	2067.37	0.0
		$\nu_\mu$ RHC N-Trks	0.0	4568.13	0.0
		$\nu_\mu$ 1-Trk Wtr	0.0	27316.74	0.0
		$\nu_\mu$ N-Trks	0.0	30904.32	0.0
		$\bar{\nu}_\mu$ RHC 1-Trk	0.0	8414.09	0.0
		$\bar{\nu}_\mu$ RHC N-Trks	0.0	4724.34	0.0
		$\nu_\mu$ RHC 1-Trk	0.0	3022.10	0.0
		$\nu_\mu$ RHC N-Trks	0.0	4928.38	0.0
		$\nu_\mu$ 1-Trk Air	0.0	23605.76	0.0
		$\nu_\mu$ N-Trks	0.0	32304.13	0.0

Parameter	$1\sigma$ value	Sample	$-1\sigma$ (%)	nominal	$+1\sigma$ (%)
<b>586 : CC-DIS shape location</b>	<b>0.40</b>	$\nu_\mu$ 1-Trk Wtr	-0.4	27316.74	0.4
		$\nu_\mu$ N-Trks	-4.2	30904.32	4.2
		$\bar{\nu}_\mu$ RHC 1-Trk	-0.3	8414.09	0.3
		$\bar{\nu}_\mu$ RHC N-Trks	-4.3	4724.34	4.3
		$\nu_\mu$ RHC 1-Trk	-0.7	3022.10	0.7
		$\nu_\mu$ RHC N-Trks	-4.4	4928.38	4.4
		$\nu_\mu$ 1-Trk Air	-0.3	23605.76	0.3
		$\nu_\mu$ N-Trks	-3.9	32304.13	3.9
		$\bar{\nu}_\mu$ RHC 1-Trk	-0.2	6767.65	0.2
		$\bar{\nu}_\mu$ RHC N-Trks	-4.2	4544.65	4.2
<b>587 : CC Coherent on <math>^{12}\text{C}</math> norm.</b>	<b>0.30</b>	$\nu_\mu$ RHC 1-Trk	-0.6	2067.37	0.6
		$\nu_\mu$ RHC N-Trks	-4.1	4568.13	4.1
		$\nu_\mu$ 1-Trk Wtr	-0.1	27316.74	0.1
		$\nu_\mu$ N-Trks	-0.2	30904.32	0.2
		$\bar{\nu}_\mu$ RHC 1-Trk	-0.1	8414.09	0.1
		$\bar{\nu}_\mu$ RHC N-Trks	-0.4	4724.34	0.4
		$\nu_\mu$ RHC 1-Trk	-0.1	3022.10	0.1
		$\nu_\mu$ RHC N-Trks	-0.2	4928.38	0.2
		$\nu_\mu$ 1-Trk Air	-0.1	23605.76	0.1
		$\nu_\mu$ N-Trks	-0.3	32304.13	0.3

Parameter	$1\sigma$ value	Sample	$-1\sigma$ (%)	nominal	$+1\sigma$ (%)
<b>588 : CC Coherent on <math>^{16}\text{O}</math> norm.</b>	<b>0.30</b>	$\nu_\mu$ 1-Trk Wtr	-0.0	27316.74	0.0
		$\nu_\mu$ N-Trks	-0.1	30904.32	0.1
		$\bar{\nu}_\mu$ RHC 1-Trk	-0.1	8414.09	0.1
		$\bar{\nu}_\mu$ RHC N-Trks	-0.2	4724.34	0.2
		$\nu_\mu$ RHC 1-Trk	-0.1	3022.10	0.1
		$\nu_\mu$ RHC N-Trks	-0.1	4928.38	0.1
		$\nu_\mu$ 1-Trk Air	-0.0	23605.76	0.0
		$\nu_\mu$ N-Trks	-0.0	32304.13	0.0
		$\bar{\nu}_\mu$ RHC 1-Trk	-0.0	6767.65	0.0
		$\bar{\nu}_\mu$ RHC N-Trks	-0.0	4544.65	0.0
<b>589 : NC Coherent norm.</b>	<b>0.30</b>	$\nu_\mu$ RHC 1-Trk	-0.0	2067.37	0.0
		$\nu_\mu$ RHC N-Trks	-0.0	4568.13	0.0
		$\nu_\mu$ 1-Trk Wtr	-0.0	27316.74	0.0
		$\nu_\mu$ N-Trks	-0.0	30904.32	0.0
		$\bar{\nu}_\mu$ RHC 1-Trk	-0.0	8414.09	0.0
		$\bar{\nu}_\mu$ RHC N-Trks	-0.0	4724.34	0.0
		$\nu_\mu$ RHC 1-Trk	-0.0	3022.10	0.0
		$\nu_\mu$ RHC N-Trks	-0.0	4928.38	0.0
		$\nu_\mu$ 1-Trk Air	-0.0	23605.76	0.0
		$\nu_\mu$ N-Trks	-0.0	32304.13	0.0

Parameter	$1\sigma$ value	Sample	$-1\sigma$ (%)	nominal	$+1\sigma$ (%)
<b>590 : NC-1<math>\gamma^*</math></b>	<b>1.00</b>	$\nu_\mu$ 1-Trk Wtr	-0.0	27316.74	0.0
		$\nu_\mu$ N-Trks	-0.0	30904.32	0.0
		$\bar{\nu}_\mu$ RHC 1-Trk	0.0	8414.09	0.0
		$\bar{\nu}_\mu$ RHC N-Trks	-0.0	4724.34	0.0
		$\nu_\mu$ RHC 1-Trk	0.0	3022.10	0.0
		$\nu_\mu$ RHC N-Trks	0.0	4928.38	0.0
		$\nu_\mu$ 1-Trk Air	-0.0	23605.76	0.0
		$\nu_\mu$ N-Trks	0.0	32304.13	0.0
		$\bar{\nu}_\mu$ RHC 1-Trk	0.0	6767.65	0.0
		$\bar{\nu}_\mu$ RHC N-Trks	-0.0	4544.65	0.0
		$\nu_\mu$ RHC 1-Trk	0.0	2067.37	0.0
		$\nu_\mu$ RHC N-Trks	0.0	4568.13	0.0
<b>591 : NC Other Near</b>	<b>0.30</b>	$\nu_\mu$ 1-Trk Wtr	-0.1	27316.74	0.1
		$\nu_\mu$ N-Trks	-0.6	30904.32	0.6
		$\bar{\nu}_\mu$ RHC 1-Trk	-0.2	8414.09	0.2
		$\bar{\nu}_\mu$ RHC N-Trks	-1.9	4724.34	1.9
		$\nu_\mu$ RHC 1-Trk	-0.2	3022.10	0.2
		$\nu_\mu$ RHC N-Trks	-0.8	4928.38	0.8
		$\nu_\mu$ 1-Trk Air	-0.1	23605.76	0.1
		$\nu_\mu$ N-Trks	-0.6	32304.13	0.6
		$\bar{\nu}_\mu$ RHC 1-Trk	-0.3	6767.65	0.3
		$\bar{\nu}_\mu$ RHC N-Trks	-1.8	4544.65	1.8
		$\nu_\mu$ RHC 1-Trk	-0.2	2067.37	0.2
		$\nu_\mu$ RHC N-Trks	-0.8	4568.13	0.8

Parameter	$1\sigma$ value	Sample	$-1\sigma$ (%)	nominal	$+1\sigma$ (%)
<b>591 : NC Other Far*</b>	<b>0.30</b>	$\nu_\mu$ 1-Trk Wtr	-0.1	27316.74	0.1
		$\nu_\mu$ N-Trks	-0.4	30904.32	0.4
		$\bar{\nu}_\mu$ RHC 1-Trk	-0.1	8414.09	0.1
		$\bar{\nu}_\mu$ RHC N-Trks	-1.2	4724.34	1.2
		$\nu_\mu$ RHC 1-Trk	-0.1	3022.10	0.1
		$\nu_\mu$ RHC N-Trks	-0.5	4928.38	0.5
		$\nu_\mu$ 1-Trk Air	-0.1	23605.76	0.1
		$\nu_\mu$ N-Trks	-0.6	32304.13	0.6
		$\bar{\nu}_\mu$ RHC 1-Trk	-0.3	6767.65	0.3
		$\bar{\nu}_\mu$ RHC N-Trks	-1.8	4544.65	1.8
		$\nu_\mu$ RHC 1-Trk	-0.2	2067.37	0.2
		$\nu_\mu$ RHC N-Trks	-0.8	4568.13	0.8

1682 **Appendix D**

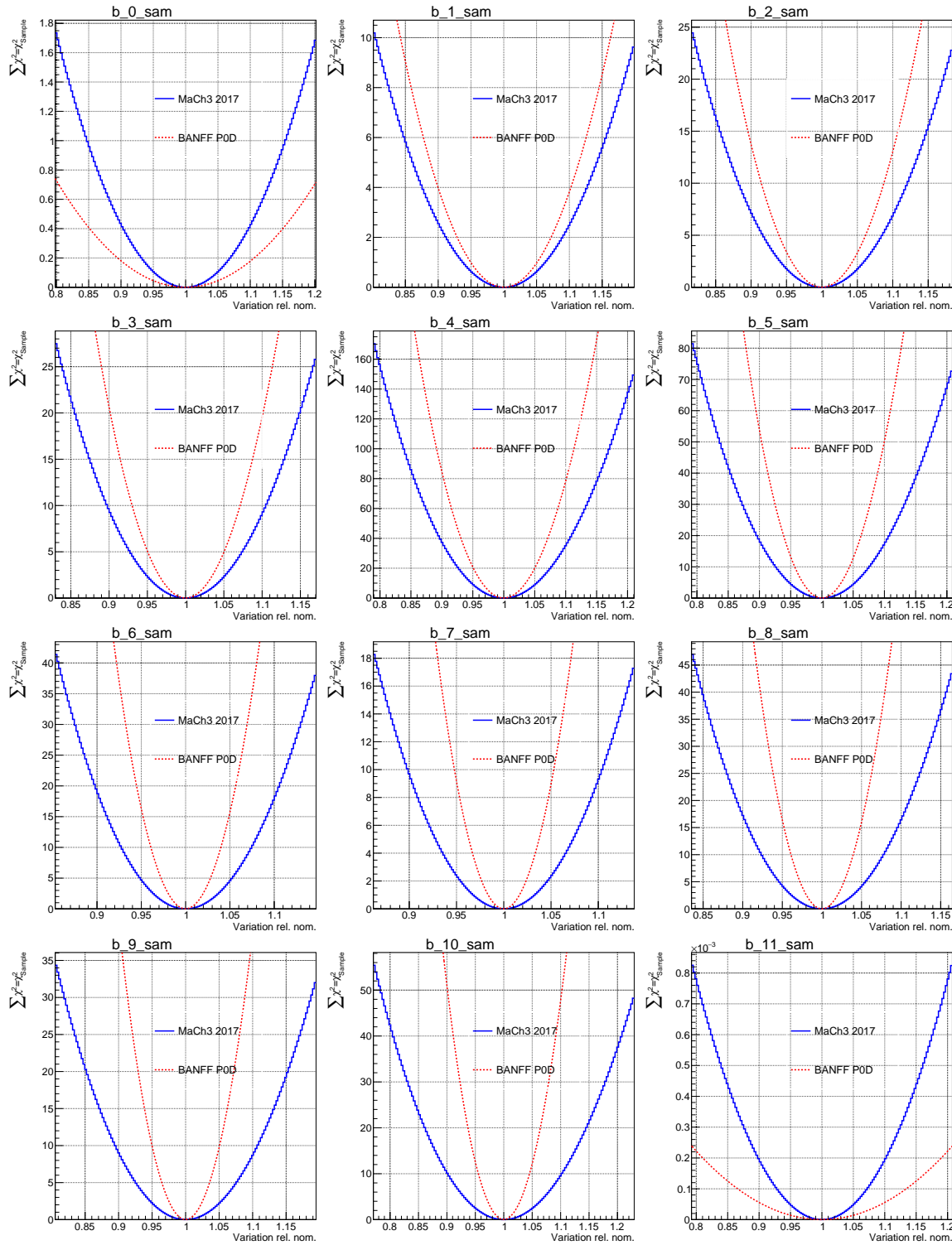
1683 **Log-Likelihood Sample Scans**

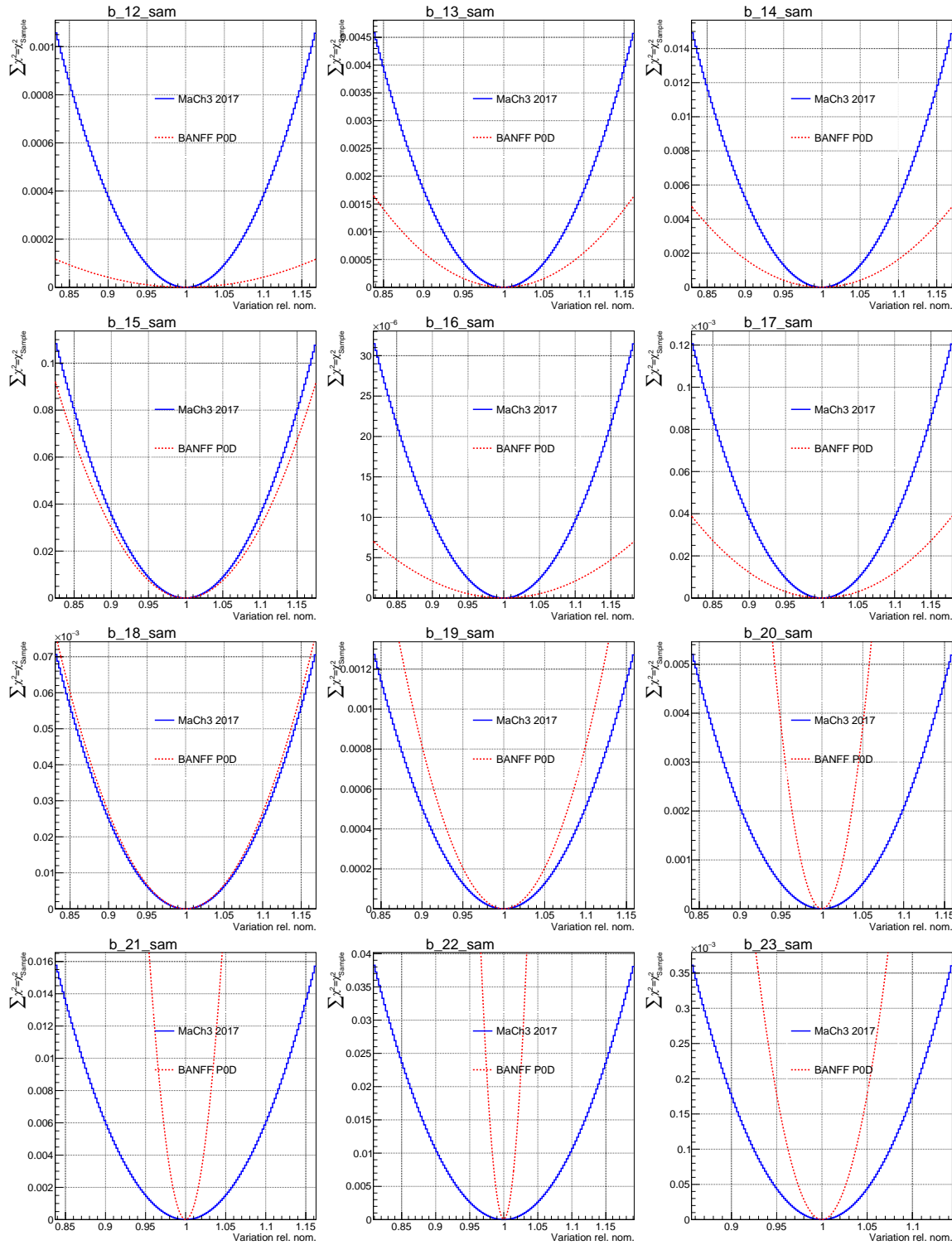
1684 This appendix examines the PØD-only BANFF fit likelihood term  $\chi_{\text{LLR}}^2 = \chi_{\text{sample}}^2$  response (scans) to  
1685 variations in flux and cross section parameters. For the cross section terms, the scans shapes correspond  
1686 to the shape of the spline weight. In addition, comparison scans are provided for the FGD MaCh3 2017  
1687 analysis. Extensive comparisons were made to ensure that the FGD MaCh3 and FGD BANFF analyses have  
1688 identical splines. So it is an equal comparison with the FGD BANFF as shown in Chapter 4. In some cases,  
1689 the PØD-only scans indicate higher sensitivity to parameters than the FGD.

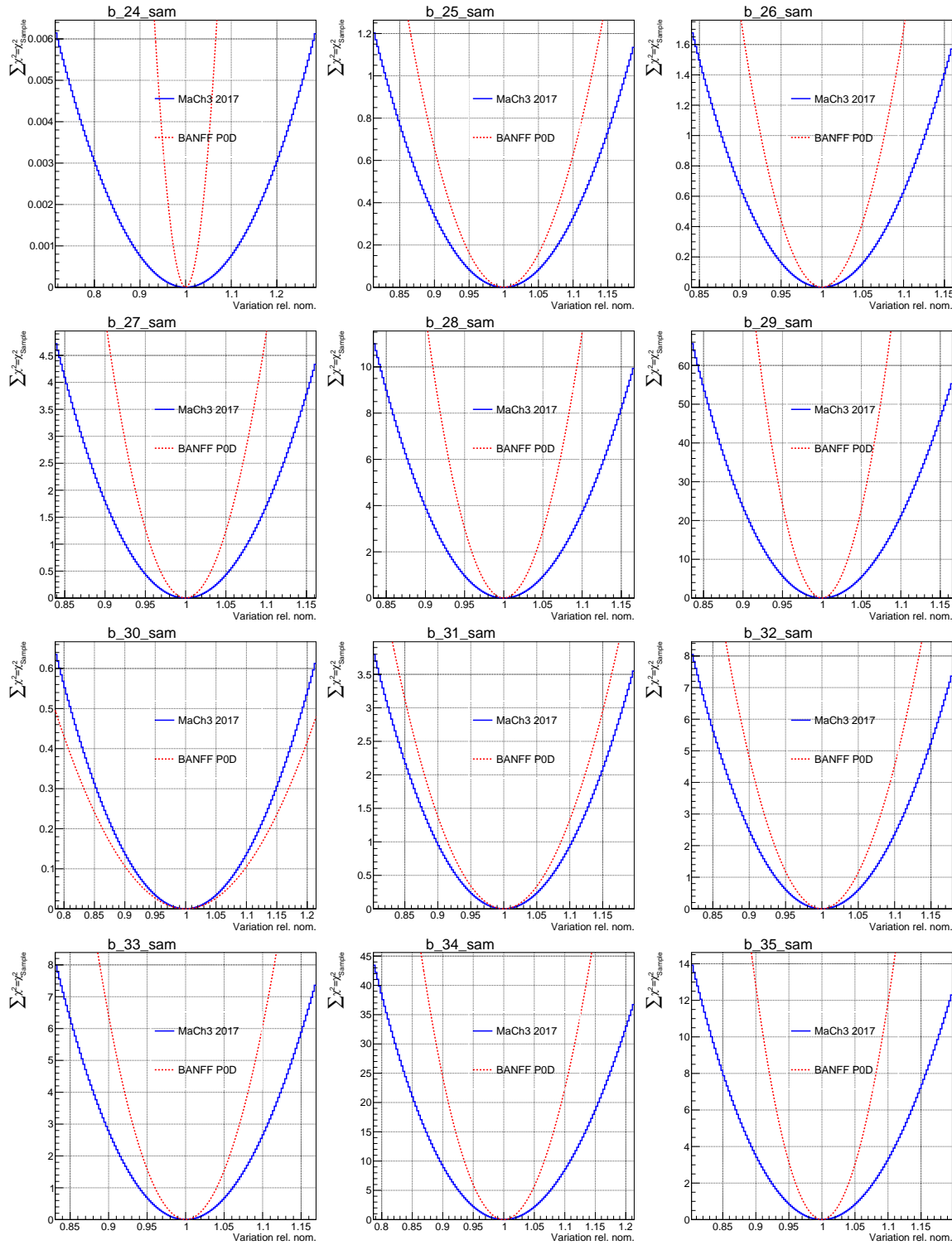
1690 These were generously produced by Clarence Wret ([c.wret@rochester.edu](mailto:c.wret@rochester.edu)) of the University of Rochester.  
1691 The likelihood scans are ordered as such. The first 50 plots “b\_0\_sam” through “b\_49\_sam” are the ND280  
1692 flux sample contributions. The next 50 “b\_50\_sam” through “b\_99\_sam” are the sample contributions  
1693 that affect the SK flux. The last scans are variations on the cross section parameters. Due to a bug in  
1694 plotting script, the scans 2p2h shape location for  $^{12}\text{C}$  and  $^{16}\text{O}$  were empty for the PØD. The correct PØD  
1695 scans are shown in Figure D.1 on page 226 with the MaCh3 inputs reproduced as faithfully as possible.

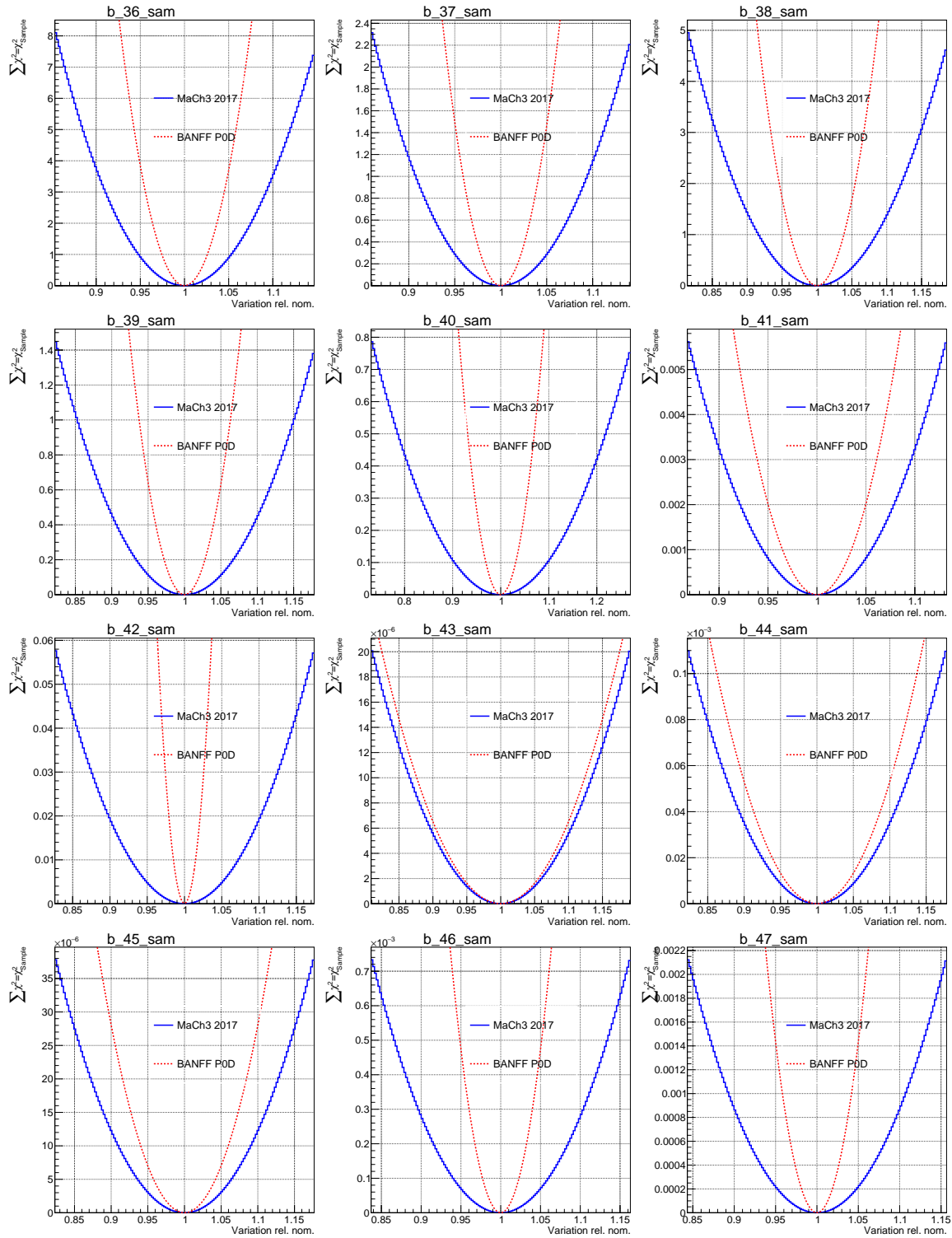
1696 As expected, the SK flux variations are flat with respect to the sample chi-squared. This is due model  
1697 parameterization in which the ND280 samples only affect the ND280 flux parameters. In other words, the  
1698 log-likelihood scans for the SK flux parameters have no affect on the ND280 sample events.

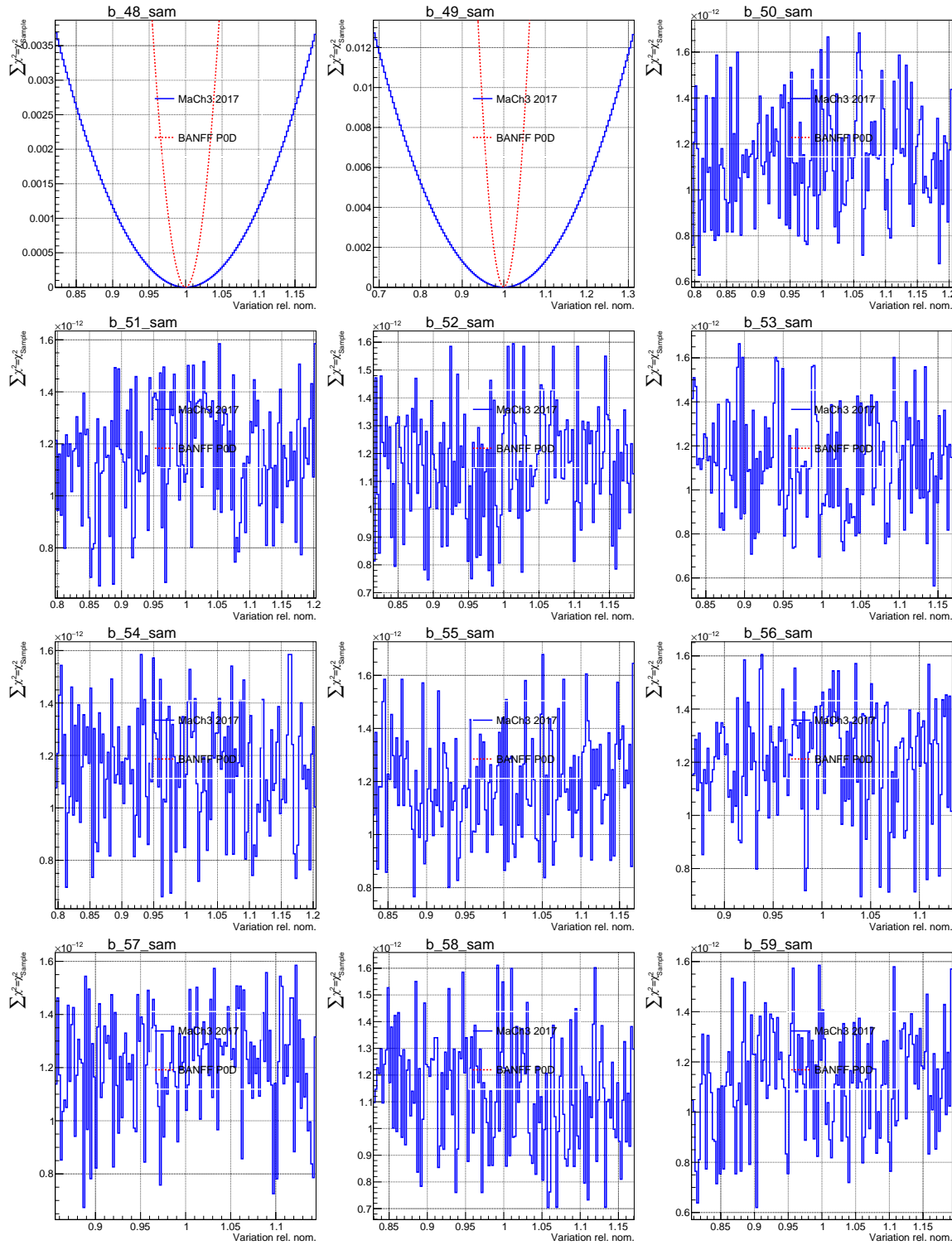
1699 Some of cross section parameter splines are reflected about a point in order to properly calculate corre-  
1700 lations between parameters. In previous fits to data, the 2p2h  $^{12}\text{C}$  and  $^{16}\text{O}$  shape location terms hit their  
1701 physical boundaries at +1. The result was that the fitter MINUIT inaccurately calculated the Hess matrix.  
1702 The decision was made to reflect, also called “mirroring”, the splines about a certain point to expand the  
1703 limit. Tests showed that this did not affect the postfit results for any parameters, but the correlations  
1704 between all other parameters was calculated to less than 1%[18].

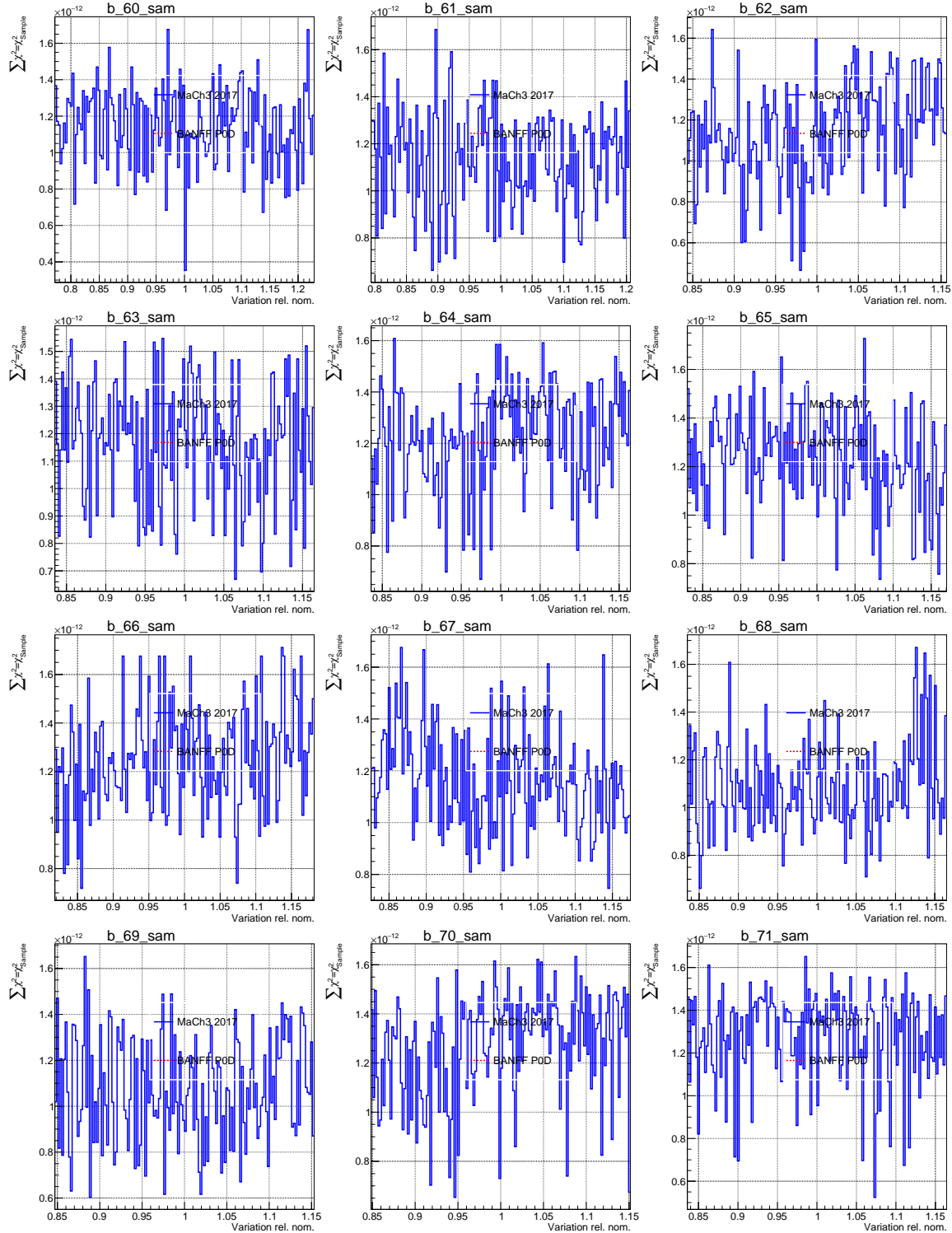


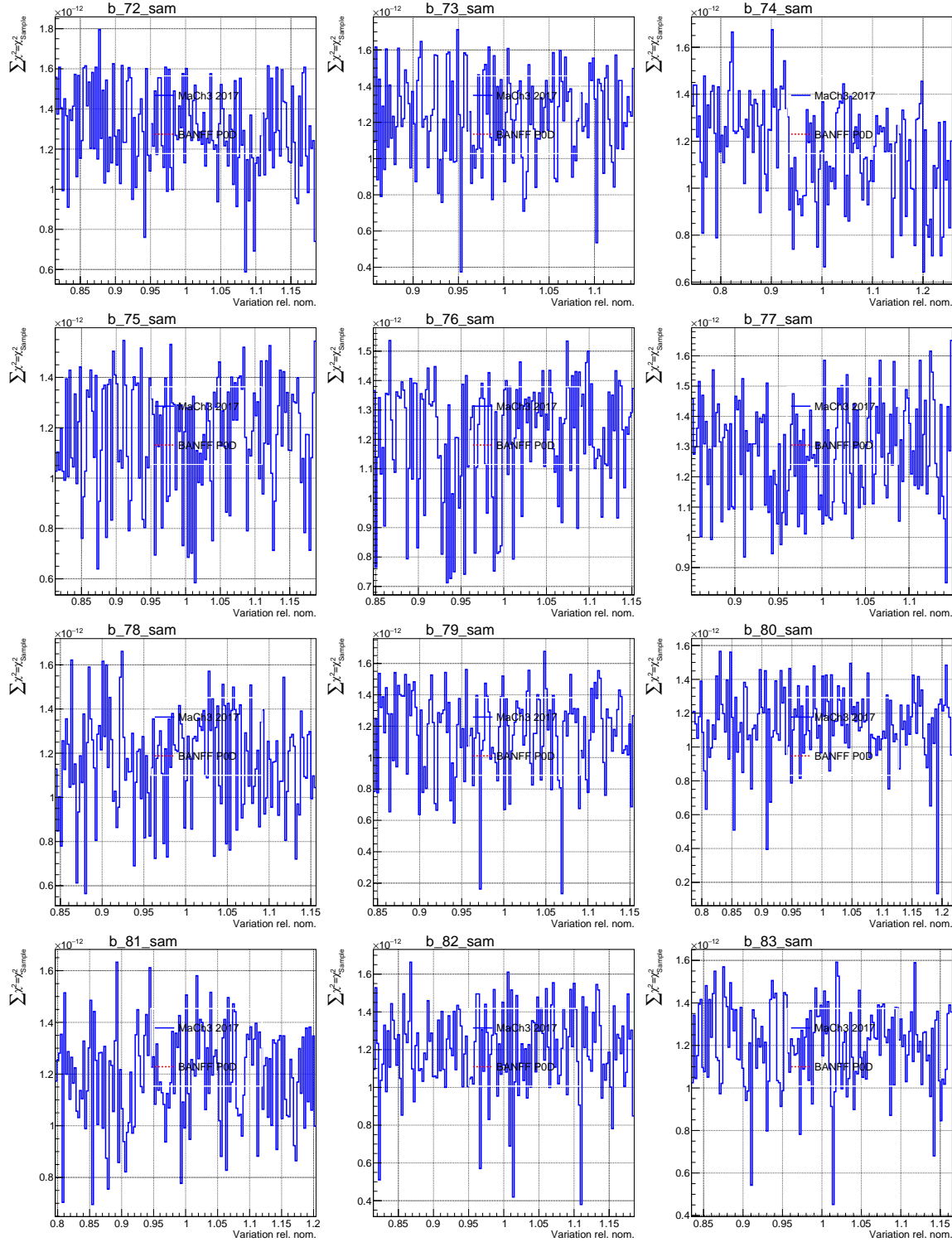


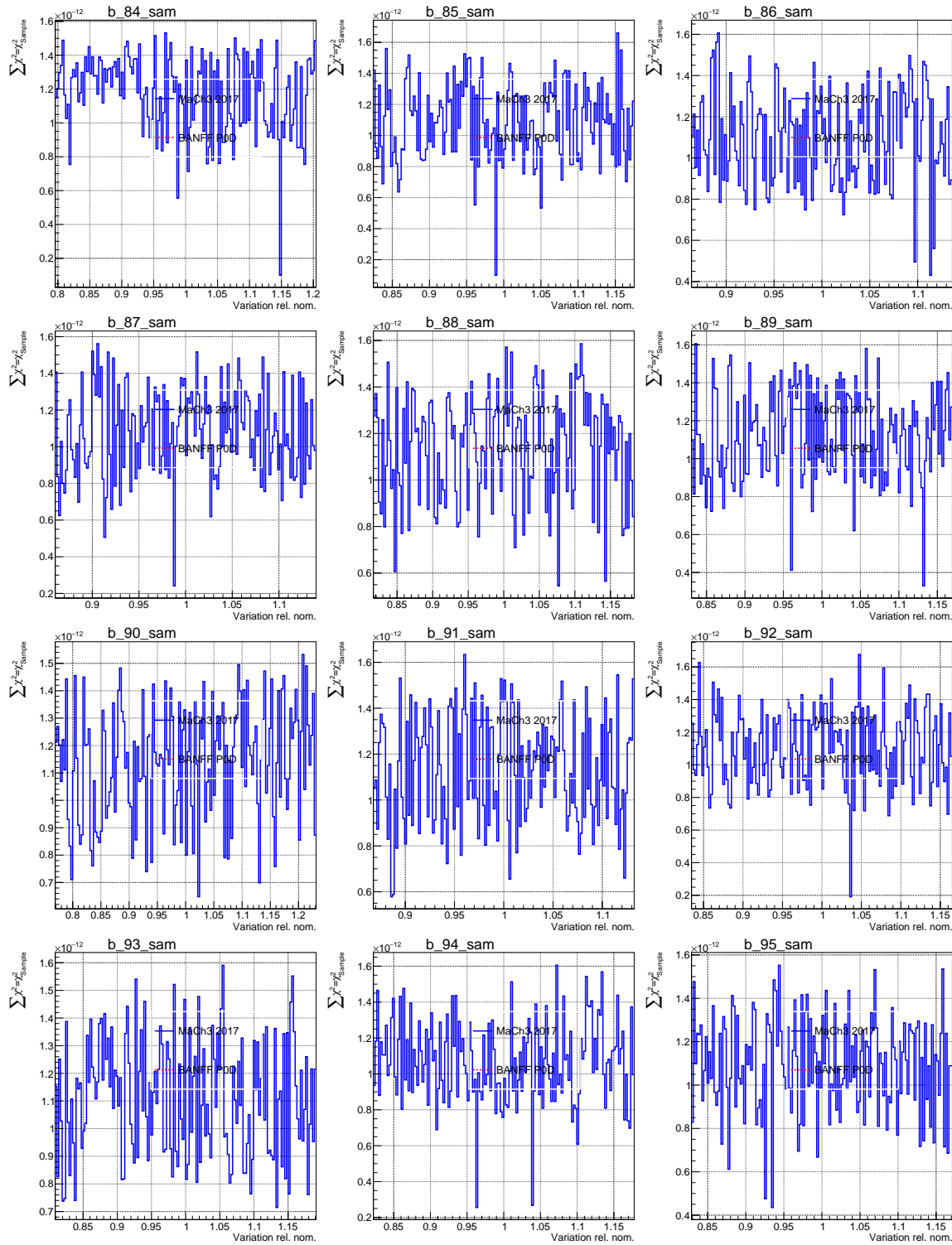


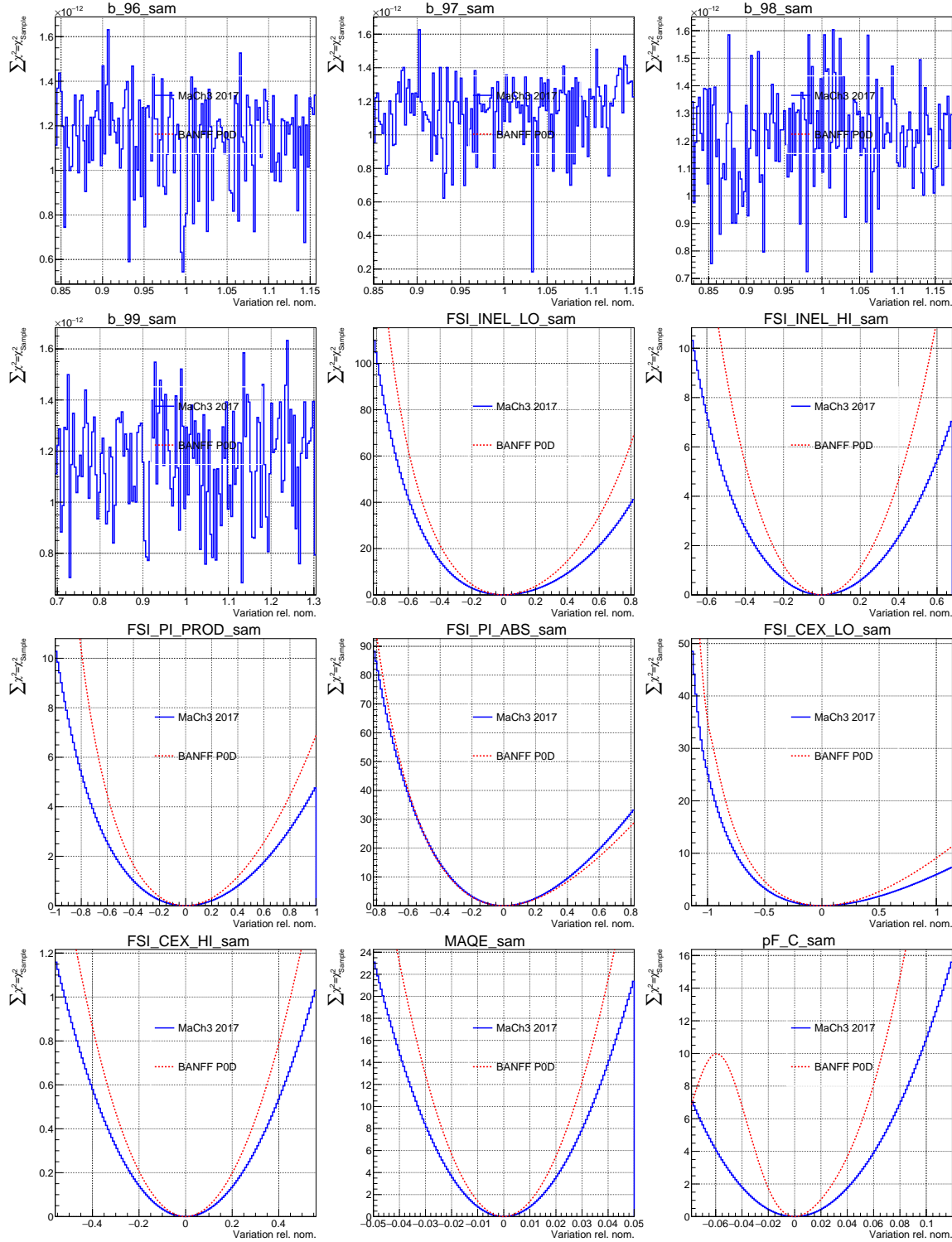


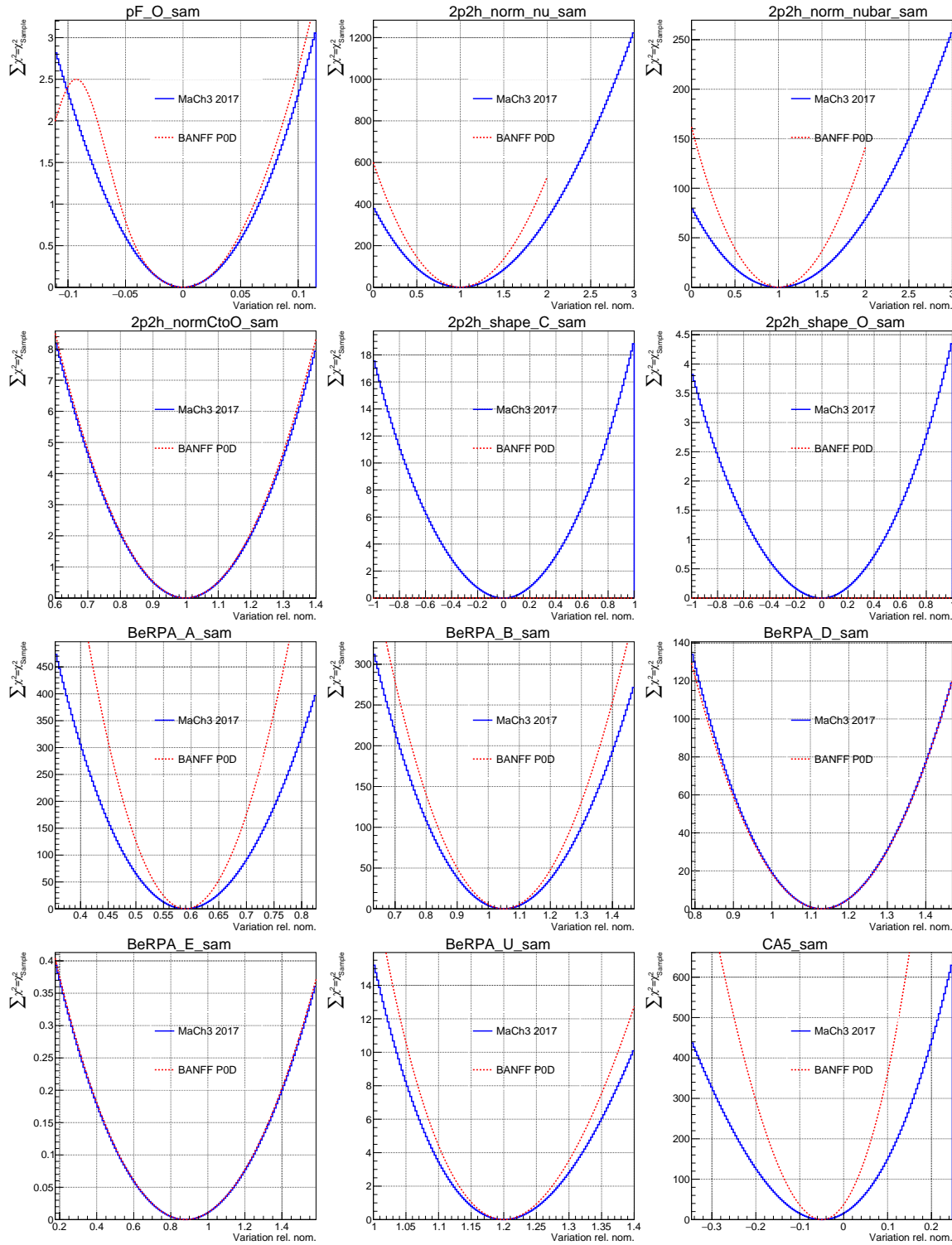


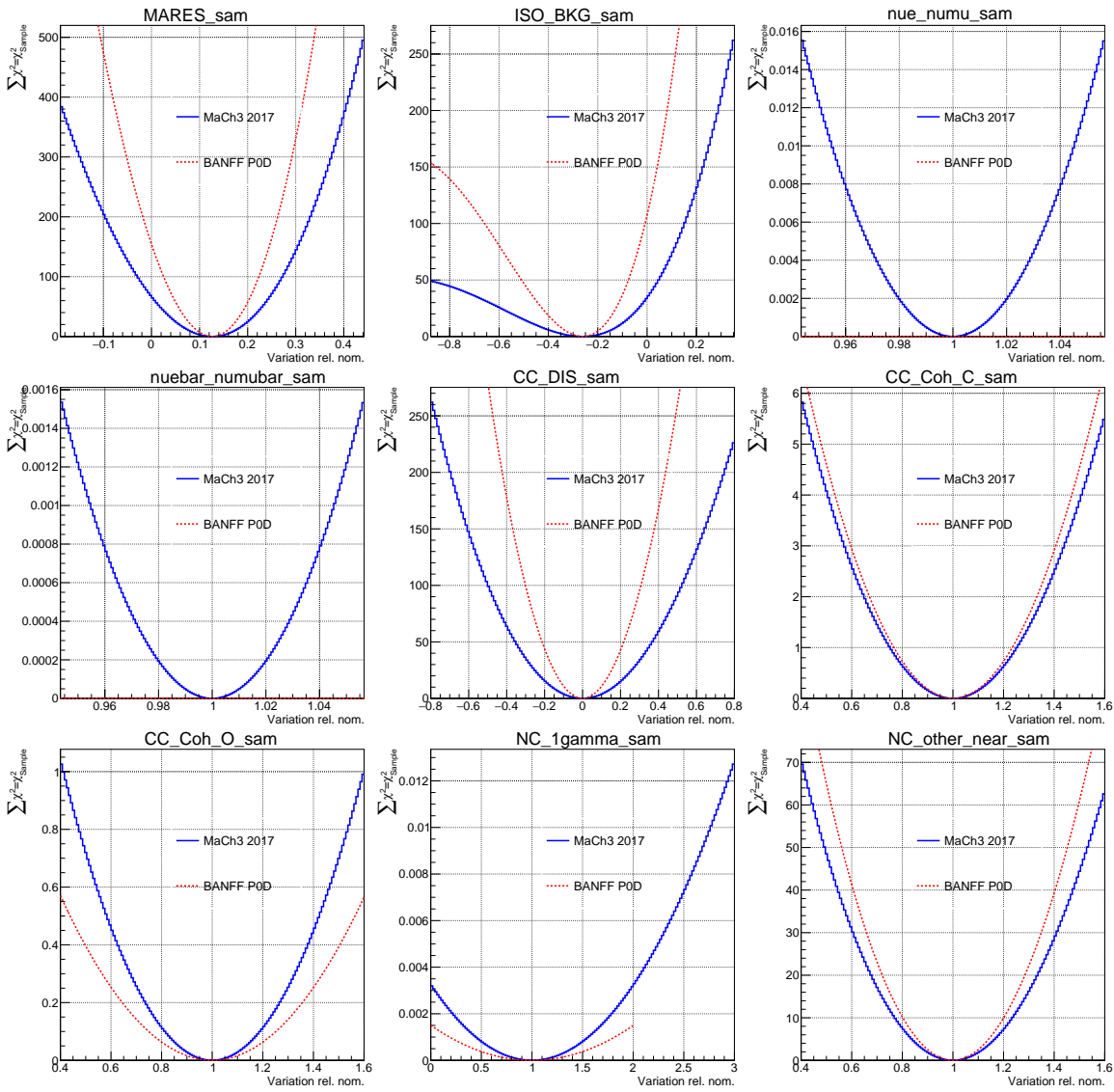












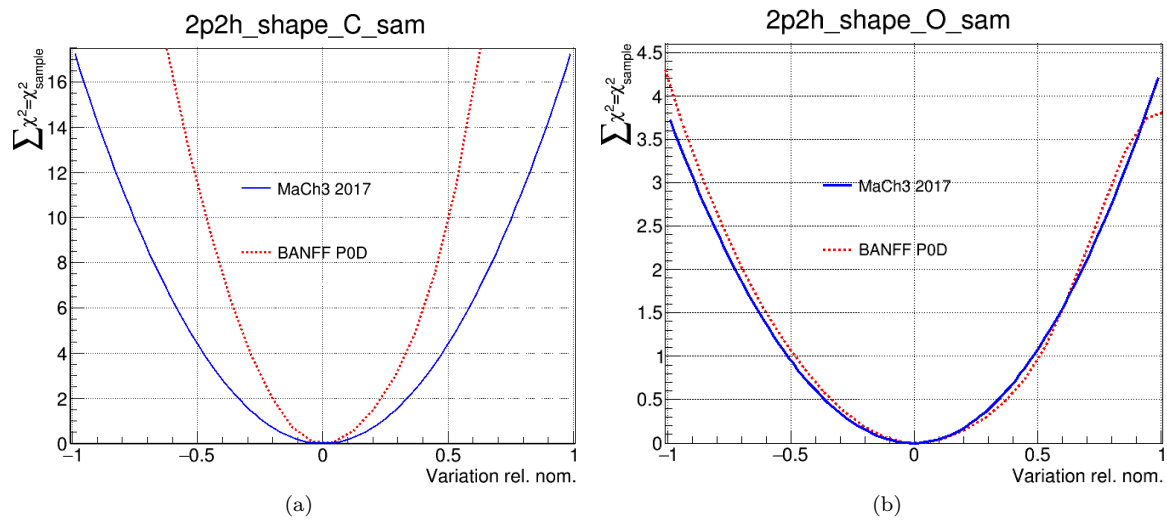
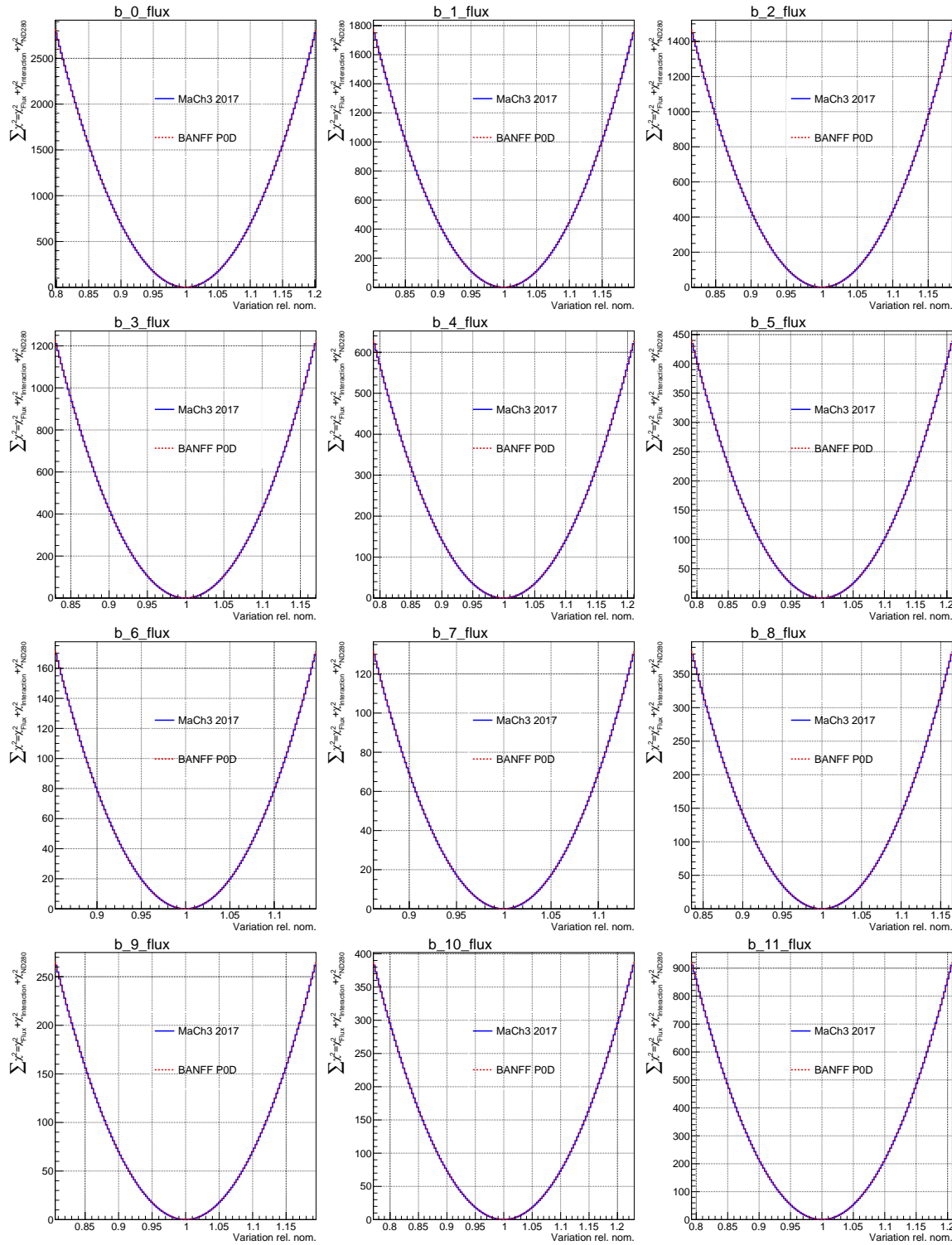


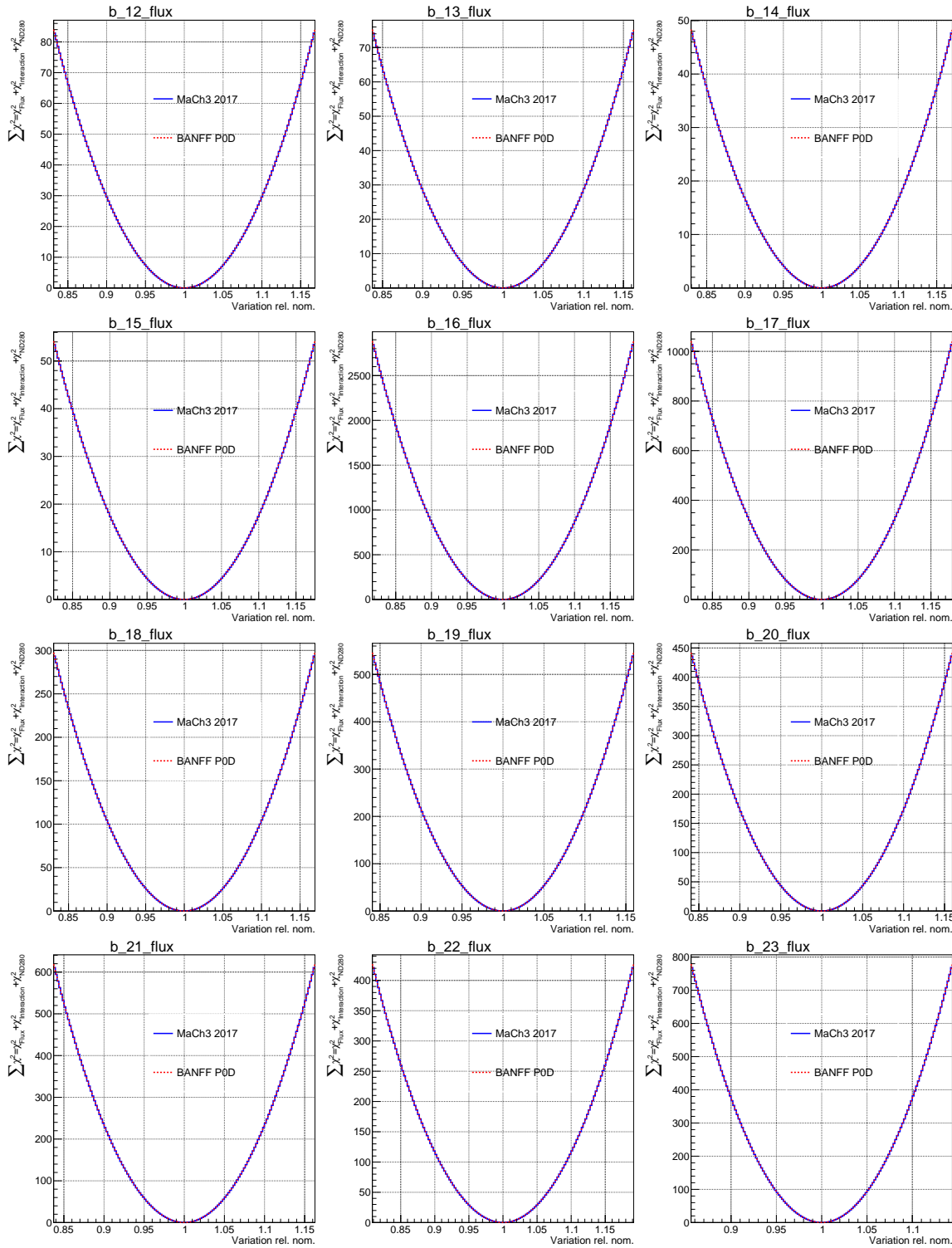
Figure D.1: Correct PØD scans with faithful reproductions of the MaCh3 scans for the 2p2h shape location cross section parameters.

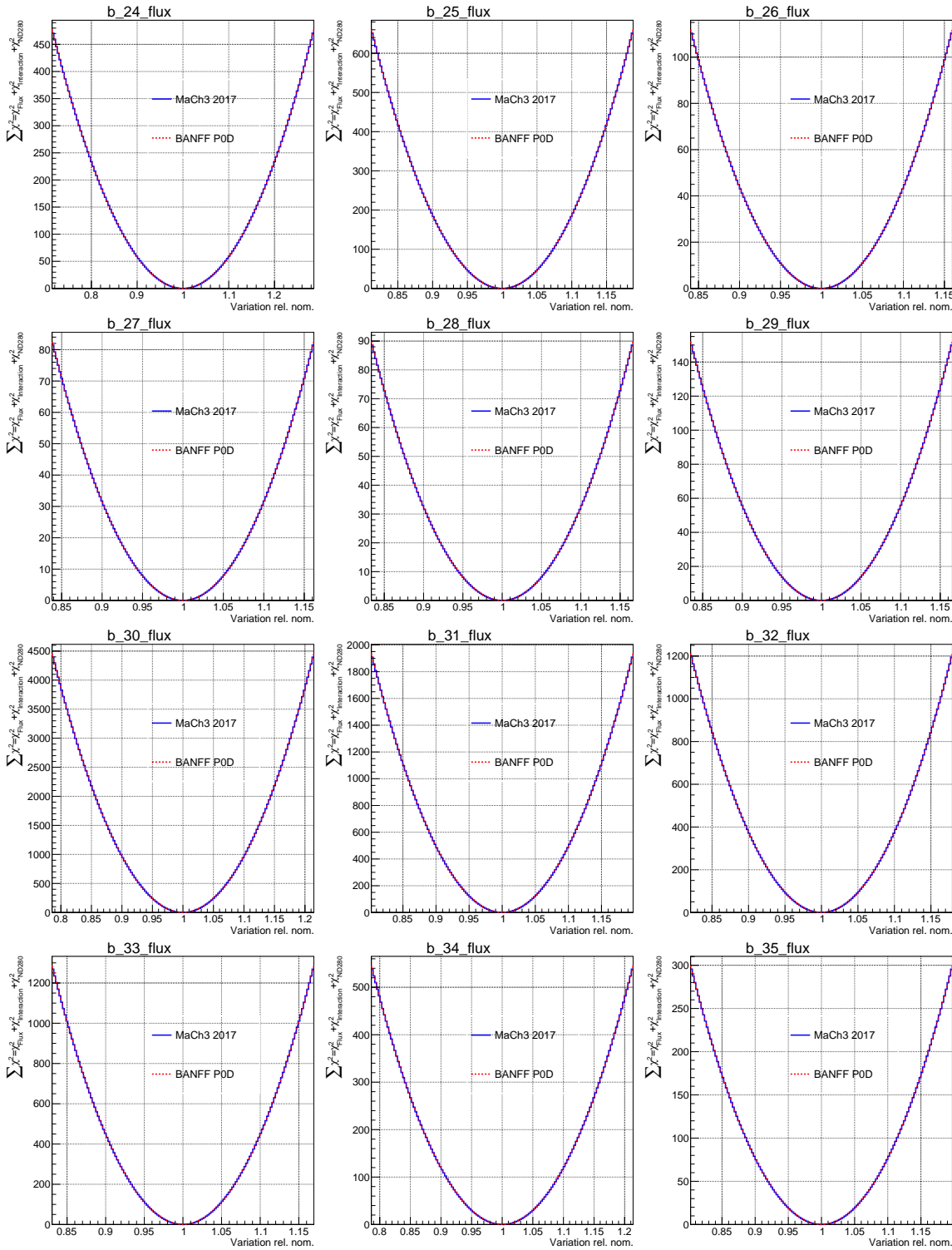
<sub>1716</sub> **Appendix E**

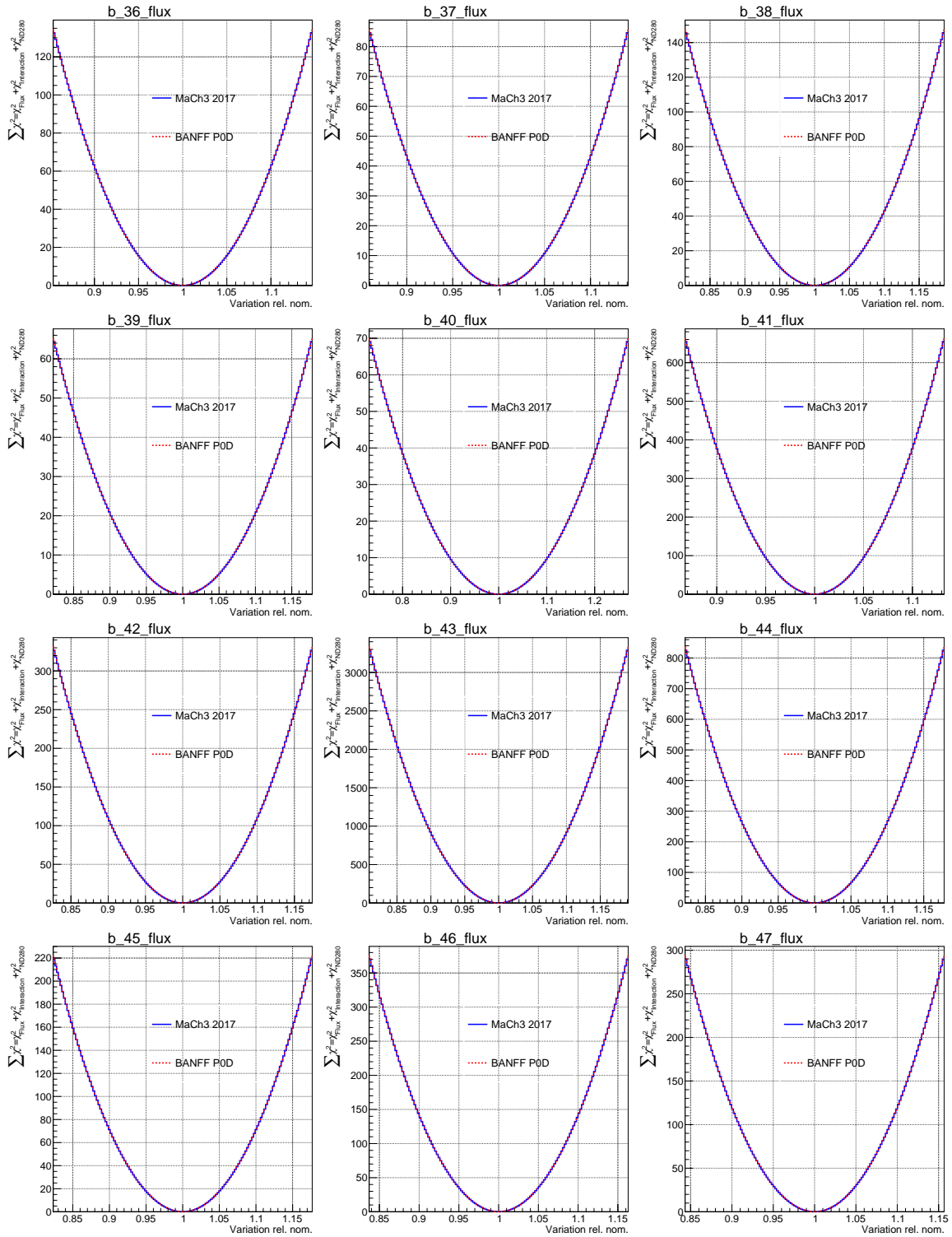
<sub>1717</sub> **Log-Likelihood Penalty Scans**

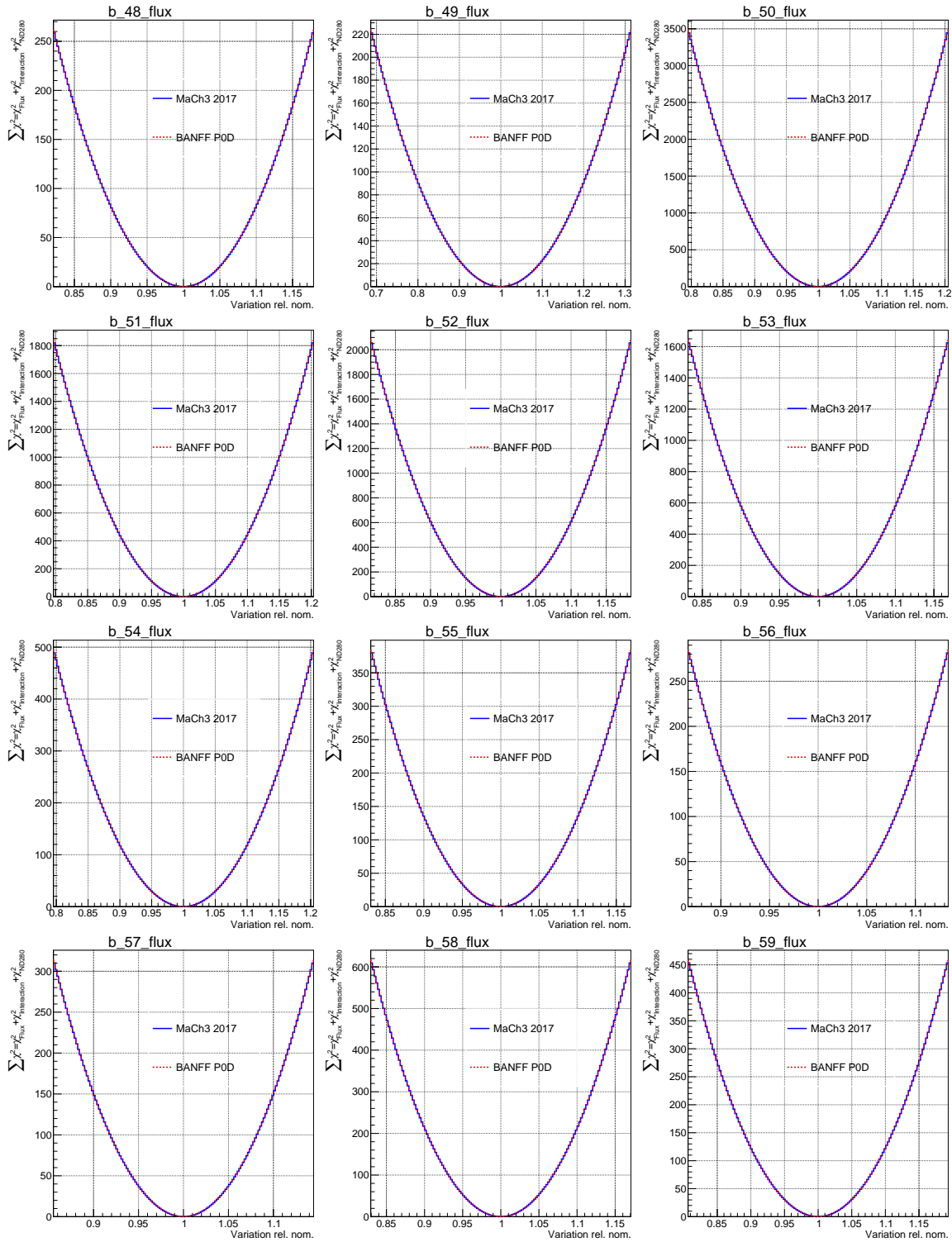
<sub>1718</sub> This appendix examines the PØD-only BANFF fit penalty terms  $\chi_{\text{Flux}}^2 + \chi_{\text{xsec}}^2 + \chi_{\text{Det}}^2$  response (scans) to  
<sub>1719</sub> variations in flux and cross section parameters. In addition, comparison scans are provided for the FGD  
<sub>1720</sub> MaCH3/BANFF 2017 analysis. In all cases, the penalty terms overlap indicating the parameters have the  
<sub>1721</sub> same prior constraints between analyses.

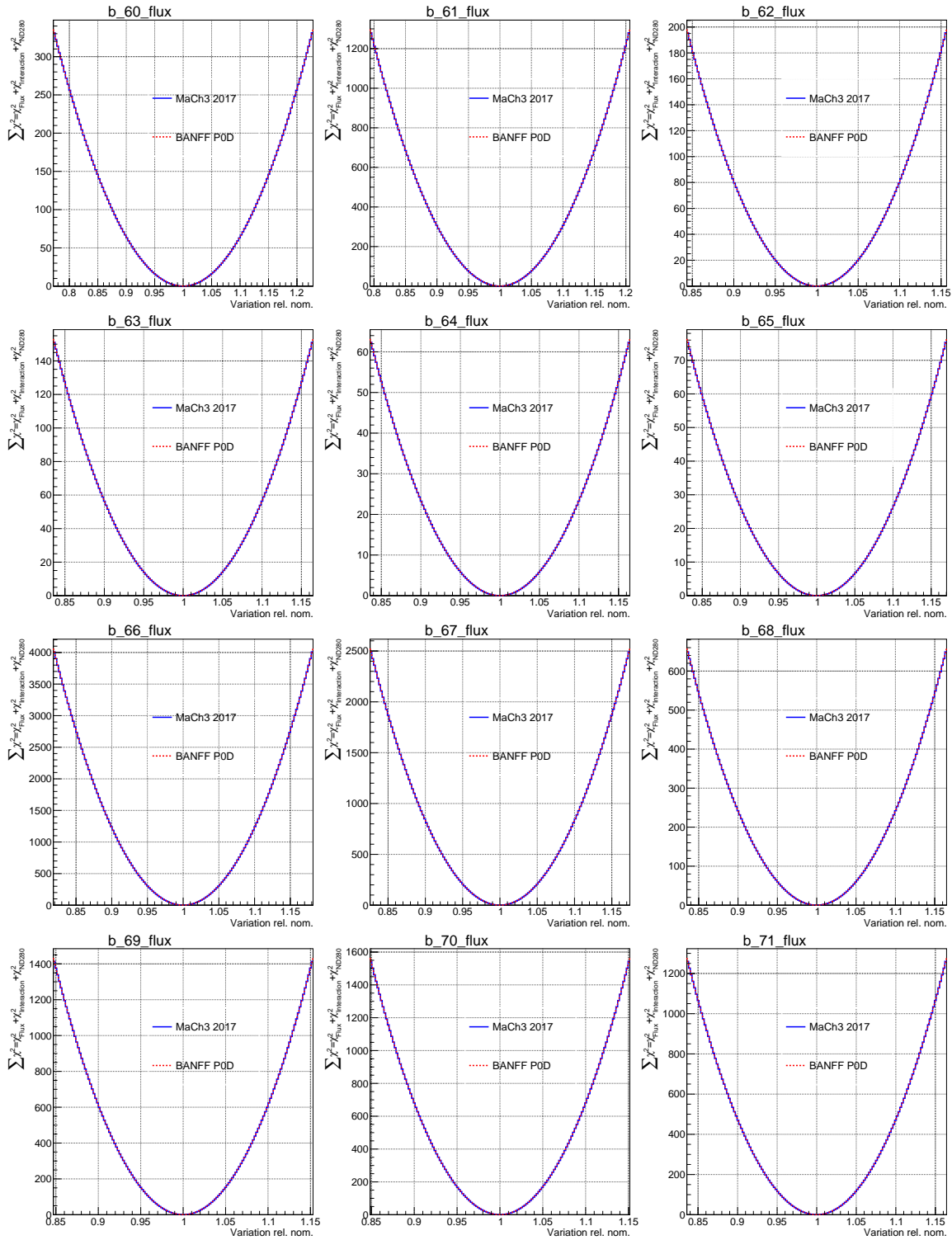


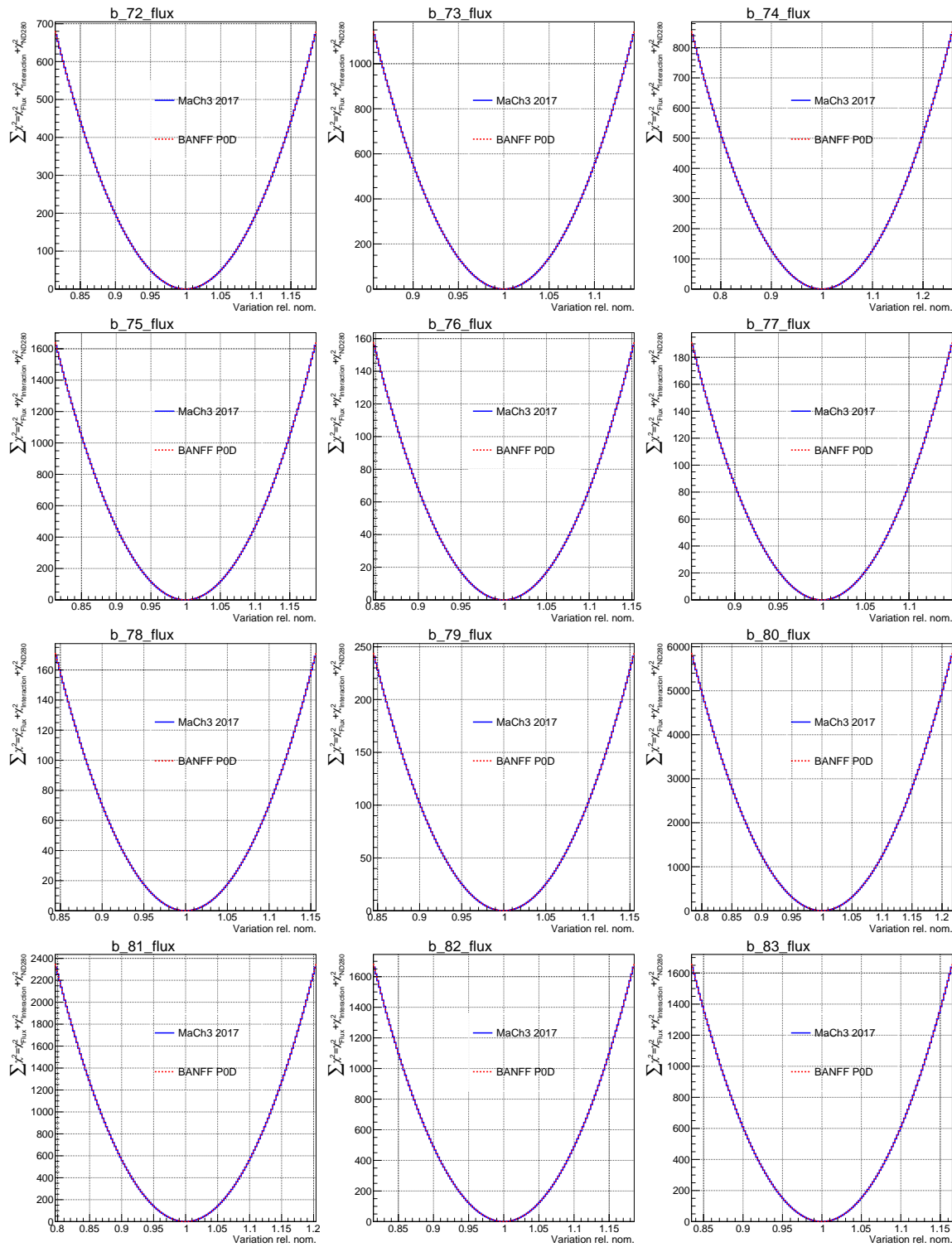


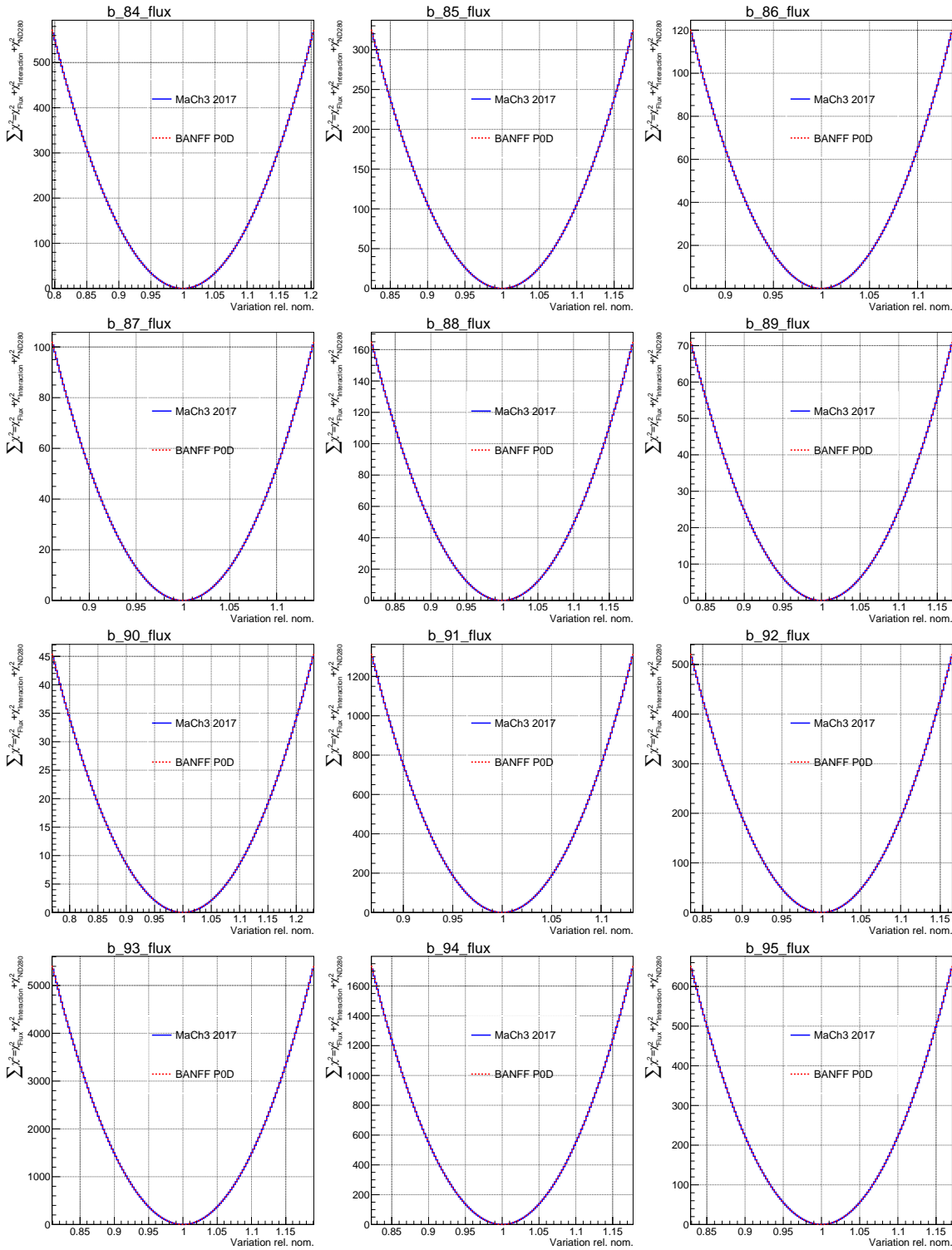


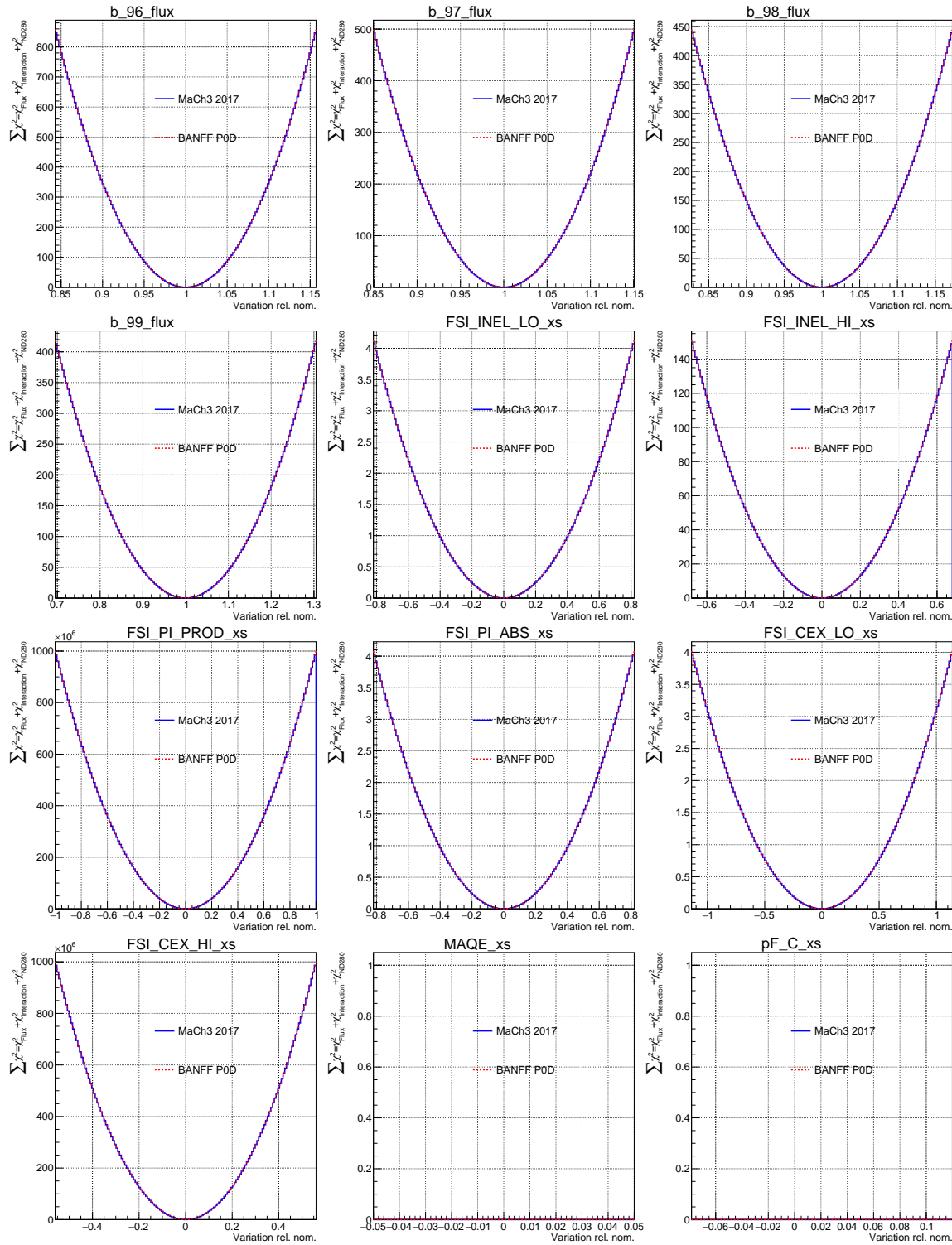


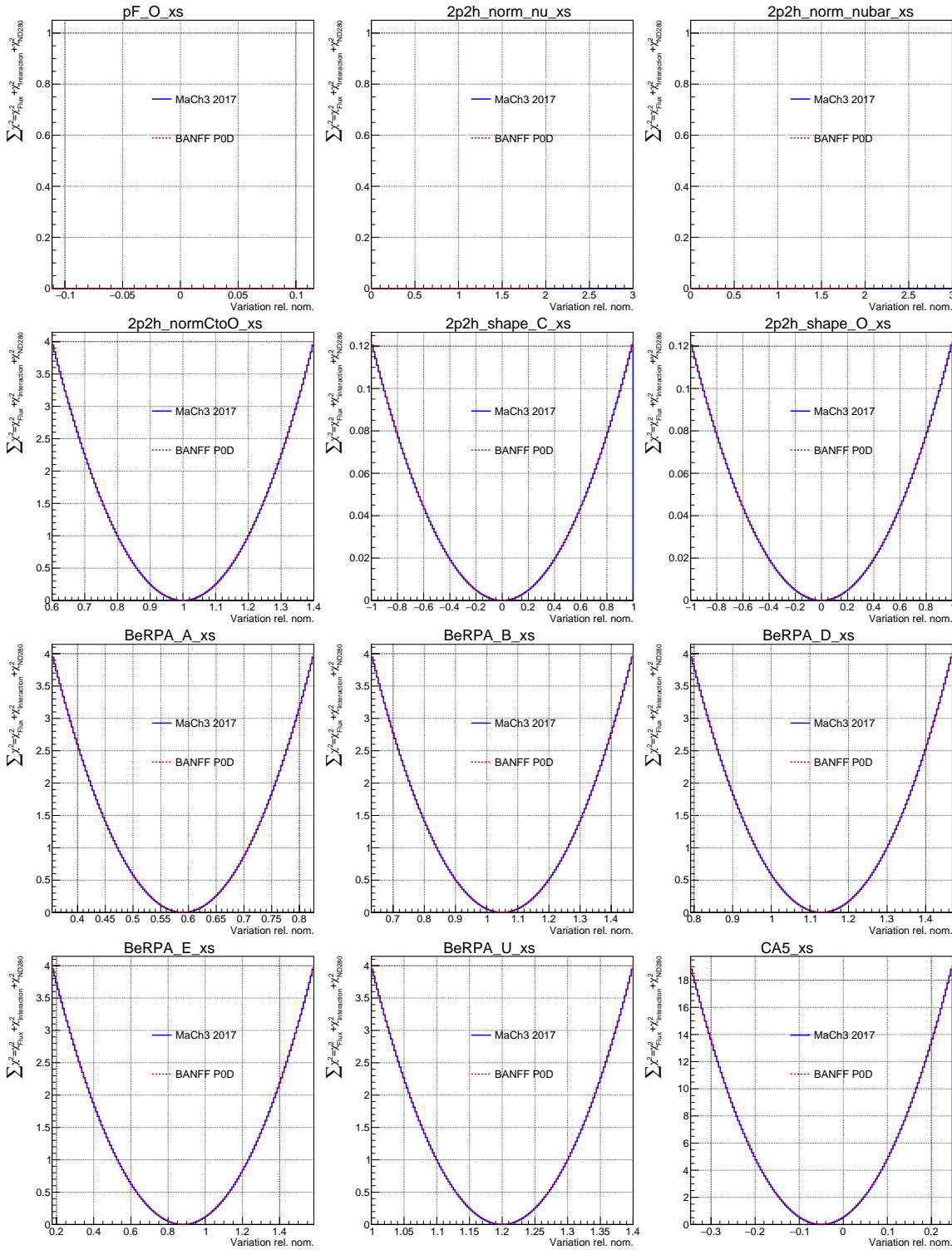


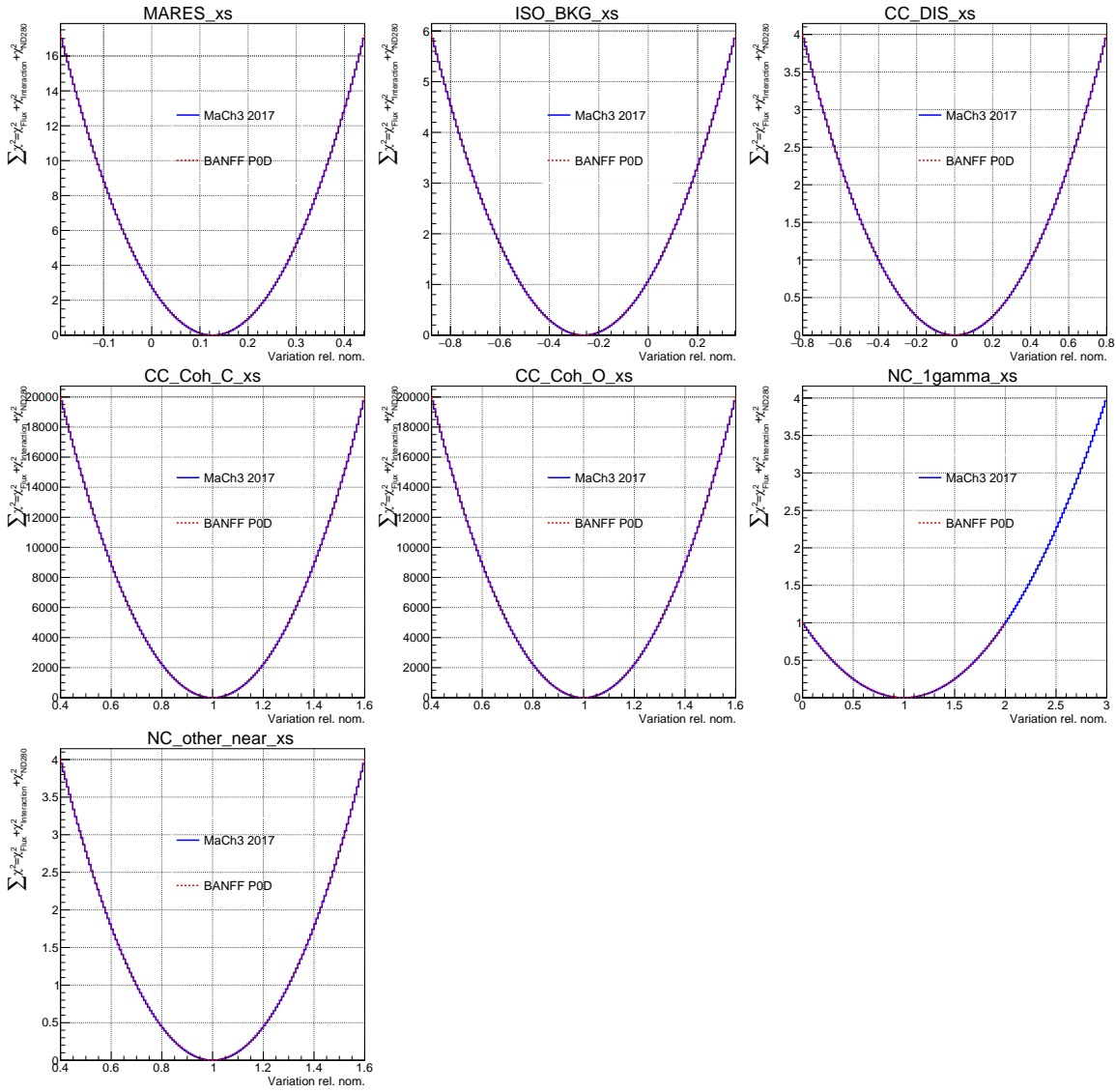












<sub>1733</sub> **Appendix F**

<sub>1734</sub> **Computing Resources**

<sub>1735</sub> This appendix provides the details on the computing resources used to produce the BANFF fit. All the  
<sub>1736</sub> computing resources were provided by the W. M. Keck high performance computing (HPC) cluster at  
<sub>1737</sub> Colorado State University. The HPC cluster is maintained by the Engineering Technology Services team at  
<sub>1738</sub> the Walter Scott, Jr. College of Engineering. A list of the computing resources used in this thesis is provided  
<sub>1739</sub> in Table F.1 on page 239.

<sub>1740</sub> The HPC cluster has a dedicated batch queue scheduler which supports the OpenMP and MPI parallel  
<sub>1741</sub> processing environments. While the user can restrict jobs to specific compute nodes in the batch queue, the  
<sub>1742</sub> scheduler will assign jobs to any available nodes on a first come, first serve basis with some exceptions. The  
<sub>1743</sub> BANFF fit studies in this thesis usually used the default scheduler options except when to prioritize certain  
<sub>1744</sub> jobs over others. The typical resource usage is explained in the next paragraph.

<sub>1745</sub> The PØD-only data BANFF fit result was calculated using a compute node with two E5-2620 v4 central  
<sub>1746</sub> processing units (CPUs) and 64 GB of random access memory (RAM). The data and Monte Carlo (MC)  
<sub>1747</sub> events are loaded in RAM from binary ROOT[54] files that are stored on the HPC cluster's hard disk drives.  
<sub>1748</sub> The total job time was 27.5 hours using the OpenMP parallel processing environment with all 16 cores  
<sub>1749</sub> employed, which is reasonable in terms of large scale computational work. This includes loading the data

Table F.1: Computing resources used in this thesis.

Avail. nodes	Node	CPU	#CPUs per node	#cores per CPU	Clock rate [GHz]	Cache [MB]	RAM [GB]
19	Xeon E5-2640		2	6	2.5	15	256
7	Xeon E5-2620 v3				2.4		64
4							256
15	Xeon E5-2620 v4			8	2.1	20	64

1750 and MC, finding the global minimum, and calculating the Hess matrix. However, a significant fraction of the  
1751 time, about 6.2 hours hours, was spent preparing the fit by preloading the data and MC events into RAM.  
1752 The maximum consumed RAM for the fit was about 40 GB.

1753 In exploring a joint PØD+FGD BANFF fit using the canonical T2K 2018 cross section parameterization,  
1754 the Asimov fit job required two weeks to complete, or about 10 times longer than the PØD-only Asimov  
1755 fit. The significant increase in job “walltime” is because the number of fit parameters almost doubled in  
1756 comparison. This illustrates the nonlinear relationship between the required fit time versus number of fit  
1757 parameters. Additionally, when using the actual PØD+FGD data, the fit failed to converge on a global  
1758 minimum due to machine precision limits. So for a future joint analysis, careful consideration on the number  
1759 of needed fit parameters is necessary.

1760 **Appendix G**

1761 **The PØD-Only Postfit Parameters**

1762 In this appendix is the complete listing of the fit parameters, both in prefit and postfit values. The parameters  
1763 are listed in Table G.1 on page 242. The first 50 are ND280 flux parameters then followed by 50 SK flux  
1764 parameters as defined in Table 4.1 on page 51,. Between 100 and 561 are the bin normalization parameters  
1765 defined in Appendix A. The last 31 are cross section parameters as defined in Table 4.4 on page 75.

---

 Table G.1: Prefit and postfit parameters with errors.

Index	Prefit	$\pm$ error	Postfit	$\pm$ error
0	1.00	0.10	1.03	0.06
1	1.00	0.10	1.02	0.05
2	1.00	0.09	1.02	0.05
3	1.00	0.09	1.03	0.05
4	1.00	0.11	0.99	0.05
5	1.00	0.10	0.97	0.04
6	1.00	0.07	1.04	0.04
7	1.00	0.07	1.07	0.04
8	1.00	0.08	1.05	0.04
9	1.00	0.10	0.99	0.04
10	1.00	0.11	0.96	0.04
11	1.00	0.10	1.11	0.08
12	1.00	0.08	1.06	0.06
13	1.00	0.08	1.07	0.06
14	1.00	0.09	1.12	0.06
15	1.00	0.09	1.13	0.07
16	1.00	0.09	1.01	0.05
17	1.00	0.09	1.02	0.05
18	1.00	0.08	1.04	0.05
19	1.00	0.08	1.05	0.04
20	1.00	0.08	1.03	0.04
21	1.00	0.08	1.05	0.04
22	1.00	0.10	1.03	0.06
23	1.00	0.07	1.08	0.06
24	1.00	0.14	1.22	0.12
25	1.00	0.09	1.10	0.07
26	1.00	0.08	1.10	0.05
27	1.00	0.08	1.10	0.05
28	1.00	0.08	1.09	0.05

Index	Prefit	$\pm$ error	Postfit	$\pm$ error
29	1.00	0.08	1.12	0.04
30	1.00	0.11	1.05	0.07
31	1.00	0.10	1.03	0.05
32	1.00	0.09	1.06	0.05
33	1.00	0.08	1.07	0.04
34	1.00	0.11	1.09	0.05
35	1.00	0.10	1.07	0.05
36	1.00	0.07	1.04	0.05
37	1.00	0.07	1.04	0.05
38	1.00	0.09	1.04	0.06
39	1.00	0.09	1.09	0.06
40	1.00	0.13	1.17	0.08
41	1.00	0.07	1.10	0.05
42	1.00	0.09	1.14	0.07
43	1.00	0.10	1.03	0.06
44	1.00	0.09	1.05	0.05
45	1.00	0.09	1.08	0.06
46	1.00	0.08	1.05	0.05
47	1.00	0.08	1.09	0.05
48	1.00	0.09	1.10	0.06
49	1.00	0.16	1.14	0.13
50	1.00	0.10	1.02	0.06
51	1.00	0.10	1.01	0.06
52	1.00	0.09	1.03	0.05
53	1.00	0.08	1.05	0.05
54	1.00	0.10	1.02	0.06
55	1.00	0.08	1.01	0.05
56	1.00	0.07	1.04	0.05
57	1.00	0.07	1.04	0.05
58	1.00	0.09	1.04	0.04
59	1.00	0.10	1.00	0.04

Index	Prefit	$\pm$ error	Postfit	$\pm$ error
60	1.00	0.11	0.98	0.05
61	1.00	0.10	1.11	0.08
62	1.00	0.08	1.08	0.05
63	1.00	0.08	1.10	0.06
64	1.00	0.08	1.12	0.06
65	1.00	0.09	1.11	0.06
66	1.00	0.09	1.02	0.05
67	1.00	0.09	1.03	0.05
68	1.00	0.08	1.04	0.05
69	1.00	0.08	1.05	0.04
70	1.00	0.08	1.05	0.04
71	1.00	0.08	1.06	0.04
72	1.00	0.09	1.07	0.06
73	1.00	0.07	1.09	0.05
74	1.00	0.13	1.18	0.11
75	1.00	0.09	1.10	0.07
76	1.00	0.08	1.07	0.05
77	1.00	0.07	1.10	0.05
78	1.00	0.08	1.10	0.05
79	1.00	0.08	1.07	0.05
80	1.00	0.11	1.04	0.07
81	1.00	0.10	1.02	0.06
82	1.00	0.09	1.03	0.05
83	1.00	0.08	1.06	0.05
84	1.00	0.10	1.09	0.06
85	1.00	0.09	1.05	0.05
86	1.00	0.07	1.04	0.05
87	1.00	0.07	1.08	0.05
88	1.00	0.09	1.04	0.06
89	1.00	0.08	1.07	0.06
90	1.00	0.12	1.06	0.09

Index	Prefit	$\pm$ error	Postfit	$\pm$ error
91	1.00	0.07	1.09	0.05
92	1.00	0.08	1.11	0.06
93	1.00	0.10	1.04	0.06
94	1.00	0.09	1.04	0.05
95	1.00	0.09	1.06	0.05
96	1.00	0.08	1.05	0.04
97	1.00	0.08	1.10	0.05
98	1.00	0.09	1.11	0.06
99	1.00	0.15	1.15	0.12
100	1.21	0.67	1.00	0.04
101	0.87	0.18	0.96	0.03
102	1.12	0.44	0.96	0.04
103	1.13	0.43	0.99	0.05
104	1.02	0.17	0.96	0.08
105	0.93	0.20	0.84	0.09
106	1.00	0.28	1.05	0.05
107	0.82	0.33	0.93	0.04
108	1.26	0.58	0.94	0.03
109	1.27	0.74	0.92	0.04
110	0.89	0.18	0.95	0.03
111	1.02	0.27	0.93	0.03
112	1.09	0.33	0.96	0.04
113	1.02	0.17	0.91	0.04
114	0.96	0.15	0.92	0.03
115	0.99	0.21	0.97	0.04
116	0.94	0.29	0.96	0.06
117	1.05	0.53	0.94	0.07
118	1.33	0.78	0.99	0.05
119	0.91	0.21	0.95	0.03
120	0.97	0.14	0.93	0.03
121	1.03	0.17	0.94	0.03

Index	Prefit	$\pm$ error	Postfit	$\pm$ error
122	1.01	0.09	0.93	0.03
123	1.00	0.05	0.94	0.04
124	1.00	0.12	0.91	0.08
125	0.95	0.15	0.98	0.08
126	0.96	0.38	0.88	0.04
127	1.29	0.73	0.95	0.04
128	0.93	0.22	0.96	0.03
129	0.96	0.09	0.92	0.03
130	1.02	0.11	0.94	0.03
131	1.00	0.07	0.93	0.03
132	1.00	0.03	0.93	0.03
133	0.99	0.08	0.89	0.03
134	1.00	0.14	0.92	0.04
135	0.99	0.20	0.99	0.04
136	1.25	0.65	0.94	0.07
137	0.94	0.20	0.95	0.04
138	0.95	0.08	0.93	0.03
139	1.01	0.11	0.94	0.03
140	1.00	0.07	0.93	0.03
141	1.00	0.06	0.94	0.03
142	1.00	0.03	0.93	0.03
143	0.98	0.10	0.90	0.03
144	0.97	0.14	0.88	0.03
145	1.25	0.58	1.00	0.06
146	0.93	0.18	0.91	0.04
147	0.96	0.11	0.89	0.03
148	1.01	0.11	0.94	0.03
149	1.01	0.08	0.95	0.03
150	1.01	0.10	0.95	0.03
151	1.00	0.06	0.95	0.03
152	1.00	0.05	0.93	0.03

Index	Prefit	$\pm$ error	Postfit	$\pm$ error
153	0.98	0.10	0.90	0.03
154	1.18	0.61	0.95	0.03
155	0.89	0.15	0.95	0.03
156	1.01	0.16	0.96	0.04
157	1.03	0.19	1.02	0.04
158	1.02	0.15	1.16	0.07
159	1.04	0.16	0.87	0.04
160	0.93	0.26	0.81	0.05
161	0.94	0.67	0.89	0.06
162	1.13	0.56	0.90	0.03
163	0.92	0.15	0.93	0.03
164	0.98	0.07	0.93	0.03
165	1.00	0.09	0.93	0.03
166	1.01	0.08	0.93	0.03
167	1.01	0.06	0.88	0.04
168	0.98	0.16	0.84	0.05
169	0.98	0.52	0.89	0.05
170	1.13	0.53	0.95	0.03
171	0.92	0.14	0.93	0.03
172	0.98	0.05	0.92	0.03
173	1.00	0.07	0.92	0.03
174	1.00	0.06	0.92	0.03
175	1.01	0.05	0.89	0.03
176	0.99	0.12	0.95	0.03
177	1.03	0.46	0.99	0.03
178	1.13	0.52	0.94	0.03
179	0.94	0.13	0.94	0.04
180	0.97	0.06	0.92	0.03
181	0.99	0.08	0.92	0.03
182	1.00	0.07	0.94	0.03
183	1.00	0.03	0.95	0.03

Index	Prefit	$\pm$ error	Postfit	$\pm$ error
184	0.99	0.10	0.89	0.04
185	0.98	0.25	0.92	0.06
186	1.09	0.47	0.95	0.04
187	0.96	0.11	0.94	0.03
188	0.96	0.09	0.95	0.03
189	1.00	0.09	0.92	0.04
190	1.01	0.09	0.93	0.03
191	1.01	0.08	0.94	0.03
192	0.99	0.05	0.92	0.03
193	0.97	0.13	0.87	0.03
194	1.00	0.36	0.97	0.03
195	0.90	0.15	0.95	0.03
196	1.05	0.26	0.92	0.04
197	1.04	0.20	0.93	0.04
198	1.00	0.17	0.94	0.06
199	1.01	0.17	0.92	0.06
200	1.00	0.39	0.97	0.06
201	1.06	0.43	0.97	0.04
202	0.91	0.13	0.95	0.03
203	0.97	0.16	0.93	0.04
204	1.04	0.17	0.94	0.04
205	1.00	0.11	0.92	0.05
206	0.99	0.11	0.88	0.05
207	0.92	0.28	0.99	0.05
208	1.07	0.44	0.95	0.05
209	0.93	0.14	0.94	0.04
210	0.96	0.11	0.94	0.03
211	1.03	0.14	0.95	0.03
212	1.01	0.08	0.95	0.03
213	0.98	0.06	0.87	0.05
214	0.95	0.17	0.89	0.08

Index	Prefit	$\pm$ error	Postfit	$\pm$ error
215	1.08	0.45	0.91	0.05
216	0.93	0.16	0.95	0.03
217	0.96	0.09	0.93	0.03
218	1.02	0.12	0.94	0.03
219	1.01	0.07	0.94	0.03
220	1.00	0.04	0.93	0.03
221	0.98	0.09	0.91	0.04
222	1.09	0.43	0.92	0.04
223	0.94	0.15	0.94	0.04
224	0.93	0.10	0.93	0.04
225	1.02	0.12	0.94	0.04
226	1.01	0.08	0.96	0.04
227	1.00	0.07	0.95	0.03
228	0.99	0.05	0.92	0.03
229	1.02	0.34	0.96	0.04
230	1.00	0.09	0.94	0.04
231	1.01	0.07	0.95	0.04
232	0.99	0.13	0.93	0.05
233	0.99	0.11	0.92	0.07
234	0.98	0.33	0.97	0.06
235	1.05	0.34	0.95	0.04
236	0.97	0.05	0.93	0.03
237	1.02	0.06	0.95	0.03
238	0.98	0.09	0.93	0.03
239	0.99	0.06	0.92	0.03
240	0.98	0.14	0.92	0.06
241	1.04	0.36	0.92	0.05
242	0.97	0.05	0.93	0.04
243	1.01	0.05	0.94	0.04
244	1.00	0.09	0.93	0.04
245	1.01	0.06	0.93	0.04

Index	Prefit	$\pm$ error	Postfit	$\pm$ error
246	0.98	0.12	0.84	0.07
247	1.03	0.37	0.90	0.05
248	1.01	0.05	0.94	0.04
249	1.00	0.05	0.92	0.04
250	0.99	0.07	0.92	0.03
251	1.01	0.07	0.92	0.03
252	0.99	0.07	0.85	0.04
253	1.07	0.39	0.84	0.05
254	0.98	0.07	0.93	0.04
255	1.02	0.08	0.99	0.04
256	1.01	0.08	0.94	0.04
257	0.99	0.09	0.91	0.04
258	0.99	0.06	0.87	0.04
259	1.24	0.60	1.00	0.08
260	0.91	0.16	0.94	0.05
261	1.00	0.13	0.95	0.05
262	1.02	0.21	0.94	0.06
263	1.03	0.17	0.94	0.08
264	0.99	0.21	1.11	0.14
265	1.27	0.64	1.03	0.15
266	0.95	0.16	0.95	0.06
267	0.99	0.06	0.92	0.05
268	0.98	0.11	0.93	0.05
269	1.04	0.14	0.93	0.06
270	0.99	0.16	0.91	0.11
271	1.20	0.60	0.94	0.11
272	0.95	0.20	0.93	0.06
273	0.97	0.07	0.94	0.05
274	1.00	0.08	0.94	0.04
275	1.00	0.08	0.93	0.04
276	1.00	0.10	0.97	0.07

Index	Prefit	$\pm$ error	Postfit	$\pm$ error
277	1.10	0.52	0.93	0.09
278	0.99	0.16	0.96	0.06
279	0.95	0.06	0.91	0.05
280	0.99	0.04	0.94	0.04
281	1.00	0.07	0.93	0.03
282	1.00	0.06	0.95	0.04
283	1.19	0.50	0.95	0.09
284	0.98	0.15	0.99	0.07
285	0.96	0.09	0.97	0.07
286	0.99	0.07	0.91	0.06
287	1.00	0.06	0.94	0.03
288	1.00	0.04	0.92	0.03
289	1.12	0.46	1.00	0.07
290	1.01	0.15	0.91	0.06
291	0.98	0.09	0.90	0.05
292	1.00	0.09	0.94	0.05
293	0.98	0.07	0.92	0.03
294	1.00	0.03	0.92	0.03
295	1.29	0.47	1.04	0.11
296	0.98	0.20	1.10	0.12
297	0.95	0.16	0.92	0.09
298	1.03	0.10	0.95	0.05
299	1.01	0.08	0.98	0.03
300	1.00	0.03	0.93	0.03
301	0.97	0.21	0.90	0.07
302	1.01	0.13	1.00	0.06
303	1.01	0.15	0.99	0.06
304	1.15	0.19	1.12	0.07
305	0.95	0.23	0.90	0.12
306	1.00	0.26	0.99	0.07
307	0.99	0.08	0.91	0.05

Index	Prefit	$\pm$ error	Postfit	$\pm$ error
308	1.01	0.11	0.93	0.04
309	0.98	0.09	0.89	0.06
310	1.00	0.16	0.87	0.05
311	1.01	0.28	0.86	0.08
312	0.98	0.06	0.90	0.05
313	1.00	0.08	0.93	0.04
314	1.02	0.08	0.92	0.05
315	0.98	0.11	0.93	0.07
316	1.02	0.25	0.92	0.05
317	0.98	0.07	0.90	0.06
318	1.00	0.07	0.92	0.04
319	1.00	0.07	0.94	0.04
320	1.00	0.06	0.90	0.06
321	1.02	0.24	0.91	0.08
322	0.96	0.10	0.99	0.05
323	1.01	0.09	0.95	0.05
324	0.99	0.09	0.93	0.04
325	0.99	0.04	0.92	0.03
326	1.00	0.25	0.94	0.08
327	0.98	0.11	0.97	0.07
328	1.00	0.09	0.93	0.03
329	1.01	0.10	1.00	0.04
330	1.00	0.04	0.94	0.03
331	1.17	0.66	0.94	0.05
332	0.86	0.19	0.95	0.03
333	1.17	0.53	0.92	0.04
334	1.15	0.44	0.93	0.06
335	0.97	0.19	0.90	0.09
336	1.02	0.19	1.18	0.11
337	1.02	0.31	0.96	0.04
338	0.97	0.37	0.91	0.04

Index	Prefit	$\pm$ error	Postfit	$\pm$ error
339	0.88	0.62	0.92	0.03
340	1.27	0.75	0.90	0.04
341	0.87	0.17	0.95	0.03
342	1.04	0.31	0.94	0.03
343	1.09	0.34	0.95	0.04
344	1.01	0.18	0.91	0.04
345	1.03	0.17	0.91	0.03
346	0.94	0.27	0.94	0.04
347	0.93	0.38	0.99	0.06
348	1.00	0.58	0.96	0.08
349	1.32	0.79	0.98	0.06
350	0.90	0.20	0.95	0.03
351	0.98	0.17	0.93	0.03
352	1.04	0.19	0.93	0.03
353	1.01	0.10	0.98	0.04
354	1.00	0.07	0.94	0.05
355	0.97	0.14	0.86	0.10
356	1.06	0.22	1.09	0.11
357	1.00	0.33	0.88	0.04
358	1.29	0.73	0.91	0.04
359	0.91	0.20	0.97	0.03
360	0.97	0.11	0.95	0.03
361	1.02	0.12	0.94	0.03
362	1.00	0.07	0.93	0.03
363	1.01	0.04	0.95	0.03
364	0.98	0.09	0.91	0.04
365	0.98	0.15	0.99	0.04
366	0.98	0.21	0.97	0.04
367	1.23	0.68	0.94	0.09
368	0.91	0.20	0.94	0.04
369	0.98	0.12	0.94	0.04

Index	Prefit	$\pm$ error	Postfit	$\pm$ error
370	1.02	0.11	0.94	0.03
371	0.99	0.08	0.93	0.03
372	1.01	0.06	0.96	0.03
373	1.00	0.04	0.93	0.03
374	0.98	0.11	0.89	0.03
375	0.98	0.15	0.89	0.04
376	1.21	0.58	0.96	0.08
377	0.90	0.16	0.91	0.04
378	0.99	0.12	0.97	0.04
379	1.02	0.12	0.93	0.04
380	1.01	0.09	0.95	0.04
381	1.01	0.10	0.95	0.03
382	1.00	0.06	0.95	0.03
383	1.00	0.05	0.93	0.03
384	0.98	0.10	0.89	0.03
385	1.18	0.62	0.94	0.04
386	0.88	0.15	0.96	0.03
387	1.03	0.21	0.98	0.04
388	1.03	0.21	1.02	0.04
389	1.01	0.16	1.18	0.07
390	1.00	0.22	0.88	0.04
391	0.99	0.32	0.93	0.05
392	0.93	0.69	1.00	0.06
393	1.13	0.58	0.92	0.03
394	0.91	0.14	0.94	0.03
395	0.99	0.10	0.92	0.03
396	1.01	0.11	0.95	0.03
397	1.01	0.08	0.93	0.03
398	1.00	0.08	0.91	0.04
399	1.03	0.18	0.91	0.05
400	0.97	0.51	0.84	0.05

Index	Prefit	$\pm$ error	Postfit	$\pm$ error
401	1.12	0.55	0.94	0.03
402	0.92	0.13	0.93	0.03
403	0.99	0.08	0.95	0.03
404	1.00	0.08	0.93	0.03
405	1.01	0.07	0.91	0.03
406	1.00	0.06	0.89	0.03
407	0.98	0.13	0.88	0.03
408	0.93	0.45	0.96	0.03
409	1.09	0.51	0.95	0.03
410	0.93	0.11	0.93	0.04
411	0.99	0.08	0.91	0.04
412	1.00	0.08	0.91	0.03
413	1.00	0.07	0.95	0.03
414	1.00	0.03	0.94	0.03
415	0.99	0.10	0.89	0.04
416	0.97	0.28	0.96	0.07
417	1.09	0.48	0.95	0.05
418	0.94	0.12	0.95	0.03
419	0.98	0.11	0.94	0.03
420	1.01	0.10	0.92	0.04
421	1.01	0.09	0.94	0.04
422	1.01	0.07	0.94	0.03
423	0.99	0.06	0.91	0.03
424	0.97	0.13	0.87	0.03
425	0.99	0.29	0.94	0.04
426	0.92	0.14	0.93	0.03
427	1.05	0.24	0.88	0.04
428	1.05	0.18	0.92	0.05
429	1.02	0.17	0.83	0.08
430	0.87	0.19	0.96	0.07
431	0.96	0.41	0.79	0.06

Index	Prefit	$\pm$ error	Postfit	$\pm$ error
432	1.03	0.35	0.99	0.05
433	0.91	0.12	0.94	0.04
434	1.00	0.16	0.91	0.05
435	1.03	0.15	0.87	0.05
436	0.99	0.12	0.93	0.05
437	0.99	0.15	0.91	0.05
438	0.93	0.31	0.90	0.05
439	1.05	0.37	0.90	0.06
440	0.92	0.11	0.95	0.04
441	0.98	0.12	0.93	0.04
442	1.03	0.12	0.94	0.04
443	1.02	0.08	0.99	0.04
444	0.97	0.08	0.84	0.06
445	0.97	0.19	0.78	0.10
446	1.06	0.37	0.92	0.06
447	0.93	0.12	0.95	0.04
448	0.97	0.11	0.91	0.04
449	1.02	0.10	0.94	0.04
450	1.00	0.07	0.93	0.04
451	0.99	0.04	0.92	0.04
452	0.99	0.10	0.90	0.05
453	1.07	0.35	0.97	0.05
454	0.89	0.12	0.94	0.05
455	0.99	0.11	0.94	0.05
456	1.02	0.11	0.94	0.05
457	0.99	0.09	0.94	0.05
458	1.01	0.07	0.98	0.03
459	0.99	0.06	0.92	0.03
460	1.00	0.29	0.98	0.04
461	1.00	0.10	0.96	0.04
462	1.04	0.09	0.97	0.05

Index	Prefit	$\pm$ error	Postfit	$\pm$ error
463	0.98	0.14	0.93	0.05
464	0.98	0.13	0.89	0.09
465	0.92	0.33	0.85	0.06
466	1.00	0.31	0.92	0.04
467	0.99	0.06	0.93	0.03
468	1.02	0.06	0.95	0.03
469	0.99	0.11	0.93	0.03
470	0.99	0.06	0.94	0.04
471	0.96	0.16	0.98	0.06
472	1.00	0.32	0.92	0.05
473	1.00	0.07	0.92	0.04
474	1.00	0.06	0.95	0.04
475	1.00	0.11	0.90	0.04
476	1.00	0.06	0.92	0.04
477	0.99	0.13	0.88	0.07
478	1.03	0.32	0.90	0.05
479	0.99	0.07	0.93	0.04
480	1.02	0.07	0.93	0.04
481	0.99	0.10	0.92	0.04
482	1.01	0.08	0.93	0.04
483	0.98	0.09	0.78	0.04
484	1.02	0.31	0.76	0.05
485	1.01	0.07	0.96	0.05
486	1.02	0.08	0.94	0.05
487	0.98	0.10	0.91	0.04
488	1.00	0.09	0.92	0.04
489	0.99	0.07	0.87	0.04
490	1.10	0.50	0.93	0.09
491	0.92	0.12	0.96	0.06
492	1.03	0.16	0.96	0.07
493	1.02	0.20	0.91	0.08

Index	Prefit	$\pm$ error	Postfit	$\pm$ error
494	1.08	0.14	1.08	0.10
495	0.81	0.31	1.06	0.16
496	1.23	0.50	1.11	0.13
497	0.93	0.18	0.96	0.07
498	0.93	0.09	0.90	0.06
499	1.03	0.12	0.92	0.07
500	1.05	0.14	0.93	0.09
501	1.00	0.21	0.87	0.14
502	1.17	0.49	1.04	0.14
503	0.95	0.15	0.95	0.08
504	0.97	0.08	0.95	0.07
505	1.00	0.10	0.92	0.06
506	1.00	0.08	0.91	0.05
507	1.04	0.16	0.88	0.11
508	1.13	0.47	0.98	0.11
509	0.99	0.13	0.94	0.08
510	0.94	0.09	0.92	0.07
511	0.99	0.07	0.94	0.05
512	1.00	0.06	0.93	0.04
513	0.99	0.08	0.94	0.05
514	1.06	0.46	0.83	0.10
515	0.95	0.14	0.95	0.09
516	0.97	0.11	0.92	0.10
517	1.01	0.10	0.92	0.08
518	1.00	0.07	0.94	0.05
519	0.99	0.06	0.92	0.04
520	1.07	0.46	0.93	0.08
521	1.00	0.15	0.98	0.08
522	1.02	0.16	0.99	0.06
523	0.96	0.10	0.85	0.07
524	1.01	0.08	0.94	0.04

Index	Prefit	$\pm$ error	Postfit	$\pm$ error
525	0.99	0.04	0.92	0.03
526	1.19	0.46	1.03	0.14
527	0.89	0.17	1.01	0.10
528	0.99	0.15	0.92	0.09
529	0.99	0.10	0.93	0.06
530	1.00	0.09	0.95	0.04
531	1.00	0.03	0.93	0.03
532	0.97	0.22	0.96	0.08
533	1.02	0.17	0.92	0.07
534	1.00	0.14	1.05	0.07
535	1.28	0.22	0.91	0.07
536	0.83	0.25	1.00	0.13
537	0.98	0.22	0.93	0.08
538	0.99	0.09	0.92	0.06
539	1.00	0.11	0.91	0.05
540	1.03	0.11	0.90	0.07
541	1.04	0.20	0.91	0.05
542	1.01	0.25	0.87	0.08
543	0.98	0.08	0.89	0.06
544	1.01	0.08	0.92	0.05
545	1.00	0.08	0.95	0.06
546	0.99	0.12	0.99	0.08
547	0.99	0.22	0.92	0.05
548	1.00	0.10	0.95	0.07
549	1.01	0.07	0.93	0.05
550	1.00	0.07	0.93	0.05
551	1.00	0.07	0.87	0.07
552	1.00	0.22	0.95	0.09
553	0.99	0.12	0.90	0.05
554	1.04	0.10	0.96	0.06
555	0.99	0.10	0.90	0.05

Index	Prefit	$\pm$ error	Postfit	$\pm$ error
556	0.99	0.04	0.91	0.04
557	1.01	0.24	0.99	0.09
558	0.99	0.16	0.80	0.10
559	0.97	0.12	0.91	0.04
560	1.06	0.10	0.94	0.04
561	1.00	0.04	0.96	0.03
562	0.00	0.41	-0.04	0.19
563	0.00	0.34	-0.03	0.18
564	0.00	0.50	0.03	0.26
565	0.00	0.41	-0.47	0.13
566	0.00	0.57	0.42	0.34
567	0.00	0.28	0.01	0.15
568	1.00	0.03	0.85	0.05
569	1.00	0.06	1.03	0.10
570	1.00	0.06	0.91	0.06
571	1.00	1.00	2.71	0.31
572	1.00	1.00	1.32	0.25
573	1.00	0.20	0.94	0.13
574	1.00	3.00	2.00	0.09
575	1.00	3.00	2.00	0.21
576	0.59	0.12	0.53	0.07
577	1.05	0.21	1.63	0.13
578	1.13	0.17	1.28	0.13
579	0.88	0.35	1.12	0.33
580	1.20	0.10	1.20	0.10
581	0.95	0.15	0.86	0.07
582	1.13	0.16	1.12	0.04
583	0.74	0.31	1.04	0.18
584	1.00	0.03	1.00	0.03
585	1.00	0.03	1.00	0.03
586	0.00	0.40	-0.23	0.20

Index	Prefit	$\pm$ error	Postfit	$\pm$ error
587	1.00	0.30	0.48	0.44
588	1.00	0.30	0.48	0.44
589	1.00	0.30	1.13	0.30
590	1.00	1.00	1.00	1.00
591	1.00	0.30	1.13	0.18
592	1.00	0.30	1.00	0.30

<sub>1766</sub> **Appendix H**

<sub>1767</sub> **Postfit Receiver Operating  
Characteristic Curves**

<sub>1769</sub> The receiver operating characteristic (ROC) curves for the PØD vs FGD-only fits are provided in this  
<sub>1770</sub> appendix. They provide a graphical diagnostic to interpret each fit's sensitivity in the fit parameter space.  
<sub>1771</sub> The first 50 (0-49) are the ND280 flux parameters. The next 50 (50-99) are the Super-Kamiokande flux  
<sub>1772</sub> parameters. The final set (100 - 131) are the cross section parameters.

<sub>1773</sub> The ROC curves are generated in the following manner. Each ROC curve measures the agreement of the  
<sub>1774</sub> PØD-only fit parameter estimate (PØD coverage) as a function of the FGD-only parameter estimate (FGD  
<sub>1775</sub> coverage). Since the postfit parameter uncertainties are assumed to be normally distributed, two normal  
<sub>1776</sub> distributions are used to evaluate the agreement using the respective fit mean and fit standard deviation.  
<sub>1777</sub> Each point on the ROC curve is the integrated overlap of each normal distribution.

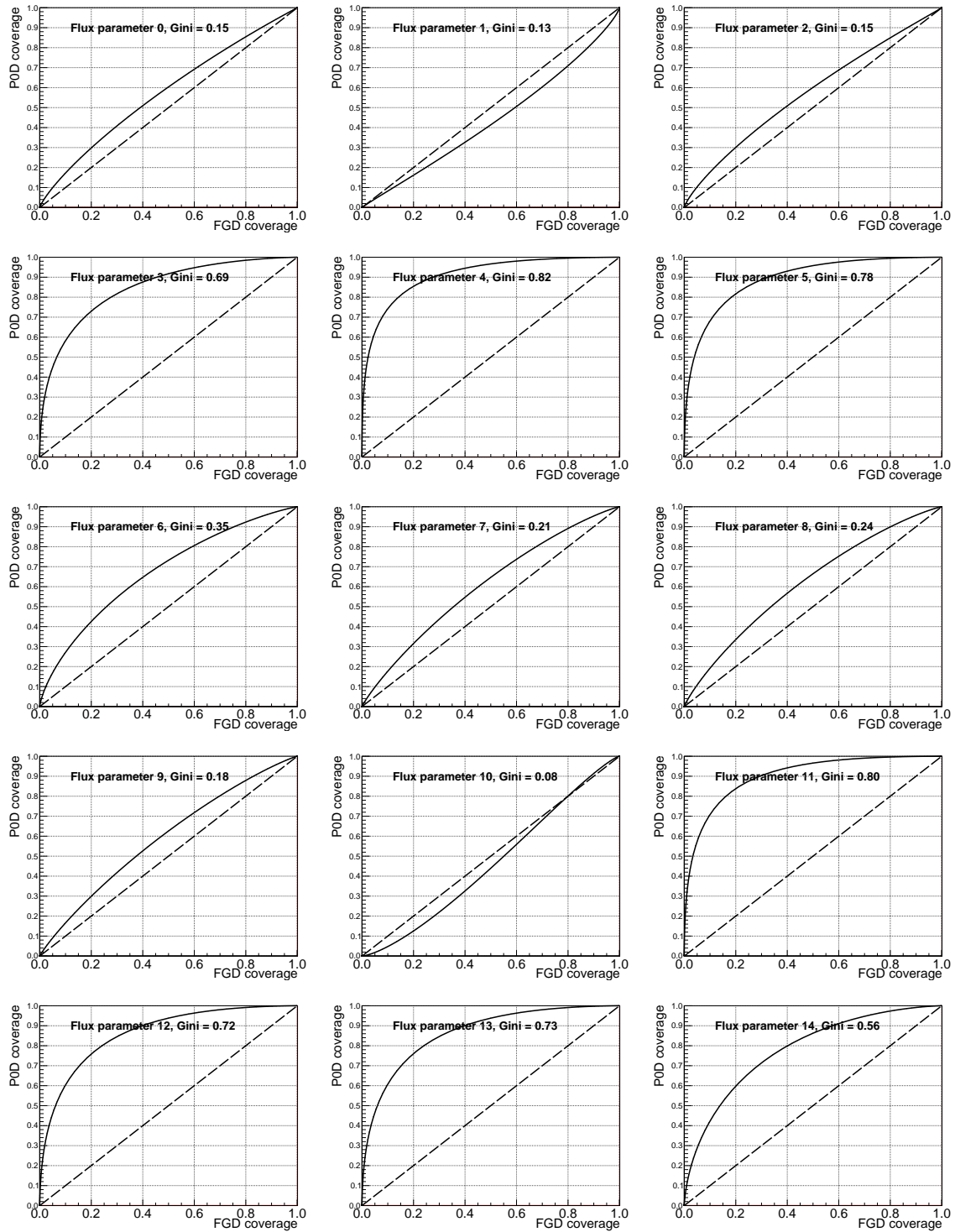
<sub>1778</sub> The level of agreement is quantified using the Gini coefficient, which measures the inequality of the fit  
<sub>1779</sub> parameter space coverage. A Gini coefficient of 0 indicates maximal agreement of the two parameters mean  
<sub>1780</sub> and standard deviation, while a value of close to 1 indicates estimates are in strong tension. The coefficient  
<sub>1781</sub> is defined as the absolute difference in area between the ROC curve and the diagonal (no-discrimination)  
<sub>1782</sub> line multiplied by two. It is explicitly calculated as

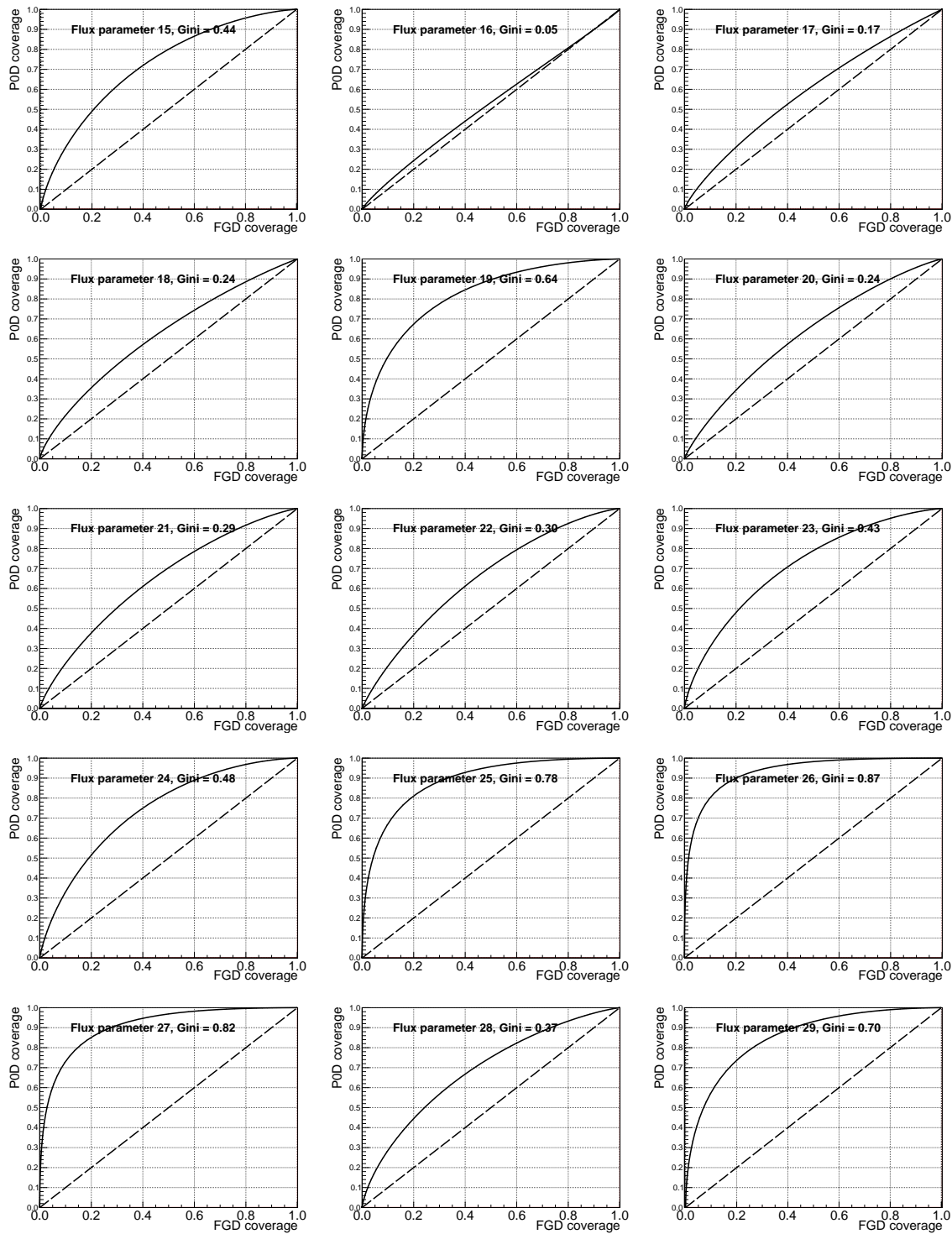
$$\begin{aligned} \text{Gini} &= 2 \left| \int_0^1 (\text{ROC}(x) - x) dx \right| \\ &= \left| 2 \int_0^1 \text{ROC}(x) dx - 1 \right|, \end{aligned}$$

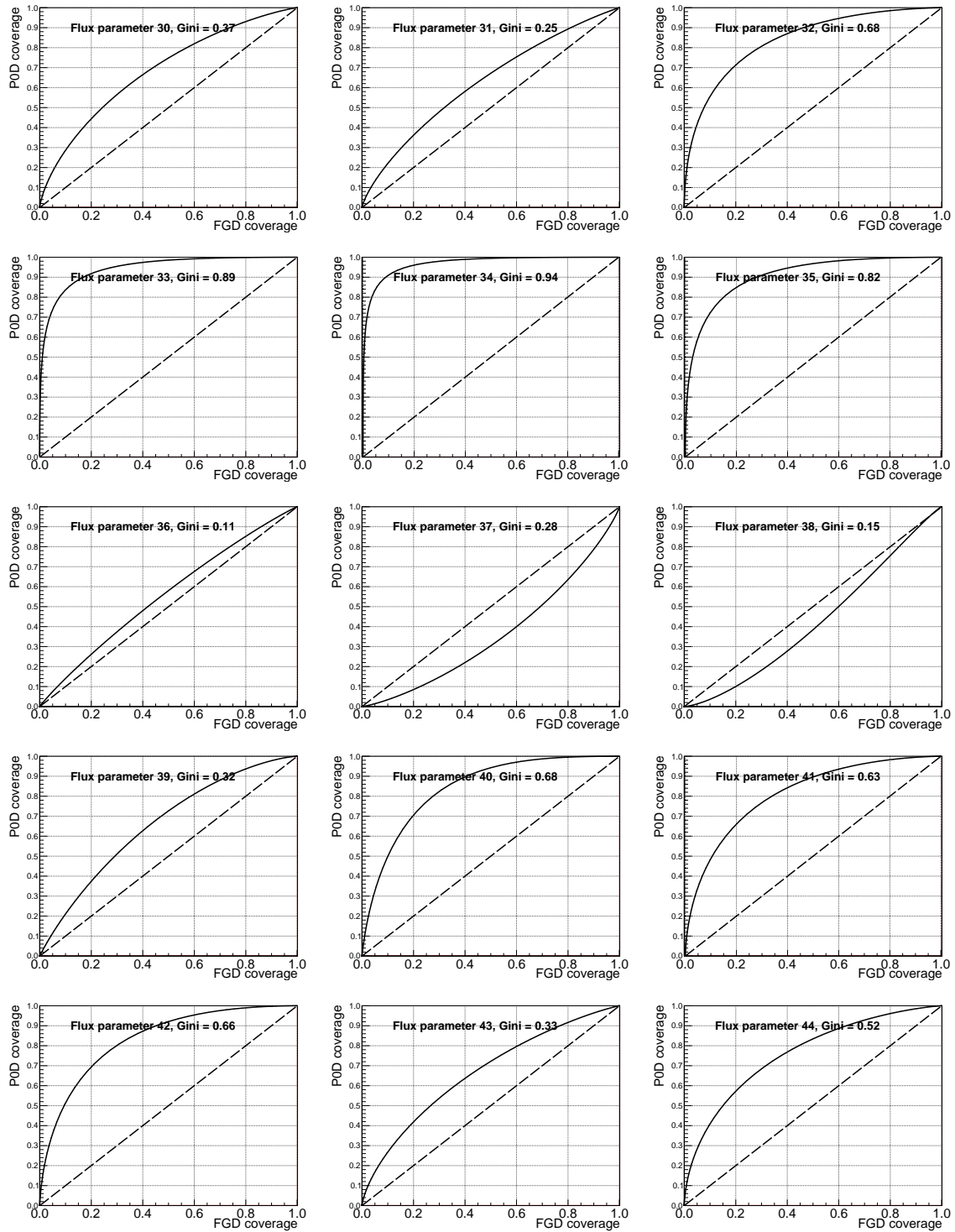
<sub>1783</sub> where  $\text{ROC}(x)$  is the PØD fit parameter space ROC curve as a function of the FGD fit parameter space

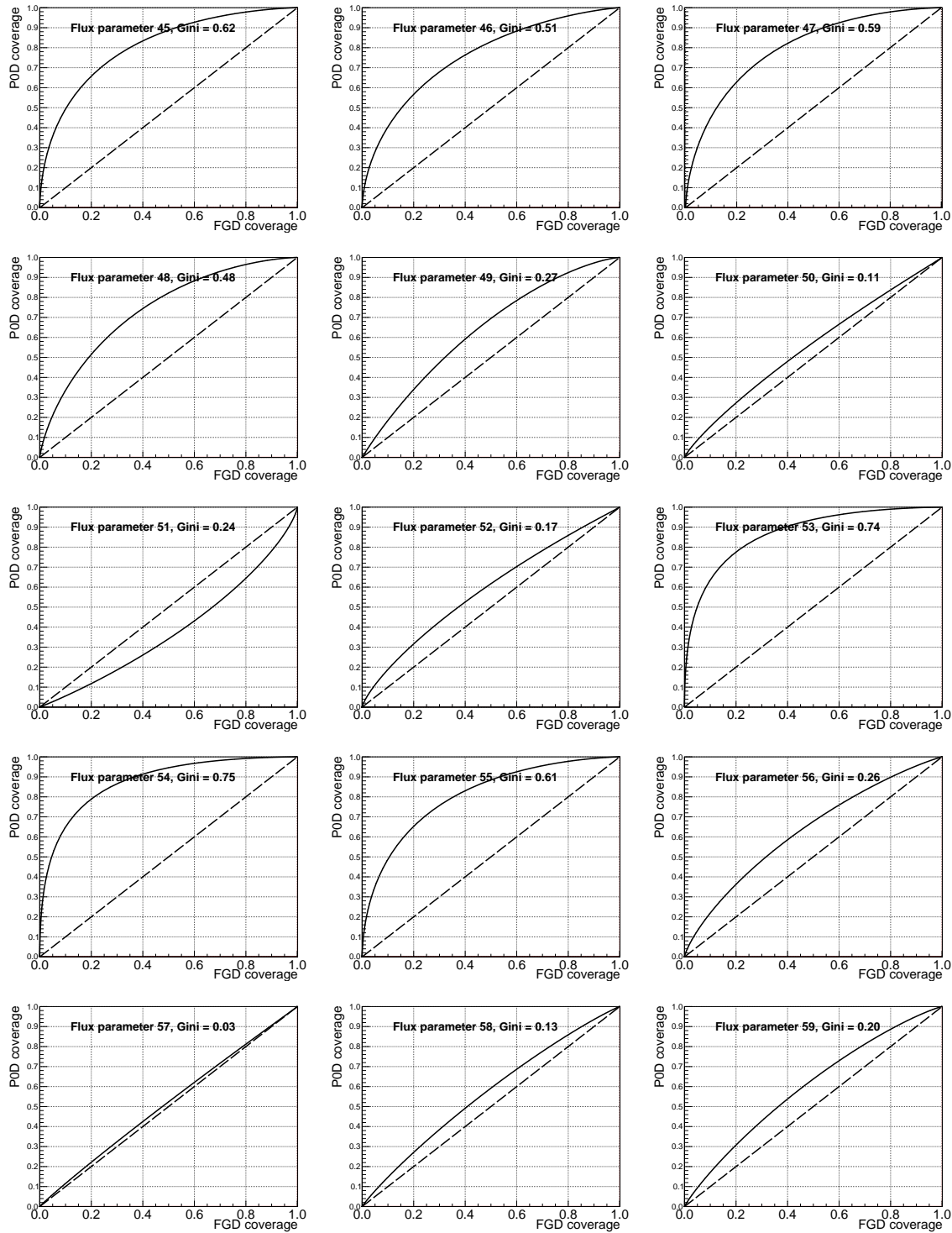
1784 coverage. This no-discrimination line is provided in each curve for the readers convenience.

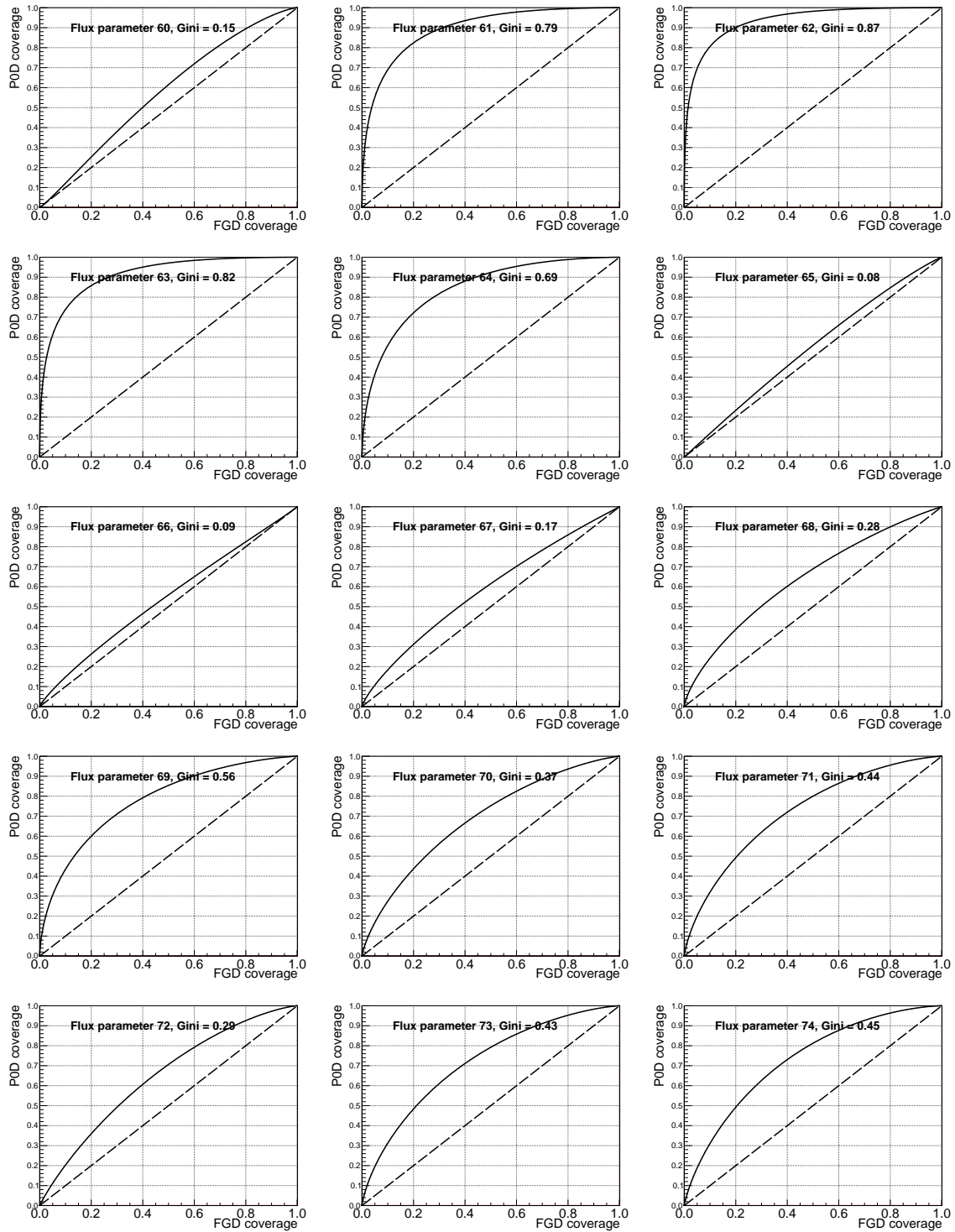
1785 When the ROC curve is only above (below) the no-discrimination line, that means the PØD-only fit  
1786 estimate prefers parameter values larger (smaller) than the FGD-only estimate. If the curve crosses the line  
1787 once between (0, 1), then the estimates are nearly identical and have a small Gini coefficient. If the ROC  
1788 curve is diagonal, then the estimates are exactly the same with a Gini coefficient of zero. And finally, if  
1789 the curve is a step function with the discontinuity at FGD coverage = 0, the parameter estimates are very  
1790 different with a Gini coefficient of one.

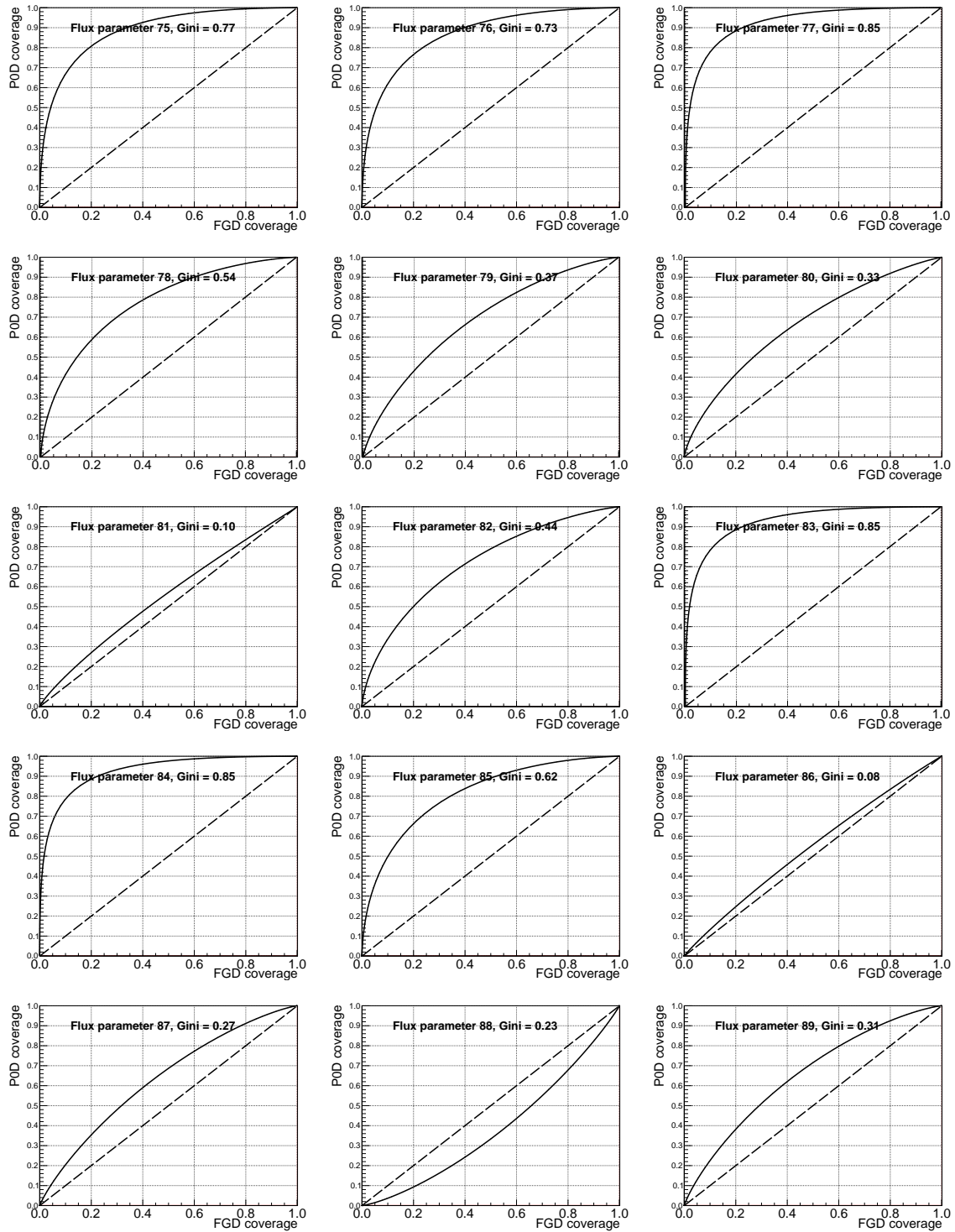


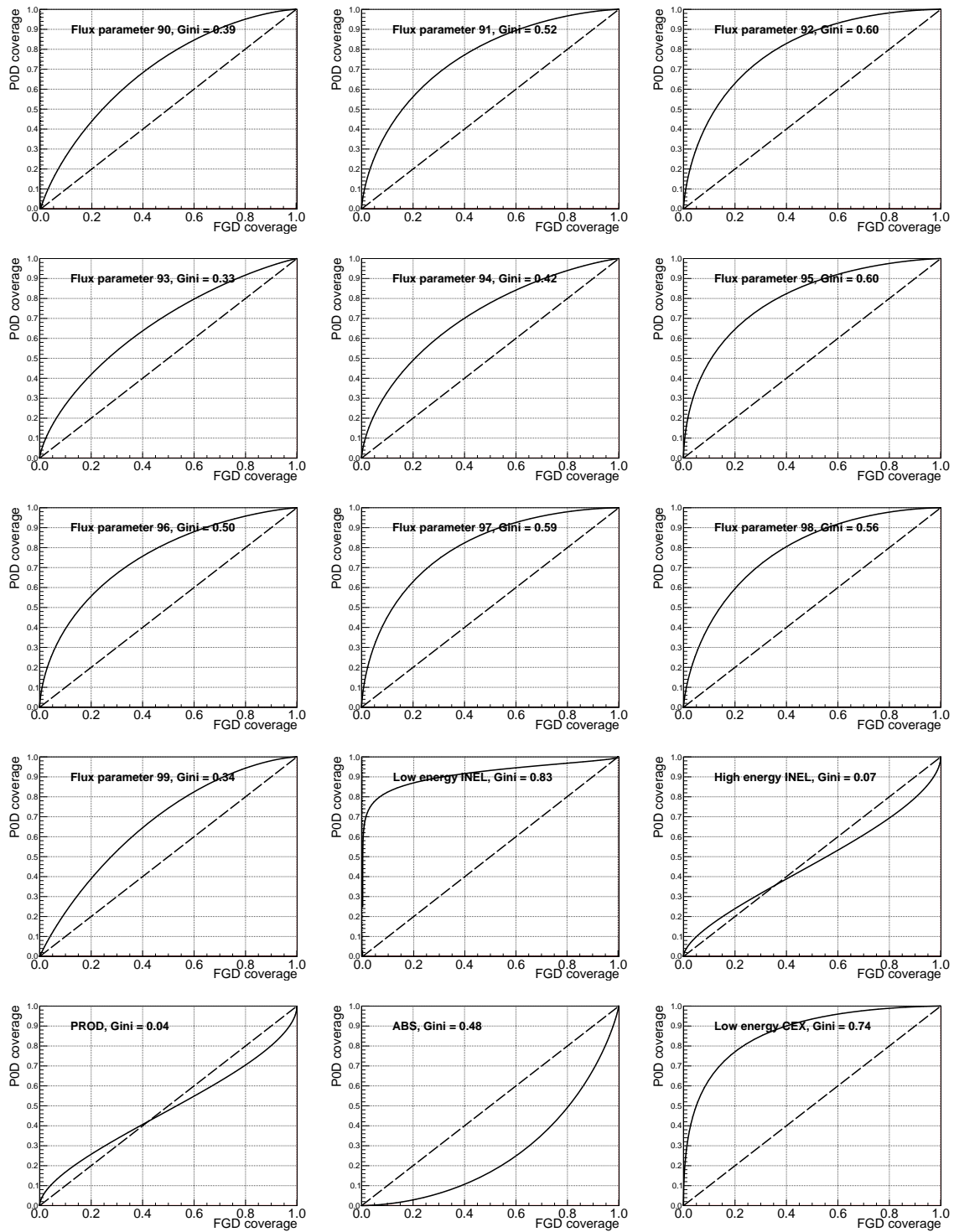


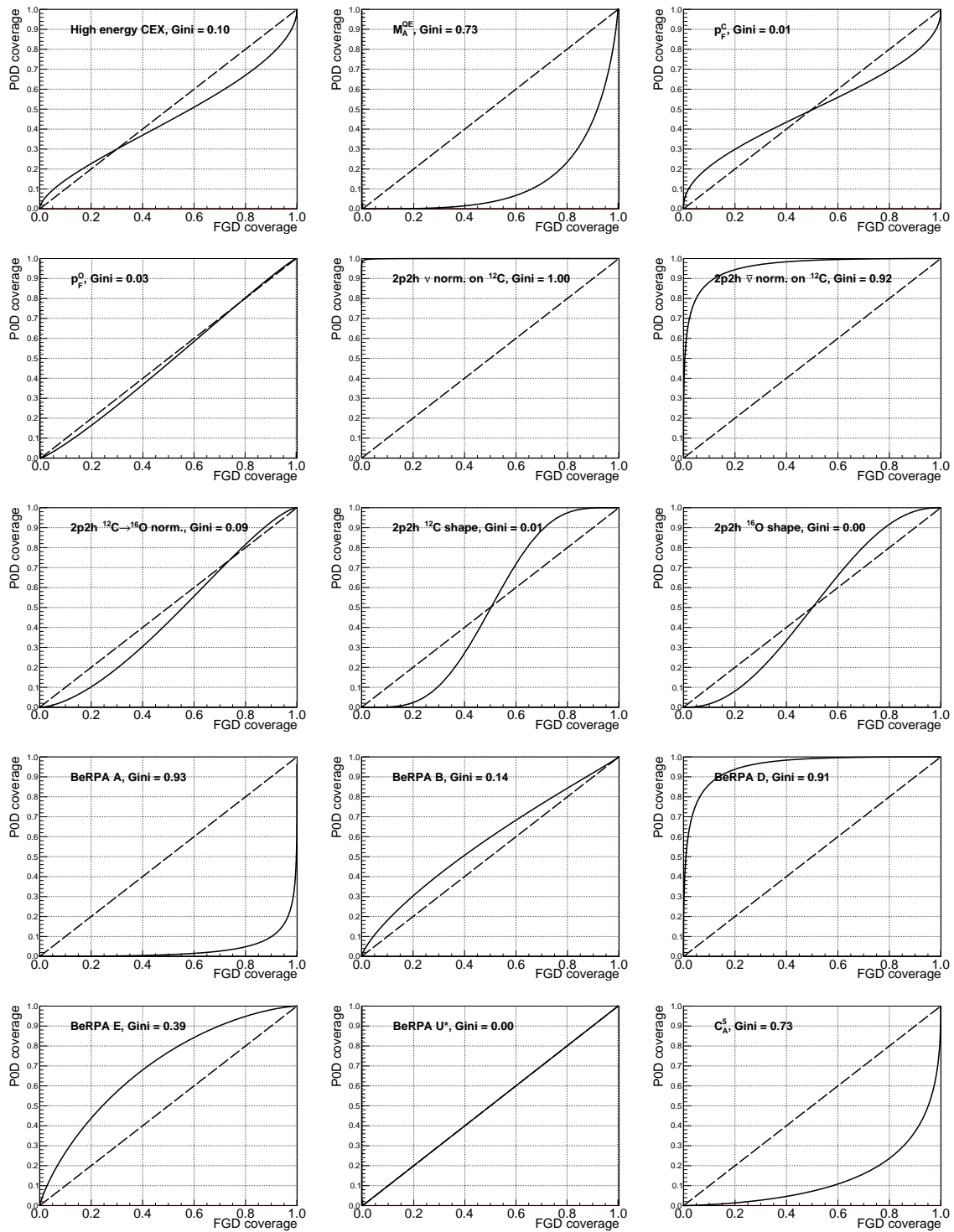


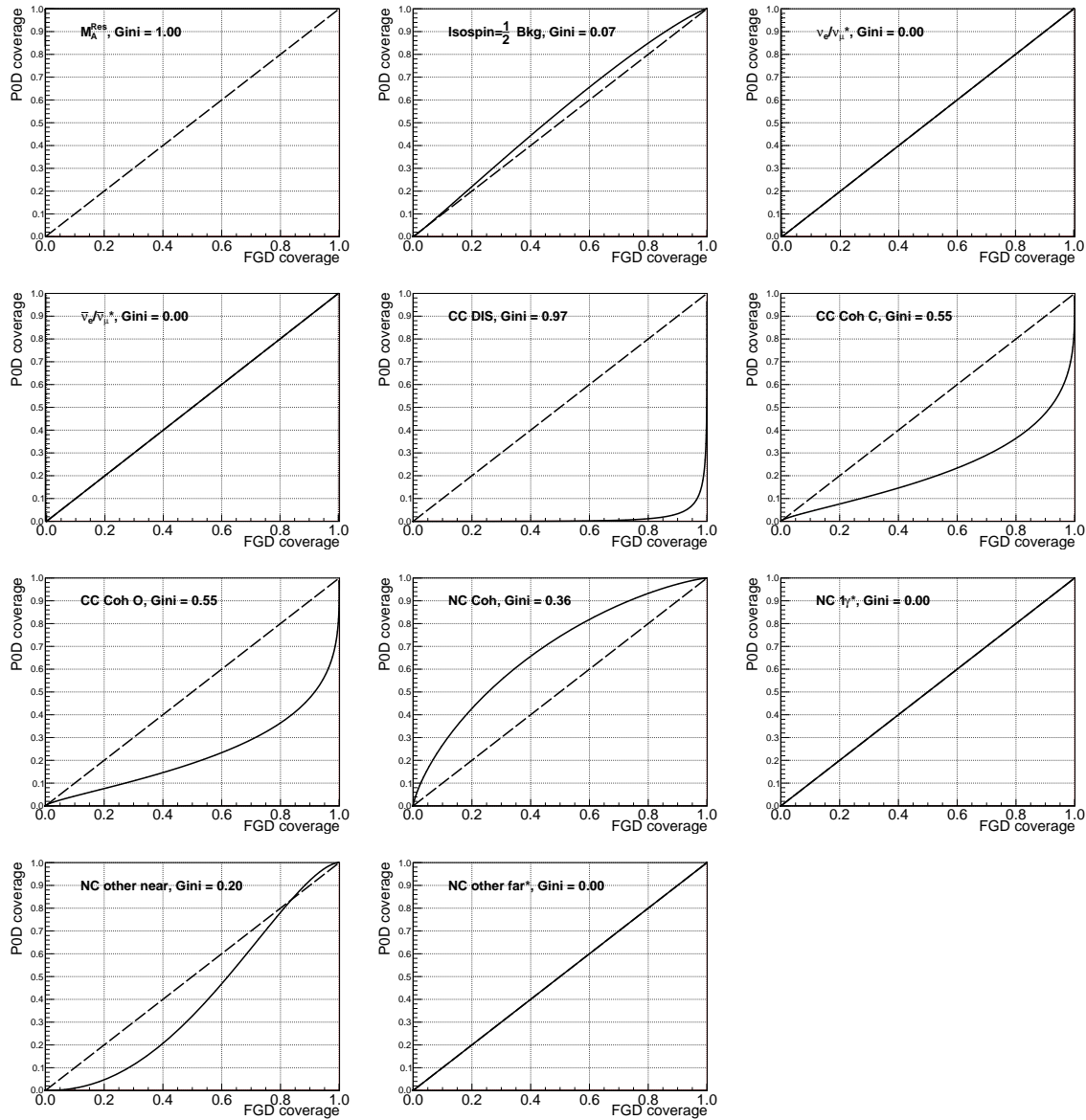












1800 **Appendix I**

1801 **Cross-Validated PØD-Only BANFF**

1802 **Fit**

1803 This appendix shows the postfit results of cross validated PØD-only fit discussed in Chapter 7. The cross  
1804 validation error Eqn. (??) was minimized with a regularization strength of  $\lambda = 1.4$ . That is to say the  
1805 penalty term in the test statistic went from

$$\chi_{\text{Penalty}}^2 = (\Delta \vec{y})^T V^{-1} (\Delta \vec{y})$$

1806 to

$$\chi_{\text{Penalty}}^2 = \lambda (\Delta \vec{y})^T V^{-1} (\Delta \vec{y}).$$

1807 We generally see the flux parameters have a slightly larger bias, but reduced uncertainty. The cross section  
1808 parameters are largely unchanged. The first eight figures are the ND280 flux parameters. The following eight  
1809 are the unoscillated Super-Kamiokande (SK) flux parameters. The next five are the cross section parameters.  
1810 The final two are the bin normalization parameters.

